UNIVERSIDADE DE SANTIAGO DE COMPOSTELA

FACULTADE DE QUÍMICA

DEPARTAMENTO DE QUÍMICA FÍSICA

PhD Thesis

Classical Trajectory Simulations of Collisions between Polyatomic Molecules and a Self-Assembled Monolayer Surface

Juan José Nogueira Pérez

Santiago de Compostela, July 2011

Dr. Emilio Martínez Núñez y Dr. Saulo A. Vázquez Rodríguez, Profesores Titulares del Departamento de Química Física de la Universidade de Santiago de Compostela, autorizan la presentación de la tesis doctoral titulada "**Classical Trajectory Simulations of Collisions between Polyatomic Molecules and a Self-Assembled Monolayer Surface"** realizada por D. Juan José Nogueira Pérez, Licenciado en Química por la Universidade de Santiago de Compostela, para optar al grado de Doctor en Química.

Y para que así conste, firmamos el presente documento a Julio de 2011.

Dr. Emilio Martínez Núñez

Dr. Saulo A. Vázquez Rodríguez

AGRADECIMIENTOS

Me gustaría empezar mis agradecimientos por mis directores de tesis, Emilio Martínez Núñez y Saulo Vázquez Rodríguez, por todo su apoyo, empeño y, sobre todo, paciencia durante estos cinco años. Todo lo que he aprendido gracias a vosotros durante este tiempo va mucho más de allá de esta tesis.

Quisiera mostrar mi agradecimiento al Profesor Antonio Fernández Ramos, miembro también de este grupo de investigación, por su inestimable ayuda siempre que se la he pedido.

A mis actuales compañeros de despacho, Ceila Fong, Daniela Josa, Luis Simón, Marcos Rellán, y en especial, a Rubén Meana, por compartir estos cinco años de amistad, cafés, cálculos, discusiones químicas y otras no tan químicas. A los miembros del grupo de Química Cuántica, Silvia Bouzón y Hubert Cybulski. También me gustaría agradecer la gran labor que ha realizado nuestro administrador de sistemas Javier López.

Muchas gracias por los buenos momentos compartidos en el despacho y fuera de él a las personas que pasaron por este grupo: Marta Pombar, Antonio Sánchez, Zahra Homayoon, David Glowacki, Javier Aguilar y Teresa Cusati. Dentro de este grupo me gustaría destacar a Nicolás Ramos y a Alejandro Ramos por la gran amistad que nos une, y por toda su ayuda incondicional tanto en la tesis como en otros asuntos personales. Muchas gracias a los dos.

I would like to thank Professor William Hase for giving the opportunity to take part in the PIRE program (Partnerships for International Research and Education) the last three years. Moreover, thank you very much for your help and discussions about the works of this thesis.

Al Profesor Jorge Marques por su amistad y su gran ayuda con los ajustes llevados a cabo en esta tesis.

Me gustaría también dar las gracias al Ministerio de Educación, a la Xunta de Galicia y la Universidade de Santiago de Compostela por su financiación sin la que hubiese sido más complicada la realización de esta tesis.

Muchas gracias a José Luis Noya y a su "tropa", Lucía, Juan, Verónica, Pepita, María, Sonia, Luis, Tania, Rocío, Sara …, es imposible mencionaros a todos. Gracias por vuestra amistad a lo largo de estos años. Sin duda, parte de esta tesis también es gracias a vosotros.

A mis compañeros de los cursos de doctorado de Santander por convertir aquel mes en una experiencia inolvidable. Gracias a Pablo, Miquel, Laia, Anna, Mireia, Víctor, Ceila, Silvia, Eli, Ramón y a todos los demás que he podido olvidar.

A mis amigos de O Carballiño: Rubio, Toni, Rubén, Neira, Laura, Ana, Marina, Víctor, Julio, Borja, Miriam, Arantxa, Pablo, Roberto … Perdonad por no mencionaros a todos; muchísimas gracias por hacerme desconectar, a veces incluso más de la cuenta.

Muchísimas gracias a mi hermano Manolo por compartir esta aventura fuera de casa durante ya 10 años. Esos cafés son los que mejor me saben. Gracias también a María por su amistad.

A mis tíos y primos Servando, Leonor, Fina, Alberto y con muchísimo cariño a Lucía. Gracias por haberme apoyado siempre y por vuestro apoyo futuro, que estoy seguro me daréis.

Por supuesto, muchísimas gracias a mis *tres madres* Concha, Fina y Libia, las personas más luchadoras y desinteresadas que uno se puede imaginar. No hay palabras que puedan mostrar mi agradecimiento, y creo que nunca os podré dar tanto como vosotras me habéis dado a mí.

Y por último, y en este caso más importante, muchísimas gracias a Trini por todo lo que compartimos y por todo lo que has hecho por mí. Creo que no pude haber tenido más suerte en la vida por haberte encontrado. *TQI*.

A Trini y a mis tres madres

Concha, Fina y Libia

The definition of insanity is doing

the same thing over and over again

and expecting different results

Albert Einstein

INDEX

Resumen

Los sistemas de tamaño nanométrico presentan propiedades muy interesantes debido a su tamaño mesoscópico. En las últimas décadas, gracias al gran desarrollo de técnicas experimentales, cada vez más complejas, el campo de la nanotecnología ha experimentado un gran crecimiento.

Las superficies monocapa autoensambladas (SAMs) son ampliamente utilizadas como modelo para llevar a cabo estudios sobre el comportamiento de dichos nanomateriales. Su síntesis relativamente sencilla, así como su fácil caracterización, han originado que este tipo de superficies sean cada vez más utilizadas.

Uno de los procesos ampliamente investigados en los últimos años, tanto de manera experimental como teórica, es la colisión de iones y moléculas neutras contra este tipo de superficies. Estas colisiones dan lugar a una gran variedad de procesos reactivos y no reactivos, sobre todo en el rango de energías hipertérmico (1-100 eV). El estudio del mecanismo que opera en este tipo de procesos proporciona información acerca de las características del nanomaterial, y por tanto acerca de sus posibles aplicaciones.

Muchos de los detalles dinámicos del mecanismo de colisión son de difícil o imposible visualización y análisis desde el punto de vista experimental. Es aquí donde las simulaciones cobran importancia. El método de trayectorias clásicas ha sido aplicado con éxito en los últimos años a una gran variedad de procesos diferentes, entre los cuales se encuentran las colisiones gas/superficie.

El objetivo principal de esta tesis es llevar a cabo simulaciones, mediante el método de trayectorias clásicas, de colisiones inelásticas entre moléculas poliatómicas y una superficie monocapa autoensamblada. En concreto, los proyectiles investigados fueron el CO_2, el NO y los iones $SiNCS^+$ y $(CH_3)_2SiNCS^+$; la superficie modelo utilizada está formada por cadenas de octanotiol perfluorado $CF_3(CF_2)_7S$ adsorbidas sobre una capa de Au{111} de un átomo de espesor. A lo largo de esta tesis esta superficie es denominada F-SAM (*perfluorinated self-assembled monolayer*) El programa utilizado para integrar las ecuaciones del movimiento fue el VENUS05, desarrollado por Hase y colaboradores.

Cuando una molécula en fase gas colisiona contra una superficie pueden tener lugar varios procesos, como se discutirá más en detalle en el Capítulo 2. Entre ellos cabe destacar, entre otros, la dispersión inelástica, las disociaciones inducidas por superficie (SID), transferencia electrónica, procesos de *sputtering* químico, reacciones proyectil/superficie y fisisorción. En las colisiones de dispersión inelástica simplemente se produce intercambio de energía entre el proyectil y la superficie sin que tenga lugar reacción química. Este proceso es ampliamente estudiado a lo largo de esta tesis. La disociación de la molécula debido a la colisión con la superficie (SID) tiene

lugar cuando la transferencia de energía a los grados de libertad vibracionales del proyectil es superior a la energía de disociación de alguno de sus enlaces. Otro proceso que puede tener lugar durante la colisión es la transferencia de uno o varios electrones desde las cadenas de la monocapa o desde la superficie metálica al proyectil. Si esta transferencia electrónica lleva asociada la disociación de algún grupo funcional de la superficie, el proceso se denomina *sputtering* químico. Finalmente, el proyectil también puede ser adsorbido en la superficie mediante interacciones físicas, sin que se forme enlace químico, dando lugar a *soft-landing*. Este tipo de colisión y la transferencia electrónica entre el metal y el proyectil son discutidos en el Capítulo 11 de esta tesis.

Antes de resolver las ecuaciones del movimiento para llevar a cabo las trayectorias, es necesario conocer la superficie de energía potencial que gobierna nuestro sistema. La parte más importante de esta superficie es aquella que nos da las interacciones intermoleculares, que son explicadas en el Capítulo 3. Según el comportamiento de la energía de interacción con la distancia intermolecular, dichas interacciones se pueden clasificar en interacciones de corto alcance e interacciones de largo alcance. En el primer caso la energía de interacción varía bruscamente con la distancia, y en el segundo tipo de interacciones esta variación es más lenta. Las interacciones de corto alcance son repulsivas, y surgen a distancias muy cortas debido a la repulsión entre las nubes electrónicas. Las fuerzas de largo alcance son atractivas y se clasifican en diferentes tipos según cual sea la naturaleza de su origen. Así, las interacciones electroestáticas son aquellas que surgen de la interacción entre cargas y multipolos permanentes que posean las moléculas. Las interacciones de inducción aparecen debido a la distorsión de las cargas de una molécula por la acción de la carga o el multipolo de otra molécula vecina. Y las interacciones de dispersión surgen debido a la fluctuación espontánea de las cargas que se puede originar en una molécula, induciendo alteraciones en la densidad electrónica de moléculas vecinas. Todas estas interacciones tienen un comportamiento distinto con la distancia intermolecular, y deben ser tenidas en cuenta cuando se escoge una función analítica para construir la superficie de energía potencial.

A lo largo de esta tesis, los parámetros que definen los potenciales intramoleculares fueron obtenidos mediante el ajuste de las frecuencias de vibración calculadas con métodos de estructura electrónica. La ecuación analítica que describe el potencial intermolecular fue determinada a partir del ajuste de energías de interacción, calculadas también con métodos mecanocuánticos, a una suma de funciones de dos cuerpos; el potencial de Buckingham exp-n-m fue la expresión utilizada en dichos ajustes. Esto significa que las interacciones de muchos cuerpos no son tenidas en cuenta. Las optimizaciones de los parámetros del potencial intermolecular fueron llevadas a

cabo con la ayuda de un algoritmo genético. Los algoritmos genéticos están basados en los principios de la selección natural. En un primer paso, parten de un conjunto de soluciones generadas de manera aleatoria. Dichas soluciones se van modificando mediante procesos de mutación y entrecruzamiento dando lugar a nuevas soluciones, es decir, a nuevos conjuntos de coeficientes. Estas nuevas soluciones son evaluadas, y las mejores son seleccionadas para intervenir en las siguientes etapas, mientras que las soluciones que conducen a un mal ajuste son descartadas. Este tipo de algoritmos proporcionan generalmente mejores resultados que los algoritmos de optimización convencionales basados en el gradiente o en la hessiana.

Los métodos de estructura electrónica, presentados en el Capítulo 4, permiten evaluar la energía (y muchas otras propiedades) de un determinado sistema. Se clasifican en tres grandes grupos: métodos *ab initio*, métodos DFT (*density functional theory*) y métodos semiempíricos. Los métodos semiempíricos no fueron utilizados en esta tesis. Los métodos *ab initio* utilizan el Hamiltoniano real sin hacer ningún tipo de simplificación. Suelen proporcionar los resultados más precisos. Tanto los métodos semiempíricos como los *ab initio* intentan encontrar la función de onda que describa mejor al sistema. Para ello, algunos de estos métodos, optimizan los coeficientes de los orbitales moleculares de manera que a partir de ellos se obtenga la energía más baja posible, es decir, hacen uso del teorema variacional. Otros métodos utilizan la teoría de perturbaciones para el cálculo de la energía. Los métodos pertenecientes a la teoría del funcional de la densidad (DFT) se basan en la densidad electrónica, en lugar de en la función de onda, para determinar la energía del sistema. También aplican el teorema variacional, optimizando los coeficientes de los orbitales moleculares para dar lugar a una densidad electrónica que produzca la energía más baja posible.

Todos los métodos mecanocuánticos utilizados a lo largo de esta tesis utilizan la aproximación de Born-Oppenheimer, es decir, suponen que el sistema se encuentra siempre en el mismo estado electrónico, y por tanto no se producen transiciones no adiabáticas. Además, los efectos relativistas tampoco son tenidos en cuenta en este tipo de cálculos. En concreto, los métodos mecanocuánticos utilizados en los trabajos de esta tesis son RI-MP2, CCSD(T), RIJ-DFT-D y SAC-CI. Todas estas técnicas están basadas en el método de Hartree-Fock (HF) que trata la interacción interelectrónica de una manera simplificada para facilitar la resolución de la ecuación de Schrödinger. En concreto, la aproximación HF considera la interacción de cada uno de los electrones con el campo promedio creado por todos los demás, es decir, no determina las interacciones entre electrones de manera explícita. Esto hace que la correlación electrónica no se tenga en cuenta totalmente. Todos los métodos

desarrollados después de la aproximación HF, incluidos los mencionados arriba, tratan de calcular de manera más exacta la energía de correlación.

La siguiente etapa de esta metodología es seleccionar las coordenadas y los momentos iniciales de todos los átomos de nuestro sistema. Esta selección es comúnmente llamada muestreo de condiciones iniciales. El Capítulo 5 trata de manera detallada los métodos utilizados en esta tesis para realizar dicho muestreo. De manera general, la selección se basa en métodos de Monte Carlo, es decir, existe cierta aleatoriedad a la hora de escoger las condiciones iniciales.

Un aspecto importante cuando se llevan a cabo simulaciones que involucren superficies, es el uso de condiciones de contorno periódicas. Esta técnica permite replicar en el espacio, de manera "infinita", la celda unidad primaria que representa a la superficie. Las réplicas de esta celda se denominan celdas imagen. De esta manera, cuando una partícula sale de la celda primaria en dirección, por ejemplo, $+x$, una partícula imagen entra en dicha celda desde una celda imagen que se encuentra en la dirección $-x$ con respecto a la celda primaria. El uso de condiciones de contorno periódicas permite que las simulaciones sean más realistas ya que estamos imitando, de manera relativamente precisa, una superficie de tamaño macroscópico.

Después de seleccionar las condiciones iniciales y de disponer de la superficie de energía potencial, ya estamos en condiciones para resolver las ecuaciones clásicas del movimiento (ecuaciones de Newton o de Hamilton). Dichas ecuaciones requieren una resolución numérica. Existe una gran cantidad de algoritmos que permiten llevar a cabo esta resolución (Capítulo 5). De manera general, estos métodos se dividen en dos grandes grupos: métodos de una etapa y métodos multi-etapa. Los métodos de una sola etapa, también denominados métodos Runge-Kutta, calculan las coordenadas q y lo momentos p del paso $n+1$ conociendo simplemente q_n y p_n, es decir, las coordenadas y los momentos de la etapa anterior. Los métodos multi-etapa son más precisos, pero también requieren más información; si el método es de orden n, necesitamos conocer las coordenadas y los momentos de las n etapas anteriores. Esto significa que los algoritmos multi-etapa no son capaces de empezar el cálculo por sí solos, es decir, en los primeros pasos de la simulación se necesita un método Runge-Kutta.

Las ecuaciones del movimiento se resuelven durante un número de pasos determinado o hasta que el proceso que estamos simulando llegue a su fin. Una vez finalizada la simulación, se pueden determinar un gran número de propiedades de manera clásica a partir de las coordenadas y de los momentos finales. Además, puesto que conocemos la posición de todos lo átomos que forman el sistema en todo momento, también podemos determinar otro tipo de

propiedades que sean dependientes del tiempo, es decir, que no dependan exclusivamente de las condiciones finales.

En los primeros tres trabajos de esta tesis, explicados en los Capítulos 6, 7 y 8, se estudió la colisión de la molécula de CO_2 contra la superficie F-SAM. La superficie de energía potencial de este sistema ya había sido desarrollada en un trabajo anterior realizado en nuestro grupo de investigación. En estas simulaciones se investigó la influencia de la energía de colisión del proyectil en la dinámica, y el papel que juega la masa de la superficie. Para describir el potencial de la F-SAM se utilizaron dos modelos diferentes. El primero de ellos, denominado *all-atom (AA) model*, trata todos los átomos de la monocapa de manera explícita, es decir, no hace ninguna simplificación en la estructura de la superficie. El segundo modelo utilizado, denominando *united atom (UA) model*, considera los grupos CF_3 y CF_2 como pseudoátomos. Los resultados de las simulaciones indican que la superficie UA es más flexible que la superficie AA. Esta conclusión surge de la observación de que existe una mayor transferencia de energía y un mayor número de trayectorias de penetración en la superficie UA. También se comprobó que la masa de los átomos de la superficie juega un papel importante en la dinámica. Para llevar a cabo este análisis se sustituyeron los átomos de F de la monocapa, primero por átomos de H, y después por átomos de Cl. Cuando se utilizaron átomos de H se observó un aumento en la eficiencia de la transferencia de energía, indicando que una disminución en la masa de la superficie incrementa la flexibilidad de las cadenas. También se llevó a cabo una comparación con datos experimentales. En concreto, las funciones de distribución de números cuánticos rotacionales y las temperaturas traslacionales, determinadas a partir de los resultados del modelo AA, mostraron una buena concordancia con los resultados extraídos de los experimentos. La concordancia del modelo UA no fue tan buena.

Con el objetivo de mejorar los datos del modelo UA, se desarrollaron otros modelos de este tipo. Uno de ellos (denominado UA3 en el Capítulo 7) proporcionó resultados claramente superiores a los calculados por el modelo UA original. El potencial UA3 fue determinado mediante la rotación aleatoria de los grupos CF_3 y CF_2, calculando la energía en cada una de estas rotaciones a partir del campo de fuerzas del modelo AA. Todas estas energías fueron promediadas para distintas distancias entre dos grupos CF_x, y posteriormente fueron ajustadas a una función analítica. Además de mostrar una exactitud similar al modelo AA, el modelo UA3 requiere 3 veces menos tiempo de cálculo.

En otro de los trabajos en donde el CO_2 fue utilizado como proyectil, se analizó la relajación vibracional debido a la interacción con la superficie.

Puesto que esta molécula es lineal y posee dos flexiones degeneradas, su acoplamiento hace que se genere un momento angular vibracional. Este hecho hace que sea de gran interés el análisis de la transferencia de energía desde las flexiones hacia la F-SAM. Durante la simulación se observó que ciertas trayectorias perdían la energía del punto cero de los modos normales de flexión en los primeros pasos de la simulación, antes de que el CO_2 colisionase con la monocapa. Un análisis más detallado de la dinámica reveló que en las trayectorias que conservaban bien la energía, existía una relación lineal entre las fases iniciales de las flexiones y de la tensión simétrica. Las trayectorias que conservan la energía en las flexiones se corresponden con órbitas periódicas, y su análisis conduce a conclusiones similares a las obtenidas a partir del análisis del conjunto total de trayectorias. De nuevo, un análisis de la temperatura vibracional proporcionó una buena concordancia con los experimentos y permitió calcular, de manera cualitativa, que el tiempo necesario para que el modo normal degenerado de la flexión alcance equilibrio térmico con la superficie es superior a 50 ps.

Otro proyectil que fue utilizado en las simulaciones fue la molécula de NO; la dinámica de este sistema NO/F-SAM es discutida en el Capítulo 9. Antes de llevar a cabo las trayectorias, se construyó la superficie de energía potencial mediante el ajuste de energías de interacción para varias orientaciones entre el NO y la molécula de CF_4, calculadas con el método fp-CCSD(T)/CBS. Los aspectos más relevantes que se obtuvieron a partir del análisis de las trayectorias son los siguientes. Primero, se observó que los grados de libertad rotacionales del NO alcanzan equilibrio térmico con la superficie cuando se produce un cierto número de cambios pequeños en la dirección del momento angular rotacional. Un nuevo modelo para describir la transferencia de energía gas/superficie fue propuesto, y se observó que ajustaba muy bien los datos obtenidos de las simulaciones. Este modelo está basado en el parámetro de adiabaticidad y predice un 100% de transferencia de energía a la superficie en el límite de altas energías de colisión. Otro aspecto investigado en las simulaciones fue la estereodinámica. Un análisis detallado del comportamiento del momento rotacional de las moléculas que salen dispersadas de la F-SAM mostró que los movimientos rotacionales favoritos son tipo *rueda* y *sacacorchos*.

En el capítulo 10 se construyeron las curvas de energía potencial intermoleculares para los sistemas $SiNCS^+$/F-SAM y $(CH_3)_2SiNCS^+$/F-SAM. En este trabajo se comprobó que el funcional B97 incluyendo un término tipo Cr^{-6} para la dispersión, proporciona energías de interacción bastante exactas si se comparan con cálculos CCSD(T)/CBS. Además, también se observó que las interacciones de muchos cuerpos son despreciables en estos sistemas. Los coeficientes obtenidos a partir de los modelos $SiNCS^+/CF_4$ y

$(CH_3)_2SiNCS^+/CF_4$ reproducen correctamente la energía de los sistemas más realistas $SiNCS^+$/mini-SAM y $(CH_3)_2SiNCS^+$/mini-SAM, donde la mini-SAM es un modelo formado por nueve cadenas de perfluorobutano $CF_3(CF_2)_2CF_3$. Esta concordancia es buena siempre y cuando se utilicen ciertas restricciones en los coeficientes durante el ajuste para que no alcancen valores poco realistas. Otra conclusión importante obtenida en este trabajo es que el potencial de Lennard-Jones con un término electroestático, utilizado en muchos campos de fuerzas universales, no tiene flexibilidad suficiente para ajustar las regiones de corto y largo alcance al mismo tiempo.

En el último trabajo de esta tesis, que aún no está terminado, se realizó la dinámica de la colisión de los iones $SiNCS^+$ y $(CH_3)_2SiNCS^+$ con la F-SAM. El objetivo de este trabajo es explicar las diferencias encontradas en los experimentos de espectrometría de masas para estos dos iones. En concreto, se observó que el ión más grande experimenta *soft-landing*, es decir, se queda atrapado de manera intacta en la monocapa durante mucho tiempo (en algunos experimentos incluso 14 días). Por otro lado, el ión $SiNCS^+$ no fue detectado en ninguno de los espectros, indicando que este proyectil no permanece adsorbido en la superficie por un período de tiempo de horas. Los resultados teóricos obtenidos hasta el momento no consiguen explicar claramente los motivos por los que el ión más voluminoso es el único que es atrapado en la superficie. Aún así, algunos análisis parecen indicar que podría haber transferencia electrónica desde la superficie de oro al ión $SiNCS^+$, neutralizando su carga e impidiendo que sea observado en el espectro de masas. Esta neutralización parece estar bastante desfavorecida en el caso del compuesto $(CH_3)_2SiNCS^+$. Análisis y cálculos adicionales son necesarios para poder corroborar esta posible explicación y proponer otras nuevas.

Después de haber analizado en detalle todos los resultados obtenidos en esta tesis, podemos concluir que el método de trayectorias clásicas es un método bastante fiable para llevar a cabo simulaciones de colisiones gas/superficie. El desarrollo de la superficie de energía potencial es, probablemente, la etapa más importante a la hora de obtener buenos resultados. El muestreo de las condiciones iniciales debe ser hecho también con cuidado ya que esta elección influye sobre la dinámica del sistema.

Chapter 1

Introduction

Nanosystems can exhibit useful and interesting physical properties due to their "special" size. They are larger than atoms but smaller than bulk materials, therefore their behaviour is neither microscopic nor macroscopic. Currently, the great potential of nanoscience in the development of the technology is unquestionable. The important advances in the last three of four decades in experimental techniques have allowed a rapid growth of the knowledge of nanosystems.

Self-assembly systems, and in particular self-assembled monolayers (SAMs), have been widely used in the last years as models for investigating the behaviour of nanosystems. SAMs have been chosen as models because they are easy to synthesize, modify and characterize. Collisions of gases with SAMs permit to study a great variety of interesting processes as will be seen in subsequent chapters. The understanding of the collision mechanism and of the interactions involved in process helps understand better the properties of the system and then, their possible applications.

In spite of the importance and complexity of some experiments which provide very detailed information about dynamic and static features of the gas/surface collisions, many microscopic characteristics cannot be observed and analysized experimentally. Computational simulations have become a powerful tool for investigating these microscopic details due to the continuous advance in computation speed and storage. Moreover, highly accurate theoretical models and theories have been developed. Nowadays, simulations of very complex processes involving large molecules formed by thousands of atoms can be performed. The effect of solvent in reactions, protein folding, enzymatic reactions, heterogeneous catalysis and many other complex and important chemical processes are simulated at present "routinely".

The classical trajectory method was successfully employed in the recent past to study the scattering dynamics of atoms and molecules colliding with surfaces. In spite of its simple methodology, classical trajectories provide, in many cases, results that compare very well with more accurate quantum mechanical calculations and with experimental measurements. Obviously, the classical trajectory approach fails when the dynamics is strongly dominated by tunneling, nonadiabatic transitions or other quantum effects.

The general aim of this thesis is to carry out classical trajectory simulations of collisions between several polyatomic molecules and a perfluorinated self-assembled monolayer (F-SAM) surface. That surface is formed by chains of $CF_3(CF_2)_7S$ adsorbed on an Au{111} surface. The polyatomic molecules are CO_2, NO, $SiNCS^+$ and $(CH_3)_2SiNCS^+$. The study of these relatively simple molecules could seem trivial, but the fact is that some features of the dynamics are difficult to be interpreted without the help of the

simulations. Only a deep knowledge of such small systems will allow us to perform reliable simulations of more complex molecules in the future. The work presented in this thesis is focussed on the influence of the incident energy and angle, rovibrational excitation of the projectile and the mass of the surface atoms on the scattering dynamics. Also, some models will be presented here to interpret energy transfer and to unveil the mechanism of thermal accommodation of the projectile's degrees of freedom with the surface. We pay special attention to the development of the potential energy surface, in particular to the part that describes the intermolecular interactions. An accurate computation of these interactions is crucial, and probably the most important stage in order to obtain realistic results from the dynamics.

The general steps for performing classical trajectory simulations are the following. Firstly, the potential energy of the system must be computed. Different strategies may be followed to perform this calculation; in this thesis, the potential energy surfaces were determined by fitting analytical functions to potential energy curves derived from electronic structure calculations. Then, the initial coordinates and momenta for all the atoms of the system must be chosen (often called initial conditions). Once the potential energy function and the initial conditions are known, the classical equations of motion must be solved numerically to know the coordinates and momenta of all atoms of the system at each time. This provides a visual, detailed and very useful description of the dynamics.

In some chapters of this thesis, the simulation results will be compared with experiment. In general, we found very good agreement between simulations and experiments despite the approximations inherent to the simulation method. These approximations are enumerated next. First, relativistic effects are not taken into account; although they are not crucial for light atoms, these effects are always present to a certain extent. The Schrödinger equation is solved under the Born-Oppenheimer approximation and by numerical (and therefore approximate) methods; moreover, the basis set selected for its resolution is necessarily finite. The fitting process of the analytical function is never free of error. The functions employed in the intermolecular potential are sums of two-body terms, that is, many body effects are neglected. Hamilton (or Newton) classical equations describe the motion of the nuclei in classical dynamics, but actual particles obey quantum mechanics. In addition, classical equations of motion are also solved numerically. Quantum effects, such as tunneling or ZPE leakage, are not accounted for in classical mechanics. With the above number of problems, one may think that the classical trajectory results will never be reliable. But the fact is that, as will be shown in the next chapters, in many cases near-quantitative agreement with

experiments was achieved. This indicates that the above shortcomings do not introduce an important error in our simulations.

This thesis is organized in two general parts. The first part extends from Chapter 2 to Chapter 5; in those chapters the methodology used in the simulations is explained. The main topics of these chapters are: (i) types of gas/surface processes, (ii) intermolecular interactions, (iii) *ab initio* and density functional theory (DFT) and (iv) the classical trajectory approach. Then, in the second part of the thesis, which extends from Chapter 6 to Chapter 11, the results obtained in our simulations are presented. Each of these chapters corresponds to a paper that has been already published or accepted for publication, except Chapter 11, which corresponds to work in progress. The title of the chapters does not correspond to that of the papers. The references of the papers that have been already published are:

- Chapter 6: Dynamics of CO_2 /F-SAM: Influence of Collision Energy, Mass and Surface Model. *J. Phys.Chem. A* **2009**, 113, 3850-3865.
- Chapter 7: Dynamics of CO_2 /F-SAM: United Atom Models. *J. Phys.Chem. C* **2009**, 113, 3300-3312.
- Chapter 8: Dynamics of CO_2 /F-SAM: Vibrational Angular Momentum. *J. Phys.Chem. C* **2010**, 114, 18455-18464.
- Chapter 9: Dynamics of NO /F-SAM: An Energy Transfer Model and Stereodynamics. *J. Phys.Chem. C* **2010**, *submitted*.
- Chapter 10: Intermolecular Potential Energy Curves for Silyl Ions/F-SAM. *Chem. Phys.* **2011**, doi: 10.1016/j.chemphys.2011.02. 014.
- Chapter 11: Dynamics of Silyl Ions/F-SAM: Analysis of Soft-landing Processes. *Work in progress*.

Finally, some general comments and the conclusions are summarized in Chapter 12.

Chapter 2

Gas-Surface Collisions

1. INTRODUCTION

The interest in the study of the interactions between molecules in gas phase and surfaces has grown in the last two decades because of the great improvements in experimental techniques such as supersonic molecular beams, laser, mass spectrometry or atomic force microscopy (AFM) and scanning tunneling microscopy (STM).

Phenomena that occur at the interfaces are of different nature from those that occur within a phase, since molecules found in the bulk material have an isotropic environment, while molecules at the interface undergo different forces and interactions depending on the spatial direction. This different behaviour makes the study of surface phenomena to require more complex analysis techniques and simulation tools.

The study of gas-surface interactions may provide physicochemical information about both, the gas[1,2] and the surface.[3,4] The range of collision energies of chemical interest is from 1 to 100 eV, often called hyperthermal range. This energy regime is of particular interest because energy transfer from ion translation to surface and ion internal degrees of freedom is of similar order of magnitude as the activation energy for many reactions. Therefore, many chemical processes, such as ion and surface dissociations and ion/surface reactions, take place in this energy range.

Self-assembled monolayers (SAMs) are widely used in the study of gas-surface interactions and reactions. Because of their well-ordered structure, they possess very attractive properties from a theoretical and experimental standpoint as shown later.

This chapter begins by describing, in Section 2, what kind of processes can take place when a projectile collides with a SAM surface. Then, in Section 3, a brief description of the structure, synthesis and applications of SAM surfaces is shown. Finally, in Section 4, the main techniques that provide information about gas-surface events are examined.

2. TYPES OF GAS/SURFACE COLLISIONS

When an ion collides against a surface, it can undergo several reactive and non-reactive processes.[5-8] The most common events are discussed below and are shown schematically in Figure 2.1.

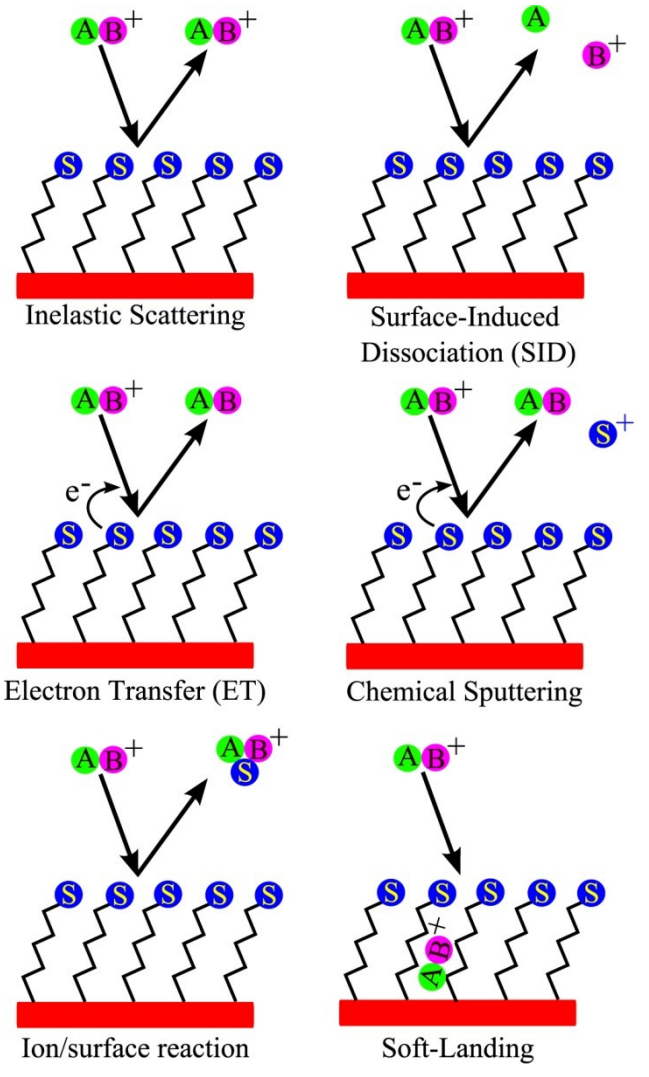

Figure 2.1: Most frequent processes during a gas-surface collision.

a. Inelastic Scattering: the translational energy of the ion is transferred to its own vibrational and rotational degrees of freedom and to the surface vibration. There are numerous experimental [9-30] and theoretical[31-45] studies where the dynamics of energy transfer, without chemical reaction, is investigated. Usually, these non-reactive gas-surface collisions are called elastic scattering in the literature, in order to emphasize that there are no reactive processes. This nomenclature might be confusing because, strictly speaking, an elastic collision is an event in which there is no energy exchange between the ion and the surface. Therefore, in this work, energy transfer processes are called inelastic scattering.

b. Surface-Induced Dissociation (SID): the ion could dissociate if the energy acquired by its vibrational normal modes is high enough to break any bond. The dissociation happens by means of two different mechanisms. In the first one, the reaction occurs immediately after the collision with the SAM, through a non-statistical process called shattering.[46-50] The second mechanism is based on the Rice-Ramsperger-Kassel-Marcus (RRKM) model[52] in which the ion is activated by collisions with the surface, and then dissociates, after intramolecular energy redistribution.[51] The amount of energy transferred to the ion vibration, which causes the bound rupture, depends on the surface nature; for instance, the percentage of energy transfer is about 20% for F-SAMs (fluorinated self-assembled monolayers), while this quantity is lower, close to 12%, for H-SAMs (hydrogenated self-assembled monolayers).[53]

c. Electron Transfer (ET): the ion and the surface can interchange their charges during the collision. The charge transfer mechanism is different depending on whether the surface is a metal[54-61] or a SAM,[5,62-66] in which organic chains are adsorbed on a substrate (typically a metallic surface). If the electron transfer happens from the organic chains to, for instance, a cation, the recombination energy (RE) of the cation must be higher than the surface ionization energy (IE). If the system is formed by a donor A and an acceptor B^+, the charge transfer process can be represented as follows:[67]

$$A + B^+ \longrightarrow A^+ + B \qquad (2.1)$$

Since energy must be conserved, the donor completes the process with its degrees of freedom excited as shown in Figure 2.2.

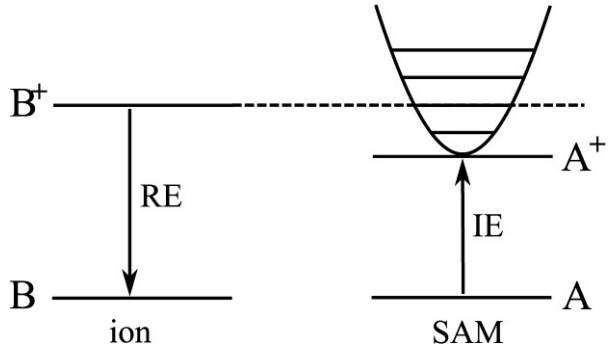

Figure 2.2: Relation between RE and IE for electron transfer takes place.

On the other hand, if the electron gets away from a metal surface, the process is more complex because three different charge transfer mechanisms are possible.[68] They will depend on the nature of the ion and the surface, the

work function ϕ of the metal and the collision energy of the ion. The main features of these three mechanisms are showed in Figure 2.3 and are discussed below. In these charge processes the ions get neutralized.

i. Auger Neutralization (AN): an electron is transferred from the valence band of the metal to the electronic ground state of the ion. The electronic ground state must lie below the highest occupied state in the metal, so that the transferred electron loses energy. This energy is used for exciting another electron from the valence band of the metal to the vacuum. The neutralization probability increases with the ionization energy of projectile, since the energy released to take out the second electron is higher. Usually, ionization potentials for atoms are higher than for molecules[8], therefore Auger neutralization happens primarily for atoms, while molecules are preferably neutralized by a resonant mechanism, which will be discussed below. The ideal ion-surface distance to produce Auger neutralization is from 1 to 2 Å; at this distance the maximum overlap between the ion orbitals and the surface takes place.

ii. Collision-Induced Neutralization CIN: isoenergetic process that only occurs if the collision is very violent, that is, the translational energy of the ion must be very large. At small distances, of the order of 0.5 Å, the ground state of the ion is aligned with the bottom of the valence band enabling charge exchange. This mechanism dominates when the metal work function (ϕ) is large.

iii. Resonant Neutralization RN: the transition arises from the metal valence band to any electronic state of the ion. Both states must be in resonance so that the neutralization is isoenergetic. As the ion approaches to the surface, the energy and the wave function shape of its electronic states change, then the electron occupation of these states varies according to the ion-surface distance. There is a distance, between 2 y 4 Å, at which the population of the ion electronic state is favoured, called freezing distance.

Charge neutralization by any mechanism is possible only if the ion states lie below the Fermi level (E_F) of the metal. In addition, the neutralization probability of the ion strongly depends on its velocity.[69] The probability that the ion leaves the surface without neutralization P^+ is given by

$$P^+ = e^{-v_c/v} \tag{2.2}$$

where v_c is the characteristic velocity, which is an estimation of the neutralization rate, and the reciprocal ion velocity $1/v$ is calculated in different ways according to the type of mechanism. Generally, as seen in equation 2.2, the lower ion velocity v, the lower the probability P^+, that is, the neutralization

probability increases. In other words, if the ion is going toward the surface slowly, the interaction time is large and the electron transfer probability is enhanced. In Figure 2.3 the three neutralization mechanisms are displayed in a simplified way:

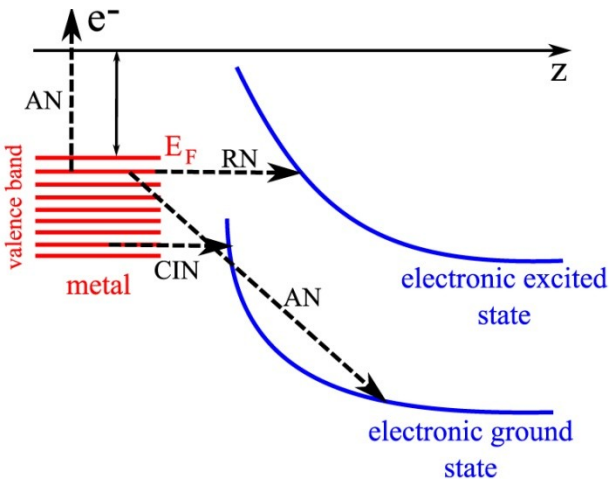

Figure 2.3: Mechanisms of gas-surface neutralization.

d. Chemical Sputtering: in this event an ionized fragment of the SAM surface is ejected, induced by the transfer of an electron from the organic chains to the projectile, neutralizing the ion.[6,70,71] This is a very useful process for surface analysis and characterization,[72,73] providing information about surface composition, physical processes and chemical reactions which might arise on the surface.

e. Ion/Surface Reaction: the projectile reacts with an atom or a functional group of the surface. A wide variety of ion/surface reactions have been studied, such as hydrogen,[74-77] fluorine[78-80] and alkyl groups[81,82] abstractions, transhalogenations (exchange of halogen atoms between the ion and the SAM)[83] or exchange of a pseudohalogen group, as isocyanate (NCO) or thioisocyanate (NCS) groups, by a halogen atom.[72]

f. Soft-landing: besides the above process, the projectile can be trapped into the surface by means of physical forces, without covalent bond formation. This non-reactive trapping event is called soft landing, and it was first detected by Cooks and co-workers,[84] who drove sylil and pyridine derivatives ions toward an F-SAM surface. They used mass spectrometry for detecting the scattering ions, and they found that some of them remained adsorbed into the fluorocarbon matrix for several hours or even days. This

process attracted a great interest because it allows to control and modify the properties of surfaces without changing their chemical nature. From this first work of Cooks, a wide variety of projectiles have been investigated in this type of process.[73,85-96]

Inelastic scattering and soft-landing are the processes which have been investigated in this thesis, therefore, in next chapters we shall delve into these kinds of processes. Most of the existing research in gas-surface collisions is experimental work, although there are a significant number of theoretical studies, especially in energy transfer dynamics. Troya and Schatz[97] summarized brightly the gas-surface processes which have been studied from a theoretical point of view.

3. SELF-ASSEMBLED MONOLAYERS (SAMs)

In experimental gas-surface studies, self-assembled monolayers are very used surfaces because their synthesis and characterization are relatively simple. Furthermore, surface properties can be changed and controlled so that factors that determine the collision mechanism, either reactive or energy transfer process, can be more easily investigated. For instance, Kane et al.[66] have studied the neutralization probability of benzene and dimethyl sulfoxide ions depending on the chain length and the amount of fluorine atoms in the SAM surface; another example is the work of Spencer *et al*.,[98] where they have investigated the variation of binding energies of electrons in 1s orbitals of C and F atoms according to the fluorine surface concentration. Another advantage of using SAMs is the ability to synthesize them so that many functional groups can be exposed to the outside, allowing the study of a large number of gas-surface reactions.

On the other hand, from a theoretical point of view, the ordered structure of SAMs facilitates their study by chemical dynamics simulations.

SAMs are formed by organic chains commonly adsorbed into a metallic surface through a chain atom, called headgroup. The metallic surface (10-200 nm thick) is anchored to a solid support, usually glass or silicon (1-2 mm thick), to handle more easily the surface. Usually, a sheet of nickel, chromium or titanium (1-5 nm) is placed between the solid support and the metal to improve the adhesion of the system. The structure solid support/metal is called substrate, on which the adsorbate stands, formed by the organic interface. Figure 2.4 displays a SAM basic structure.

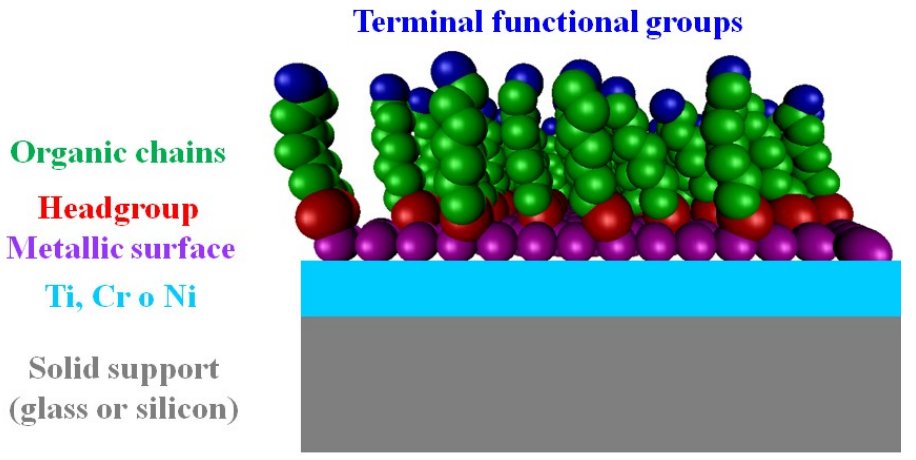

Figure 2.4: Self-Assembled Monolayer (SAM) structure.

The most common case is the use of flat structures as solid supports, as shown in Figure 2.4, but curved structures, such as colloids[99-101] or cylindrical rods,[102,103] are of particular interest because SAM properties (for example acidity or redox potential) are modified due to the curvature of the structure and consequently, present a lower packing density.

In the literature a wide choice of SAMs are available depending on the substrate and adsorbate nature.[104,105] Metals (Au, Ag, Pt, Pd), semiconductors (GaAs, ZnSe) or oxides (ZrO_2, SiO_2, Al_2O_3) have been used as substrates due to their well-defined structure and chemistry, while a variety of heteroatom-containing molecules (alkanethiols, carboxylic acids, sulfones, aryles, pyrenes) have been shown to self-assemble on such substrates. Much research has been focused on the self-assembly of n-alkanethiolate on gold substrates. Gold is very used as substrate because of its very interesting properties such as easiness of forming flat and thin films, cellular compatibility for biological researches and low reactivity with atmospheric O_2.[105] The simulations performed in this thesis were carried out using a self-assembled monolayer formed by perfluorinated alkanethiolate ($CF_3(CF_2)_7S$) chains adsorbed on an one-atom thick gold surface.

The most common protocol for preparing alkanethiolate on gold SAMs is immersion of metallic substrate into a dilute (about 1-10 mM) ethanolic solution of alkanethiolate for several hours (12-18 h) at room temperature.[73,76,86,89,91] Dense coverages of adsorbates are obtained quickly (milliseconds to minutes) and spontaneously, but a slow reorganization process requires hours to maximize the density of molecules and minimize the defects in the SAM. The monolayer prepared in this way must be purified to avoid

secondary unwanted processes which could lead to mistaken conclusions. The purification often consists of ultrasonic washing in ethanol.

In addition to the ability to be synthesized and characterized, this type of surface has other advantages and numerous applications in many scientific fields. There is a wide variety of examples in the literature about applications of SAMs in electrochemistry, catalysis, biology, electronic devices, optic or nanotechnology. Some of these examples are mentioned now to highlight the potential of such surfaces. Lim *et al.*[106] have used self-assembled monolayers as receivers in explosive detectors. In other work, Cooks and co-workers[107] purified the lysozyme (protein responsible for degrading the cell wall of some bacteria) by trapping into a glycerol/sucrose liquid matrix; after the desorption, mass spectrum showed impurities remaining in the surface while the pure protein was ejected, retaining its structure and, therefore, its biological function was not deactivated. Nakajima group[108] synthesized vanadium-benzene sandwich clusters VPh_2 in gas phase, which subsequently were soft-landed onto an F-SAM surface; atomic force microscopy revealed that the clusters kept their native sandwich structure intact. Laskin[85] and co-workers successfully prepared a protein microarray with α helical secondary structure (with interesting applications due to its large dipole momentum) by soft-landing proteins into a SAM surface; the synthesis in solution led to a mixture of conformations dominated by the β sheet and a small fraction of α helix.

4. EXPERIMENTAL TECHNIQUES

There are a large number of experimental tools that are able to analyze what processes take place when a projectile collides with a surface. Below, a very brief description of the most widely used techniques is shown, without going into detail. A general classification into two groups should be made, according to the type of analysis. That is, we can analyze either the properties of the scattered projectiles (after a reactive or non-reactive event) or changes in the surface.

Mass spectrometry is within the first group, where the molecules under consideration must be ions, both before and after the collisions.[72,82,109] The ions are detected and selected according to their mass/charge relation; the main drawback of this technique is the inability to detect neutral species and to distinguish between isomers with the same charge. If the projectile or the products formed due to a reaction on/with the surface are trapped into the SAM, the collision of a secondary ion (often a noble gas) is necessary to eject the adsorbed species to be detected by the mass spectrometer; this technique is called secondary ion mass spectrometry (SIMS).[73,86,87,90-95,110] Mass

spectrometry just allows to detect mass and charge of the scattered ions, but it is not able to provide additional information such as structure or energy distributions. If these properties are to be analyzed, mass spectrometer must be combined with another instrument, for instance, IR or UV-VIS spectrophotometer.

If the projectiles aimed to the surface are neutral molecules, supersonic molecular beams are often used; in this technique molecules are directed to the surface from a valve in short duration pulses (microseconds).[28,29,111,112] This type of devices try to minimize collisions among molecules within the gas and to maximize the translational energy collimation, that is, only molecules which travel with the desirable velocity are selected.

Microscopies are involved in the second analysis technique group, with which the surface is characterized after the collision. Scanning tunneling microscopy (STM) and atomic force microscopy (AFM) supply atomic-level images, so that any surface modification due to the impact is detected.[76,89] Another usual technique in surface analysis is the X-ray photoelectron spectroscopy (X XPS),[88,113,114] where an X-ray beam irradiates the surface, causing the escape of electrons. The kinetic energy of the electrons will be different depending on the atom from which they were ejected. Therefore, an energetic analysis of the ejected electrons allows to know the composition of the surface.

There are many analytical techniques besides those mentioned above. The most common ones were listed in order to highlight that the study of gas-surface interactions requires very complex experimental set-ups. In spite of the large number of existing analysis tools to study this type of process, elucidating some microscopic and dynamic properties experimentally is very difficult (if not impossible). In some cases, chemical dynamics simulations are required to get more insight into some collision mechanisms.

REFERENCES

(1) Cooks, R. G.; Mabud, M. A.; Horning, S. R.; Jiang, X. Y.; Paradisi, C.; Traldi, P. *J. Am. Chem. Soc.* **1989**, *111*, 859-65.
(2) Dongre, A. R.; Somogyi, A.; Wysocki, V. H. *J. Mass Spectrom.* **1996**, *31*, 339-50.
(3) Gu, C.; Wysocki, V. H. *J. Am. Chem. Soc.* **1997**, *119*, 12010-12011.
(4) Pradeep, T.; Shen, J.; Evans, C.; Cooks, R. G. *Anal. Chem.* **1999**, *71*, 3311-3317.
(5) Cooks, R. G.; Ast, T.; Pradeep, T.; Wysocki, V. *Acc. Chem. Res.* **1994**, *27*, 316-23.
(6) Cooks, R. G.; Jo, S.-C.; Green, J. *Appl. Surf. Sci.* **2004**, *231-232*, 13-21.
(7) Gologan, B.; Green, J. R.; Alvarez, J.; Laskin, J.; Graham, C. R. *Phys. Chem. Chem. Phys.* **2005**, *7*, 1490-1500.
(8) Jacobs, D. C. *Annu. Rev. Phys. Chem.* **2002**, *53*, 379-407.
(9) Saecker, M. E.; Govoni, S. T.; Kowalski, D. V.; King, M. E.; Nathanson, G. M. *Science (Washington, D. C., 1883-)* **1991**, *252*, 1421-4.
(10) Kenyon, A. J.; McCaffery, A. J.; Quintella, C. M.; Zidan, M. D. *Chem. Phys. Lett.* **1992**, *190*, 55-8.
(11) Saecker, M. E.; Nathanson, G. M. *J. Chem. Phys.* **1993**, *99*, 7056-75.
(12) King, M. E.; Nathanson, G. M.; Hanning-Lee, M. A.; Minton, T. K. *Phys. Rev. Lett.* **1993**, *70*, 1026-9.
(13) Saecker, M. E.; Nathanson, G. M. *J. Chem. Phys.* **1994**, *100*, 3999-4005.
(14) King, M. E.; Saecker, M. E.; Nathanson, G. M. *J. Chem. Phys.* **1994**, *101*, 2539-47.
(15) Nathanson, G. M.; Davidovits, P.; Worsnop, D. R.; Kolb, C. E. *J. Phys. Chem.* **1996**, *100*, 13007-13020.
(16) King, M. E.; Fiehrer, K. M.; Nathanson, G. M.; Minton, T. K. *J. Phys. Chem. A* **1997**, *101*, 6556-6561.
(17) Ringeisen, B. R.; Muenter, A. H.; Nathanson, G. M. *J. Phys. Chem. B* **2002**, *106*, 4988-4998.
(18) Ringeisen, B. R.; Muenter, A. H.; Nathanson, G. M. *J. Phys. Chem. B* **2002**, *106*, 4999-5010.
(19) Manning, M.; Morgan, J. A.; Castro, D. J.; Nathanson, G. M. *J. Chem. Phys.* **2003**, *119*, 12593-12604.
(20) Nathanson, G. M. *Annu. Rev. Phys. Chem.* **2004**, *55*, 231-255.
(21) Zhang, J.; Garton, D. J.; Minton, T. K. *J. Chem. Phys.* **2002**, *117*, 6239-6251.
(22) Kelso, H.; Koeler, S. P. K.; Henderson, D. A.; McKendrick, K. G. *J. Chem. Phys.* **2003**, *119*, 9985-9988.
(23) Perkins, B. G., Jr.; Haber, T.; Nesbitt, D. J. *J Phys Chem B* **2005**, *109*, 16396-405.

(24) Perkins, B. G., Jr.; Nesbitt, D. J. *J Phys Chem B* **2006**, *110*, 17126-37.
(25) Perkins, B. G., Jr.; Nesbitt, D. J. *J Phys Chem A* **2007**, *111*, 7420-30.
(26) Perkins, B. G., Jr.; Nesbitt, D. J. *Proc. Natl. Acad. Sci. U. S. A.* **2008**, *105*, 12684-12689.
(27) Perkins, B. G., Jr.; Nesbitt, D. J. *J Phys Chem A* **2008**, *112*, 9324-35.
(28) Perkins, B. G., Jr.; Nesbitt, D. J. *J Phys Chem B* **2008**, *112*, 507-19.
(29) Perkins, B. G., Jr.; Nesbitt, D. J. *Phys. Chem. Chem. Phys.* **2010**, *12*, 14294-14308.
(30) Perkins, B. G., Jr.; Nesbitt, D. J. *J. Phys. Chem. A* **2010**, *114*, 1398-1410.
(31) Bosio, S. B. M.; Hase, W. L. *J. Chem. Phys.* **1997**, *107*, 9677-9686.
(32) Day, B. S.; Morris, J. R.; Troya, D. *J. Chem. Phys.* **2005**, *122*, 214712/1-214712/12.
(33) Yan, T.; Hase, W. L. *Phys. Chem. Chem. Phys.* **2000**, *2*, 901-910.
(34) Yan, T.; Hase, W. L.; Barker, J. R. *Chem. Phys. Lett.* **2000**, *329*, 84-91.
(35) Yan, T.; Hase, W. L. *J. Phys. Chem. A* **2001**, *105*, 2617-2625.
(36) Yan, T.; Hase, W. L. *J. Phys. Chem. B* **2002**, *106*, 8029-8037.
(37) Yan, T.; Isa, N.; Gibson, K. D.; Sibener, S. J.; Hase, W. L. *J. Phys. Chem. A* **2003**, *107*, 10600-10607.
(38) Isa, N.; Gibson, K. D.; Yan, T.; Hase, W.; Sibener, S. J. *J. Chem. Phys.* **2004**, *120*, 2417-2433.
(39) Gibson, K. D.; Isa, N.; Sibener, S. J. *J. Chem. Phys.* **2003**, *119*, 13083-13095.
(40) Alexander, W. A.; Morris, J. R.; Troya, D. *J. Phys. Chem. A* **2009**, *113*, 4155-4167.
(41) Alexander, W. A.; Troya, D. *J. Phys. Chem. C* **2011**, *115*, 2273-2283.
(42) Tasic, U.; Troya, D. *Phys. Chem. Chem. Phys.* **2008**, *10*, 5776-5786.
(43) Nogueira, J. J.; Martinez-Nunez, E.; Vazquez, S. A. *J. Phys. Chem. C* **2009**, *113*, 3300-3312.
(44) Nogueira, J. J.; Vazquez, S. A.; Lourderaj, U.; Hase, W. L.; Martinez-Nunez, E. *J. Phys. Chem. C* **2010**, *114*, 18455-18464.
(45) Nogueira, J. J.; Vazquez, S. A.; Mazyar, O. A.; Hase, W. L.; Perkins, B. G., Jr.; Nesbitt, D. J.; Martinez-Nunez, E. *J. Phys. Chem. A* **2009**, *113*, 3850-3865.
(46) Laskin, J.; Bailey, T. H.; Futrell, J. H. *J. Am. Chem. Soc.* **2003**, *125*, 1625-1632.
(47) Kang, H.; Lee, H. W.; Cho, W. R.; Lee, S. M. *Chem. Phys. Lett.* **1998**, *292*, 213-217.

(48) Schultz, D. G.; Hanley, L. *J. Chem. Phys.* **1998**, *109*, 10976-10983.

(49) Meroueh, S. O.; Wang, Y.; Hase, W. L. *J. Phys. Chem. A* **2002**, *106*, 9983-9992.

(50) Park, K.; Deb, B.; Song, K.; Hase, W. L. *J. Am. Soc. Mass Spectrom.* **2009**, *20*, 939-948.

(51) Laskin, J.; Yang, Z.-B.; Song, T.; Lam, C.; Chu, I. K. *J. Am. Chem. Soc.* **2010**, *132*, 16006-16016.

(52) Gilbert, R. G. S., Sean C. *Theory of Unimolecular and Recombination Reactions*; Blackwell Scientific Publications: Oxford, 1990.

(53) Jo, S.-C.; Cooks, R. G. *Eur. J. Mass Spectrom.* **2003**, *9*, 237-244.

(54) Morris, J. R.; Kim, G.; Barstis, T. L. O.; Mitra, R.; Quinteros, C. L.; Jacobs, D. C. *Nucl. Instrum. Methods Phys. Res., Sect. B* **1997**, *125*, 185-193.

(55) Sasaki, M.; Scanlon, P. J.; Ermolov, S.; Brongersma, H. H. *Nucl. Instrum. Methods Phys. Res., Sect. B* **2002**, *190*, 127-130.

(56) Rousseau, P.; Gugiu, M.; Khemliche, H.; Roncin, P. *Nucl. Instrum. Methods Phys. Res., Sect. B* **2005**, *230*, 361-368.

(57) Martin, J. S.; Feranchak, B. T.; Morris, J. R.; Greeley, J. N.; Jacobs, D. C. *J. Phys. Chem.* **1996**, *100*, 1689-97.

(58) van, d. S. D. A.; Levine, Y. K. *J. Chem. Phys.* **1994**, *100*, 6791-812.

(59) Britton, A. J.; Rienzo, A.; O'Shea, J. N.; Schulte, K. *J Chem Phys* **2010**, *133*, 094705.

(60) Nieuwjaer, N.; Benazeth, C.; Benoit-Cattin, P.; Cafarelli, P.; Richard-Viard, M. *Nucl. Instrum. Methods Phys. Res., Sect. B* **2005**, *230*, 317-322.

(61) Lorente, N.; Borisov, A. G.; Teillet-Billy, D.; Gauyacq, J. P. *Surf. Sci.* **1999**, *429*, 46-53.

(62) Somogyi, A.; Kane, T. E.; Ding, J. M.; Wysocki, V. H. *J. Am. Chem. Soc.* **1993**, *115*, 5275-83.

(63) Gu, C.; Wysocki, V. H.; Harada, A.; Takaya, H.; Kumadaki, I. *J. Am. Chem. Soc.* **1999**, *121*, 10554-10562.

(64) Somogyi, A.; Smith, D. L.; Wysocki, V. H.; Colorado, R.; Lee, T. R. *J. Am. Soc. Mass Spectrom.* **2002**, *13*, 1151-1161.

(65) Smith, D. L.; Wysocki, V. H.; Colorado, R., Jr.; Shmakova, O. E.; Graupe, M.; Lee, T. R. *Langmuir* **2002**, *18*, 3895-3902.

(66) Kane, T. E.; Angelico, V. J.; Wysocki, V. H. *Langmuir* **1997**, *13*, 6722-6725.

(67) Macha, S. F.; McCarley, T. D.; Limbach, P. A. *Anal. Chim. Acta* **1999**, *397*, 235-245.

(68) Cortenraad, R.; Denier, v. d. G. A. W.; Brongersma, H. H.; Ermolov, S. N.; Glebovsky, V. G. *Phys. Rev. B: Condens. Matter Mater. Phys.* **2002**, *65*, 195414/1-195414/10.

(69) Los, J.; Geerlings, J. J. C. *Phys. Rep.* **1990**, *190*, 133-90.

(70) Busharov, N. P.; Gorbatov, E. A.; Gusev, V. M.; Guseva, M. I.; Martynenko, Y. V. *J. Nucl. Mater.* **1976**, *63*, 230-4.

(71) Ast, T.; Riederer, D. E., Jr.; Miller, S. A.; Morris, M.; Cooks, R. G. *Org. Mass Spectrom.* **1993**, *28*, 1021-33.

(72) Miller, S. A.; Luo, H.; Jiang, X.; Rohrs, H. W.; Cooks, R. G. *Int. J. Mass Spectrom. Ion Processes* **1997**, *160*, 83-105.

(73) Luo, H.; Miller, S. A.; Cooks, R. G.; Pachuta, S. J. *Int. J. Mass Spectrom. Ion Processes* **1998**, *174*, 193-217.

(74) Riederer, D. E., Jr.; Cooks, G.; Linford, M. R. *J. Mass Spectrom.* **1995**, *30*, 241-6.

(75) Ast, T.; Mabud, M. A.; Cooks, R. G. *Int. J. Mass Spectrom. Ion Processes* **1988**, *82*, 131-50.

(76) Qin, X.; Tzvetkov, T.; Jacobs, D. C. *J. Phys. Chem. A* **2006**, *110*, 1408-1415.

(77) Layfield, J. P.; Troya, D. *J Chem Phys* **2010**, *132*, 134307.

(78) Pradeep, T.; Riederer, D. E., Jr.; Hoke, S. H., II; Ast, T.; Cooks, R. G.; Linford, M. R. *J. Am. Chem. Soc.* **1994**, *116*, 8658-65.

(79) Riederer, D. E.; Miller, J. S. A.; Ast, T.; Cooks, R. G. *J. Am. Soc. Mass Spectrom.* **1993**, *4*, 938-42.

(80) Shen, J.; Grill, V.; Cooks, R. G. *J. Am. Chem. Soc.* **1998**, *120*, 4254-4255.

(81) Hayward, M. J.; Mabud, M. A.; Cooks, R. G. *J. Am. Chem. Soc.* **1988**, *110*, 1343-6.

(82) Wade, N.; Shen, J.; Koskinen, J.; Cooks, R. G. *J. Mass Spectrom.* **2001**, *36*, 717-725.

(83) Pradeep, T.; Ast, T.; Cooks, R. G.; Feng, B. *J. Phys. Chem.* **1994**, *98*, 9301-11.

(84) Miller, S. A.; Luo, H.; Pachuta, S. J.; Cooks, R. G. *Science (Washington, D. C.)* **1997**, *275*, 1447-1450.

(85) Wang, P.; Lashkin, J. *Angew. Chem., Int. Ed.* **2008**, *47*, 6678-6680.

(86) Hadjar, O.; Wang, P.; Futrell, J. H.; Dessiaterik, Y.; Zhu, Z.; Cowin, J. P.; Iedema, M. J.; Laskin, J. *Anal Chem* **2007**, *79*, 6566-74.

(87) Wang, P.; Hadjar, O.; Laskin, J. *J Am Chem Soc* **2007**, *129*, 8682-3.

(88) Bindu, V.; Venkataramanan, M.; Pradeep, T. *Mol. Phys.* **1999**, *96*, 367-370.

(89) Nagaoka, S.; Ikemoto, K.; Fujio, K.; Hiehata, K.; Sasahara, A.; Mitsui, M.; Onishi, H.; Nakajima, A. *Eur. Phys. J. D* **2009**, *52*, 103-106.

(90) Johnson, G. E.; Lysonski, M.; Laskin, J. *Anal. Chem. (Washington, DC, U. S.)* **2010**, *82*, 5718-5727.

(91) Hadjar, O.; Wang, P.; Futrell, J. H.; Laskin, J. *J. Am. Soc. Mass Spectrom.* **2009**, *20*, 901-906.

(92) Laskin, J.; Wang, P.; Hadjar, O.; Futrell, J. H.; Alvarez, J.; Cooks, R. G. *Int. J. Mass Spectrom.* **2007**, *265*, 237-243.

(93) Alvarez, J.; Futrell, J. H.; Laskin, J. *J. Phys. Chem. A* **2006**, *110*, 1678-1687.

(94) Nie, Z.; Li, G.; Goodwin, M. P.; Gao, L.; Cyriac, J.; Cooks, R. G. *J. Am. Soc. Mass Spectrom.* **2009**, *20*, 949-956.

(95) Laskin, J.; Wang, P.; Hadjar, O. *Phys. Chem. Chem. Phys.* **2008**, *10*, 1079-1090.

(96) Nanita, S. C.; Takats, Z.; Cooks, R. G.; Myung, S.; Clemmer, D. E. *J. Am. Soc. Mass Spectrom.* **2004**, *15*, 1360-1365.

(97) Troya, D.; Schatz, G. C. *Int. Rev. Phys. Chem.* **2004**, *23*, 341-373.

(98) Venkataraman, N. V.; Zurcher, S.; Rossi, A.; Lee, S.; Naujoks, N.; Spencer, N. D. *J. Phys. Chem. C* **2009**, *113*, 5620-5628.

(99) Browne, K. P.; Grzybowski, B. A. *Langmuir* **2011**, *27*, 1246-1250.

(100) Jones, R. L.; Pearsall, N. C.; Batteas, J. D. *J. Phys. Chem. C* **2009**, *113*, 4507-4514.

(101) Bernardoni, F.; Kouba, M.; Fadeev, A. Y. *Chem. Mater.* **2008**, *20*, 382-387.

(102) Li, Y.; Yu, D.; Dai, L.; Urbas, A.; Li, Q. *Langmuir* **2011**, *27*, 98-103.

(103) Bulliard, X.; Yun, S.; Ihn, S.-G.; Choi, Y. S.; Kim, Y.; Choi, D.; Choi, J.-Y.; Choi, W. *Cryst. Growth Des.* **2010**, *10*, 4697-4700.

(104) Smith, R. K.; Lewis, P. A.; Weiss, P. S. *Prog. Surf. Sci.* **2004**, *75*, 1-68.

(105) Love, J. C.; Estroff, L. A.; Kriebel, J. K.; Nuzzo, R. G.; Whitesides, G. M. *Chem. Rev. (Washington, DC, U. S.)* **2005**, *105*, 1103-1169.

(106) Lim, S.-H.; Raorane, D.; Satyanarayana, S.; Majumdar, A. *Sensors and Actuators B* **2006**, *119*, 466-474.

(107) Gologan, B.; Takats, Z.; Alvarez, J.; Wiseman, J. M.; Talaty, N.; Ouyang, Z.; Cooks, R. G. *J Am Soc Mass Spectrom* **2004**, *15*, 1874-84.

(108) Mitsui, M.; Nagaoka, S.; Matsumoto, T.; Nakajima, A. *J. Phys. Chem. B* **2006**, *110*, 2968-2971.

(109) Hayward, M. J.; Park, F. D. S.; Phelan, L. M.; Bernasek, S. L.; Somogyi, A.; Wysocki, V. H. *J. Am. Chem. Soc.* **1996**, *118*, 8375-8380.

(110) Wang, P.; Hadjar, O.; Gassman, P. L.; Laskin, J. *Phys. Chem. Chem. Phys.* **2008**, *10*, 1512-1522.

(111) Wodtke, A. M.; Yuhui, H.; Auerbach, D. J. *Chem. Phys. Lett.* **2005**, *413*, 326-330.

(112) Ma, P. F.; Dube, A.; Killampalli, A. S.; Engstrom, J. R. *J. Chem. Phys.* **2006**, *125*, 034706/1-034706/12.

(113) Nuzzo, R. G.; Zegarski, B. R.; Dubois, L. H. *J. Am. Chem. Soc.* **1987**, *109*, 733-40.

(114) Prime, K. L.; Whitesides, G. M. *J. Am. Chem. Soc.* **1993**, *115*, 10714-21.

Chapter 3

Intermolecular Interactions

1. INTRODUCTION

When molecules are close together, forces of attraction and repulsion come into play. These forces arise from interactions between electrons and nuclei of the different molecules, that is, they have an electric origin. These non-bonded forces are known as intermolecular interactions.

Much chemistry is concerned with chemical reactions that involve the breaking of bonds and the formation of new ones. But before any reaction can begin, molecules must approach each other to a critical distance. This process is controlled by the forces between them, that is, by intermolecular interactions. These interactions are important because they are precursors not only of a chemical reaction but also of many other physical and chemical processes. For example, clustering of molecules in the solid and liquid state, the structure of biomolecules like DNA and proteins, adsorption of substrates on surfaces, charge transfer processes or nanostructure formation like micelles or colloids, are dominated by intermolecular interactions.[1,2]

The importance of intermolecular forces is clearly reflected in the fact that in their absence our world would be a uniform ideal gas. Therefore, although intermolecular forces are much weaker than chemical forces creating bonds within molecules, they control a wide variety of processes and properties which are of great relevance in nature.

The existence of intermolecular forces can be deduced from two simple macroscopic observations.[3] The first one is that all substances form condensed phases at sufficiently low temperatures, indicating the existence of intermolecular attractions that are strong enough to bind molecules together with low kinetic energy. The second observation is that all condensed phases strongly resist further compression; this indicates the existence of short-range repulsive forces that avoid coalescence of molecules under pressure.

Scattering of molecular beams, spectroscopy measurements or transport coefficients studies are some of the experiments which can provide information about intermolecular interactions, but the interaction energy cannot be measured directly in an experiment.[2] Therefore, theoretical methods are necessary to compute the interaction energy between molecules although some potential energy functions are based on experimental properties as seen below.

In classical trajectory simulations of gas-surface collisions, knowledge of the intermolecular forces is essential because the classical equations of motion must be integrated as will be seen in Chapter 5. In addition, the main properties of the system, such as the amount of energy transfer or the yield of trapping adsorbates into the surface, depend on the

strength of the intermolecular interactions between the projectile and the surface. Therefore, developing a reliable intermolecular potential is necessary to obtain precise results from the dynamics.

This Chapter is arranged as follows. Section 2 starts with the definition of the interaction energy. Section 3 touches on some aspects of the basis set superposition error, associated with the supermolecular method. The intermolecular interaction types and some topics of their behaviour are discussed in Section 4. Finally, the most common functions to describe the interactions are analyzed in Section 5, and optimization methods for fitting electronic structure calculations to these analytical functions are introduced in Section 6.

2. DEFINITION OF INTERACTION ENERGY

In the supermolecular method the intermolecular interaction energy E_{int} or intermolecular potential energy between two molecules (A and B) is defined as[4]

$$E_{int}(Q_{AB}, q_A, q_B) = E_{AB}(Q_{AB}, q_A, q_B) - E_A(q_A) - E_B(q_B) \qquad (3.1)$$

where E_{AB} is the total energy of the dimer, E_A and E_B are the energies of each monomer, Q_{AB} denotes the intermolecular coordinates (distance between monomers and Euler angles) defining the relative orientation of monomers in space, and q_A and q_B are the sets of internal coordinates of A and B, respectively. Frequently, the monomers are assumed to be rigid, that is, the internal coordinates q_i are fixed at their equilibrium geometries, so that the intermolecular potential depends only on intermolecular coordinates Q_{AB}. This approximation means that the effect of monomer vibrations is included in an averaged way.

The interaction potential energy given by equation 3.1 is applicable in the framework of the Born-Oppenheimer approximation, which will be discussed in Chapter 4, and loses its usefulness when nonadiabatic effects are significant. We will assume that equation 3.1 is correct for developing the intermolecular potential energy surfaces.

In general, analytical functions with adjustable parameters are employed to calculate the interaction energy. The parameters of the function are fitted to a set of experimental and theoretical properties of some model compounds; the properties can be for instance enthalpies of vaporization and densities of liquids, gas-phase structures from microwave spectra, electron diffraction data, crystal structures from X-ray data or calculated interaction

energies. Such empirical potentials are part of extensively used molecular mechanics force fields, like AMBER[5] (Assisted Model Building with Energy Refinement), CHARMM[6] (Chemistry at HARvard Macromolecular Mechanics) or OPLS[7] (Optimized Potentials for Liquid Simulations). The intermolecular potential energy in the previous force fields is given by pairwise Lennard-Jones 12-6 and Coulomb terms with the form

$$V = \sum_{i,j} 4\varepsilon_{ij} \left[\left(\frac{\sigma_{ij}}{R_{ij}} \right)^{12} - \left(\frac{\sigma_{ij}}{R_{ij}} \right)^{6} \right] + \frac{q_i q_j}{\varepsilon R_{ij}} \qquad (3.2)$$

where ε_{ij} is the well depth, σ_{ij} is the value of R at $V = 0$, q_i is the partial atomic charge, ε is the permittivity or dielectric constant and R_{ij} is the distance between atoms i and j.

Molecular mechanical models can be inaccurate in some cases. For example, Hase and co-workers[8] found the repulsive short-range potential energy curves for $CH_3NH_3^+/CH_4$ system are poorly reproduced by AMBER and CHARMM parameters in comparison with high level MP2/aug-cc-pVTZ calculations. This is an expected result since parameters of these models are chosen to approximate thermal conditions, and not the highly repulsive interactions between molecules. Hobza and co-workers[9] calculated stabilization energies of DNA H-bonded base pairs using various empirical potentials; these results were tested against MP2 energies and they found some of the empirical models led to energies with high errors. Conformational dynamics of trialanine in water was carried out by Stock and co-wokers[10] in which several force fields were employed; they found that the lifetimes differ by more than an order of magnitude depending on the model employed.

Although molecular mechanical force fields are very useful in many cases, their parameters are not transferable to any system. Therefore, in some cases, the development of an *ad hoc* potential energy surface is necessary to obtain more precise results. In general, the potential energy is obtained by fitting electronic structure energies to analytical functions. The most widely used potential functions will be explained in Section 5. Frequently, the electronic structure calculations are carried out for several relative orientations between monomers, maintaining the internal coordinates fixed and changing only the relative distance between monomers. For example, Figure 3.1 shows possible orientations of an AB---C system that could be employed to develop the AB---C intermolecular potential energy surface.

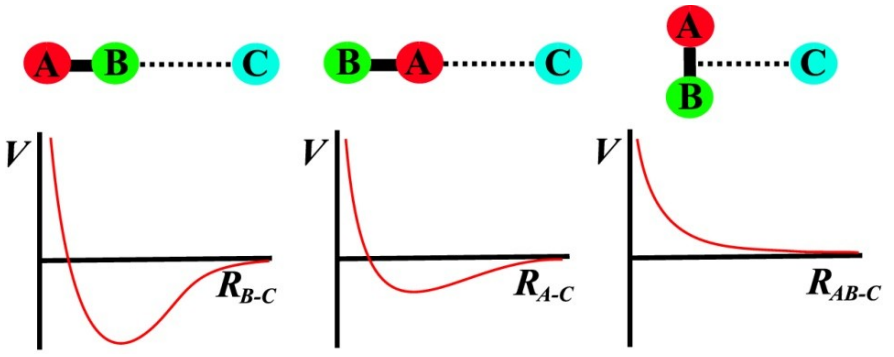

Figure 3.1: Possible orientations and corresponding potential energy curves for an AB---C system.

Analytical functions expressed as sums of two-body or pairwise additive interactions are usually employed to fit intermolecular potential energy curves calculated by electronic structure methods. Therefore, nonadditive effects or many-body interactions, caused by polarization and exchange forces,[2] are not taken into account. Many-body interactions are neglected throughout this thesis; this is common practice in the development of gas/surface potential energy functions.[8,11-17] In Chapter 10, it will be shown that nonadditive effects are not important for $SiNCS^+$ and CH_3SiNCS^+ interacting with an F-SAM surface. In Section 4 nonadditive effects will be briefly discussed.

3. BASIS SET SUPERPOSITION ERROR (BSSE)

As seen above in equation 3.1, in the supermolecular method the interaction energy is computed subtracting the individual energies E_A and E_B from E_{AB}:

$$E_{int} = E_{AB}(AB) - E_A(A) - E_B(B) \qquad (3.3)$$

where the basis sets used to calculate each energy are in parenthesis. Such basis sets are finite and, as a result, the energy of each fragment within the dimer is improved (with respect to the energy of the isolated fragment) because the basis functions of the interacting partner are employed. In other words, on dimer AB, electrons of monomer A are polarized into the virtual orbitals of monomer B and vice versa, while in separate monomers, electrons must remain in orbitals belonging to the monomer in which they are; Figure 3.2 shows this situation. This leads to a spurious decrease (or increase in absolute value) of the interaction energy, referred to as the basis set superposition error (BSSE).

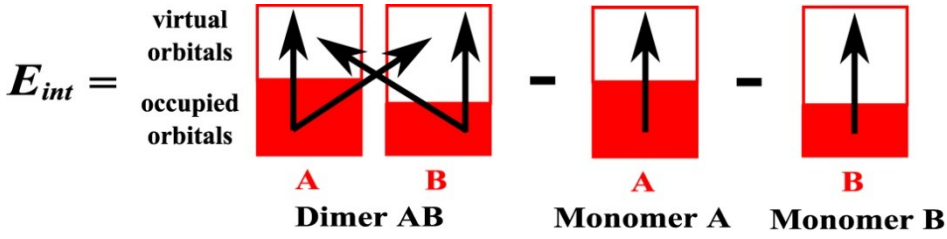

Figure 3.2: Available orbitals for the electrons in the supermolecular method.

Kestner[18] detected this problem in 1968; he noted that the minimum of the potential energy curve of the helium dimer disappeared in SCF calculations that used large basis set. Liu and McLean[19] introduced in 1973 the term basis set superposition error for this type of problem in the potential energy curves of molecular complexes. Boys and Bernardi[20] found a way to overcome the problem in 1970, introducing the counterpoise (CP) technique. Since BSSE arises from the fact that the AB basis at a given geometry of the complex is more complete than the A or B basis sets alone, the solution to the problem according to the CP method is to calculate the total energy of the dimer and monomers using the same basis set, that is, the AB basis set.

$$E_{int}^{CP} = E_{AB}(AB) - E_A(AB) - E_B(AB) \tag{3.4}$$

The basis set superposition error can be computed from equations 3.3 and 3.4 as

$$BSSE = E_{int}^{CP} - E_{int} \tag{3.5}$$

$$BSSE = E_A(A) - E_A(AB) + E_B(B) - E_B(AB) \tag{3.6}$$

Soon after the counterpoise correction was suggested, several researchers found an important (and false) flaw in the method. BSSE takes place because in the calculation of the total energy of the complex, the fragments can use the unoccupied part of the basis set of neighbouring fragments to improve their own energy. Occupied orbitals are not available for this purpose. Now, in the counterpoise recipe, the energy of the fragments is calculated using the whole basis set (including ghost basis); that is, their energies become lower than the real one. This means that, the counterpoise method overcorrects the basis set superposition error.[1] Figure 3.3 shows the orbital spaces taken into account in the standard (also called full) CP correction.

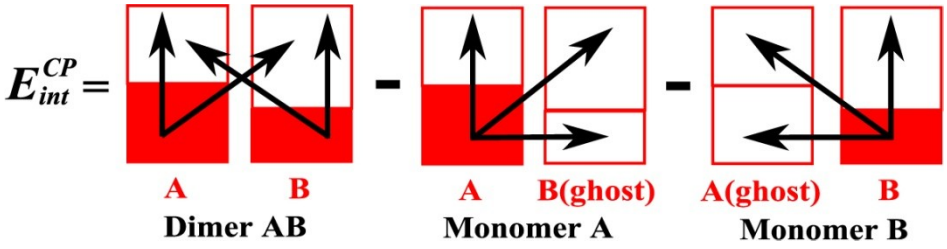

Figure 3.3: Available orbitals for the electrons in the standard counterpoise correction.

Another correction, called virtual counterpoise (VCP), was proposed to overcome the above problem of CP. In this new correction, only virtual space of a monomer is available for the improvement of the other monomer as shown in Figure 3.4.

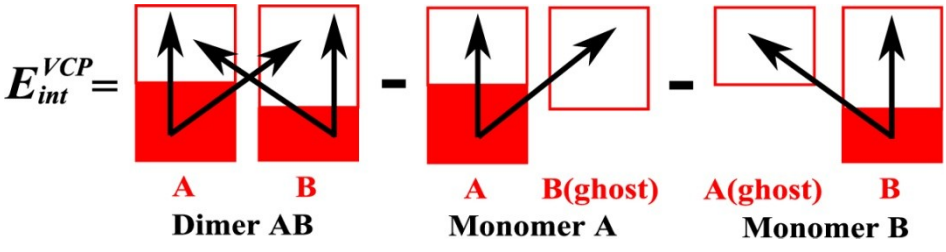

Figure 3.4: Available orbitals for the electrons in the virtual counterpoise correction.

Chalasinski and Gutowski[21] (1985) have proved that the CP energy (full orbital space), using a full-CI (configuration interaction) description of the monomer wavefunctions, is identical to the BSSE-free energy of SAPT (Symmetry Adaptation in Perturbation Theory). SAPT theory is BSSE-free because it obtains the interaction energy directly rather than as a difference of energies. Therefore, it has been demonstrated that the CP recipe provides the correct interaction energy.

BSSE can be of the same order of magnitude as the interaction energy, so correcting this error is clearly necessary, especially in systems which are dominated by weak interactions. The uncorrected energy will have BSSE error, unless a very large basis set is used in the calculation; in this case the error will be negligible.

4. INTERMOLECULAR INTERACTION TYPES

Intermolecular interactions must be rigorously characterized via quantum mechanical description by perturbation theory.[4] However, it is very useful to analyze such interactions into contributions that may be explained qualitatively by classical models. In this Section, this qualitative classical description will be discussed, because a deep analysis of the nature of intermolecular interactions is not the aim of this thesis.

The usual partitioning of an intermolecular pairwise potential is in terms of electrostatic, induction (or polarization), dispersion and exchange-repulsion contributions.[3,23,24] Short-range energies are those which vary strongly with the distance; repulsive energies fall into this category. Long-range energies vary less strongly with the distance; electrostatic, induction and dispersion interactions are in this group. Electrostatic and induction terms can be qualitatively understood in terms of classical electrostatics, while repulsion and dispersion forces need a quantum mechanical description. Table 3.1 summarizes the most important two-body interactions that will be explained in this Section.

Table 3.1: Classification and properties of the intermolecular interactions.

Interaction type	Multipoles	Range	Dependence on distance	Pairwise additivity
Exchange-repulsion	All	Short	R^{-12} or $exp(-R)$	No
Electrostatic	Ion-ion	Long	R^{-1}	Yes
	Ion-dipole	Long	R^{-2} and R^{-4*}	Yes
	Dipole-dipole	Long	R^{-3} and R^{-6*}	Yes
Induction	Ion-induced dipole	Long	R^{-4}	No
	Dipole-induced dipole	Long	R^{-6}	No
Dispersion	Induced dipole-induced dipole	Long	R^{-6}	No

*If the average of all the orientations is taken into account; see text below.

4.1 Short-range interactions: exchange-repulsion

The origin of the repulsion between two molecules is purely quantum mechanical and is a combination of two effects.[25] The exchange energy is a consequence of the fact that the electron motions can extend over both molecules, and it is an attractive term. The repulsion energy arises when the electrons attempt to occupy the same region of space, and are forced to redistribute because the Pauli principle forbids electrons of the same spin to be in the same place; this is a repulsive term. The magnitude of the Pauli or exchange-repulsion interaction depends on the orbital overlap of the interacting species, that is, depends on the intermolecular distance R. Interatomic repulsions are often represented by terms with a R^{-12} dependence (as in the Lennard-Jones potential) or by exponential type terms that yield more realistic repulsive walls.[23] The exchange-repulsion interaction is not pairwise additive.[1]

$$V_{rep} = \frac{B}{R^{12}} \; or \; V_{rep} = exp(-BR) \tag{3.7}$$

4.2 Long-range interactions

All long-range interactions are attractive (except the interaction between two ions with the same charge sign) and they are important when the distance between molecules is large enough and, therefore, the overlap of electrons can be neglected. These sorts of interactions vary with R^{-n}, where the power n changes depending on the interaction type as will be seen below. Long-range interactions can be classified into electrostatic, induction and dispersion contributions.

i. Electrostatic interactions

This interactions are exactly pairwise additive[24] and can be described by the classical theory. Electrostatic energy is caused by the interaction between charges and/or permanent multipole moments. In general, the strength of the interaction between two moments has the form

$$V_{elect} \propto \varepsilon^{-1}|M_1||M_2|R^{-n_1-n_2-1} \tag{3.8}$$

where M_1 and M_2 are the multipole moments of orders n_1 and n_2, R is the distance between molecules and ε is the permittivity of the environment. In this way, the longest-range interactions (those which fall off most slowly with distance) are those between two monopoles or charges in which $n_1 = n_2 = 0$, and equation 3.8 predicts an energy proportional to R^{-1}. If one molecule is charged and the other is neutral but dipolar, the monopole-dipole interaction,

with $n_1 = 0$ and $n_2 = 1$, varies as R^{-2}. Similarly, dipole-dipole interactions fall off as R^{-3}, dipole-quadrupole as R^{-4}, quadrupole-quadrupole as R^{-5} and so forth. Table 3.2 shows the energy dependence on the distance for multipole-multipole interactions from monopoles to hexadecapoles.

Table 3.2: Dependence of the multipole-multipole interactions on the distance.

	Monopole	Dipole	Quadrupole	Octopole	Hexadecapole
Monopole	R^{-1}	R^{-2}	R^{-3}	R^{-4}	R^{-5}
Dipole	R^{-2}	R^{-3}	R^{-4}	R^{-5}	R^{-6}
Quadrupole	R^{-3}	R^{-4}	R^{-5}	R^{-6}	R^{-7}
Octopole	R^{-4}	R^{-5}	R^{-6}	R^{-7}	R^{-8}
Hexadecapole	R^{-5}	R^{-6}	R^{-7}	R^{-8}	R^{-9}

If the molecules are charged or have large permanent dipole moments, the strongest electrostatic interactions are ion-ion (monopole-monopole), ion-dipole and dipole-dipole, that is, the multipoles of order greater than 1 can be neglected. Figure 3.5 shows these three strongest interactions, where dipole vectors point from negative charge toward positive charge q.

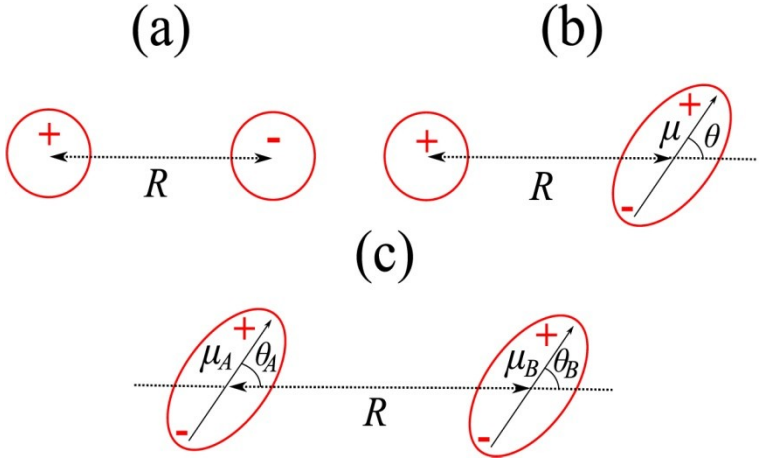

Figure 3.5: (a) Two ions. (b) An ion and a dipolar molecule. (c) Two dipolar molecules.

If two ions with charges $z_A e$ and $z_B e$ are separated by a distance R as can be seen in Figure 3.5a, the energy of attraction or repulsion (depending on the charge signs) obeys the equation

$$V_{i-i} = \frac{z_A z_B e^2}{4\pi\varepsilon R} \tag{3.9}$$

Figure 3.5b shows a dipolar molecule with an ion at a distance R from its center of charge. The interaction energy between them depends on the angle θ formed by the vectors R and μ, and is given by

$$V_{i-d}(\theta) = -\frac{z_A e\mu cos\theta}{4\pi\varepsilon R^2} \tag{3.10}$$

Depending on the relative orientation between the ion and the dipole, the energy can be repulsive or attractive. In general, the dipole will be orientated so that the interaction is attractive, that is, the system is stable. In a gas or a liquid, the potential energy will be an average over the various orientations of the dipole with respect to the ion. The weight of each orientation will be in accordance with the Boltzmann distribution. When this is taken into account, the ion-dipole potential energy is found to be

$$V_{i-d} = -\left(\frac{z_A e\mu}{4\pi\varepsilon}\right)^2 \frac{2}{3k_B T R^4} \tag{3.11}$$

where k_B is the Boltzmann constant and T is the temperature. Now the dependence is on the inverse fourth power of the distance.

When two permanent dipole moments μ_A and μ_B are in the same plane, and they are separated by a distance R as shown Figure 3.5c, the interaction energy between them is

$$V_{d-d}(\theta_A, \theta_B) = -\frac{\mu_A \mu_B}{4\pi\varepsilon R^3}(2\cos\theta_A \cos\theta_B - \sin\theta_A \sin\theta_B) \tag{3.12}$$

Dipole-dipole potential energy depends on the relative orientation of the two molecules. Taking into account the average weighted orientations in the same way as ion-dipole energy, the interaction energy is given by

$$V_{d-d} = -\frac{{\mu_A}^2 {\mu_B}^2}{24\pi^2\varepsilon^2 k_B T R^6} \tag{3.13}$$

The ion-dipole and dipole-dipole energies, as seen in equations 3.11 and 3.13, depend on the temperature because the orientation of the molecules changes with the thermal agitation. At low temperatures, the system takes the most stable configuration because thermal energy is not enough for overcoming the intermolecular interactions, therefore the attraction is increased. If the temperature is high enough for breaking the intermolecular interactions, the

movement of the molecules is essentially free, and the system can adopt stable and unstable orientations, therefore the potential energy is less attractive.

ii. Induction interactions

A molecule (with or without permanent dipole) can have a dipole moment induced by an electric field. If the field strength is E, the induced dipole moment μ^* is αE, where α is the electric polarizability of the molecule, that is, the ability to distort its electronic density. The electric field can be created by an ion or a molecule with permanent dipole moment. Figure 3.6 displays these two situations, that is, an ion (a) and a polar molecule (b) inducing a dipole moment in another molecule. Equation 3.14 gives the interaction between an ion with charge $z_A e$ and a nonpolar molecule with an induced dipole moment αE:

$$V_{i-id} = -\frac{\alpha(z_A e)^2}{8\pi\varepsilon R^4} \tag{3.14}$$

In the case of a permanent dipole A interacting with a nonpolar molecule B, the potential energy is

$$V_{d-id} = -\frac{\mu_A^2 \alpha_B}{(4\pi\varepsilon)^2 R^6} \tag{3.15}$$

And the energy for two polar molecules must take into account the induction of molecule A on molecule B and vice versa; the corresponding interaction follows the equation

$$V_{d-id} = -\frac{\mu_A^2 \alpha_B + \mu_B^2 \alpha_A}{(4\pi\varepsilon)^2 R^6} \tag{3.16}$$

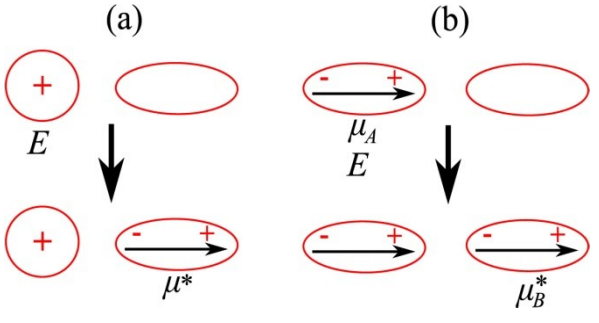

Figure 3.6: (a) Ion-induced dipole and (b) dipole-induced dipole interactions

Note that temperature not appears in equations 3.14-3.16 since the induced moment is always parallel to the electric field, therefore, induction

energies do not depend on the relative orientation between the molecules and it is always attractive. In addition, induction forces are not pair additive and the cause is the following. If a molecule is inducing a dipole in other molecule, and a third molecule is near, it will alter the dipole induced by the first molecule.

iii. Dispersion interactions

The final kind of long-range attractive interaction is that arising from the so-called dispersion forces. These forces are always present between any two molecules whether or not there are permanent multipoles of any order. The dispersion forces are quantum mechanical in origin, and they result from the correlated motion of electrons in the two molecules. From a classical view, if two nonpolar atoms or molecules are close together, on average the electron densities are arranged symmetrically. But at any given instant, the electron distribution in one of the molecules may be unsymmetrical, and this molecule is momentarily a dipole. This dipole generates a transient electric field that tends to polarize the electrons in the neighbouring molecule, producing a transient dipole moment there. Both molecules are hence dipoles at this instant, and the direction of the dipoles is such that they attract one another. The effect is greatest in molecules with high polarizability, that is, in big molecules where electrons are less strongly linked to the nuclei.

The accurate calculation of the dispersion forces is extremely complicated. One relatively simple model gives equation 3.17 for computing the dispersion or London interactions:

$$V_{disp} = -\frac{3}{2}\left(\frac{h\nu_A\nu_B}{\nu_A + \nu_B}\right)\frac{\alpha_A\alpha_B}{(4\pi\varepsilon)^4 R^6} \tag{3.17}$$

where h is the Planck constant, ν_A and ν_B are approximately equal to the frequencies of the first allowed electronic transitions in the molecules A and B.

The dispersion energy exists in all kind of molecules and it is the dominant contribution to the long-range interaction for nonpolar molecules. As for induction, dispersion forces are nonadditive because the presence of other molecules will modify the induced dipolar moments between two molecules.

iv. van der Waals interactions

The term van der Vaals forces is often used to include all the attractive forces between neutral molecules, but these are not a new type of interactions. The forces that are included in this term are dipole-dipole, dipole-induced dipole and dispersion. Moreover, any other multipole interaction of higher order is also included, such as dipole-quadrupole or quadrupole-

quadrupole, but, frequently, these are not important in comparison with the interactions between dipoles. As seen in equations 3.13, 3.16 and 3.17, all the interactions between dipoles vary with distance as R^{-6}, therefore, they can be comprised in only one equation with the form

$$V_{vdW} = -\frac{C_6}{R^6} \tag{3.18}$$

being C_6 a constant to be parameterized. The Lennard-Jones 12-6 potential, used in the most common molecular mechanics force fields includes the van der Waals interactions in its attractive term only. The positive term describes the exchange-repulsion interaction:

$$V = 4\varepsilon\left[\left(\frac{\sigma}{R}\right)^{12} - \left(\frac{\sigma}{R}\right)^{6}\right] \tag{3.19}$$

5. MODEL POTENTIALS

A potential energy function needs to incorporate information about the system it describes, in the form of numerical parameters. These parameters, as mentioned above, can be obtained by fitting to a range of experimental data as in molecular mechanics force fields. Another way is to obtain the potential parameters from a fit to interaction energies calculated by electronic structure methods for different configurations between the two molecules. Except for very small molecules, it is usual to write the intermolecular potential as a sum of atom-atom or two body terms

$$V^{AB} = \sum_{i \in A}\sum_{j \in B} V^{ij}\left(R_{ij}\right) \tag{3.20}$$

where the sum is taken over the atoms i of molecule A and the atoms j of molecule B, and V^{ij} depends on the distance R_{ij} between the atoms.

As seen in Section 4, the main contributions of the potential energy are the exchange-repulsion, the electrostatic, the induction and the dispersion terms. Additional contributions, like charge transfer energy, which is important in systems that undergo electron transfer between molecules, can be significant for some particular systems, but in general, the previous four contributions are the most relevant. Therefore, the potential function must be developed taking into account the kind of interactions involved in the system. Kaplan[2] has described the most used potential functions for modelling intermolecular interactions, and here some of them are summarized.

The Lennard-Jones 12-6 potential is probably the most used function for describing the non-bonded interactions, and it is written as

$$V = 4\varepsilon\left[\left(\frac{\sigma}{R}\right)^{12} - \left(\frac{\sigma}{R}\right)^{6}\right] \tag{3.21}$$

where ε is the depth of the potential well with the minimum at $R_m = 2^{1/6}\sigma$ and σ is the value of the distance at $V = 0$ as Figure 3.7 shows. The attractive term corresponds to the van der Waals interactions between two neutral molecules, and the repulsion is approximated by the power term of order 12. The variation of repulsion with the distance described by an exponential term is a more realistic choice than the power term, but the term of R^{-12} is used due to mathematical convenience.

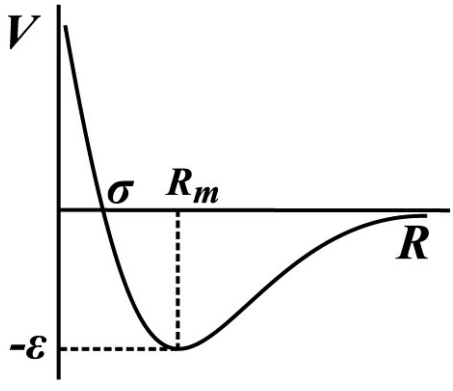

Figure 3.7: The Lennard-Jones potential.

The Lennard-Jones potential must be modified for describing systems formed by ions and neutral molecules. Mason and Schamp included a term proportional to R^{-4} to take into account the ion-dipole interaction

$$V = 2\varepsilon\left[(1+\gamma)\left(\frac{\sigma}{R}\right)^{12} - 2\gamma\left(\frac{\sigma}{R}\right)^{6} - 3(1-\gamma)\left(\frac{\sigma}{R}\right)^{4}\right] \tag{3.22}$$

where the parameter γ measures the importance of the induction and van der Waals terms. If $\gamma = 1$ the term of R^{-4} vanishes, and this 12-6-4 potential transforms into the 12-6 one.

Another modified Lennard-Jones potential is the one proposed by Klein and Hanley. They added a dipole-quadrupole term and considered the order m in the repulsive term as a parameter giving rise to an m-6-8 potential

$$V = \frac{A}{R^m} - \frac{B}{R^6} - \frac{C}{R^8} \tag{3.23}$$

Kihara proposed a modification of the Lennard-Jones potential that takes into account the size of the molecules under study. The distance used in the intermolecular potential is that between the surfaces "wrapping" the molecules, instead of atom-atom distances; that means that the molecules are treated as a whole so that the potential is simpler than a conventional pairwise potential. The potential has the form

$$V = \varepsilon\left[\left(\frac{\rho_0}{\rho}\right)^{12} - 2\left(\frac{\rho_0}{\rho}\right)^{6}\right] \tag{3.24}$$

with ρ being the distance between the nearest points of the molecules, ρ_0 corresponds to the minimum of the potential curve and ε is the depth of the potential well.

Another analytical function is that proposed by Buckingham, which includes attractive terms due to dipole-dipole (permanent or induced) interactions, proportional to R^{-6}, and dipole-quadrupole interactions that vary with R^{-8}. The repulsive term is approximated by an exponential function

$$V = Ae^{-BR} - \frac{C}{R^6} - \frac{D}{R^8} \tag{3.25}$$

where A, B, C and D are parameters. Simulations using this potential require more computational time than those using Lennard-Jones potentials due to the exponential term. But an exponential function describes better the repulsion between two molecules. Note that the Buckingham potential can not be applied at very small distances; it has a spurious maximum and approaches $-\infty$ at $R \to 0$ as Figure 3.8 displays.

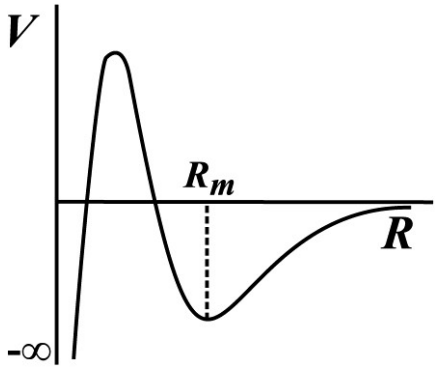

Figure 3.8: The Buckingham potential.

In the Buckingham-Cornel potential the incorrect behaviour at small R is removed by adding an exponential term to the attractive part of the Buckingham potential:

$$V = \begin{cases} Ae^{-B\frac{R}{R_m}} - \left(\frac{C}{R^6} + \frac{D}{R^8}\right) e^{\left(-4\left(\frac{R_m}{R}-1\right)^3\right)}, & R < R_m \\ Ae^{-B\frac{R}{R_m}} - \left(\frac{C}{R^6} + \frac{D}{R^8}\right), & R > R_m \end{cases} \quad (3.26)$$

If $R < R_m$ the exponential term multiplying the attractive part avoids the value $-\infty$ at $R \to 0$.

Many other functions can be employed for describing the intermolecular energy. For instance, other multipole terms can be added to the Lennard-Jones and Buckingham potentials depending on the importance of the different multipoles interactions and the required level of accuracy. In this way, attractive terms that vary with R^{-10}, R^{-12}, R^{-14}, etc. can be used for modelling interactions for quadrupole-quadrupole, quadrupole-octopole, octopole-octopole, etc. One must take into account that, in theory, many multipole terms will fit better the molecular structure calculations, but if many parameters are included, the CPU time of the parameterization will be too long. Therefore, a compromise between accuracy and CPU time must be reached.

The potential energy surfaces developed throughout this thesis were obtained by fitting interaction energies, calculated by electronic structure methods, to analytical functions. The systems for which these potentials were calculated are $SiNCS^+/CF_4$ and $(CH_3)_2SiNCS^+/CF_4$ (Chapter 10), and NO/CF_4 (Chapter 9); the CF_4 molecule was chosen as a model to represent the fluorocarbon chains of the F-SAM surface. The Buckingham exp-*n*-*m* potential was used for describing the interaction energy for the three systems

$$V = Ae^{-BR} - \frac{C}{R^n} - \frac{D}{R^m} \quad (3.27)$$

The dominant interactions for the systems $SiNCS^+/CF_4$ and $(CH_3)_2SiNCS^+/CF_4$ are ion/dipole and dipole/dipole; the CF_4 is nonpolar but one can consider the dipole moments of each C-F bond. In any case, even if one regards CF_4 as a molecule with no-permanent dipole moment, the leading interactions would be ion-induced dipole and dipole-induced dipole, which vary with distance in the same way as ion-dipole and dipole-dipole. Therefore two attractive terms with n and m equal or close to 4 and 6, respectively, may be necessary.

For the NO/CF_4 system the dipole-dipole (permanent or induced) interaction is the most important, but another term of dipole-quadrupole type was introduced in the potential to improve the quality of the fit. In this case the attractive *n* and *m* parameters should approach 6 and 8, respectively.

More details about these potential optimizations will be discussed in subsequent chapters.

6. OPTIMIZATION METHODS

Usually, the above analytical functions are fitted to electronic structure calculations by means of some optimization algorithm. This part of the Chapter describes the different optimization methods.

There are three general algorithms to direct the curve fitting; these are interpolation, least-square regression and genetic algorithms.[26,27] In this thesis, a genetic algorithm developed by Marques et al.,[28] that combines a quasi-Newton least-square optimization with a genetic method, was employed. In this Section, the conventional least-square and the genetic methods will be discussed. The interpolation technique will not be tackled here but it is also widely used. For instance, Collins group[29-31] has developed a powerful method for obtaining a potential energy surface, in Cartesian and internal coordinates, for polyatomic systems as an interpolation of local Taylor expansions.

6.1 Least-squares regression

The least-squares method minimizes the summed squared of residuals S. The residual r_i for an ith data point is defined as the difference between the observed response value y_i and the fitted response value f_i

$$r_i = y_i - f_i \tag{3.28}$$

The summed squared of residuals is given by

$$S = \sum_{i=1}^{n} r_i^2 = \sum_{i=1}^{n} (y_i - f_i)^2 \tag{3.29}$$

A linear model is defined as an equation that is linear in the coefficients. For example, suppose one has n data points that can be modelled by a first degree polynomial:

$$f = b_1 x + b_2 \tag{3.30}$$

Writing S as a function of the parameters

$$S = \sum_{i=1}^{n} r_i^2 = \sum_{i=1}^{n} \left(y_i - (b_1 x_i + b_2)\right)^2 \tag{3.31}$$

The least-square fitting process minimizes the summed square of the residuals, therefore the coefficients are determined by differentiating S with respect to each parameter, and setting the result equal to zero

$$\frac{\partial S}{\partial b_1} = -2\sum_{i=1}^{n} x_i\left(y_i - (b_1 x_i + b_2)\right) = 0 \tag{3.32}$$

$$\frac{\partial S}{\partial b_2} = -2\sum_{i=1}^{n} \left(y_i - (b_1 x_i + b_2)\right) = 0 \tag{3.33}$$

Setting the sum to zero

$$\sum_{i=1}^{n} x_i\left(y_i - (b_1 x_i + b_2)\right) = 0 \tag{3.34}$$

$$\sum_{i=1}^{n} \left(y_i - (b_1 x_i + b_2)\right) = 0 \tag{3.35}$$

Reorganizing equations 3.34 and 3.35

$$b_1 = \frac{n\sum_{i=1}^{n} x_i y_i \sum_{i=1}^{n} x_i \sum_{i=1}^{n} y_i}{n\sum_{i=1}^{n} x_i^2 - \left(\sum_{i=1}^{n} x_i\right)^2} \tag{3.36}$$

$$b_2 = \frac{1}{n}\left(\sum_{i=1}^{n} y_i - b_1 \sum_{i=1}^{n} x_i\right) \tag{3.37}$$

As shown in equations 3.36 and 3.37, estimating parameters b_1 and b_2 requires only a few calculations. Extending this simple example to a higher degree polynomial is straightforward. Therefore, an optimization using a linear model by least-square is very easy to achieve, but unfortunately, potential energy surfaces never have these linear forms, and a regression by nonlinear least-square is required.

A nonlinear model is defined as an equation that is nonlinear in the coefficients, for example, exponentials, ratios of polynomials and power functions. The equation used for fitting the potential energy in Chapters 9 and 10 is

$$V = Ae^{-BR} - \frac{C}{R^n} - \frac{D}{R^m} \tag{3.27}$$

where the coefficients B, n and m are nonlinear with respect to the potential energy. In this case the coefficients can not be estimated solving a simple system of equations, instead an iterative approach is required. An iterative algorithm starts from some initial values of the parameters and then repeatedly calculates next available values according to a particular rule, until a minimum of residuals is reached.

If the set of coefficients b_i is called β, to minimize the summed squared of residuals $S(\beta)$, a generic algorithm can be expressed as

$$\beta^{(j+1)} = \beta^{(j)} + s^{(j)} d^{(j)} \tag{3.38}$$

so that the $(j+1)$th iterated value $\beta^{(j+1)}$ is obtained from $\beta^{(j)}$, the value from the previous iteration, by adjusting the amount $s^{(j)} d^{(j)}$, where $d^{(j)}$ characterizes the direction of change in the parameter space and $s^{(j)}$ controls the amount of change. Different algorithms result from different choices of s and d.

If the first-order Taylor expansion of $S(\beta)$ about a set of parameter values β^* is considered, one can write:

$$S(\beta) = S(\beta^*) + \frac{\partial S(\beta^*)}{\partial \beta^*}(\beta - \beta^*) \tag{3.39}$$

and replacing β with $\beta^{(j+1)}$ and β^* with $\beta^{(j)}$ we obtain

$$S\left(\beta^{(j+1)}\right) = S\left(\beta^{(j)}\right) + \nabla_\beta S\left(\beta^{(j)}\right)\left(\beta^{(j+1)} - \beta^{(j)}\right) \tag{3.40}$$

The term $\left(\beta^{(j+1)} - \beta^{(j)}\right)$ is equal to $s^{(j)} d^{(j)}$ as equation 3.38 shows, therefore equation 3.40 turns into

$$S\left(\beta^{(j+1)}\right) = S\left(\beta^{(j)}\right) + \nabla_\beta S\left(\beta^{(j)}\right) s^{(j)} d^{(j)} \tag{3.41}$$

Note that this approximation is valid when $\beta^{(j+1)}$ is in the neighbourhood of $\beta^{(j)}$. If $g(\beta)$ denotes the gradient of $S(\beta)$, $g^{(j)}$ denotes $g(\beta)$ evaluated at $\beta^{(j)}$ and the direction $d^{(j)}$ is given by $-g^{(j)}$, we get

$$S\left(\beta^{(j+1)}\right) = S\left(\beta^{(j)}\right) - s^{(j)}\left(g^{(j)'} g^{(j)}\right) \tag{3.42}$$

As $g^{(j)'} g^{(j)}$ is non-negative, one can find a positive and small value of s such that S is decreasing. When $\beta^{(j)}$ is already a minimum of S, $g^{(j)}$ is zero so that the parameterization finishes because $S\left(\beta^{(j+1)}\right) = S\left(\beta^{(j)}\right)$. This suggests the following algorithm:

$$\beta^{(j+1)} = \beta^{(j)} - s^{(j)} g^{(j)} \tag{3.43}$$

Given the search direction, one can chose $s^{(j)}$ so that the next value of the objective function $S\left(\beta^{(j+1)}\right)$ is a minimum, differentiating $S\left(\beta^{(j+1)}\right)$ with respect to $s^{(j)}$ and setting the derivative to zero. Using the chain rule, the derivative can be expressed as

$$\frac{\partial S\left(\beta^{(j+1)}\right)}{\partial s^{(j)}} = \frac{\partial S\left(\beta^{(j+1)}\right)}{\partial \beta^{(j+1)}} \frac{\partial \beta^{(j+1)}}{\partial s^{(j)}} = 0 \tag{3.44}$$

where $\frac{\partial S(\beta^{(j+1)})}{\partial \beta^{(j+1)}}$ is the gradient $g^{(j+1)}$ and $\frac{\partial \beta^{(j+1)}}{\partial s^{(j)}}$ is equal to $-g^{(j)}$. Therefore equation 3.44 can be rewritten as

$$\frac{\partial S(\beta^{(j+1)})}{\partial s^{(j)}} = -g^{(j+1)'} g^{(j)} = 0 \tag{3.45}$$

Now, the Hessian matrix of S at $\beta^{(j)}$ is denoted by $H^{(j)}$

$$H^{(j)} = \nabla_{\beta}^{2} S(\beta^{(j)}) = \nabla_{\beta} g(\beta) \tag{3.46}$$

Then, writing g as a first-order Taylor expansion, one obtains

$$g^{(j+1)} = g^{(j)} + \nabla_{\beta} g(\beta^{(j)})(\beta^{(j+1)} - \beta^{(j)}) \tag{3.47}$$

Since $\nabla_{\beta} g(\beta^{(j)})$ is the Hessian $H^{(j)}$ and $(\beta^{(j+1)} - \beta^{(j)})$ is equal to $-s^{(j)} g^{(j)}$ (equation 3.43), equation 3.47 can be written as

$$g^{(j+1)} = g^{(j)} - H^{(j)} s^{(j)} g^{(j)} \tag{3.48}$$

and replacing 3.48 into 3.45 we have

$$g^{(j+1)'} g^{(j)} = 0 = (g^{(j)'} - H^{(j)} s^{(j)} g^{(j)'}) g^{(j)} \tag{3.49}$$

$$g^{(j)'} g^{(j)} - s^{(j)} g^{(j)'} H^{(j)} g^{(j)} = 0 \tag{3.50}$$

or equivalently

$$s^{(j)} = \frac{g^{(j)'} g^{(j)}}{g^{(j)'} H^{(j)} g^{(j)}} \tag{3.51}$$

The step $s^{(j)}$ is non-negative whenever $H^{(j)}$ is positive. Replacing equation 3.51 in equation 3.43, the algorithm reads

$$\beta^{(j+1)} = \beta^{(j)} - \frac{g^{(j)'} g^{(j)}}{g^{(j)'} H^{(j)} g^{(j)}} g^{(j)} \tag{3.52}$$

which is known as the **steepest descent algorithm**. This method may point to a wrong direction if H is not positive. In addition, this algorithm adjusts parameters β along the opposite of the gradient direction, therefore, it may run into difficulty when the nonlinear function being optimized is flat around the minimum. An alternative is to consider the second-order Taylor expansion of $S(\beta)$ around some β^{*}

$$S(\beta) = S(\beta^{*}) + g^{*'}(\beta - \beta^{*}) + \frac{1}{2}(\beta - \beta^{*})' H^{*}(\beta - \beta^{*}) \tag{3.53}$$

where g^{*} and H^{*} are the gradient and the Hessian evaluated at β^{*} respectively. The minimum is obtained differentiating $S(\beta)$ with respect to the coefficients β:

$$\frac{dS(\beta)}{d\beta} = g^* + H^*(\beta - \beta^*) = 0 \tag{3.54}$$

$$\beta = \beta^* - (H^*)^{-1} g^* \tag{3.55}$$

The next algorithm arises from replacing β with $\beta^{(j+1)}$ and β^* with $\beta^{(j)}$ in equation 3.55:

$$\beta^{(j+1)} = \beta^{(j)} - \left(H^{(j)}\right)^{-1} g^{(j)} \tag{3.56}$$

where the direction vector is $-\left(H^{(j)}\right)^{-1} g^{(j)}$ and the step length is 1. This method is known as the **Newton-Raphson algorithm**. Note that the Hessian matrix must be non-singular so that its inverse exists. This algorithm requires the computation of both second derivatives and matrix inversion at each iteration step. Thus, the method is not very useful in practice for functions with a large number of variables. Alternatively, a step length can be added to equation 3.56 and we obtain

$$\beta^{(j+1)} = \beta^{(j)} - s^{(j)}\left(H^{(j)}\right)^{-1} g^{(j)} \tag{3.57}$$

where $s^{(j)}$ is chosen so that $S(\beta)$ is decreasing at each iteration.

Both steepest descent and Newton-Raphson algorithms calculate second-order derivatives, that is, these methods are high computing demanding. An algorithm that avoids calculating the Hessian matrix is the so-called **Gauss-Newton algorithm**. As seen above, in equation 3.29, the summed squared of residuals is defined as

$$S = \sum_{i=1}^{n} r_i^2 = \sum_{i=1}^{n} \left(y_i - f_i(\beta)\right)^2 \tag{3.29}$$

Rewriting this equation as,

$$S = \sum_{i=1}^{n} \left(y_i - f_i(\beta)\right)\left(y_i - f_i(\beta)\right) \tag{3.58}$$

the first-order derivative of S with respect to the coefficients β is given by,

$$\nabla_\beta S = -2 \sum_{i=1}^{n} \nabla_\beta f_i(\beta)\left(y_i - f_i(\beta)\right) \tag{3.59}$$

and the second-order derivative, that is the Hessian, follows the equation

$$H = \nabla_\beta^2 S = -2 \sum_{i=1}^{n} \nabla_\beta^2 f_i(\beta)\left(y_i - f_i(\beta)\right) + 2 \sum_{i=1}^{n} \nabla_\beta f_i(\beta) \nabla_\beta f_i(\beta) \tag{3.60}$$

In the Gauss Newton regression the first term on the right hand side is ignored, so that the Hessian is given by

$$H = 2\sum_{i=1}^{n} \nabla_\beta f_i(\beta) \nabla_\beta f_i(\beta) \tag{3.61}$$

There are two main advantages of this approximation. Firstly, only the first-order derivative needs to be computed. Secondly, the Hessian is guaranteed to be positive, therefore, the algorithm never points to a wrong direction during the iterations. But, in general, the performance of this algorithm is lower than that of the Newton-Raphson method because it utilizes only an approximation to the Hessian matrix. The main disadvantage is its slow convergence on problems that are sufficiently nonlinear or have reasonably large residuals.

Unfortunately, in the steepest descent and Newton-Raphson algorithms, the Hessian can change its sign during the iterative steps causing convergence problems. Therefore, it is important to ensure that H is positive at each iteration. A simple approach can be used to correct the Hessian, if necessary, by adding an appropriate matrix to it:

$$H_c = H + cI \tag{3.62}$$

where H_c is the corrected Hessian, c is a positive number to force H_c to be a positive matrix and I is the identity matrix. Such a correction is used in the so-called **Levenberg-Marquardt algorithm**.

The **quasi-Newton methods**, on the other hand, corrects H iteratively by adding a symmetric matrix C:

$$H_c^{(j+1)} = H^{(j)} + C^{(j)} \tag{3.63}$$

where the superscript indicates the number of the iteration step. The initial Hessian is the identity matrix, that is, $H^{(0)} = I$ and the matrix $C^{(j)}$ is calculated in different ways depending on the method. The most used quasi-Newton method is the Broyden-Fletcher-Goldbarb-Shanno (BFGS) algorithm that calculates the matrix C as

$$C^{(j)} = \frac{q^{(j)} q^{(j)'}}{q^{(j)'} s^{(j)}} + \frac{H^{(j)'} s^{(j)\prime} s^{(j)} H^{(j)}}{s^{(j)'} H^{(j)} s^{(j)}} \tag{3.64}$$

where $s^{(j)} = \beta^{(j+1)} - \beta^{(j)}$ and $q = g^{(j+1)} - g^{j}$, being g the gradient. As a starting point $H^{(0)}$ can be set to any symmetric positive definite matrix, for example, the identity matrix I. Another quasi-Newton method, and often less efficient, is the Davidon-Fletcher-Powell (DFP) algorithm that uses the same formula as the BFGS method except that $q^{(j)}$ is substituted by $s^{(j)}$. The

algorithm employed in this thesis to fit the analytical functions contains a least-square part that uses the BFGS method before the genetic step.

In general, the least-square algorithms are sufficiently effective for functions that do not depend on a large number of coefficients. One can select among the available methods depending on the features of the system. For instance, if the function to be fitted has a simple form, a quasi-Newton or the Gauss-Newton method is a good choice because they require not much computational time since they do not calculate second-order derivatives. If one knows a set of coefficients that are near the solution, the Newton-Raphson algorithm is the most suitable method because its convergence is very fast near the minimum. On the other hand, if the coefficient space is very large and one does not know the approximate value of the solution, the steepest descent algorithm is probably the best choice because it runs reliably from poor initial starting values. But, if the analytical function depends on many parameters, the residual surface has lots of local minima and a global convergence is very difficult to achieve. In other words, if the algorithm falls into a relatively deep local minimum, the system is not able to escape from this well. In Chapter 10, an analytical potential energy surface for the $(CH_3)_2SiNCS^+/CF_4$ system was developed. The sylil ion and the CF_4 molecule have 6 and 2 atom types, respectively, that is, there are 12 different types of interatomic interactions. As mentioned above, each two-body interaction reads:

$$V = Ae^{-BR} - \frac{C}{R^n} - \frac{D}{R^m} \tag{3.27}$$

This means that each interatomic interaction depends on 6 parameters, and therefore, 72 parameters are necessary for describing the total intermolecular potential. Such a large number of coefficients are very difficult to optimize employing a conventional least-square algorithm. In the next section, an efficient genetic algorithm, which allows optimizations with an important number of parameters, will be explained.

6.2 Genetic algorithms

Genetic algorithms (GAs) are stochastic search algorithms based on principles of natural selection and genetics.[32,33] The GAs as very robust function optimizers are employed in this thesis to fit analytical functions, but GAs have been used in many areas[33] such as image processing, laser technology, spacecraft trajectories, facial recognition and a lot of more besides. GAs are not guaranteed to converge to the global solution, but a careful manipulation of the input parameters makes the chances of success higher than using conventional least-square methods.

GAs start from several sets of coefficients or solutions, called population, and modify them to obtain improved coefficients. Since these algorithms optimize the function using several sets of solutions, the search for the optimal coefficients is faster, in comparison with least-square regressions, because GAs cover a more extensive region on the search space. In general, a typical GA consists in the following. Frequently, the initial population is generated randomly. Each set of parameters of this population, called individual, is evaluated to determine how well it enables the adjustment of the data points to the model function. The individuals with better performance are selected as parents of the next generation. GAs create new individuals using simple randomized operators that resemble sexual recombination (crossover) and mutation in natural organisms. The new solutions are evaluated with the fitness function, and the cycle of selection, recombination and mutation is repeated until a termination criterion is satisfied.

A genetic algorithm developed by Marques *et al.*[28] was employed throughout this thesis to fit the potential energy functions to electronic structure energy data. Next, this algorithm is briefly described. The initial population formed by k individuals or solutions is generated randomly within an interval selected intuitively. Each individual encodes a specific set of M parameters or gens $(b_1, b_2 \ldots b_M)$ as Figure 3.9 shows.

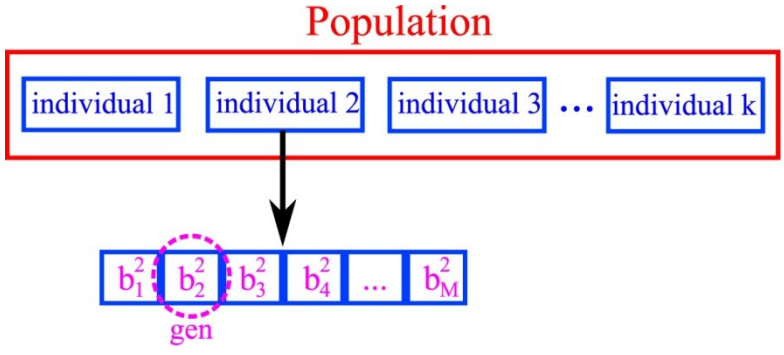

Figure 3.9: Structure of the population formed by k sets of parameters.

The quasi-Newton BFGS method, seen above, is applied to carry out a local optimization of the population. After that, the fitness of each individual is evaluated calculating the summed squared of residuals S that are given by equation 3.29

$$S = \sum_{i=1}^{n} r_i^2 = \sum_{i=1}^{n} (y_i - f_i)^2 \tag{3.29}$$

In order to improve the quality of the fit, each data point is weighted during the optimization so that S is calculated as

$$S = \sum_{i=1}^{n} \omega_i r_i^2 = \sum_{i=1}^{n} \omega_i (y_i - f_i)^2 \tag{3.65}$$

where the weights are chosen by trial and error, that is, the highest weights are assigned to the energies with the highest relative errors after a prior optimization. In subsequent optimizations, if some values of energy are badly reproduced by the function, their weights are increased. That means that the weights are iteratively changed until all the energies are reproduced by the function with similar accuracy.

After evaluating the fitness of each individual with equation 3.65, the whole population is replaced by its offspring. The new generation, that is, the new set of solutions, is obtained after a series of steps. First, the parents of the new generation are selected from the current generation by mean of the tournament selection. To select one parent, this method chooses randomly T individuals from the current population. The best solution from this set of T individuals is selected as a parent of the new generation. For a population with k individuals, the procedure is repeated k times in order to obtain k parents as shown in Figure 3.10. That means the number of individuals along the optimization process is always the same.

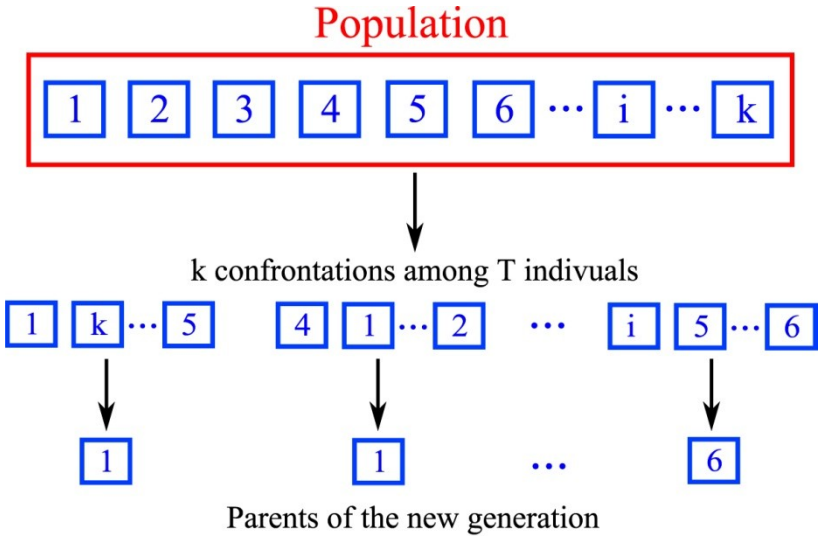

Figure 3.10: Tournament selection.

After the tournament selection, crossover and mutation operators are applied to the selected parents to obtain the descendants, that is, the new improved sets of parameters. Two different crossover operators are considered. The first one is a discrete recombination operator that selects a random cut point along the sequence of parameters in two parents. Then, the two children are obtained by exchanging the fragments of the parents. This procedure is depicted in Figure 3.11. The second operator is known as arithmetic crossover and it calculates each children parameter as a linear combination of the corresponding values from the parents following the next steps:

a. Select a random value μ between 0 and 1.
b. Calculate

$$\begin{aligned} \beta &= (2\mu)^{1/(\eta+1)} \quad \text{if} \quad \mu \leq 0.5 \\ \beta &= \left(\frac{1}{2}(1-\mu)\right)^{1/(\eta+1)} \quad \text{if} \quad \mu > 0.5 \end{aligned} \tag{3.66}$$

c. Obtain the children

$$\begin{aligned} Child^1 &= 0.5\big((1+\beta)Parent^1 - (1-\beta)Parent^2\big) \\ Child^2 &= 0.5\big((1-\beta)Parent^1 + (1+\beta)Parent^2\big) \end{aligned} \tag{3.67}$$

where η is a non-negative real number that controls the resemblance among parents and children. Decreasing the value of η allows to obtain solutions very different from their parents, and increasing η causes the descendants to be close to their parents.

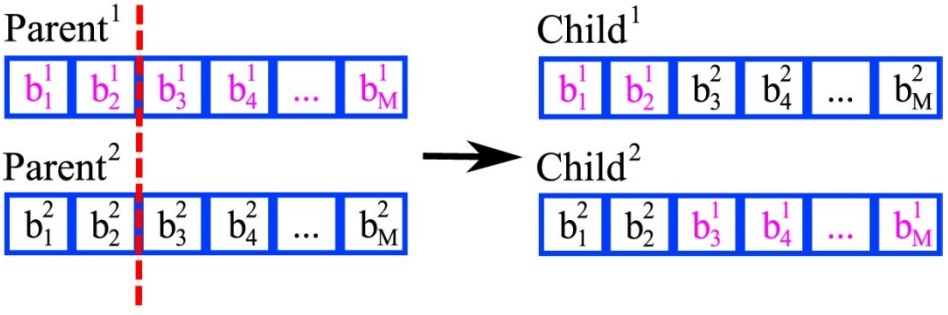

Figure 3.11: Discrete crossover.

The other process that allows to modify the individuals is the mutation. In this process the algorithm randomly selects one gen of the individual and mutates it to a new value. Two different operators act in the

algorithm; the first one changes randomly the value of the gen, and the second one modifies the gen according to the following expression.

$$b_i^{(j+1)} = b_i^{(j)} + \sigma\left(b_i^{max} - b_i^{min}\right)N(0,1) \tag{3.68}$$

where σ is a parameter from the algorithm, $N(0,1)$ is a random value and b_i^{max} and b_i^{min} represent the upper and lower bounds for the parameter b_i undergoing mutation.

When the new population is formed after the crossover and the mutation, the individuals are locally optimized by the quasi-Newton BFGS method and evaluated again. An elitist strategy ensures that the quality of the best individual never decreases along the optimization. The described process is repeated until a termination criterion is reached. The final solution, that is, the best set of coefficients is the best individual obtained in the last step. Figure 3.12 shows the whole process carried out by this genetic algorithm.

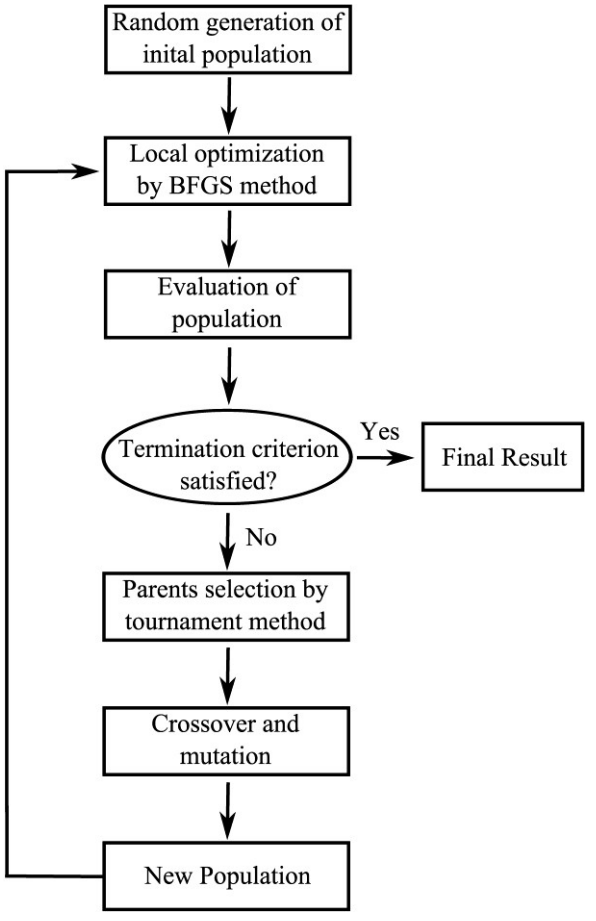

Figure 3.12: Steps of the genetic algorithm.

REFERENCES

(1) Scheiner, S. *Molecular Interactions*; John Wiley & Sons: Illinois, 1994.

(2) Kaplan, I. G. *Intermolecular Interactions: Physical Picture, Computational Methods and Model Potentials*; John Wiley and Sons: Mexico, 2006.

(3) Berry, R. S.; Rice, S. A.; Ross, J. *Physical Chemistry*; Second ed.; Oxford University Press: New York, 2000.

(4) Jezioski, B.; Szalewicz, K. In *Encyclopedia of Computational Chemistry*; von Ragué Schleyer, P., Ed.; Jonh Wiley & Sons: Chichester, 1998; Vol. 2, p 1376-1398.

(5) Cornell, W. D.; Cieplak, P.; Bayly, C. I.; Gould, I. R.; Merz, K. M., Jr.; Ferguson, D. M.; Spellmeyer, D. C.; Fox, T.; Caldwell, J. W.; Kollman, P. A. *J. Am. Chem. Soc.* **1995**, *117*, 5179-97.

(6) MacKerell, A. D., Jr.; Bashford, D.; Bellott, M.; Dunbrack, R. L.; Evanseck, J. D.; Field, M. J.; Fischer, S.; Gao, J.; Guo, H.; Ha, S.; Joseph-McCarthy, D.; Kuchnir, L.; Kuczera, K.; Lau, F. T. K.; Mattos, C.; Michnick, S.; Ngo, T.; Nguyen, D. T.; Prodhom, B.; Reiher, W. E., III; Roux, B.; Schlenkrich, M.; Smith, J. C.; Stote, R.; Straub, J.; Watanabe, M.; Wiorkiewicz-Kuczera, J.; Yin, D.; Karplus, M. *J. Phys. Chem. B* **1998**, *102*, 3586-3616.

(7) Jorgensen, W. L.; Maxwell, D. S.; Tirado-Rives, J. *J. Am. Chem. Soc.* **1996**, *118*, 11225-11236.

(8) Deb, B.; Hu, W.; Song, K.; Hase, W. L. *Phys. Chem. Chem. Phys.* **2008**, *10*, 4565-4572.

(9) Hobza, P.; Hubalek, F.; Kabelac, M.; Mejzlik, P.; Sponer, J.; Vondrasek, J. *Chem. Phys. Lett.* **1996**, *257*, 31-35.

(10) Mu, Y.; Kosov, D. S.; Stock, G. *J. Phys. Chem. B* **2003**, *107*, 5064-5073.

(11) Alexander, W. A.; Morris, J. R.; Troya, D. *J. Chem. Phys.* **2009**, *130*, 084702/1-084702/15.

(12) Tasic, U.; Troya, D. *Phys. Chem. Chem. Phys.* **2008**, *10*, 5776-5786.

(13) Tasic, U.; Day, B. S.; Yan, T.; Morris, J. R.; Hase, W. L. *J. Phys. Chem. C* **2008**, *112*, 476-490.

(14) Vazquez, S. A.; Morris, J. R.; Rahaman, A.; Mazyar, O. A.; Vayner, G.; Addepalli, S. V.; Hase, W. L.; Martinez-Nunez, E. *J. Phys. Chem. A* **2007**, *111*, 12785-12794.

(15) Yan, T.; Hase, W. L.; Barker, J. R. *Chem. Phys. Lett.* **2000**, *329*, 84-91.

(16) Yang, L.; Mazyar, O. A.; Lourderaj, U.; Wang, J.; Rodgers, M. T.; Martinez-Nunez, E.; Addepalli, S. V.; Hase, W. L. *J. Phys. Chem. C* **2008**, *112*, 9377-9386.

(17) Martinez-Nunez, E.; Rahaman, A.; Hase, W. L. *J. Phys. Chem. C* **2007**, *111*, 354-364.

(18) Kestner, N. R. *J. Chem. Phys.* **1968**, *48*, 252-7.

(19) Liu, B.; McLean, A. D. *J. Chem. Phys.* **1973**, *59*, 4557-8.
(20) Boys, S. F.; Bernardi, F. *Mol. Phys.* **1970**, *19*, 553-566.
(21) Chalasinski, G.; Gutowski, M. *Mol. Phys.* **1985**, *54*, 1173-84.
(22) van, D. F. B.; van, D.-v. d. R. J. G. C. M.; van, L. J. H. *Chem. Rev. (Washington, D. C.)* **1994**, *94*, 1873-85.
(23) Bacskay, G. B.; Reimers, J. R. In *Encyclopedia of Computational Chemistry*; von Ragué Schleyer, P., Ed.; Jonh Wiley & Sons: Chichester, 1998; Vol. 4, p 2620-2632.
(24) Laidler, K. J.; Meiser, J. H.; Sanctuary, B. C. *Physical Chemistry*; Houghton Mifflin Company: Boston, 2003.
(25) Stone, A. J. *The Theory of Intermolecular Forces*; Oxford University Press: New York, 1997.
(26) Chapra, S. C.; Canale, R. P. *Numerical Methods for Engineers: With Software and Programming Aplications* 4ed.; McGraw-Hill Higher Education: New York, 2002.
(27) Burden, R. L.; Faires, J. D. *Análisis Numérico*; 7 ed.; Thomson Learning: México, D. F., 2002.
(28) Marques, J. M. C.; Prudente, F. V.; Pereira, F. B.; Almeida, M. M.; Maniero, A. M.; Fellows, C. E. *J. Phys. B: At., Mol. Opt. Phys.* **2008**, *41*, 085103/1-085103/15.
(29) Ischtwan, J.; Collins, M. A. *J. Chem. Phys.* **1994**, *100*, 8080-8.
(30) Thompson, K. C.; Jordan, M. J. T.; Collins, M. A. *J. Chem. Phys.* **1998**, *108*, 564-578.
(31) Thompson, K. C.; Jordan, M. J. T.; Collins, M. A. *J. Chem. Phys.* **1998**, *108*, 8302-8316.
(32) Cantú-Paz, E. *Efficient and Accurate Parallel Genetic Algorithms*; 2 ed.; Kluwer Academic Publishers: Massachusetts, 2001.
(33) Coley, D. A. *An Introduction to Genetic Algorithms for Scientists and Engineers*; World Scientific Publishing: Singapore, 1999.

Chapter 4

Electronic Structure

1. INTRODUCTION

The main potential energy functions and the most common parameterization methods have been explained in Chapter 2. Throughout this thesis the parameterizations were performed to adjust energies from electronic structure calculations. The available quantum mechanical methods for computing energies will be explained in this Chapter.

The time evolution of any system is given by the nonrelativistic time-dependent Schrödinger equation

$$i\hbar\frac{\partial\psi(q,t)}{\partial t} = H(q,t)\psi(q,t) \tag{4.1}$$

where $H(q,t)$ is the Hamiltonian operator that represents the total energy of the system and $\psi(q,t)$ is the wave function that describes completely the state of a system. Both Hamiltonian and wave function depend on the coordinates q and time t. The Hamiltonian for a system formed by N particles has the form[1-3]

$$H(q,t) = T(q) + V(q,t) \tag{4.2}$$

$$\hat{H}(q,t) = -\frac{\hbar^2}{2}\sum_{i=1}^{N}\frac{1}{m_i}\frac{\partial}{\partial q_i} + \hat{V}(q,t) \tag{4.3}$$

being $V(q,t)$ and $T(q)$ the potential energy and kinetic energy operators, respectively, and m_i is the mass of each particle. If the potential energy of the system is independent of the time, the Hamiltonian is then also time-independent and equation 4.1 admits particular solutions of the form

$$\psi(q,t) = \psi(q)e^{\frac{-iEt}{\hbar}} \tag{4.4}$$

which are stationary states because their energies have the precise values E. It can be demonstrated that the general solution of equation 4.1 (for time-independent potential energy) can be expressed as sum of wavefunctions of stationary states. Using equation 4.4 and separation of variables, the time-dependent Schrödinger equation turns to the time-independent Schrödinger equation given by

$$H(q)\psi(q) = E\psi(q) \tag{4.5}$$

This equation can not be solved analytically even for the simplest molecule H_2^+ that only consists of three particles (two nuclei and one electron). To overcome this difficulty, most of the theoretical methods for solving the Schrödinger equation are based on the Born-Oppenheimer approximation that uncouples the motion of electrons and nuclei. These theoretical methods are classified into *ab initio*, density functional theory (DFT) and semiempirical. Semiempirical

methods use a simplified Hamiltonian that contains parameters whose values are adjusted to fit experimental data or the results of *ab initio* calculations. Semiempirical calculations are used in systems formed by hundreds or thousands of atoms for which the use of other methodology is unworkable; semiempirical calculations will not be considered here. On the other side, *ab initio* calculations use the correct Hamiltonian and do not employ any experimental data to simplify the equations. Both semiempirical and *ab initio* methods calculate the energy and any other property from the wave function that describes the system. DFT methods compute the energy as a function of the electronic density of the system, which depends only on the three spatial coordinates. DFT utilizes, as will see below, some empirical data to calculate the electronic density, therefore this methodology is not classified as *ab initio*.

This Chapter touches the general topics of the molecular structure calculations that have been used in this thesis. In Section 2 a general description of the Born-Oppenheimer approximation will be discussed. Then, in Section 3, the *ab initio* methods will be presented. And finally, Section 4 treats the DFT methodology. There is extensive and detailed literature about both *ab initio* and DFT methodologies.[1-11] Here, only the most general features of these methods will be discussed.

2. THE BORN-OPPENHEIMER APPROXIMATION

The main interest in quantum mechanics is finding solutions of the time-independent Schrödinger equation

$$H(q)\psi(q) = E\psi(q) \tag{4.5}$$

The Hamiltonian depends on the coordinates q of all the particles of the system, that is, electrons and nuclei. Figure 4.1 shows a molecular coordinate system, where R_A and r_i are the position vectors of nuclei and electrons, respectively. The distance between the ith electron and the Ath nucleus is $r_{iA} = |r_i - R_A|$, the distance between the ith and jth electrons is $r_{ij} = |r_i - r_j|$, and the distance between the Ath nucleus and the Bth nucleus is $R_{AB} = |R_A - R_B|$. The Hamiltonian for a system formed by N electrons and M nuclei is given by

$$H(r_i, R_A) = -\frac{\hbar^2}{2m_e}\sum_{i=1}^{N}\nabla_i^2 - \frac{\hbar^2}{2}\sum_{A=1}^{M}\frac{1}{m_A}\nabla_A^2 - \sum_{i=1}^{N}\sum_{A=1}^{M}\frac{Z_A e^2}{4\pi\varepsilon_0 r_{iA}} + \sum_{i=1}^{N}\sum_{j>i}^{N}\frac{e^2}{4\pi\varepsilon_0 r_{ij}} + \sum_{A=1}^{M}\sum_{B>A}^{M}\frac{Z_A Z_B e^2}{4\pi\varepsilon_0 R_{AB}} \tag{4.6}$$

where m_e is the electron mass, m_A is the nucleus mass, Z_A and Z_B are the atomic numbers of the nuclei, e is electron charge, ε_0 is the vacuum permittivity and the Laplacian operators ∇_i and ∇_A involve the differentiation with respect to the coordinates of the ith electron and the Ath nucleus. The first two terms in equation 4.6 are the kinetic energy operators of the electrons and nuclei, respectively; the third term represents the Coulomb attraction between electrons and nuclei; the fourth and fifth terms describe the repulsion between electrons and between nuclei, respectively.

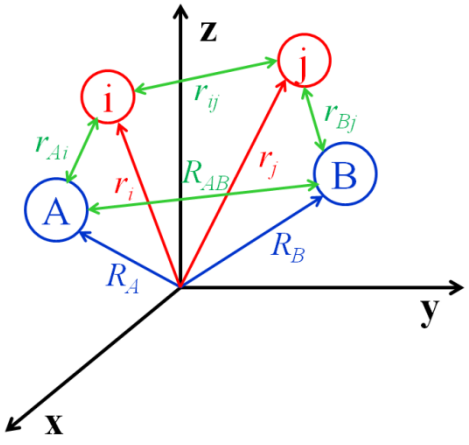

Figure 4.1: Coordinates system for 2 nuclei A and B and 2 electrons i and j.

The Hamiltonian given by equation 4.6 can be simplified as follows. Since nuclei are much heavier than electrons, they move more slowly. Hence, as a good approximation one can consider the electrons in a molecule to move in the field of fixed nuclei. Speaking classically, during the time of a cycle of electronic motion, the change in nuclear configuration is negligible. Thus, considering the nuclei as fixed, the kinetic energy of nuclei in equation 4.6 can be ignored, and the last term corresponding to the repulsion between nuclei can be considered to be constant. The remaining terms in equation 4.6 are called the electronic Hamiltonian, and they describe the motion of N electrons in the field of M fixed point charges. This simplification is called the Born-Oppenheimer approximation and the Hamiltonian is given by

$$H_{el}(r_i; R_A) = -\frac{\hbar^2}{2m_e}\sum_{i=1}^{N}\nabla_i^2 - \sum_{i=1}^{N}\sum_{A=1}^{M}\frac{Z_A e^2}{4\pi\varepsilon_0 r_{iA}} + \sum_{i=1}^{N}\sum_{j>i}^{N}\frac{e^2}{4\pi\varepsilon_0 r_{ij}} \qquad (4.7)$$

Thus, considering the nuclei fixed, the electronic Schrödinger equation is written as

$$H_{el}(r_i;R_A)\psi_{el}(r_i;R_A) = E_{el}(R_A)\psi_{el}(r_i;R_A) \tag{4.8}$$

where $E_{el}(R_A)$ is the purely electronic energy that depends on the nuclei coordinates. The electronic wave function $\psi_{el}(r_i;R_A)$ describes the motion of electrons and explicitly depends on the electronic coordinates and parametrically on the nuclear coordinates. This means that for different arrangements of the nuclei, $\psi_{el}(r_i;R_A)$ is a different function of the electronic coordinates, but the nuclear coordinates do not appear explicitly in the wave function. The total electronic energy U includes the nuclear repulsion

$$U(R_A) = E_{el}(R_A) + \sum_{A=1}^{M}\sum_{B>A}^{M}\frac{Z_A Z_B e^2}{4\pi\varepsilon_0 R_{AB}} \tag{4.9}$$

Different arrangements of nuclei may be adopted calculating the total electronic energy $U(R_A)$ for each nuclear configuration. The set of solutions so obtained allows us to construct the potential energy surface. In the Born-Oppenheimer picture the nuclei move on the potential energy surface, and this is independent on the nuclear mass, that is, it is the same for isotopic molecules. The next sections are focused on numerical methods for solving equation 4.8, which does not have an analytical solution because of the interelectronic interaction term.

Once the electronic Schrödinger equation is solved and the total electronic energy is known, the nuclear motion can be treated. The Schrödinger equation for nuclear motion is

$$H_N(R_A)\psi_N(R_A) = E(R_A)\psi_N(R_A) \tag{4.10}$$

where the nuclear Hamiltonian involves the kinetic energy of the nuclei and the total electronic energy given by

$$H_N(R_A) = -\frac{\hbar^2}{2}\sum_{A=1}^{M}\frac{1}{m_A}\nabla_A^2 + U(R_A) \tag{4.11}$$

The nuclear wave function $\psi_N(R_A)$ describes the vibration, rotation and translation of the system and the energy E is the total energy that includes electronic, vibrational, rotational and translational energy. The total wave function that fully describes the system is given by

$$\psi(r_i;R_A) = \psi_{el}(r_i;R_A)\psi_N(R_A) \tag{4.12}$$

For the majority of systems the Born-Oppenheimer approximation introduces only very small errors, or in other words, the behaviour of these systems is adiabatic. Adiabaticity implies that there are two sets of variables that describe the system, and the system is well characterized by the eigenstates defined at each fixed value of one set of variables which change slowly

compared to the other set.[12] The set of variables that moves slowly is called adiabatic parameters and the states are called adiabatic states. Therefore, the nuclear coordinates are the adiabatic parameters and the wave functions that are solution of equation 4.8 describe the adiabatic states. But in some regions, the adiabatic parameters (nuclear coordinates) can change rapidly and the electron coordinates cannot fully follow the change of the adiabatic parameters and the state of the system changes accordingly. That means that adiabaticity breaks down and a transition between two adiabatic states may happen; this transition is called nonadiabatic transition. In general, nonadiabatic transitions can take place when two or more adiabatic states come close together energetically. At these positions, a small electronic energy change is enough to induce a transition; that energy can be gained from the nuclear motion. Therefore, it is clear that nonadiabatic transitions occur more effectively when the nuclei move fast.

An extensively studied system for which adiabaticity breaks down is the LiF molecule.[13] In the equilibrium region the ionic state (Li^+F^-) is lower in energy, whereas the neutral state (Li---F) is lower at the dissociation region. Therefore, when the molecule dissociates the two states must cross at some point and a nonadiabatic transition occurs. In fact, they do not cross, instead they make an avoided crossing because both states have the same symmetry $^1\Sigma^+$ and the crossing is forbidden according to the non-crossing rule of Neumann and Wigner. Figure 4.2 shows the nonadiabatic transition in the dissociation of LiF.

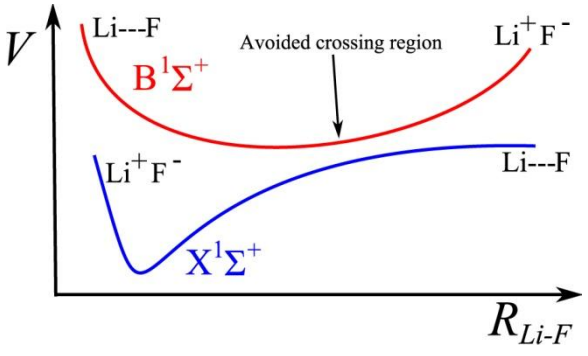

Figure 4.2: Avoided crossing of potential energy surfaces for LiF.

Either the time-dependent or the time-independent Schrödinger equation neglects relativistic effects. The central theme in relativity is that the speed of light c is constant in all inertia frames. One of the consequences of this is that the mass of a particle moving at a substantial fraction of c increases according to:[4]

$$m = m_0 \left(\sqrt{1 - \frac{v^2}{c^2}} \right)^{-1} \tag{4.13}$$

where v is the particle speed and m_0 is the particle mass at rest. Relativistic effects are normally negligible for the first three rows in the periodic table (up to Kr corresponding to a mass correction of 1.04 in equation 4.13).

Throughout this thesis, the relativistic effects were not taken into account since all the systems are formed by atoms of the two first rows. Moreover, all the calculations were carried out under the Born-Oppenheimer approximation. The methods used in this thesis were RI-MP2, CCSD(T), RIJ-DFT-D and SAC-CI. All of them will be explained below.

3. AB INITIO METHODS

The main *ab initio* methods for solving the time-independent Schrödinger equation (equation 4.5) will be discussed in the present Section. These methods are called *ab initio* (from the Latin "from the beginning") because they do not use experimental or theoretical data to simplify the Hamiltonian. All methods that will be explained in this section work under the Born-Oppenheimer approximation, that is, the system remains all the time in the same electronic state.

3.1 Hartree-Fock self-consistent field (SCF) method

The most important complication in all electronic structure calculations is the presence of the electron-electron potential energy in the electronic Hamiltonian, given by the last term of equation 4.7:

$$H_{el}(r_i; R_A) = -\frac{\hbar^2}{2m_e} \sum_{i=1}^{N} \nabla_i^2 - \sum_{i=1}^{N} \sum_{A=1}^{M} \frac{Z_A e^2}{4\pi\varepsilon_0 r_{iA}} + \sum_{i=1}^{N} \sum_{j>i}^{N} \frac{e^2}{4\pi\varepsilon_0 r_{ij}} \tag{4.7}$$

If this potential energy between electrons is ignored, the Schrödinger equation can be rewritten as

$$H^0(r_i; R_A)\psi^0(r_i; R_A) = E^0(R_A)\psi^0(r_i; R_A) \tag{4.14}$$

where the superscript indicates the absence of the potential between electrons. Under this approximation, the Hamiltonian of a system with N electrons can be expressed as the sum of N one-electron Hamiltonians:

$$H^0(r_i; R_A) = \sum_{i=1}^{N} h_i\,(r_i; R_A) \tag{4.15}$$

where $h_i(r_i; R_A)$ is the core Hamiltonian for electron i, and for instance, for electron 1 has the form

$$h_1(1; R_A) = -\frac{\hbar^2}{2m_e}\nabla_1^2 - \sum_{A=1}^{M} \frac{Z_A e^2}{4\pi\varepsilon_0 r_{1A}} \tag{4.16}$$

The N-electron Schrödinger equation (equation 4.14) can be separated into N one-electron equations which depend on N wave functions $\psi_a^0(r_i; R_A)$. To simplify the notation, this wave function a describing the electron i, with coordinates r_i and parametrically depending on the nuclear coordinates R_A, will be represented as $\psi_a^0(i)$. In the same way, the core Hamiltonian $h_i(r_i; R_A)$ will be denoted as h_i. Therefore, one can write N one-electron Schrödinger equations as the following:

$$h_i\psi_a^0(i) = E_a^0\psi_a^0(i) \tag{4.17}$$

with E_a^0 being the energy of electron i in orbital a. The overall wave function is the following product of one-electron wave functions:

$$\psi^0 = \psi_a^0(1)\psi_b^0(2)\ldots\psi_z^0(N) \tag{4.18}$$

At this stage, the wave function only describes the spatial state of the electrons, but the spin is not taken into account. To do so, the spatial wave function in equation 4.18 must be multiplied by a spin function; the result is a wave function called spinorbital that will be denoted as $\phi_a(i)$. Moreover, the overall wave function must obey the Pauli principle, that is, the wave function must be antisymmetric with respect to the interchange of electrons. To satisfy the antisymmetry requirement the wave function can be written as the so-called Slater determinant.

$$\psi^0(x; R) = (N!)^{-1/2} det|\phi_a(1)\phi_b(2)\ldots\phi_z(N)| \tag{4.19}$$

where now, the wave function depends on the spatial and spin coordinates x of the electrons and parametrically on the nuclear arrangement R.

The Hartree-Fock method searches a product wave function of the form of equation 4.19, but taking into account the electron-electron repulsions treated in an average way. This means that each electron is considered to be moving in the field of the nuclei and the average field of the other $N-1$ electrons. The variation theorem states that the spinorbitals that give the best wave function are those that minimize the Rayleigh ratio

$$E = \frac{\int \psi^*(x;R) H \psi(x;R) dx}{\int \psi^*(x;R)\, \psi(x;R) dx} \tag{4.20}$$

where E is the calculated energy which will never be lower than the exact energy of the system, and the integrals depends on the coordinates of the N electrons. The lowest value of E is the electronic energy for the selected nuclear configuration R. The application of this procedure leads to the Hartree-Fock equations for the individual spinorbitals. For instance, the Hartree-Fock equation for electron 1 described by the spinorbital ϕ_a is

$$f_1 \phi_a(1) = E_a \phi_a(1) \tag{4.21}$$

where E_a is the energy of the spinorbital ϕ_a and f_1 is the Fock operator given by:

$$f_1 = h_1 + \sum_u \big(J_u(1) - K_u(1)\big) \tag{4.22}$$

In this equation h_1 is the core Hamiltonian for electron 1, given by equation 4.16, the sum is over all spinorbitals $u = a, b, \ldots z$, and the Coulomb operator J_u and the exchange operator K_u are defined as follows:

$$J_u(1)\phi_a(1) = \left[\int \phi_u^*(2) \left(\frac{e^2}{4\pi\varepsilon_0 r_{12}}\right) \phi_u(2) dx_2\right] \phi_a(1) \tag{4.23}$$

$$K_u(1)\phi_a(1) = \left[\int \phi_u^*(2) \left(\frac{e^2}{4\pi\varepsilon_0 r_{12}}\right) \phi_a(2) dx_2\right] \phi_u(1) \tag{4.24}$$

The Coulomb operator represents the electrostatic potential created by an electron 2 described by the spinorbital ϕ_u in the point corresponding to the coordinates of electron 1. That is, this operator represents the Coulombic repulsion between electrons. The exchange operator takes into the account the modification of the energy due to the spin correlation, that is, electron 2 can be in different spinorbitals interacting with electron 1.

Each spinorbital ϕ_u must be obtained by solving an equation of the form of equation 4.21 that depends on the Fock operator f_i. But the Fock operator depends on the spinorbitals (equations 4.22-4.24), therefore an iterative procedure is necessary to solve the equations. The calculation starts with a trial set of spinorbitals which are used to formulate the Fock operator; then, the Hartree-Fock equations are solved to calculate a new set of spinorbitals which are used to construct again the Fock operator and so on. This cycle is repeated until a convergence criterion is satisfied and the solutions are self-consistent, hence the name of self-consistent field (SCF).

In theory, the Fock operator has an infinite number of eigenfunctions, in other words, there is an infinite number of spinorbitals ϕ_u. But in practice, of

course, one has to solve the Hartree-Fock equations for a finite number M of spinorbitals with $M > N$. From the M optimized spinorbitals obtained from the SCF calculation, the N spinorbitals with the lowest energy are selected to contain the N electrons. These spinorbitals are called occupied orbitals. The remaining unoccupied $M - N$ orbitals are called virtual orbitals. The Slater determinant (equation 4.19) composed of the occupied spinorbitals is the Hartree-Fock ground state wave function for the molecule with N electrons.

The procedure described above is only computationally feasible for atoms and diatomic molecules due to the great number of integrals in Hartree-Fock equations. Roothaan and Hall independently suggested using a known set of basis functions to represent the spatial function ψ_a. In this method, each spatial function ψ_a is represented as a linear combination of M basis functions θ_j:

$$\psi_i = \sum_{j=1}^{M} c_{ji}\,\theta_j \tag{4.25}$$

where c_{ji} are the unknown coefficients. Therefore the problem of calculating the wavefunctions has been transformed to an easier one of computing the coefficients c_{ji}. The known functions θ_j are centred on the atoms and therefore, they are considered atomic orbitals, and the total wave functions are molecular orbitals. If a set of M basis functions is employed, M linearly independient spatial functions (molecular orbitals) are obtained, and the $N/2$ ones with the lowest energy are selected to construct the Hartree-Fock wave function.

If equation 4.21 is rewritten with the new functions one obtains:

$$f_1\psi_a(1) = E_a\psi_a(1) \tag{4.26}$$

The substitution of the expanded wave function 4.25 into equation 4.26 yields

$$f_1 \sum_{j=1}^{M} c_{ja}\,\theta_j(1) = E_a \sum_{j=1}^{M} c_{ja}\,\theta_j(1) \tag{4.27}$$

Multiplying both sides of this equation by the basis function $\theta_i^*(1)$ drives to

$$\sum_{j=1}^{M} c_{ja} \int \theta_i^*(1) f_1\,\theta_j(1) dr_1 = E_a \sum_{j=1}^{M} c_{ja} \int \theta_i^*(1)\,\theta_j(1) dr_1 \tag{4.28}$$

where the overlap matrix S_{ij} and the Fock matrix F_{ij} are defined as

$$S_{ij} = \int \theta_i^*(1)\,\theta_j(1) dr_1 \tag{4.29}$$

$$F_{ij} = \int \theta_i^*(1) f_1 \, \theta_j(1) dr_1 \tag{4.30}$$

The S_{ij} matrix is not in general the unit matrix because the basis functions are not necessarily orthogonal. Using these matrixes, equation 4.28 becomes

$$\sum_{j=1}^{M} F_{ij} \, c_{ja} = E_a \sum_{j=1}^{M} S_{ij} \, c_{ja} \tag{4.31}$$

Reorganizing this equation it turns into

$$\sum_{j=1}^{M} c_{ja} \left(F_{ij} - E_a S_{ij} \right) = 0 \tag{4.32}$$

Equations 4.32 form a set of M linear homogeneous equations known as the Roothaan equations. These equations have a non-trivial solution when the following secular equation is satisfied:

$$det\left| F_{ij} - E_a S_{ij} \right| = 0 \tag{4.33}$$

Roothaan equations must be solved by an iterative process since the F_{ij} integrals depend on the unknown coefficients c_{ja} through the dependence of the Fock operator f_1 on the molecular orbitals (equations 4.22-4.24). The iterative process starts with guesses for the coefficients c_{ja} to compute the Fock operator f_1 from equations 4.22-4.24. Then the matrixes 4.29 and 4.30 are calculated and the secular equation 4.33 is solved to give an initial set of energies E_a. These energies are used to solve equation 4.32 for obtaining an improved set of coefficients c_{ja}, which are then used to compute an improved Fock operator f_1, and the process is repeated until a convergence criterion has been reached.

3.2 Electron correlation

The Hartree-Fock SCF wave function takes into account the interaction between electrons only in an average way. But, obviously, this is an approximation because the motions of electrons depend on the instantaneous positions of the other electrons, that is, the motions of electrons are correlated. Since electrons repel each other, they tend to keep out of each other´s way. Surrounding each electron in an atom, there is a region where the probability of finding another electron of different spin is small; this region is called Coulomb hole. On the other hand, a Fermi hole is a region around each electron where the probability of finding another electron of the same spin is small. Therefore, one can speak about Coulomb correlation and Fermi correlation for electrons with different and equal spin respectively. Both correlation types are named

dynamic correlation. The most important methods which include dynamic correlation are configuration interaction (CI), Møller-Plesset perturbation theory (MPPT) and coupled cluster (CC).

In some systems the ground state Hartree-Fock wave function does not describe correctly the system because electronic excited configurations are energetically near to the fundamental configuration. For these cases for which the excited configuration must be taken into account, multiconfiguration and multireference methods were developed. This type of interaction between electrons of different electronic configurations is called nondynamic correlation.

All methods that correct the electron correlation (dynamic and nondynamic) are called post Hartree-Fock methods because they are based on the SCF theory, and they used the Hartree-Fock wavefunction as starting point.

The correlation energy is defined as the difference between the exact nonrelativistic energy of the system E_{exact} and the Hartree-Fock energy $E_{HF-limit}$ obtained in the limit that the basis set approaches completeness

$$E_{corr} = E_{exact} - E_{HF-limit} \tag{4.34}$$

Since the Hartree-Fock method is variational, the exact energy is always below the Hartree-Fock energy, and therefore, the correlation energy is negative by definition.

3.3 Configuration interaction (CI) method

The exact electronic wave function ψ_s for any state s of the system can be written as a linear combination of Slater determinants arising from a complete basis set:

$$\psi_s = C_0\Phi_0 + \sum_p^a C_a^p \Phi_a^p + \sum_{\substack{a<b \\ p<q}} C_{ab}^{pq} \Phi_{ab}^{pq} + \sum_{\substack{a<b<c \\ p<q<r}} C_{abc}^{pqr} \Phi_{abc}^{pqr} + \cdots \tag{4.35}$$

where the Cs are the expansion coefficients and the restrictions on the summations ensure that a given excited determinant is included in the sum only once. The determinant formed from the N lowest spinorbitals (or $N/2$ orbitals) Φ_0 is the Hartree-Fock wave function, and the other determinants describe excited electronic configurations. Thus, for instance, the singly excited determinants Φ_a^p differ from Φ_0 in an electron in the initially virtual spinorbital ϕ_p from the initially occupied spinorbital ϕ_a; the doubly excited determinants Φ_{ab}^{pq} are formed by promoting two electrons from ϕ_a and ϕ_b to ϕ_p and ϕ_q. If the basis set is complete, there is an infinite number of excitations, and the wave function is the exact one and the energy calculated from this wave function is the exact nonrelativistic energy. The difference between the exact

energy of the ground state and the Hartree-Fock limit energy is the correlation energy as seen in equation 4.34. But, of course, a finite basis set must be selected to develop the wave function. If all the excitations are taken into account for a given finite basis set, one obtains the exact wave function within the subspace of this finite basis set, and the method is referred to as full CI. Thus, full CI constitutes a benchmark to compute the correlation energy.

Unfortunately, even with a small number of N electrons and a relatively small number of M basis functions, the total number of determinants can be extremely large and the calculation is computationally unworkable. For example, for benzene (42 electrons) using the minimum basis set, that is, 1s orbitals for H and 1s, 2s and 2p orbitals for C, a total of 36 basis functions are necessary for the calculation, and the number of determinants to consider is

$$\binom{2M}{N} = \frac{2M!}{(2M-N)!\,N!} = \frac{(2\times 36)!}{(2\times 36-42)!\,42!} = 1.64\times 10^{20} \qquad (4.36)$$

Therefore, the expansion in equation 4.35 must be truncated for most of the systems. If L determinants are selected for developing the wavefunction, equation 4.35 can be written in a simpler form as

$$\psi_s = \sum_{j=1}^{l} C_{js}\,\Phi_j \qquad (4.37)$$

where $j = 0$ represents the Hartree-Fock determinant, $j = 1$ the singly excitated determinants and so on. The coefficients C_{js} are determined variationally by minimizing the Rayleigh ratio (equation 4.20). This minimization is equivalent to solving the following equations:

$$\sum_{j=1}^{l} H_{ij}\,C_{js} = E_s \sum_{j=1}^{l} S_{ij}\,C_{js} \qquad (4.38)$$

where

$$H_{ij} = \int \Phi_i^* H \Phi_j\, dx_1 dx_2 \ldots dx_N \qquad (4.39)$$

$$S_{ij} = \int \Phi_i^* \Phi_j\, dx_1 dx_2 \ldots dx_N \qquad (4.40)$$

A common form of truncated CI wavefunction is that for which only single and double excitations are taken into account. Such an approximation is referred to CISD. A deficiency of limited or truncated CI calculations is the lack of size-consistency. A method is size-consistent when the energy of a system AB computed when the fragments are infinitely separated is equal to the sum of the energies of A and B separately computed:

$$E(AB)_{r\to\infty} = E(A) + E(B) \tag{4.41}$$

For instance, if one uses the CID method, when the energies of A and B are computed separately, the calculation takes into account double excitations for each monomer. On the other hand, when the supermolecule AB energy is computed, those excitations are not taken into account because they would correspond to quadruple excitations. That means that the energy $(AB)_{r\to\infty}$ is higher than $E(A) + E(B)$. This shortage can be overcome by means of Davidson correction. For instance, for the CISD method this correction has the form:

$$\Delta E_{Davidson} = (1 - C_o^2)E(CISD) \tag{4.42}$$

and the corrected CISD energy is

$$E_{corrected} = E(CISD) + \Delta E_{Davidson} \tag{4.43}$$

with C_0 being the Hartree-Fock coefficient in the expansion of the CISD wavefunction.

3.4 Many-body perturbation theory (MBPT)

A different systematic procedure for finding the correlation energy, which is not variational but is size-consistent at each level, is the perturbation theory. In this approach the total Hamiltonian of the system is divided into two pieces: a zeroth-order part H^0 of which eigenfunctions and eigenvalues are known, and a perturbation H':

$$H = H^0 + H' \tag{4.44}$$

If the perturbation is applied gradually, a parameter λ can be introduced in equation 4.44:

$$H = H^0 + \lambda H' \tag{4.45}$$

When $\lambda = 0$ we have the unperturbed system, and as λ increases the perturbation becomes larger; when $\lambda = 1$ the perturbation is fully included. This parameter λ is added for convenience, but at the end of the development it is set to 1.

Suppose that $\psi_n^{(0)}$ are the known wavefunctions of the unperturbed system for levels n with energies $E_n^{(0)}$. Let ψ_n be the perturbed and unknown wavefunctions for the system at which we are interested, and E_n their eigenvalues. The time-independent Schrödinger equation for the perturbed system is

$$H\psi_n = (H^0 + \lambda H')\psi_n = E_n\psi_n \tag{4.46}$$

Since the Hamiltonian depends on the parameter λ, their eigenfunctions ψ_n and eigenvalues E_n also depend on it. Therefore, if the perturbation is not too large, one can expand ψ_n and E_n as Taylor series in powers of λ:

$$\psi_n = \psi_{n,\lambda=0} + \left(\frac{\partial \psi_n}{\partial \lambda}\right)_{\lambda=0} \lambda + \left(\frac{\partial^2 \psi_n}{\partial \lambda^2}\right)_{\lambda=0} \frac{\lambda^2}{2!} + \cdots \tag{4.47}$$

$$E_n = E_{n,\lambda=0} + \left(\frac{\partial E_n}{\partial \lambda}\right)_{\lambda=0} \lambda + \left(\frac{\partial^2 E_n}{\partial \lambda^2}\right)_{\lambda=0} \frac{\lambda^2}{2!} + \cdots \tag{4.48}$$

Now, the next notation is included for simplicity:

$$\psi_n^{(k)} = \frac{1}{k!}\left(\frac{\partial^k \psi_n}{\partial \lambda^k}\right)_{\lambda=0} \tag{4.49}$$

$$E_n^{(k)} = \frac{1}{k!}\left(\frac{\partial^k E_n}{\partial \lambda^k}\right)_{\lambda=0} \tag{4.50}$$

Using this notation, equations 4.47 and 4.48 become

$$\psi_n = \psi_n^{(0)} + \lambda \psi_n^{(1)} + \lambda^2 \psi_n^{(2)} + \cdots + \lambda^k \psi_n^{(k)} \tag{4.51}$$

$$E_n = E_n^{(0)} + \lambda E_n^{(1)} + \lambda^2 E_n^{(2)} + \cdots + \lambda^k E_n^{(k)} \tag{4.52}$$

The terms $\psi_n^{(k)}$ and $E_n^{(k)}$ are called kth-order corrections to the wave function and energy, respectively. For a small perturbation, the first terms in equations 4.51 and 4.52 (up to second-order term) are a good approximation to the exact energy and wave function.

Now we assume that the wavefunctions ψ_n satisfy the intermediate normalization that is defined as:

$$\int \psi_n^{(0)*} \psi_n d\tau = \left\langle \psi_n^{(0)} \middle| \psi_n \right\rangle = 1 \tag{4.53}$$

where $d\tau$ indicates that the integration is over all space. Here and from now on, the braket or Dirac notation is used in order to simplify the equations. Substitution of equation 4.51 into the intermediate normalization 4.53 gives

$$\left\langle \psi_n^{(0)} \middle| \psi_n^{(0)} \right\rangle + \lambda \left\langle \psi_n^{(0)} \middle| \psi_n^{(1)} \right\rangle + \lambda^2 \left\langle \psi_n^{(0)} \middle| \psi_n^{(2)} \right\rangle + \cdots = 1 \tag{4.54}$$

Since $\psi_n^{(0)}$ is normalized the first term of equation 4.54 is equal to 1 and we have

$$\left\langle \psi_n^{(0)} \middle| \psi_n^{(0)} \right\rangle = 1 \tag{4.55}$$

This means that the corrections $\psi_n^{(1)}$, $\psi_n^{(2)}$… $\psi_n^{(k)}$ to the wavefunction are orthogonal to the unperturbed wavefunction $\psi_n^{(0)}$:

$$\left\langle \psi_n^{(0)} \middle| \psi_n^{(1)} \right\rangle = 0, \left\langle \psi_n^{(0)} \middle| \psi_n^{(2)} \right\rangle = 0, \ \ldots \tag{4.56}$$

Substitution of 4.51 and 4.52 into 4.46 allows to write the Schrödinger equation as follows

$$\begin{aligned}(H^0 + \lambda H')\left(\psi_n^{(0)} + \lambda\psi_n^{(1)} + \lambda^2\psi_n^{(2)} + \cdots\right) \\ = \left(E_n^{(0)} + \lambda E_n^{(1)} + \lambda^2 E_n^{(2)} + \cdots\right)\left(\psi_n^{(0)} + \lambda\psi_n^{(1)}\right. \\ \left. + \lambda^2\psi_n^{(2)} + \cdots\right)\end{aligned} \tag{4.57}$$

Collecting together the terms of the same power of λ we get to:

$$\begin{aligned}H^0\psi_n^{(0)} + \lambda\left(H'\psi_n^{(0)} + H^0\psi_n^{(1)}\right) + \lambda^2\left(H^0\psi_n^{(2)} + H'\psi_n^{(1)}\right) + \cdots \\ = E_n^{(0)}\psi_n^{(0)} + \lambda\left(E_n^{(1)}\psi_n^{(0)} + E_n^{(0)}\psi_n^{(1)}\right) \\ + \lambda^2\left(E_n^{(2)}\psi_n^{(0)} + E_n^{(1)}\psi_n^{(1)} + E_n^{(0)}\psi_n^{(2)}\right) + \cdots\end{aligned} \tag{4.58}$$

The two series on each side of equation 4.58 are equal for any value of λ only if the terms with the same power of λ are equals. Equating the terms corresponding to λ^0 we have

$$H^0\psi_n^{(0)} = E_n^{(0)}\psi_n^{(0)} \tag{4.59}$$

which is the Schrödinger equation for the unperturbed system for which the solutions $\psi_n^{(0)}$ and $E_n^{(0)}$ are known. Now, equating the terms of λ^1 we have

$$H'\psi_n^{(0)} + H^0\psi_n^{(1)} = E_n^{(1)}\psi_n^{(0)} + E_n^{(0)}\psi_n^{(1)} \tag{4.60}$$

and reorganizing this equation it turns into

$$H^0\psi_n^{(1)} - E_n^{(0)}\psi_n^{(1)} = E_n^{(1)}\psi_n^{(0)} - H'\psi_n^{(0)} \tag{4.61}$$

Now, to obtain the first-order perturbation, equation 4.61 is multiplied by $\psi_m^{(0)*}$ and is integrated over all space, giving the next equation:

$$\begin{aligned}\left\langle \psi_m^{(0)} \middle| H^0 \middle| \psi_n^{(1)} \right\rangle - E_n^{(0)}\left\langle \psi_m^{(0)} \middle| \psi_n^{(1)} \right\rangle \\ = E_n^{(1)}\left\langle \psi_m^{(0)} \middle| \psi_n^{(0)} \right\rangle - \left\langle \psi_m^{(0)} \middle| H' \middle| \psi_n^{(0)} \right\rangle\end{aligned} \tag{4.62}$$

Since H^0 is hermitian it must obey the next property:

$$\left\langle \psi_m^{(0)} \middle| H^0 \middle| \psi_n^{(1)} \right\rangle = \left\langle \psi_n^{(1)} \middle| H^0 \middle| \psi_m^{(0)} \right\rangle^* = \left\langle \psi_n^{(1)} \middle| H^0\psi_m^{(0)} \right\rangle^* \tag{4.63}$$

and using the Schrödinger equation (4.59) for the unperturbed system we can write:

$$\left\langle \psi_n^{(1)} \middle| H^0 \psi_m^{(o)} \right\rangle^* = \left\langle \psi_n^{(1)} \middle| E_m^{(0)} \psi_m^{(o)} \right\rangle^* = E_m^{(0)} \left\langle \psi_n^{(1)} \middle| \psi_m^{(o)} \right\rangle^* = E_m^{(0)} \left\langle \psi_m^{(0)} \middle| \psi_n^{(1)} \right\rangle \tag{4.64}$$

Substituting 4.64 into 4.62 and using the orthonormality $\left\langle \psi_m^{(0)} \middle| \psi_n^{(0)} \right\rangle = \delta_{mn}$ property for the unperturbed eigenfunctions we obtain:

$$E_m^{(0)} \left\langle \psi_m^{(0)} \middle| \psi_n^{(1)} \right\rangle - E_n^{(0)} \left\langle \psi_m^{(0)} \middle| \psi_n^{(1)} \right\rangle = E_n^{(1)} \delta_{mn} - \left\langle \psi_m^{(0)} \middle| H' \middle| \psi_n^{(0)} \right\rangle \tag{4.65}$$

and reorganizing the equation it turns into

$$\left(E_m^{(0)} - E_n^{(0)} \right) \left\langle \psi_m^{(0)} \middle| \psi_n^{(1)} \right\rangle = E_n^{(1)} \delta_{mn} - \left\langle \psi_m^{(0)} \middle| H' \middle| \psi_n^{(0)} \right\rangle \tag{4.66}$$

If $m = n$ the left side of equation 4.66 equals to zero, and we get

$$E_n^{(1)} = \left\langle \psi_n^{(0)} \middle| H' \middle| \psi_n^{(0)} \right\rangle \tag{4.67}$$

This equation is the first-order correction to the energy and it is calculated by averaging the perturbation H' over the known unperturbed wavefunctions. The total energy of the system, including only the first-order correction, is computed with equation 4.52 setting $\lambda = 1$:

$$E_n = E_n^{(0)} + \left\langle \psi_n^{(0)} \middle| H' \middle| \psi_n^{(0)} \right\rangle \tag{4.68}$$

On the other hand, the first-order correction to the wave function is calculated from equation 4.66 when $m \neq n$. In this case we obtain:

$$\left(E_m^{(0)} - E_n^{(0)} \right) \left\langle \psi_m^{(0)} \middle| \psi_n^{(1)} \right\rangle = - \left\langle \psi_m^{(0)} \middle| H' \middle| \psi_n^{(0)} \right\rangle \tag{4.69}$$

It can be demonstrated that the wave function $\psi_n^{(1)}$ can be expanded in terms of the complete and orthonormal set of unperturbed eigenfunctions $\psi_m^{(0)}$ of the hermitian operator H^0:

$$\psi_n^{(1)} = \sum_m a_m \, \psi_m^{(0)} \tag{4.70}$$

with a_m being coefficients defined as

$$a_m = \left\langle \psi_m^{(0)} \middle| \psi_n^{(1)} \right\rangle \tag{4.71}$$

Use of 4.71 in 4.69 gives the next equation:

$$\left(E_m^{(0)} - E_n^{(0)} \right) a_m = - \left\langle \psi_m^{(0)} \middle| H' \middle| \psi_n^{(0)} \right\rangle \tag{4.72}$$

If we suppose that the level n is not degenerate, that is, $E_m^{(0)} \neq E_n^{(0)}$ the coefficients a_m can be calculated as:

$$a_m = \frac{\left\langle \psi_m^{(0)} \middle| H' \middle| \psi_n^{(0)} \right\rangle}{\left(E_m^{(0)} - E_n^{(0)} \right)} \tag{4.73}$$

The coefficients a_m are given by 4.73 except for a_n; in this case from equation 4.71 we have

$$a_n = \left\langle \psi_n^{(0)} \middle| \psi_n^{(1)} \right\rangle \tag{4.74}$$

and equation 4.74 is equal to zero as seen in equation 4.56, that is, $a_n = 0$. Therefore, the first-order correction to the wavefunction is obtained by replacing the coefficients of equation 4.73 into equation 4.70:

$$\psi_n^{(1)} = \sum_{m \neq n} \frac{\left\langle \psi_m^{(0)} \middle| H' \middle| \psi_n^{(0)} \right\rangle}{\left(E_m^{(0)} - E_n^{(0)} \right)} \psi_m^{(0)} \tag{4.75}$$

The sum in equation 4.75 is over all the unperturbed states except state n. Setting $\lambda = 1$ and replacing 4.75 by 4.51 we obtain the total wave function of the perturbed system as

$$\psi_n = \psi_n^{(0)} + \sum_{m \neq n} \frac{\left\langle \psi_m^{(0)} \middle| H' \middle| \psi_n^{(0)} \right\rangle}{\left(E_m^{(0)} - E_n^{(0)} \right)} \psi_m^{(0)} \tag{4.76}$$

If the perturbed system is not very similar to the unperturbed one, a second-order correction can be necessary. This correction is obtained equating the λ^2 terms in equation 4.58:

$$H^0 \psi_n^{(2)} + H' \psi_n^{(1)} = E_n^{(2)} \psi_n^{(0)} + E_n^{(1)} \psi_n^{(1)} + E_n^{(0)} \psi_n^{(2)} \tag{4.77}$$

Reorganizing this equation we get

$$H^0 \psi_n^{(2)} - E_n^{(0)} \psi_n^{(2)} = E_n^{(2)} \psi_n^{(0)} + E_n^{(1)} \psi_n^{(1)} - H' \psi_n^{(1)} \tag{4.78}$$

Multiplication by $\psi_m^{(0)*}$ followed by integration over all space gives the next equation:

$$\begin{aligned} \left\langle \psi_m^{(0)} \middle| H^0 \middle| \psi_n^{(2)} \right\rangle - E_n^{(0)} \left\langle \psi_m^{(0)} \middle| \psi_n^{(2)} \right\rangle \\ = E_n^{(2)} \left\langle \psi_m^{(0)} \middle| \psi_n^{(0)} \right\rangle + E_n^{(1)} \left\langle \psi_m^{(0)} \middle| \psi_n^{(1)} \right\rangle \\ - \left\langle \psi_m^{(0)} \middle| H' \middle| \psi_n^{(1)} \right\rangle \end{aligned} \tag{4.79}$$

The integral $\left\langle \psi_m^{(0)} \middle| H^0 \middle| \psi_n^{(2)} \right\rangle$ in equation 4.79 is the same as the integral in 4.63 and 4.64 $\left\langle \psi_m^{(0)} \middle| H^0 \middle| \psi_n^{(1)} \right\rangle$, therefore applying the same procedure we can write:

$$\left\langle \psi_m^{(0)} \middle| H^0 \middle| \psi_n^{(2)} \right\rangle = E_m^{(0)} \left\langle \psi_m^{(0)} \middle| \psi_n^{(2)} \right\rangle \tag{4.80}$$

now, replacing 4.80 into 4.79 and using the orthonormality of the unperturbed wavefunctions we get

$$\begin{aligned} E_m^{(0)} \left\langle \psi_m^{(0)} \middle| \psi_n^{(2)} \right\rangle - E_n^{(0)} \left\langle \psi_m^{(0)} \middle| \psi_n^{(2)} \right\rangle \\ = E_n^{(2)} \delta_{mn} + E_n^{(1)} \left\langle \psi_m^{(0)} \middle| \psi_n^{(1)} \right\rangle - \left\langle \psi_m^{(0)} \middle| H' \middle| \psi_n^{(1)} \right\rangle \end{aligned} \tag{4.81}$$

and reorganizing the equation it becomes

$$\begin{aligned} \left(E_m^{(0)} - E_n^{(0)} \right) \left\langle \psi_m^{(0)} \middle| \psi_n^{(2)} \right\rangle \\ = E_n^{(2)} \delta_{mn} + E_n^{(1)} \left\langle \psi_m^{(0)} \middle| \psi_n^{(1)} \right\rangle - \left\langle \psi_m^{(0)} \middle| H' \middle| \psi_n^{(1)} \right\rangle \end{aligned} \tag{4.82}$$

For $m = n$ the left side of 4.82 is zero and we obtain

$$E_n^{(2)} = \left\langle \psi_n^{(0)} \middle| H' \middle| \psi_n^{(1)} \right\rangle - E_n^{(1)} \left\langle \psi_n^{(0)} \middle| \psi_n^{(1)} \right\rangle \tag{4.83}$$

Since $\left\langle \psi_n^{(0)} \middle| \psi_n^{(1)} \right\rangle = 0$ from equation 4.56, the second-order correction can be computed as

$$E_n^{(2)} = \left\langle \psi_n^{(0)} \middle| H' \middle| \psi_n^{(1)} \right\rangle \tag{4.84}$$

Equation 4.84 shows that to determine the second-order correction to the energy, we have to know only the first-order correction to the wavefunction. In general, it can be demonstrated that if the corrections of kth order to the wavefunction are known, one can compute the corrections to the energy of order $2k + 1$.

Substitution of first-order correction to the wavefunction from equation 4.75 into equation 4.84 gives the next equation for the second-order correction to the energy:

$$E_n^{(2)} = \sum_{m \neq n} \frac{\left\langle \psi_m^{(0)} \middle| H' \middle| \psi_n^{(0)} \right\rangle}{\left(E_m^{(0)} - E_n^{(0)} \right)} \left\langle \psi_n^{(0)} \middle| H' \middle| \psi_m^{(0)} \right\rangle \tag{4.85}$$

and since H' is hermitian we have

$$\begin{aligned} \left\langle \psi_m^{(0)} \middle| H' \middle| \psi_n^{(0)} \right\rangle \left\langle \psi_n^{(0)} \middle| H' \middle| \psi_m^{(0)} \right\rangle = \left\langle \psi_m^{(0)} \middle| H' \middle| \psi_n^{(0)} \right\rangle \left\langle \psi_m^{(0)} \middle| H' \middle| \psi_n^{(0)} \right\rangle^* \\ = \left| \left\langle \psi_m^{(0)} \middle| H' \middle| \psi_n^{(0)} \right\rangle \right|^2 \end{aligned} \tag{4.86}$$

Therefore, replacing 4.86 into 4.85 the energy becomes

$$E_n^{(2)} = \sum_{m \neq n} \frac{\left|\left\langle \psi_m^{(0)} \middle| H' \middle| \psi_n^{(0)} \right\rangle\right|^2}{\left(E_m^{(0)} - E_n^{(0)}\right)} \tag{4.87}$$

Finally, the total energy of the perturbed system with first and second-order corrections is obtained by substitution of 4.87 and 4.67 into 4.52 and setting $\lambda = 1$:

$$E_n = E_n^{(0)} + \left\langle \psi_n^{(0)} \middle| H' \middle| \psi_n^{(0)} \right\rangle + \sum_{m \neq n} \frac{\left|\left\langle \psi_m^{(0)} \middle| H' \middle| \psi_n^{(0)} \right\rangle\right|^2}{\left(E_m^{(0)} - E_n^{(0)}\right)} \tag{4.88}$$

That means that to calculate the energy with equation 4.88 one must know the perturbation H' and the wavefunctions and energies for the unperturbed system.

3.4.1 Møller-Plesset perturbation theory (MPPT)

Since the *ab initio* calculations attempt to obtain the correlation energy of the ground state, the Hartree-Fock Hamiltonian is chosen as the zeroth-order Hamiltonian H^0. This choice of H^0 was applied to N-electron systems by C. Møller and M. S. Plesset and hence, this approach sometimes is called Møller-Plesset perturbation theory (MPPT or simply MP). Therefore H^0 is given by the sum of the Fock operators seen in equation 4.22. For an electron i this equation is:

$$f_i = h_i + \sum_u \left(J_u(i) - K_u(i)\right) \tag{4.22}$$

where h_i is the core Hamiltonian for an electron i and the sum is over all spinorbitals u. The core Hamiltonian follows equation 4.16:

$$h_i = -\frac{\hbar^2}{2m_e}\nabla_i^2 - \sum_{A=1}^{M} \frac{Z_A e^2}{4\pi\varepsilon_0 r_{iA}} \tag{4.16}$$

with M being the number of nuclei of the molecule. Therefore if the system is formed by N electrons i that can occupy N spinorbitals j, the Fock operator can be written as:

$$f = h + \sum_{i=1}^{N}\sum_{j=1}^{N} \left(J_j(i) - K_j(i)\right) \tag{4.89}$$

where the total core Hamiltonian h is given by

$$h = -\frac{\hbar^2}{2m_e}\sum_{i=1}^{N}\nabla_i^2 - \sum_{i=1}^{N}\sum_{A=1}^{M}\frac{Z_A e^2}{4\pi\varepsilon_0 r_{iA}} \tag{4.90}$$

The total unperturbed Hamiltonian for N electrons is obtained by substitution of 4.90 into 4.89:

$$H^0 = -\frac{\hbar^2}{2m_e}\sum_{i=1}^{N}\nabla_i^2 - \sum_{i=1}^{N}\sum_{A=1}^{M}\frac{Z_A e^2}{4\pi\varepsilon_0 r_{iA}} + \sum_{i=1}^{N}\sum_{j=1}^{N}\Big(J_j(i) - K_j(i)\Big) \tag{4.91}$$

On the other side, the Hamiltonian of the perturbed system follows equation 4.7:

$$H = -\frac{\hbar^2}{2m_e}\sum_{i=1}^{N}\nabla_i^2 - \sum_{i=1}^{N}\sum_{A=1}^{M}\frac{Z_A e^2}{4\pi\varepsilon_0 r_{iA}} + \sum_{i=1}^{N}\sum_{j>i}^{N}\frac{e^2}{4\pi\varepsilon_0 r_{ij}} \tag{4.7}$$

The perturbation H' is the difference between the perturbed Hamiltonian and the unperturbed Hamiltonian as equation 4.44 shows. Subtracting 4.7 and 4.91 one obtains:

$$H' = H - H^0 = \sum_{i=1}^{N}\sum_{j>i}^{N}\frac{e^2}{4\pi\varepsilon_0 r_{ij}} - \sum_{i=1}^{N}\sum_{j=1}^{N}\Big(J_j(i) - K_j(i)\Big) \tag{4.92}$$

As seen above, the first-order correction to the energy is given by equation 4.67:

$$E_n^{(1)} = \left\langle \psi_n^{(0)} \middle| H' \middle| \psi_n^{(0)} \right\rangle \tag{4.67}$$

where now $\psi_n^{(0)}$ is the ground state Hartree-Fock wavefunction Φ_0. Rewriting equation 4.67 we have

$$E_n^{(1)} = \langle \Phi_0 | H' | \Phi_0 \rangle \tag{4.93}$$

The ground state energy E_0 of the perturbed system, using only the first-order correction, is equal to the Hartree-Fock energy as can be seen in the next equation:

$$\begin{aligned} E_0 = E_0^{(0)} + E_0^{(1)} &= \langle \Phi_0 | H^0 | \Phi_0 \rangle + \langle \Phi_0 | H' | \Phi_0 \rangle \\ &= \langle \Phi_0 | H^0 + H' | \Phi_0 \rangle = \langle \Phi_0 | H | \Phi_0 \rangle = E_{HF} \end{aligned} \tag{4.94}$$

That means that in order to improve the Hartree-Fock energy, we must include, at least, the second-order correction $E_0^{(2)}$ that is given by equation 4.87:

$$E_n^{(2)} = \sum_{m \neq n} \frac{\left| \left\langle \psi_m^{(0)} \middle| H' \middle| \psi_n^{(0)} \right\rangle \right|^2}{\left(E_m^{(0)} - E_n^{(0)} \right)} \tag{4.87}$$

where now, $\psi_n^{(0)}$ is the Hartree-Fock wavefunction Φ_0 and $\psi_m^{(0)}$ are all possible Slater determinants $\Phi_s^{(0)}$ for the unperturbed system. Writing equation 4.87 with the new notation it turns into:

$$E_0^{(2)} = \sum_{s \neq 0} \frac{\left| \left\langle \Phi_s^{(0)} \middle| H' \middle| \Phi_0 \right\rangle \right|^2}{\left(E_0^{(0)} - E_s^{(0)} \right)} \tag{4.95}$$

where the integrals $\left\langle \Phi_s^{(0)} \middle| H' \middle| \Phi_0 \right\rangle$ can be simplified and evaluated by means of the Condon-Slater rules. According to these rules the integral vanishes for all singly excited determinants $\Phi_s^{(0)}$, that is, $\langle \Phi_i^a | H' | \Phi_0 \rangle = 0$ for all occupied spinorbitals i and all virtual spinorbitals a. In the same way, the integral also vanishes for all determinants $\Phi_s^{(0)}$ whose excitation level is three or higher. This means that only the doubly excited determinants must be taken into account. Therefore, using equation 4.92 for H' and the Condon-Slater rules, one gets:

$$E_0^{(2)} = \sum_a \sum_{b>a} \sum_i \sum_{j>i} \frac{\left| \left\langle \Phi_a \Phi_b \middle| r_{12}^{-1} \middle| \Phi_i \Phi_j \right\rangle - \left\langle \Phi_a \Phi_b \middle| r_{12}^{-1} \middle| \Phi_j \Phi_i \right\rangle \right|^2}{\left(\varepsilon_i + \varepsilon_j - \varepsilon_a - \varepsilon_b \right)} \tag{4.96}$$

where atomic units are used for simplicity. The terms ε are the energies of the occupied spinorbitals i and j and of the virtual spinorbitals a and b. When the energy is computed using the second-order correction, it is called MP2 energy. The MP2 level is widely used in electronic structure calculations. Third and higher order corrections can be evaluated giving rise to MP3, MP4, etc. calculations, but these corrections are very time consuming and, in general, they are not included.

Finally, the total ground state MP2 energy is computed by adding the second-order energy given by equation 4.96 to the Hartree-Fock energy:

$$E_0 = E_0^{(0)} + E_0^{(1)} + E_0^{(2)} = E_{HF} + E_0^{(2)} \tag{4.97}$$

Note that before the MP2 correction a SCF calculation is necessary to obtain the Hartree-Fock energy E_{HF}, the Hartree-Fock wave function Φ_0 and the virtual orbitals.

3.4.2 Resolution of the identity Møller-Plesset (RI-MP2) approximation

The critical stage of many electronic structure calculations is the computation of bielectronic integrals which arise from the interelectronic Coulomb repulsion. In the case of MP2 calculations these integrals appear in equation 4.96 when the second-order correction is evaluated. In this equation,

the integrals depend on two electrons. If we use the labels 1 and 2 for denoting those electrons, the integrals in 4.96 can be rewritten as:

$$\left\langle \Phi_a \Phi_b \left| r_{12}^{-1} \right| \Phi_i \Phi_j \right\rangle = \left\langle \Phi_a(1)\Phi_b(1) \left| r_{12}^{-1} \right| \Phi_i(2)\Phi_j(2) \right\rangle = \langle ab|ij\rangle \qquad (4.98)$$

These sort of integrals are called four-index two-electron integrals because they depend on four orbitals Φ_a, Φ_b, Φ_i and Φ_j, and two electrons 1 and 2. The number of such integrals scales with the fourth power of the size of the system N^4, therefore, methods which compute and store integrals are clearly limited by the size of the system.

Almlöf *et al.*[14-19] contributed to the development of several methods to improve the efficiency of MP2 calculations. The RI-MP2 approximation was one of these methods, which is based on the use of auxiliary basis sets to simplify the evaluation of two-electron interactions.[18,19]

The RI technique approximate four-index two-electron integrals through the use of the resolution of the identity (RI):

$$I = \sum_m |m\rangle\langle m| \qquad (4.99)$$

where $|m\rangle$ represents an orthonormal auxiliary basis. The resolution of the identity is inserted before the two electron operator in equation 4.98:

$$\langle ab|ij\rangle = \langle abm\rangle\langle m|ij\rangle \qquad (4.100)$$

where $\langle abm\rangle$ is a three-index one-electron overlap integral,

$$\langle abm\rangle = \int \Phi_a(1)\Phi_b(1)\Phi_m(1)d\tau \qquad (4.101)$$

and $\langle m|ij\rangle$ is a three-index two-electron repulsion integral

$$\langle m|ij\rangle = \int \Phi_m(1) r_{12}^{-1} \Phi_i(2)\Phi_j(2)d\tau \qquad (4.102)$$

The integrals $\langle abm\rangle$ and $\langle m|ij\rangle$ are significantly less time consuming than the corresponding four-index two-electron integrals. Moreover, the space required to store these integrals in memory is reduced with respect to four-index terms. In the case of N conventional basis functions and m expansion functions in the auxiliary basis set, the RI-MP2 approximation requires on the order of $N^2 m$ words of storage, whereas the conventional MP2 method needs on the order of N^4. These time and storage savings cause that, in some cases, the RI-MP2 approach is ten times (or more) faster than the conventional MP2. Of course, this saving is significant when the expansion basis is much smaller than the square of the conventional basis $m < N^2$. A problem arises from this requirement; when the auxiliary basis set is not complete in the space of the product $|ij\rangle$, the equality in equation 4.100 no longer holds. Even so, the right

hand side on equation 4.100 is a reasonable approximation for the bielectronic integral.

There are a large number of works in the literature which have demonstrated the accuracy of the RI approximation. For instance, Katouda *et al.*[20] calculate the energy of trans-polyacetylene using periodic boundary conditions (PBC) with both RI-MP2 and conventional MP2 methods, and they found that the energy difference between both methods is only of 0.4 mhartrees, but PBC RI-MP2 is 98 times faster than PBC MP2. Quiñonero *et al.*[21] computed anion-π and cation-π interaction energies and intermolecular distances for benzene and derivatives of benzene interacting with several cations and anions using several electronic structure methods; they found that RI-MP2 results differ only slightly from those evaluated with MP2, and they conclude that RI-MP2 is able to give an accurate description of the charge-π interactions. Feller *et al.*[22] also found a very good agreement between RI-MP2 and MP2 in the evaluation of geometries and energies of potassium-ether complexes.

3.5 Coupled cluster (CC) method

Another technique for evaluating the electron correlation energy is coupled cluster (CC) theory. It has similarities with the CI theory, but CC is not variational and it is size-consistent. The exact nonrelativistic wavefunction (within the basis set approximation) can be described as

$$\psi = e^{T}\Phi_0 \tag{4.103}$$

where Φ_0 is the Hartree-Fock wave function and T is the cluster operator and it is defined as

$$T = T_1 + T_2 + T_3 + \cdots + T_N \tag{4.104}$$

where N is the total number of electrons and the T_i operators generate all possible excited determinants having i excitations from the reference wavefuntion Φ_0. For instance, when the T_1 operator acts on the Hartree-Fock wavefunction, it generates a linear combination of all possible singly excited determinants Φ_i^a, where an electron from the occupied spinorbital i is promoted to the virtual spinorbital a. The T_2 operator generates a linear combination of all doubly excited determinants Φ_{ij}^{ab}, promoting two electrons from i and j to a and b spinorbitals. The single and double excitations are described by the next equations:

$$T_1\Phi_0 = \sum_i \sum_a t_i^a \Phi_i^a \tag{4.105}$$

$$T_2\Phi_0 = \sum_{i<j}\sum_{a<b} t_{ij}^{ab}\,\Phi_{ij}^{ab} \tag{4.106}$$

The coefficients t in equations 4.105 and 4.106 are called amplitudes, and they are equivalents to the coefficients C in the CI wave function (equation 4.35). The term e^T in equation 4.103 is defined by the following Taylor expansion:

$$e^T = 1 + T + \frac{T^2}{2!} + \frac{T^3}{3!} + \cdots = \sum_{k=0}^{\infty} \frac{T^k}{k!} \tag{4.107}$$

The effect of e^T operator in equation 4.103 is to express the wavefunction ψ as a linear combination of Slater determinants that include Φ_0 and all possible excitations from occupied to virtuals spinorbitals. The aim of the CC method is to find the coefficients (amplitudes) t_i^a, t_{ij}^{ab}, t_{ijk}^{abc} … for all the terms in the linear combination. As for the CI method, if the basis set is complete (infinite) and all the excitations are taken into account, one obtains the exact wavefunction. But this exact calculation is unworkable, therefore in a CC calculation, as for a CI calculation, it is necessary to make two approximations. First, instead of using a complete set of basis functions, one uses a finite basis set to express the spinorbitals in the SCF wave function; therefore the number of virtual orbitals to use in forming excited determinants is finite. Second, instead of including all the operators $T_1, T_2, \ldots T_N$, only some of these operators are employed.

From equations 4.107 and 4.104 the exponential operator may be written as

$$\begin{aligned} e^T = 1 + T_1 + \left(T_2 + \frac{1}{2}T_1^2\right) + \left(T_3 + T_2T_1 + \frac{1}{6}T_1^3\right) \\ + \left(T_4 + T_3T_1 + \frac{1}{2}T_2^2 + \frac{1}{2}T_2T_1^2 + \frac{1}{24}T_1^4\right) \end{aligned} \tag{4.108}$$

The first term in equation 4.108 generates the SCF wavefunction and the second term all singly excited states. The first parenthesis generates all doubly excited states, which may be considered as connected (T_2) or disconnected (T_1^2). Physically, a connected excitation such as T_2 corresponds to two electrons interacting simultaneously, while a disconnected term such as T_1^2 corresponds to two non-interacting electrons. In the rest of the parenthesis we have the same situation; for instance T_3 is a connected excitation where three electrons are interacting simultaneously, while T_2T_1 is a disconnected excitation with a pair of interacting electrons and one electron that does not interact with that pair.

The disconnected excitations are a clear and important difference between CC and CI methods. For instance, let us suppose that only the double

excitation operator is considered in a coupled cluster calculation, that is, $T = T_2$. In this case, a Taylor expansion of the exponential gives

$$e^T = 1 + T_2 + \frac{T_2^2}{2!} + \frac{T_2^3}{3!} + \cdots \tag{4.109}$$

When the exponential is applied on the Hartree-Fock wavefunction one obtains

$$\psi_{CCD} = \left(1 + T_2 + \frac{T_2^2}{2!} + \frac{T_2^3}{3!} + \cdots\right)\Phi_0 \tag{4.110}$$

where CCD means coupled cluster with only the double excitation operator. The first two terms in parentheses $1 + T_2$ acting on Φ_0 are equivalent to the configuration interaction wavefunction with only double excitacions (CID). The remaining terms in equation 4.110 describe disconnected excitations of order higher than two, in spite of the fact that we are using only the T_2 operator. Since T_2 generates double excitations, the term T_2^2 generates quadruple excitations, T_2^3 generates hextuple excitations and so on. These high-order terms do not appear in the CID wavefunction, and the failure to include these excitations makes CI non-size-consistent.

The CC energy is computed by substitution of the wavefunction 4.103 in the Schrödinger equation

$$He^T\Phi_0 = Ee^T\Phi_0 \tag{4.111}$$

Multiplication by Φ_0^* and integration gives

$$\langle\Phi_0|H|e^T\Phi_0\rangle = E\langle\Phi_0|e^T\Phi_0\rangle \tag{4.112}$$

Because of the orthogonality of the spinorbitals, all excited Slater determinants which arises from $e^T\Phi_0$ are orthogonal to Φ_0, therefore the integral $\langle\Phi_0|e^T\Phi_0\rangle = 1$, and equation 4.112 turns into

$$E = \langle\Phi_0|H|e^T\Phi_0\rangle \tag{4.113}$$

The use of single and double excitations, that is $T = T_1 + T_2$, in equation 4.113 gives rise to CCSD model. This model is widely used in CC calculations because it has a good relation accuracy/cost, scaling as N^6. Inclusion of connected triple excitations T_3 defines CCSDT model, but this is very computationaly expensive, scaling as N^8. Alternatively, the triple contribution can be evaluated by perturbation theory and added to the CCSD results. One of these hybrid methods is CCSD(T), where the triple excitations are calculated by the MP4 method, but using the CCSD amplitudes instead of the perturbation coefficients for the wavefunction corrections. Moreover a term arising from fifth-order perturbation theory is added for describing the coupling between singles and triples.

3.6 Multiconfiguration and multireference methods

The post Hatree-Fock methods seen so far include the dynamic correlation. This is accurate for systems for which the Hartree-Fock configuration dominates the total wavefunction. However, in some cases, the importance of one or more excited configurations may be of similar magnitude in the total wavefunction than the Hartree-Fock configuration. This means, as mentioned in Section 3.2, that in some systems the nondynamic correlation may be significant. Multiconfiguration and multireference methods have been developed for these cases.

The multiconfiguration self-consistent field (MCSCF) method can be considered as a CI method, where the wavefunction is expressed as a linear combination of ground state and excited determinants:

$$\psi = C_0\Phi_0 + C_s\Phi_s + C_D\Phi_D + \cdots + C_N\Phi_N \tag{4.114}$$

where the coefficients C reflect the weight of each determinant in the expansion. Φ_0 is the Hartree-Fock determinant, Φ_s represents all the singly excited determinants, Φ_D represents all the doubly excited determinants and so on. As seen in Section 3.1, the different configurations are represented by Slater determinants of molecular orbitals:

$$\Phi_i = (N!)^{-1/2} det|\phi_a(1)\phi_b(2)\ldots\phi_z(N)| \tag{4.115}$$

and the molecular orbitals are expressed as linear combinations of M basis functions θ_j:

$$\phi_i = \sum_{j=1}^{M} c_{ji}\,\theta_j \tag{4.116}$$

There is an important difference between CI and MCSCF methods. In the CI method, the coefficients c_{ji} of equation 4.116 are evaluated by an initial SCF calculation. Once they have been determined, they are held fixed during the optimization of coefficients C of equation 4.114 to obtain the CI wavefunction. On the other hand, an MCSCF calculation optimizes the coefficients c_{ji} and C simultaneously, at each step of the process. This simultaneous optimization makes MCSCF computationally demanding, but accurate results can be obtained with the inclusion of even a relatively small number of configurations.

The MCSCF methods are not only used in the determination of the ground state wavefunction, but they are of particular importance for obtaining excited states. The major problem with these methods is selecting which configurations are necessary to include in the total wavefunction. One of the most used approaches is the complete active space self-consistent field

(CASSCF). Here the selection of configurations is done by partitioning the molecular orbitals into active and inactive spaces. Typically, the active molecular orbitals are some of the highest occupied and some of the lowest unoccupied molecular orbitals from a Hartree-Fock calculation. The inactive orbitals have either 2 or 0 electrons, that is, they are totally full or totally empty. Within the active space a full CI is performed and all the configurations are included in the MCSCF optimization. The molecular orbitals to be included in the active space must be decided manually. A common notation used in this type of calculation is $[n, m]$-CASSCF, which indicates that n electrons are distributed in m orbitals obtaining all possible excitations for this active space.

As for any full CI expansion, the CASSCF becomes unworkable when the active space is relatively large. For these cases, a variation of CASSCF procedure is the restricted active space self-consistent field (RASSCF). Here the active molecular orbitals are divided into three sections RAS1, RAS2 and RAS3. A typical model performs a full CI calculation in RAS2 space; the RAS1 space consists of molecular orbitals that are doubly occupied in the SCF reference determinant, and the RAS3 space is formed by molecular orbitals that are empty in the SCF determinant. Configurations additional to those from the RAS2 are generated by promoting, for example, a maximum of two electrons from the RAS1 to the RAS3 space and from the RAS2 to the RAS3 space. That is, a typical RASSCF procedure generates the excited configurations by performing a full CI in the RAS2 space, and a CISD between the RAS1, RAS2 and the RAS3 spaces. Figure 4.3 displays the different active and inactive spaces for CASSCF and RASSCF methods.

The MCSCF calculation takes into account nondynamic correlation, but since the Hartree-Fock wavefunction is employed as reference to generate the excitations, the dynamic correlation is not completely introduced. If a dynamic correlated method is employed after the MCSCF calculation, this problem is overcome. For instance, the CASPT2 method applies second-order perturbation theory over the wavefunction obtained from a MCSCF calculation, thus introducing both types of correlation.

As seen in Section 3.3, the conventional CI method considers the SCF wavefunction as reference. However, an MCSCF wavefunction may also be chosen as reference, and then, one can perform, for example, a CISD calculation obtaining excitations from the MCSCF wavefunction. This procedure defines the multi-reference configuration interaction (MRCI) method. This method allows to generate more excited configurations than the conventional CISD procedure, and therefore, it usually reduces the size-consistency error encountered in CISD calculations. Obviously, MRCI are more computational demanding than CI calculations.

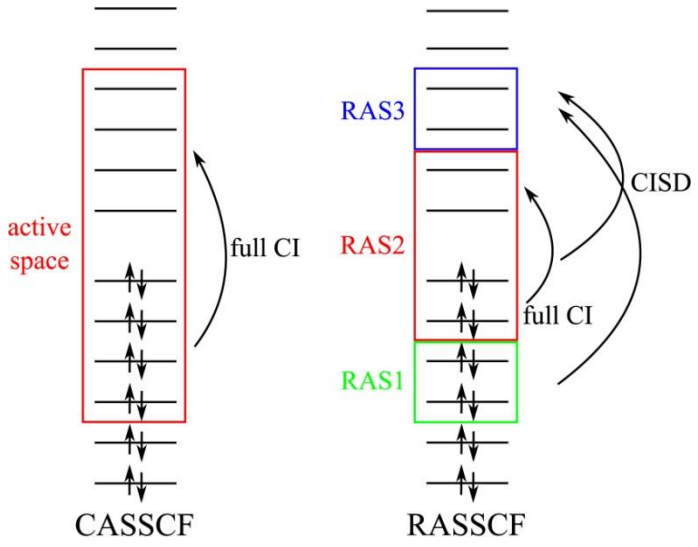

Figure 4.3: Active and inactive molecular orbitals in CASSCF and RASSCF methods.

A different approach to include the nondynamic correlation is the symmetry adapted cluster-configuration interaction (SAC-CI).[23-25] This method was successfully used for calculations of ground, excited and ionizated states of atoms and molecules in various spin multiplicities.[26,27] The SAC-CI method calculates the ground state wavefunction by using the SAC theory, and then, the excited state wavefunctions are computed from the SAC ground state wavefunction. The SAC method belongs to the coupled cluster theory, and therefore, its formulation is similar. The SAC wavefunction for the ground state ψ_g^{SAC} is written as

$$\psi_g^{SAC} = e^S \Phi_0 \tag{4.117}$$

where Φ_0 is the Hartree-Fock determinant and S is a linear combination of the excitation operators,

$$S = C_1 S_1 + C_2 S_2 + \cdots + C_N S_n = \sum_i C_i S_i \tag{4.118}$$

where the coefficients can be determined through variational or nonvariational methods. The main difference between SAC and CC is that the operators S_i of the SAC theory are spin-symmetry and space-symmetry adapted. This means, without going into detail, that the method calculates a pure spin state and is free from spin-contamination problem that may appear in the CC method. Moreover, as CC theory, SAC is size-consistent. Based on the SAC wavefunction, we can define a set of basis functions Φ_k for describing the excited states. These functions are defined as follows

$$\Phi_k = PS_k\psi_g^{SAC} \tag{4.119}$$

where P is an operator which projects out the undesired spin symmetries. The excited state wavefunction ψ_e^{SAC-CI} can be described by a linear combination of the excited basis functions Φ_k:

$$\psi_e^{SAC-CI} = \sum_k d_k \Phi_k \tag{4.120}$$

where d_k are coefficients to be determined.

Other methods available for excited state calculations are coupled cluster linear response theory (CC-LRT) and the equation of motion coupled cluster (EOM-CC) method, but they follow basically the same approximations that SAC-CI theory.[27] Time-dependent density functional theory (TD-DFT) is another useful and widely used technique for excited states calculations, although it showed faults in some cases such as Rydberg states or excited states with substantial double excitation character.

4. DENSITY FUNCTIONAL THEORY (DFT)

The *ab initio* methods seen in Section 3 are based on the knowledge of the wavefunction which depends on $4N$ coordinates, three spatial and one spin coordinate for each electron. Density functional theory (DFT) is a method which also includes electron correlation, and allows to replace the complicated N-electron wavefunction and the associated Schrödinger equation by the much simpler electron density ρ and its associated calculational scheme. While the complexity of the wavefunction increases exponentially with the number of electrons, the electron density has the same number of variables (3 spatial coordinates), independent of the system size. It has been proven that each electron density yields different ground state energy, that is, there exists a one-to-one correspondence between the electron density of a system and the energy. The problem is that the functional connecting these two properties is unknown. Therefore, the goal of DFT methods is to design functionals connecting electron density with the energy.

The energy in the DFT formulation is represented as a functional, that is, the energy does not depend on variables, instead it depends on a function (the electron density), which in turn depends on variables.

The original idea of representing the energy as a function of the electron density was formulated by Thomas and Fermi in 1927, but it was not applied until 1964 when Hohenberg and Kohn demonstrated the existence and variational theorems.

4.1 Hohenberg and Kohn theorems

The first theorem of Hohenberg and Kohn is the existence theorem. It says that any property of a non-degenerate ground state can be calculated exactly from the electron density. The electron density must be positive within all space and its integration over all space is equal to the number of electrons:

$$\rho(r) \geq 0 \tag{4.121}$$

$$\int \rho(r)\, dr = N \tag{4.122}$$

Moreover, the non-degenerate ground state density must determine the external potential which represents the attraction between electrons and nuclei. Under these conditions, the electronic energy can be written as

$$E(\rho) = T(\rho) + V_{ee}(\rho) + V_{eN}(\rho) \tag{4.123}$$

where $T(\rho)$ is the kinetic energy, $V_{ee}(\rho)$ is the interaction between electrons and $V_{eN}(\rho)$ is the electron-nuclear attraction. The $V_{ee}(\rho)$ term may be divided into Coulomb $J(\rho)$ and exchange $W_{XC}(\rho)$ parts (as in the Hartree-Fock theory but now the exchange operator K is represented by $W_{XC}(\rho)$).The nuclear-nuclear repulsion is a constant within the Born-Oppenheimer approximation. The first two terms are usually represented together by one functional $F_{HK}(\rho)$. The derivative of the electron-nuclear potential with respect to the electron density is the external potential:

$$\frac{\partial V_{eN}(\rho)}{\partial \rho} = v(r) \tag{4.124}$$

Therefore, the electronic energy can be expressed as follows:

$$E(\rho) = F_{HK}(\rho) + \int \rho(r) v(r) dr \tag{4.125}$$

The second Hohenberg and Kohn theorem is the variational theorem which says that the ground state electron density can be exactly calculated by searching the electron density which minimizes the ground state energy. Therefore one can write the so-called fundamental equation of the DFT as follows:

$$\frac{\partial E(\rho)}{\partial \rho(r)} = v(r) + \frac{\partial F_{HK}(\rho)}{\partial \rho(r)} \tag{4.126}$$

4.2 Kohn-Sham methodology

The problem to solve equation 4.126 is that the relation between $F_{HK}(\rho)$ and the electron density is unknown. In particular, there is not a known connection between the kinetic energy $T(\rho)$ and the electron density. But if we

know the wavefunction ψ that describes the system, one can easily calculate the kinetic energy. Based on that, Kohn and Sham developed a method to calculate the electron density. Next, this method is briefly discussed.

Suppose a system formed by N non-interacting electrons, that is $V_{ee}(\rho) = 0$, subjected to an external potential $v_r(r)$. This reference system is described by a wavefunction ψ_r which can be exactly calculated by the Hartree-Fock method because there are not interelectronic interactions. The Hamiltonian of this system is a sum of the kinetic energy of the electrons and the electron-nuclear interaction, which is described by the external potential $v_r(r)$:

$$H = \sum_{i=1}^{N} h_i = -\frac{\hbar^2}{2m_e}\sum_{i=1}^{N}\nabla_i^2 + \sum_{i=1}^{N} v_r(r) \tag{4.127}$$

and the exact wavefunction is expressed by the Slater determinant:

$$\psi_r = (N!)^{-1/2} det|\phi_a(1)\phi_b(2)\dots\phi_m(N)| \tag{4.128}$$

where the molecular orbitals ϕ_i are expressed as a linear combination of known basis function θ_j as seen in Section 3.1:

$$\phi_i = \sum_{j=1}^{m} c_{ji}\,\theta_j \tag{4.129}$$

The coefficients of the molecular orbitals are calculated iteratively solving the monoelectronic Schrödinger equations:

$$\left(-\frac{\hbar^2}{2m_e}\nabla_i^2 + v_r(r)\right)\phi_i = E_i\phi_i \tag{4.130}$$

Once the wavefunction ψ_r is known, the kinetic energy and the electron density can be evaluated exactly as follows:

$$\rho(r) = \sum_{i=1}^{m}|\phi_i|^2 \tag{4.131}$$

$$T_r(\rho) = \sum_{i=1}^{m}\left\langle\phi_i\left|-\frac{\hbar^2}{2m_e}\nabla_i^2\right|\phi_i\right\rangle \tag{4.132}$$

In the previous equations m is the number of occupied molecular orbitals and the subscript r indicates that the equations describe the reference system without interelectronic repulsions. Once we know the kinetic energy, the total energy of the reference system is calculated with equation 4.125 but ignoring the interelectronic term:

$$E_r(\rho) = T_r(\rho) + \int \rho(r) v_r(r) dr \tag{4.133}$$

and the fundamental equation of DFT is

$$\frac{\partial E_r(\rho)}{\partial \rho(r)} = v_r(r) + \frac{\partial T_r(\rho)}{\partial \rho(r)} \tag{4.134}$$

Now, if we have a real system, that is, with electron-electron interactions, the total energy is given by:

$$E(\rho) = T(\rho) + V_{ee}(\rho) \int \rho(r) v(r) dr \tag{4.135}$$

If we add and subtract the reference kinetic energy $T_r(\rho)$ and Coulombic repulsion between two electrons $J(\rho)$ to equation 4.135, we obtain

$$\begin{aligned} E(\rho) = T_r(\rho) + \big(T(\rho) - T_r(\rho)\big) + J(\rho) \\ + \big(V_{ee}(\rho) - J(\rho)\big) + \int \rho(r) v(r) dr \end{aligned} \tag{4.136}$$

where the Coulombic repulsion between two electrons $J(\rho)$ is defined as

$$J(\rho) = \frac{1}{2} \int \int \frac{\rho(r_1)\rho(r_2)}{r_{12}} dr_1 dr_2 \tag{4.137}$$

The difference between the interelectronic interaction $V_{ee}(\rho)$ and the Coulombic repulsion $J(\rho)$ is the exchange-correlation electronic energy $W_{XC}(\rho)$, and the difference between the kinetic energy of the real and reference systems is called correlation kinetic energy $T_c(\rho)$. The next equations define these quantities:

$$W_{XC}(\rho) = V_{ee}(\rho) - J(\rho) \tag{4.138}$$

$$T_c(\rho) = T(\rho) - T_r(\rho) \tag{4.139}$$

Therefore, the total exchange-correlation energy $E_{XC}(\rho)$ is the sum of these two energies:

$$E_{XC}(\rho) = T_c(\rho) + W_{XC}(\rho) \tag{4.140}$$

The total exchange-correlation energy takes into account the interaction between electrons which is ignored in the reference system. Now, an exchange-correlation potential can be defined in the same way that the external potential defined by equation 4.124:

$$\frac{\partial E_{XC}(\rho)}{\partial \rho} = v_{XC}(r) \tag{4.141}$$

Replacing equations 4.137 and 4.140 into equation 4.136 one gets,

$$E(\rho) = T_r(\rho) + E_{XC}(\rho) + \frac{1}{2}\int\int \frac{\rho(r_1)\rho(r_2)}{|r_1 - r_2|} dr_1 dr_2 + \int \rho(r) v(r) dr \tag{4.142}$$

and applying the fundamental equation of the DFT theory one obtains

$$\frac{\partial E(\rho)}{\partial \rho} = \frac{\partial T_r(\rho)}{\partial \rho} + \frac{\partial E_{XC}(\rho)}{\partial \rho} + v(r) + \int \frac{\rho(r_2)}{|r_1 - r_2|} dr_2 \tag{4.143}$$

Now, the Coulomb potential $v_C(r)$ is defined as follows

$$v_C(r) = v(r) + \int \frac{\rho(r_2)}{|r_1 - r_2|} dr_2 \tag{4.144}$$

Replacing equations 4.141 and 4.144 in the fundamental equation 4.143 we can write

$$\frac{\partial E(\rho)}{\partial \rho} = \frac{\partial T_r(\rho)}{\partial \rho} + v_C(r) + v_{XC}(r) \tag{4.145}$$

The fundamental equation for the real system (4.145) is equivalent to the fundamental equation for the reference system (4.134) but substituting the external potential $v_r(r)$ for the Coulomb $v_C(r)$ and exchange-correlation $v_{XC}(r)$ potentials which appear due to the interelectronic correlation. Therefore, the equations that one must solve to find the ground state energy for the real system should be equivalent to the equations for the reference system. This means that one can write monoelectronic Schrödinger equations similar to 4.130, but using the new potentials $v_C(r)$ and $v_{XC}(r)$:

$$\left(-\frac{\hbar^2}{2m_e}\nabla_i^2 + v_C(r) + v_{XC}(r)\right)\phi_i = E_i\phi_i \tag{4.146}$$

where the operator acting over the one-electron wavefunction is called Kohn-Sham operator h_{KS}, and the monoelectronic wavefunctions are called Kohn-Sham orbitals. The Kohn-Sham equations (4.146) are similar to the Hartree-Fock equations (4.21). The most important difference is that the exchange operator K is replaced by the exchange-correlation operator $v_{XC}(r)$ which includes the electron correlation in the equations. Once the Kohn-Sham orbitals are known, the electron density may be computed by equation 4.131.

The process to calculate the energy is iterative as for the *ab initio* calculations. The calculation starts with a trial set of orbitals ϕ_i which are used to compute the electron density (equation 4.131); then the electron density is used for calculating the Coulomb $v_C(r)$ and exchange-correlation $v_{XC}(r)$ potentials which are necessary for solving the Kohn-Sham equations (4.146) and obtaining a new set of orbitals which will be used to compute the electron density and so on.

The problem of using the Kohn-Sham equations is that the exchange-correlation energy expression $E_{XC}(\rho)$ is unkown, and therefore $v_{XC}(r)$ is also unknown.

4.3 Exchange-correlation functionals

The difference between various DFT methods is the choice of the functional form for the exchange-correlation energy. It can be proven that the exchange-correlation potential is a unique functional, valid for all systems, but this explicit functional form is unknown.

Exchange-correlation potentials have a mathematical form containing parameters. Some of these parameters are assigned by fits to experimental data or high-level wave mechanics properties. This means that DFT methods do not use the exact Hamiltonian, and therefore, they are not classified as *ab initio* methods.

There exist four general ways of developing the DFT exchange-correlation energy depending on its relation with the electron density. The first one is the local density approximation (LDA) where $E_{XC}(\rho)$ depends on the electron density of a uniform electron gas. In a more general case the local spin density approximation (LSDA) gives different electron densities for electrons with different spin. Frequently, using this method, the electron correlation is overestimated, often by a factor close to 2, and bond strengths are as a consequence overestimated, by 100 kJ/mol. Despite their simplicity, LSDA methods provide results with accuracy similar to that obtained by the Hartree-Fock method.

Improvements over the LSDA approach must consider a non-uniform electron gas. In this direction the generalized gradient approximation (GGA) methods were developed including as a variable the first derivative of the electron density with respect to the coordinates. Therefore, the exchange correlation energy depends on the electron density ρ and on its gradient $\nabla\rho$.

The logical extension of GGA methods is to allow the exchange-correlation energy to depend on higher order derivatives of the electron density. In particular, the higher-order gradient or meta-GGA methods use the Laplacian $\nabla^2\rho$ to evaluate $E_{XC}(\rho)$.

The last way of constructing the functional is called hybrid or hyper-GGA method where the exchange-correlation energy depends on ρ, $\nabla\rho$ and $\nabla^2\rho$, and moreover, part of the exact Hartree-Fock exchange energy is introduced into the functional. Inclusion of the Hartree-Fock exchange energy often improves the results, but the optimum fraction to include depends on the

specific property of interest. In general, the hyper-GGA functionals provide the best results, although unfortunately, the accuracy of the DFT calculations depends on the property and the system of interest, therefore, it is difficult to know *a priori* what functional will give us the most accurate result.

Table 4.1 shows some of the most popular exchange-correlation functionals:

Table 4.1: Examples of exchange-correlation functional.

Functional type	Examples
LSDA	VWN, PW
GGA	BLYP, OPTX, OLYP, PW86, PW91, PBE, HCTH, B97
Meta-GGA	BR, B95, VSXC, PKZB, TPSS, τ-HTCH
Hyper-GGA or Hybrid	ACM, B3LYP, B3PW91, O3LYP, PBE0, TPSSh, τ-HTCH-hybrid

4.4 Resolution of the identity density functional theory (RIJ-DFT)

During the iterative resolution of the Kohn-Sham equations, one must evaluate the interelectronic repulsion. This term is given by equation 4.138:

$$V_{ee}(\rho) = W_{XC}(\rho) + J(\rho) \tag{4.138}$$

The computational cost of the evaluation of $W_{XC}(\rho)$ is a small percentage of the whole cost of a DFT calculation. It is the evaluation of the Coulomb term which dominates the computational procedure. In this Section an approximate method for the evaluation of the Coulomb term is discussed.

As seen above, the Coulomb repulsion J is given by equation 4.137:

$$J(\rho) = \frac{1}{2}\int\int \frac{\rho(r_1)\rho(r_2)}{r_{12}} dr_1 dr_2 = \frac{1}{2}\langle\rho|\rho\rangle \tag{4.137}$$

On the other hand the electron density can be computed from molecular orbitals by equation 4.131:

$$\rho(r) = \sum_{i=1}^{m} |\phi_i|^2 \tag{4.131}$$

Since the molecular orbitals are expressed as a linear combination of basis functions (equation 4.129), one can write the electron density as follows

$$\rho(r) = \sum_{i=1}^{m} |\phi_i|^2 = \sum_{i=1}^{m} \sum_{j=1}^{m} \left(c_{ji}\, \theta_j\right)^2 \tag{4.147}$$

and expanding the square one can write:

$$\rho(r) = \sum_{i=1}^{m} \sum_{a=1}^{l} \sum_{b=1}^{l} c_{ai}\, c_{bi}\, \theta_a(r) \theta_b(r) \tag{4.148}$$

The expansion coefficients, which actually contain all relevant information about the charge density, are usually collected in the so-called density matrix *P* with elements

$$P_{ab} = \sum_{i=1}^{m} c_{ai}\, c_{bi} \tag{4.149}$$

Thus, we can alternatively express the Coulomb contribution J in terms of the basis functions by substituting equation 4.148 into 4.137 as follows:

$$\begin{aligned} J &= \sum_{a=1}^{l} \sum_{b=1}^{l} P_{ab} \int\int \frac{\theta_a(r_1)\theta_b(r_1)\theta_c(r_2)\theta_d(r_2)}{r_{12}} dr_1 dr_2 \\ &= \sum_{a=1}^{l} \sum_{b=1}^{l} P_{ab} \langle ab|cd\rangle \end{aligned} \tag{4.150}$$

The integral into equation 4.150 is a four-center two-electron integral. Thus, the bottle-neck for DFT calculations is the evaluation of these types of integrals, as for *ab initio* calculations. An approximate method was proposed by Eichkorn *et al.*[28] for which the electron density is expressed as a linear combination of an auxiliary basis g_α (or g_β) according to

$$\rho(r_2) \approx \tilde{\rho}(r_2) = \sum_{\alpha} c_\alpha g_\alpha \tag{4.151}$$

where the tilde indicates that we are dealing with an approximate density except in the case for which the auxiliary basis set is complete within the space of the molecular orbitals ϕ_i. The auxiliary basis set is never complete (but there is not computational saving) but equation 4.151 is considered a good approximation for the electron density. The coefficients c_α in equation 4.151 are determined by minimizing the Coulomb repulsion of the residual density:

$$\int\int \frac{\left(\rho(r_1) - \tilde{\rho}(r_1)\right)\left(\rho(r_2) - \tilde{\rho}(r_2)\right)}{r_{12}} = \langle \rho - \tilde{\rho} | \rho - \tilde{\rho} \rangle min \tag{4.152}$$

The condition 4.152 leads to a system of linear equations involving two and three-center integrals

$$\sum_{\beta} \langle \alpha | \beta \rangle \, c_{\beta} = \gamma_{\gamma} \tag{4.153}$$

with

$$\gamma_{\alpha} = \sum_{ab} \langle \alpha | ab \rangle \, P_{ab} \tag{4.154}$$

where α and β are the auxiliary basis and P_{ab} is the density matrix of the coefficients of the molecular orbitals.

The condition 4.152 is mathematically equivalent to the replacement

$$\langle ab|cd\rangle \approx \sum_{\alpha,\beta} \langle ab|\alpha\rangle \langle \alpha|\beta\rangle^{-1} \langle \beta|cd\rangle \tag{4.155}$$

This approximation formally resembles the resolution of the identity and is called RI-J because the RI approximation is applied on the Coulomb operator J.

Finally, the Coulomb operator can be written as

$$J(\rho) = \frac{1}{2}\langle \rho|\rho\rangle \approx \tilde{J}(\rho) = \frac{1}{2}\langle \tilde{\rho}|\rho\rangle \tag{4.156}$$

and substituting 4.148 and 4.151 into 4.155 we obtain

$$J(\rho) = \frac{1}{2} c_{\alpha} \langle \alpha | ab \rangle P_{ab} = \frac{1}{2} c_{\alpha} \gamma_{\alpha} \tag{4.157}$$

where $\langle \alpha|ab\rangle P_{ab}$ is equal to γ_{α} by equation 4.153. Therefore, the four-center two-electron integral in equation 4.150 turns into a three-center two-electron integral in equation 4.157 which is are much faster to evaluate.

4.5 Dispersion correction to density functional theory (DFT-D)

Despite the many successes of DFT, there are some areas where the current functionals are known to perform poorly. Most of these failures are caused by the rapid decay of electron density with distance to the nuclei, that is, by the non-correct long-range behaviour of the functional. For instance, weak interactions due to dispersion forces, which arise from electron correlation, are badly described by current DFT methods because they do not reproduce the correct interaction behaviour of R^{-6}. Loosely bound electrons, such as anions arising from neutral systems with relatively low electron affinities represent a problem for the DFT methods; since loosely bound electrons have most of the associated density far from the nuclei, this may lead erroneously to an unbond electron. The prediction of Rydberg states, where the electron is excited into a diffuse orbital, can also be a problem for DFT methods; the non-correct asymptotic behaviour of the exchange-correlation potential is the error source

again. A charge transfer system for which an electron is transferred over a large distance is another example where DFT often fails. The bad description of dispersion forces is the DFT failure of interest in this thesis, in particular, in Chapter 10 where the potential energy surface for $SiNCS^+/CF_4$ and $(CH_3)_2SiNCS^+/CF_4$ is calculated by a DFT functional. There, an empirical correction dispersion proposed by Grimme[29] was used. This approach is based on the Becke GGA functional B97.[30] This correction calculates the total energy E_{DFT-D} as

$$E_{DFT-D} = E_{KS} + E_{disp} \tag{4.158}$$

where E_{KS} is the usual Kohn-Sham energy and E_{disp} is the empirical dispersion correction given by

$$E_{disp} = -s_6 \sum_{i=1}^{N_{at}} \sum_{j>i}^{N_{at}} \frac{C_6^{ij}}{R_{ij}^6} f_{dmp}\left(R_{ij}\right) \tag{4.159}$$

Here, N_{at} is the number of atoms, C_6^{ij} is the dispersion coefficient for the atom pair ij, s_6 is a global scaling factor that only depends on the functional used, R_{ij} is the interatomic distance between atoms i and j, and f_{dmp} is a damping function to avoid wrong behaviour at small distances. The s_6 scale factors have been determined by least-squares optimization of interaction energy deviations for 40 complexes. The damping function f_{dmp} is given by

$$f_{dmp}\left(R_{ij}\right) = \frac{1}{1 + e^{-d\left(R_{ij}/R_r - 1\right)}} \tag{4.160}$$

where R_r is the sum of atomic van der Waals radii from ROHF/TZV computations and d is a constant setting to 20. The interatomic coefficients C_6^{ij} are computed from the geometric mean of the form

$$C_6^{ij} = \sqrt{C_6^i C_6^j} \tag{4.161}$$

where atomic coefficients C_6^i are derived from the London formula for dispersion given as

$$C_6^i = 0.05 N I_p^i \alpha^i \tag{4.162}$$

where N has values 2, 10, 18, 36 and 54 for atoms from rows 1-5 of the periodic table. The values of this constant have been adjusted to reproduce binding energies and bond distances of several complexes. I_p^i and α^i are the ionization potentials and polarizabilities from PBE0/QZVP calculations.

Finally, the dispersion correction was tested against experimental and high-level theoretical properties, and it shows to be reliable for most of the comparisons.

REFERENCES

(1) Bertrán Rusca, J.; Branchadell Gallo, V.; Moreno Ferrer, M.; Sodupe Roure, M. *Química Cuántica*; Editotial Síntesis: Madrid, 2000.

(2) Levine, I. N. *Quantum Chemistry*; 4 ed.; Prentice Hall: New Jersey, 1991.

(3) Atkins, P. W.; Friedman, R. S. *Molecular Quantum Mechanics*; 3 ed.; Oxford University Press: New York, 1997.

(4) Jensen, F. *Introduction to Computational Chemistry*; John Willey & Sons: Chichester, 1999.

(5) Szabo, A.; Ostlund, N. S. *Modern Quantum Chemistry: Introduction to Advanced Electronic Structure Theory*; McGraw-Hill: New York, 1989.

(6) McWeeny, R. *Methods of Molecular Quantum Mechanics*; 2 ed.; Academic Press: London, 2001.

(7) Helgaker, T.; Jorgensen, P.; Olsen, J. *Molecular Electronic-Structure Theory*; John Willey & Sons: Chichester, 2000.

(8) Cramer, C. J. *Essentials of Computational Chemistry: Theories and Models*; 2 ed.; John Willey & Sons: Chichester, 2004.

(9) Parr, R. G.; Yang, W. *Density-Functional Theory of Atoms and Molecules*; Oxford University Press: New York, 1989.

(10) Koch, W.; Holthausen, M. C. *A Chemist's Guide to Density Functional Theory*; WILEY-VCH: Weinheim, 2000.

(11) Cook, D. B. *Handbook of Computational Chemistry*; Oxford University Press: New York, 1998.

(12) Nakamura, H. *Nonadiabatic Transitions: Concepts, Basic Theories and Applications*; World Scientific Printers: Singapore, 2002.

(13) Chattopadhyay, S.; Chaudhuri, R. K.; Mahapatra, U. S. *J. Chem. Phys.* **2008**, *129*, 244108/1-244108/9.

(14) Saebo, S.; Almlof, J. *Chem. Phys. Lett.* **1989**, *154*, 83-9.

(15) Haeser, M.; Almloef, J.; Feyereisen, M. W. *Theor. Chim. Acta* **1991**, *79*, 115-22.

(16) Almlof, J. *Chem. Phys. Lett.* **1991**, *181*, 319-20.

(17) Haeser, M.; Almloef, J. *J. Chem. Phys.* **1992**, *96*, 489-94.

(18) Feyereisen, M.; Fitzgerald, G.; Komornicki, A. *Chem. Phys. Lett.* **1993**, *208*, 359-63.

(19) Vahtras, O.; Almloef, J.; Feyereisen, M. W. *Chem. Phys. Lett.* **1993**, *213*, 514-18.

(20) Katouda, M.; Nagase, S. *J. Chem. Phys.*, *133*, 184103/1-184103/9.

(21) Quiñonero, D.; Garau, C.; Frontera, A.; Ballester, P.; Costa, A.; Deya, P. M. *J. Phys. Chem. A* **2005**, *109*, 4632-4637.

(22) Feller, D.; Apra, E.; Nichols, J. A.; Bernholdt, D. E. *J. Chem. Phys.* **1996**, *105*, 1940-1950.

(23) Nakatsuji, H. *Chem. Phys. Lett.* **1978**, *59*, 362-4.

(24) Nakatsuji, H. *Chem. Phys. Lett.* **1979**, *67*, 329-33.

(25) Nakatsuji, H. *Chem. Phys. Lett.* **1979**, *67*, 334-42.

(26) Shukla, M.; Leszczynski, J. *Radiation Induced Molecular Phenomena in Nucleic Acids*; Springer: New York, 2008.

(27) Dykstra, C. E.; Frenking, G.; Kim, K. S.; Scuseria, G. E. *Theory and Applications of Computational Chemistry: The Fist Forty Years*; Elsevier: Oxford, 2005.

(28) Eichkorn, K.; Treutler, O.; Oehm, H.; Haeser, M.; Ahlrichs, R. *Chem. Phys. Lett.* **1995**, *240*, 283-90.

(29) Grimme, S. *J. Comput. Chem.* **2006**, *27*, 1787-1799.

(30) Becke, A. D. *J. Chem. Phys.* **1997**, *107*, 8554-8560.

Chapter 5

Classical Trajectory Method

1. INTRODUCTION

The classical trajectory method, of which the pioneer was Bunker[1-3] in the sixties, provides a direct route from the potential energy surface to the dynamics of reactive or non-reactive collisions, from which one can investigate the essential nonquantual features of such collisions.[4-9] Classical trajectory studies are useful because they yield an easy picture of the dynamics. This sort of simulation is widely used to study elemental reactions and inelastic collisions between atoms, molecules and clusters, and collisions of these species with surfaces. Examples of all these collisions can be found in reference 7 and in references therein.

The classical trajectory approach assumes that each atom is a structureless point moving deterministically as a function of time under the influence of the forces between that atom and its neighbours. The motion of the system obeys classical Newton (or Hamilton) equations which relate, as will be seen below, coordinates and momenta with the potential energy of the system. Once we know the potential energy, the numerical resolution of the equations of motion is straightforward, starting from a given initial condition.

As seen in previous Chapters, throughout this thesis, the potential energy surfaces were developed by fitting analytical functions to electronic structure data. The construction of an analytical potential energy surface requires a relatively large number of electronic structure calculations, that is, tens, hundreds or even thousands depending on the complexity of the system. Therefore, this analytical procedure of obtaining the potential energy is only feasible for small and medium-size systems, that is, up to few tens of atoms, or for big systems which are well-described by smaller models as in our case, where the CF_4 molecule describes faithfully the behaviour of the fluorocarbon chains of the F-SAM surface. When the size of the system is relatively large, one must turn to other techniques. For instance, the use of molecular mechanical force fields is very common in large systems such as proteins or nucleic acids, but as mentioned in Chapter 2, in some cases its reliability is not good enough.

Another possibility for relatively large systems is the use of direct dynamics. This method does not use an analytical potential to integrate the Newton equations, but at each step of the trajectory the energy and its gradient are obtained from *ab initio*, semiempirical or density functional theory calculations. This approach started being used successfully by Helgaker *et al.*[10-12] for unimolecular fragmentations of H_3 and CH_2OH^+, and later, by Hase and co-workers for other unimolecular reactions.[13-15] One useful approach for describing reactions in condensed phase is to combine quantum mechanical and

molecular mechanical methods (QM/MM), where reacting portions of the system are treated quantum mechanically, while the remaining portions of the system are treated with molecular mechanical potentials. After the landmark work of Warshel and Levitt,[16] many systems, especially enzymatic reactions, have been treated by QM/MM methods.

All the methods mentioned above treat the nuclei classically but, in reality, atoms obey quantum mechanics rather than classical mechanics. Quantum dynamics[17,18] solves the nuclear time-dependent Schrödinger equation and, in principle, provides accurate results because all the system, electrons and nuclei, are treated quantum mechanically. The problem is that, nowadays, only systems formed by a small number of atoms can be studied by this method.

In general, classical trajectories have shown to be reliable in the calculation of many properties such as rate constants, reactive cross sections or product energy distributions. But some problems may arise when quantum effects become significant; the most important ones being tunneling, adiabatic leak and electronic nonadiabaticity.[7]

Classically, whenever a molecule approaches a potential energy barrier with less energy than the energy of the barrier maximum, the molecule is completely reflected. But a quantum mechanical system with the same energy will have a nonzero probability of transmission through the barrier. This effect becomes more important in reactions where a light atom is being transferred. Therefore, classical trajectories will underestimate rate constants for systems which undergo tunneling.

Another problem in classical mechanical methods is the problem of adiabatic leak. In quantum mechanics, each normal mode must contain at least the zero point energy (ZPE), but classical mechanics has no such restriction. Even if ZPE is initially put into a normal mode, it can leak out during the course of the trajectory, and as a consequence, unrealistic behaviours may appear such as the evaporation of the system (if it is initially in a condensed phase) or the decrease of the reactive energy threshold with respect to the quantum threshold due to the formation of products without ZPE.

An assumption made in the classical trajectory method is the Born-Oppenheimer approximation. Under this approximation, the system must remain in the same potential energy surface during the trajectory, that is, the process must be electronically adiabatic. But, in reality, there are geometries at which more than one surface may take part, and the system may carry out a nonadiabatic transition.

The processes studied in this thesis are unreactive inelastic gas/surface collisions at relatively low collision energies and room temperature.

Under these conditions, the most likely quantum effect is the ZPE leakage, but probably it will not influence significantly the results since the collisions are unreactive. As was mentioned in Chapter 2, some studies of energy transfer in gas/surface inelastic collisions (apart from those reported in this thesis) have been performed in the last years by classical trajectory simulations.[19-31]

This chapter is organized as follows. Section 2 introduces the classical equations of motion and Section 3 shows the most common methods for its numerical resolution. The sampling of initial conditions is explained in Section 4. And finally, Section 5 touches the analysis of final conditions that allow to compute any property from the final coordinates and momenta.

2. CLASSICAL EQUATIONS OF MOTION

In the classical trajectory approach, the motion of each atom is calculated by numerically solving the classical differential equations of motion, either second-order with respect to time in the positions (Newton law), or equivalently, first-order with respect to time in both the positions and the momenta (Hamilton equations). The most common is the use of the classical Hamilton equations. The classical Hamiltonian for an N-atom system is given by:

$$H(q_i,p_i) = \sum_{i=1}^{N} \frac{p_i^2}{2m_i} + V(q_i) \tag{5.1}$$

where the first term is the kinetic energy that depends on the momenta p_i, and the second term represents the potential energy and depends on the coordinates q_i. The positions and momenta obey the Hamilton equations which are given by:

$$\frac{dq_i}{dt} \equiv \dot{q}_i = \frac{\partial H(q_i,p_i)}{\partial p_i} = \frac{\partial T(p_i)}{\partial p_i} \tag{5.2}$$

$$\frac{dp_i}{dt} \equiv \dot{p}_i = -\frac{\partial H(q_i,p_i)}{\partial q_i} = -\frac{\partial V(q_i)}{\partial q_i} \tag{5.3}$$

where q_i and p_i represents all coordinates and momenta of the system, that is:

$$q_i = (x_1, y_1, z_1 \dots x_N, y_N, z_N) \tag{5.4}$$

$$p_i = \left(p_{x_1}, p_{y_1}, p_{z_1} \dots p_{x_N}, p_{y_N}, p_{z_N}\right) \tag{5.5}$$

In general, the potential energy is expressed as a function of interatomic distances $V(R)$ instead of Cartesian coordinates, therefore the chain rule must appear for solving the Hamilton equations. For instance, suppose we have a

diatomic system formed by atoms i and j whose interaction is described by a stretching harmonic potential as

$$V_{ij}\left(R_{ij}\right) = \frac{1}{2}k\left(R_0 - R_{ij}\right)^2 \tag{5.6}$$

where k is the stretching force constant, R_0 is the equilibrium distance between the atoms and the interatomic distance R_{ij} is given by

$$R_{ij} = \sqrt{\left(x_i - x_j\right)^2 + \left(y_i - y_j\right)^2 + \left(z_i - z_j\right)^2} \tag{5.7}$$

For this diatomic system, the term of equation 5.3 corresponding to x_i can be written as:

$$\frac{dp_{x_i}}{dt} = -\frac{\partial V(q_i)}{\partial x_i} = -\frac{\partial V\left(R_{ij}\right)}{\partial R_{ij}}\frac{\partial R_{ij}}{\partial x_i} \tag{5.8}$$

with

$$\frac{\partial V\left(R_{ij}\right)}{\partial R_{ij}} = k\left(R_0 - R_{ij}\right) \tag{5.9}$$

and

$$\frac{\partial R_{ij}}{\partial x_i} = \frac{x_i - x_j}{R_{ij}} \tag{5.10}$$

Equations 5.2 and 5.3 enable us to calculate the change in position and momentum along each coordinate. By taking small time steps and integrating these equations numerically, we can know the trajectory of the system at any time. When the trajectory is completed, the final values of coordinates and momenta are transformed into properties of the system. Next, the most common numerical methods are discussed.

3. NUMERICAL METHODS

The Hamilton equations are first-order ordinary differential equations with the general form

$$\frac{dy}{dx} = f(x, y) \tag{5.11}$$

This means that variation of the dependent variable y with respect to the independent variable x depends on a function f that, in turn, depends on x and y. In other words, the time variation of coordinates and momenta depends on the Hamiltonian which, in turn, depends on the coordinates and the momenta.

Numerical resolution of an equation as 5.11 allows to calculate the value of y_{i+1} given the value of previous steps y_i. Therefore, the starting of the resolution requires to know the initial value y_0 at x_0. The selection of these initial conditions will be explained in the next Section.

The two most common categories of numerical methods[32-34] for initial-value problems are one-step and multistep methods. One-step methods permit the calculation of y_{i+1} given the value of the previous step y_i; in general these methods are called Runge-Kutta techniques. On the other hand, multistep methods require more than one value of y from previous steps; since these methods needs several previous values of y, they are non-self-starting because, at the beginning of the trajectory, the only known value is y_0.

3.1 Runge-Kutta methods

One-step methods calculate a new value y_{i+1} from the previous value y_i according to the expression

$$y_{i+1} = y_i + \phi h \tag{5.12}$$

where ϕ is the slope and h is the step size, that is, the variation of the variable x between two consecutive steps. This formula can be applied step by step to compute the whole trajectory of the solution. The only difference among different one-step methods is the manner in which the slope is estimated.

i. Euler method

The simplest method takes the slope at the beginning of the interval as an approximation of the average slope in the whole interval. In this approach, called Euler or point slope method, the first derivative provides a direct estimate of the slope at x_i:

$$\phi = \left(\frac{dy}{dx}\right)_i = f(x_i, y_i) \tag{5.13}$$

where the second equality of this equation comes from equation 5.11. Substitution of equation 5.13 into equation 5.12 drives to:

$$y_{i+1} = y_i + f(x_i, y_i)h \tag{5.14}$$

This formula computes a new value y_{i+1} using the slope, which is equal to the first derivative at the original value of x_i, to extrapolate linearly over the step size h as Figure 5.1 shows.

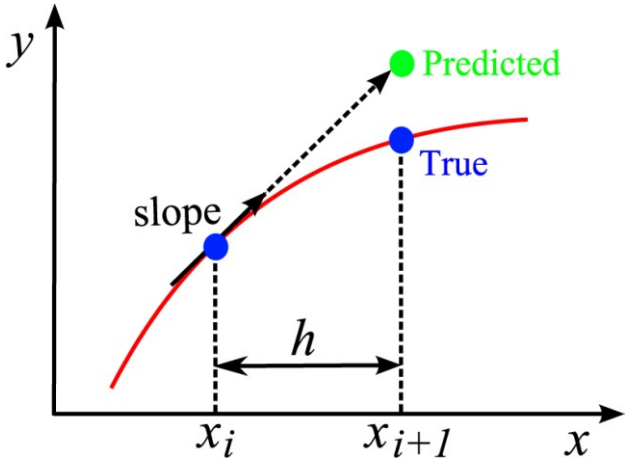

Figure 5.1: Euler method.

During the numerical integration, the error caused by the nature of the technique is called truncation error. This error is composed of two parts, the local truncation error that results from an application of the method in a single step, and the propagated truncation error that results from the approximations produced in the previous steps. The sum of the two errors is the global truncation error. The local truncation error can be analyzed as follows. The value of y_{i+1} can be represented exactly by a Taylor expansion about the previous value of y_i at x_i as

$$y_{i+1}^t = y_i + y_i^{'}h + \frac{y_i^{''}}{2!}h^2 + \cdots + \frac{y_i^{(n)}}{n!}h^n + \cdots \tag{5.15}$$

where the superscript t indicates that we are computed the true value of y_{i+1}, h is the step size $x_{i+1} - x_i$, $y_i^{'}$ is the first derivative of y, $y_i^{''}$ is the second derivative and so on. If the Taylor expansion is truncated by the nth term, equation 5.15 turns into

$$y_{i+1}^t = y_i + y_i^{'}h + \frac{y_i^{''}}{2!}h^2 + \cdots + \frac{y_i^{(n)}}{n!}h^n + R_n \tag{5.16}$$

where R_n is the error due to the truncation and is defined as

$$R_n = \frac{y^{(n+1)}(\xi)}{(n+1)!}h^{n+1} \tag{5.17}$$

where the $(n+1)$th-order derivative is evaluated at ξ which lies somewhere in the interval from x_i to x_{i+1}. An alternative form of equation 5.16 can be developed by replacing equation 5.11 into equation 5.16 to yield

$$y_{i+1}^{t} = y_i + f(x_i, y_i)h + \frac{f^{'}(x_i, y_i)}{2!}h^2 + \cdots + \frac{f^{(n-1)}(x_i, y_i)}{n!}h^n + O(h^{n+1}) \tag{5.18}$$

where $O(h^{n+1})$ indicates that the local truncation error R_n is proportional to the step size to the $(n+1)$th power.

By comparing equations 5.18 and 5.14, it can be seen that Euler method corresponds to the Taylor series up to the term $f(x_i, y_i)h$. The local truncation error in Euler method is attributable to the remaining terms in the Taylor series expansion that were not included in equation 5.14. Subtracting equation 5.14 from equation 5.18 yields

$$E_t = \frac{f^{'}(x_i, y_i)}{2!}h^2 + \cdots + \frac{f^{(n-1)}(x_i, y_i)}{n!}h^n + O(h^{n+1}) \tag{5.19}$$

where E_t is the true local truncation error. For small values of the step size h, the terms of equation 5.19 usually decreases as the order increases, and the error is often represented by the first term:

$$E_a = \frac{f^{'}(x_i, y_i)}{2!}h^2 \tag{5.20}$$

where E_a is the approximate local truncation error. Usually, equation 5.20 is written in a simpler way by

$$E_a = O(h^2) \tag{5.21}$$

indicating that the local truncation error is proportional to the square of the step size. It also can be demonstrated that the global truncation error is $O(h)$, that is, it is proportional to the step size. Therefore the error can be reduced by decreasing the step size, and in the particular case in which the exact solution of the differential equation is linear, the Euler method is error-free since for a straight line, the second and higher order derivatives in equation 5.18 are zero.

Euler method is referred to as a first-order method because it uses straight-line segments to approximate the solution. It should also be noted that this general pattern holds for the higher-order one-step methods described below. That is, an nth-order method will yield error-free solutions if the exact solution is an nth-order polynomial. Moreover, the local truncation error will be $O(h^{n+1})$ and the global truncation error $O(h^n)$.

ii. Improvements of Euler method

An important source of error in the Euler method is that the derivative at the beginning of the interval h is assumed to apply across the entire interval. Two simple modifications are available to overcome this shortcoming. The first improvement consists in estimating two derivatives for the interval, one at the initial point and another at the end point. Then, the two derivatives are averaged to obtain an improved slope for the entire interval. This approach, called **Heun method**, is depicted in Figure 5.2.

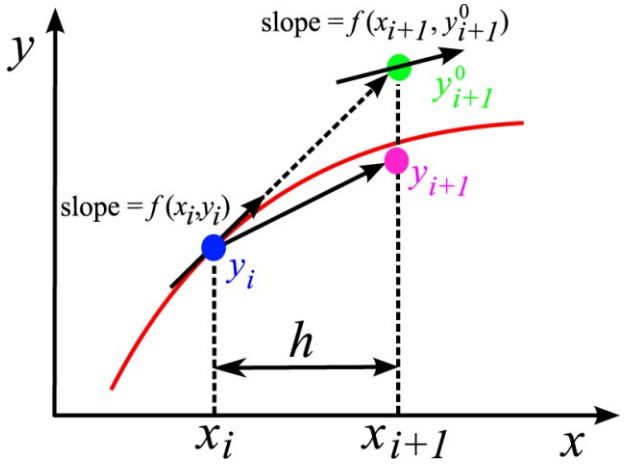

Figure 5.2: Heun method.

The slope at the beginning of the interval is calculated by Euler method (equation 5.13):

$$y_i^{'} = f(x_i, y_i) \tag{5.13}$$

Then, the slope is used to extrapolate linearly to y_{i+1}:

$$y_{i+1}^0 = y_i + f(x_i, y_i)h \tag{5.22}$$

The standard Euler method stops at this point. However, in the Heun method this value of y_{i+1}^0 is only an intermediate prediction, that is why we use the superscript 0. Equation 5.22 is called predictor equation. Now, with the estimate of y_{i+1}^0, we can calculate an estimated slope at the end of the interval:

$$y_{i+1}^{'} = f\left(x_{i+1}, y_{i+1}^0\right) \tag{5.23}$$

Thus, the two slopes given by equations 5.13 and 5.23 can be combined to obtain an average slope for the entire interval:

$$\bar{y}' = \frac{y_i' + y_{i+1}'}{2} = \frac{f(x_i, y_i) + f\left(x_{i+1}, y_{i+1}^0\right)}{2} \tag{5.24}$$

This average slope is then used to extrapolate linearly from y_i to y_{i+1} using the Euler method:

$$y_{i+1} = y_i + \frac{f(x_i, y_i) + f\left(x_{i+1}, y_{i+1}^0\right)}{2} h \tag{5.25}$$

Equation 5.25 is called corrector equation.

The Heun method is a predictor-corrector approach. All the multistep methods which will be discussed below are of this type. These methods are represented succinctly by the predictor and corrector equations; in the case of the Heun method the equations are the followings:

Predictor $$y_{i+1}^0 = y_i + f(x_i, y_i)h \tag{5.22}$$

Corrector $$y_{i+1} = y_i + \frac{f(x_i, y_i) + f\left(x_{i+1}, y_{i+1}^0\right)}{2} h \tag{5.25}$$

Note that y_{i+1} appears on both sides of the equal sign in equation 5.25, therefore, an iterative process can be performed to improve the estimate of y_{i+1}.

The local and global truncation error are $O(h^3)$ and $O(h^2)$, respectively. This means that decreasing the step size the error decreases faster than for the Euler method.

Another simple modification of the Euler approach is the so-called **midpoint method**. This technique uses the Euler method to predict a value of y at the midpoint of the interval h:

$$y_{i+1/2} = y_i + f(x_i, y_i)\frac{h}{2} \tag{5.26}$$

Then, this predicted value is used to calculate a slope at the midpoint:

$$y_{i+1/2}' = f\left(x_{i+1/2}, y_{i+1/2}\right) \tag{5.27}$$

The slope obtained in equation 5.27 is assumed to be a valid approximation of the average slope for the entire interval, and then, this slope is used to extrapolate linearly from y_i to y_{i+1}:

$$y_{i+1} = y_i + f\left(x_{i+1/2}, y_{i+1/2}\right)h \tag{5.28}$$

The local and global errors of the midpoint method are $O(h^3)$ and $O(h^2)$, respectively. Therefore, both midpoint and Heun methods are of similar accuracy, and both are better than the conventional Euler approach, but they require more computational effort to determine the slope. Since the global

truncation errors are $O(h^2)$, midpoint and Heun methods are second-order methods as will be explained later.

The Euler technique and its improvements are a particular case of the one-step general approaches called Runge-Kutta methods.

iii. Runge-Kutta methods

Runge-Kutta (RK) methods achieve the accuracy of a Taylor series approach without the evaluation of higher derivatives. In general, they can be expressed by a generalized form of equation 5.12:

$$y_{i+1} = y_i + \phi(x_i, y_i, h)h \tag{5.29}$$

where $\phi(x_i, y_i, h)$ is called increment function, which can be interpreted as a representative slope over the interval h. The increment function is defined as

$$\phi(x_i, y_i, h) = a_1 k_1 + a_2 k_2 + \cdots + a_n k_n \tag{5.30}$$

where the a's are constants and the k's are given by:

$$k_1 = f(x_i, y_i) \tag{5.31}$$

$$k_2 = f(x_i + p_1 h, y_i + q_{11} k_1 h) \tag{5.32}$$

$$k_3 = f(x_i + p_2 h, y_i + q_{21} k_1 h + q_{22} k_2 h) \tag{5.33}$$

...

$$k_n = f\big(x_i + p_{n-1} h, y_i + q_{n-1,1} k_1 h + q_{n-1,2} k_2 h + \cdots + q_{n-1,n-1} k_{n-1} h\big) \tag{5.34}$$

where the p's and the q's are constants. Note that the k's are recurrence relationship, that is k_1 appears in the equation for k_2, which appears in the equation for k_3, and so forth.

There exist different RK methods depending on the number of terms in the increment function as specified by n. Note that the first-order RK method with $n = 1$ is the Euler method. Once n is chosen, values for the a's, p's and q's are evaluated by setting equation 5.29 to terms in a Taylor series expansion. As seen above, for an nth-order RK method the local error is $O(h^{n+1})$ and the global error is $O(h^n)$, that is, increasing the number of terms in the increment function (equation 5.30) yields to an improvement of the method. Now, the most common RK approaches will be discussed.

The **second-order RK method** follows the equation

$$y_{i+1} = y_i + (a_1 k_1 + a_2 k_2)h \tag{5.35}$$

where

$$k_1 = f(x_i, y_i) \tag{5.36}$$

$$k_2 = f(x_i + p_1 h, y_i + q_{11} k_1 h) \tag{5.37}$$

Values for a_1, a_2, p_1 and q_{11} are evaluated by setting equation 5.35 to a Taylor expansion to the second-order term. By doing this (it is not developed here) one obtains:

$$a_1 + a_2 = 1 \tag{5.38}$$

$$a_2 p_1 = \frac{1}{2} \tag{5.39}$$

$$a_2 q_{11} = \frac{1}{2} \tag{5.40}$$

Since we have three equations with four unknowns, we must specify a value for one of the unknowns, for instance for a_2, and then calculate the other three. Because one can choose an infinite number of values for a_2, there are an infinite number of second-order RK methods. Next, the most frequently used are shown.

If a_2 is assumed to be $1/2$, equations 5.38-5.40 can be solved yielding $a_1 = 1/2$ and $p_1 = q_{11} = 1$. Replacing this parameters into equations 5.35-5.37 one gets

$$y_{i+1} = y_i + \left(\frac{1}{2}k_1 + \frac{1}{2}k_2\right)h \tag{5.41}$$

where

$$k_1 = f(x_i, y_i) \tag{5.42}$$

$$k_2 = f(x_i + h, y_i + k_1 h) \tag{5.43}$$

Note that k_1 is the slope at the beginning of the interval and k_2 is the slope at the end of the interval. Therefore, this second-order RK method is the **Heun approach** seen above.

If a_2 is assumed to be 1, then $a_1 = 0$ and $p_1 = q_{11} = 1/2$ and equations 5.35-5.37 become

$$y_{i+1} = y_i + k_2 h \tag{5.44}$$

where

$$k_1 = f(x_i, y_i) \tag{5.45}$$

$$k_2 = f\left(x_i + \frac{1}{2}h, y_i + \frac{1}{2}k_1 h\right) \tag{5.46}$$

with k_2 being the slope at the midpoint of the interval h, therefore, this is the **midpoint method**.

Another very common approach is the **Ralston method** which arises when a_2 is set to $2/3$ and consequently $a_1 = 1/3$ and $p_1 = q_{11} = 3/4$. The equations for this method are the following:

$$y_{i+1} = y_i + \left(\frac{1}{3}k_1 + \frac{2}{3}k_2\right)h \tag{5.47}$$

where

$$k_1 = f(x_i, y_i) \tag{5.48}$$

$$k_2 = f\left(x_i + \frac{3}{4}h, y_i + \frac{3}{4}k_1 h\right) \tag{5.49}$$

Third-order RK methods are defined for $n = 3$ in equation 5.30. One common version of this approach is

$$y_{i+1} = y_i + \frac{1}{6}(k_1 + 4k_2 + k_3)h \tag{5.50}$$

with

$$k_1 = f(x_i, y_i) \tag{5.51}$$

$$k_2 = f\left(x_i + \frac{1}{2}h, y_i + \frac{1}{2}k_1 h\right) \tag{5.52}$$

$$k_3 = f(x_i + h, y_i - k_1 h + 2k_2 h) \tag{5.53}$$

The most popular one-step approximations are the fourth-order RK methods. As with the second and third-order approach, there are an infinite number of versions. The most commonly used is the so-called **classical fourth-order RK method** and it is given by

$$y_{i+1} = y_i + \frac{1}{6}(k_1 + 2k_2 + 2k_3 + k_4)h \tag{5.54}$$

where

$$k_1 = f(x_i, y_i) \tag{5.55}$$

$$k_2 = f\left(x_i + \frac{1}{2}h, y_i + \frac{1}{2}k_1 h\right) \tag{5.56}$$

$$k_3 = f\left(x_i + \frac{1}{2}h, y_i + \frac{1}{2}k_2 h\right) \tag{5.57}$$

$$k_4 = f(x_i + h, y_i + k_3 h) \tag{5.58}$$

The RK methods estimate several slopes, represented by the k's, in different regions of the interval and then, use an averaged value of these to arrive at the improved slope. For instance, the classical fourth-order RK method calculates one slope k_1 at the beginning of the interval, then calculates the slope k_2 at the midpoint of the interval from k_1 and, with the values of k_1 and k_2, an improved slope k_3 is determined at the midpoint. Then, one slope at the end of the interval k_4 is computed using the values of the previous slopes. Finally, these slopes are employed in equation 5.54 with different weights to compute the final improved slope $\phi = \frac{1}{6}(k_1 + 2k_2 + 2k_3 + k_4)$. This procedure is depicted in Figure 5.3.

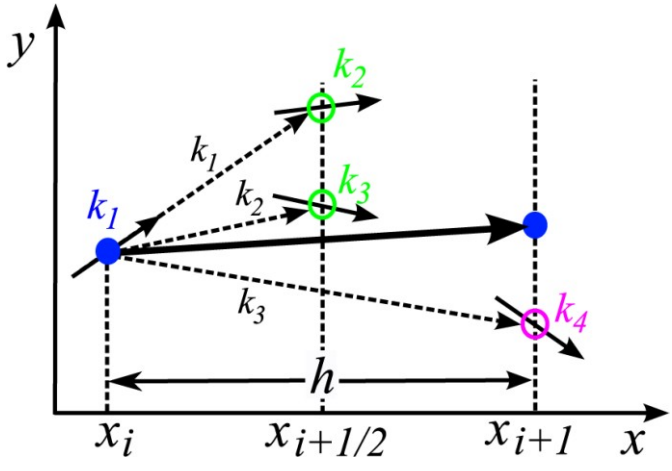

Figure 5.3: Fourth-order Runge-Kutta method.

Another fourth-order approach is the **Runge-Kutta-Gill method** which follows the equations:

$$y_{i+1} = y_i + \frac{1}{6}\left(k_1 + \left(2 - \sqrt{2}\right)k_2 + \left(2 + \sqrt{2}\right)k_3 + k_4\right)h \qquad (5.59)$$

where

$$k_1 = f(x_i, y_i) \qquad (5.60)$$

$$k_2 = f\left(x_i + \frac{1}{2}h, y_i + \frac{1}{2}k_1 h\right) \qquad (5.61)$$

$$k_3 = f\left(x_i + \frac{1}{2}h, y_i + \frac{1}{2}\left(-1 + \sqrt{2}\right)k_1 h + \left(1 - \frac{1}{2}\sqrt{2}\right)k_2 h\right) \qquad (5.62)$$

$$k_4 = f\left(x_i + h, y_i - \frac{1}{2}\sqrt{2}k_2 h + \left(1 + \frac{1}{2}\sqrt{2}\right)k_3 h\right) \qquad (5.63)$$

Higher-order RK formulas are available, but in general, beyond fourth-order methods the gain in accuracy is offset by the added computational effort and complexity. This effort is equivalent to the number of function evaluations required to obtain the final result, as in

$$Effort = n_f \frac{b-a}{h} \tag{5.64}$$

where n_f is the number of function evaluations, for instance, in the fourth-order RK method this quantity is equal to 4 because the method must calculate 4 slopes to obtain the value of y_{i+1}. For orders ≤ 4, n_f is equal to the order of the method, but for orders higher than 4, the number of evaluations is larger than the order of the method. The quantity $b-a$ is the total region over the equation is been integrated and h is the size step.

3.2 Multistep methods

The one-step methods discussed above utilize one point y_i to predict the value of the next point y_{i+1}. On the other side, multistep methods are based on the computation of the current point from information of several previous points. Figure 5.4 displays graphically the difference between one-step and multistep methods.

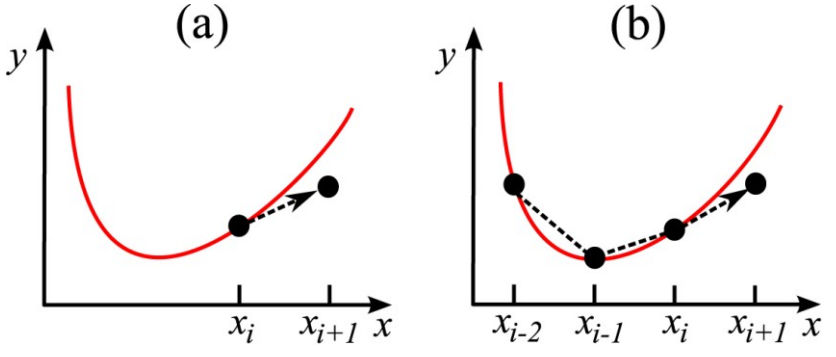

Figure 5.4: (a) One-step and (b) multistep methods.

In general, multistep methods can be derived from two ways. Here, a general description of these two ways will be commented but without going into detail. The first manner to develop multistep approaches is based on the Newton-Cotes formulas which arise from equation 5.11:

$$\frac{dy}{dx} = f(x,y) \tag{5.11}$$

Reorganization and integration of this equation drive to

$$\int_{y_i-n}^{y_{i+1}} dy = \int_{x_i-n}^{x_{i+1}} f(x,y)dx \tag{5.65}$$

and integrating the left side, we obtain one of the Newton-Cotes equations:

$$y_{i+1} = y_{i-n} + \int_{x_i-n}^{x_{i+1}} f(x,y)dx \tag{5.66}$$

One of simplest multistep methods which are derived from equation 5.66 is a correction of the one-step Heun method. As seen above, the Heun method uses the Euler formula as a predictor, and then, improves this result by a corrector equation:

Predictor $$y_{i+1}^0 = y_i + f(x_i, y_i)h \tag{5.22}$$

Corrector $$y_{i+1} = y_i + \frac{f(x_i, y_i) + f\left(x_{i+1}, y_{i+1}^0\right)}{2} h \tag{5.25}$$

The predictor and the corrector have local truncation errors of $O(h^2)$ and $O(h^3)$, respectively. Therefore the predictor has the greatest error, and one way to improve the accuracy of the method is to develop a predictor that has a local error of $O(h^3)$. This is achieved by using extra information from a previous point y_{i-1} in equation 5.22:

$$y_{i+1}^0 = y_{i-1} + f(x_i, y_i)2h \tag{5.67}$$

Two important features emerge from equation 5.67. Firstly, the size step increases twice but the error decreases to $O(h^3)$ because of the use of the point y_{i-1}. Secondly, we need the point y_{i-1} to compute the value of y_{i+1}^0, but the value of y_{i-1} is not available at the beginning of the integration. Because of this fact, equations 5.67 and 5.25 are called the **non-self-starting Heun method**.

The second manner to obtain a multistep integration method is based on the Adams formulas. These formulas can be derived in a variety of ways. One technique is to write a Taylor series expansion around x_i:

$$y_{i+1} = y_i + f_i h + \frac{f_i^{'}}{2!} h^2 + \frac{f_i^{''}}{3!} + \cdots \tag{5.68}$$

From this equation, the **Adams-Bashforth method** can be developed, whose formula has the form

$$y_{i+1} = y_i + h \sum_{k=0}^{n-1} \beta_k f_{i-k} + O(h^{n+1}) \tag{5.69}$$

where n is the order of the method and $O(h^{n+1})$ means that the local truncation error is proportional to the size step to the $(n+1)$th power.

Other similar approach is the so-called **Adams-Moulton method** which follows the formula

$$y_{i+1} = y_i + h\sum_{k=0}^{n-1} \beta_k f_{i+1-k} + O(h^{n+1}) \tag{5.70}$$

The only but important difference between equations 5.69 and 5.70 is the subscript in the function f. In the Adams-Bashforth method the subscript $i-k$ indicates that we are taking several previous values of the function f up to the point i, that is, the point just prior to the value that is being evaluated. However, in the Adams-Moulton formula, the subscript $i+1-k$ indicates that we are using the own value that is being evaluated (when $k=0$); this means that the process is iterative and, therefore, its accuracy will be better but at the expense of an increase of the computational effort. The coefficients β_k of equations 5.69 and 5.70 for different orders are collected in Tables 5.1 and 5.2, respectively.

Table 5.1: Coefficients for Adams-Bashforth formula.

Order	β_0	β_1	β_2	β_3	β_4	β_5
1	1					
2	3/2	-1/2				
3	23/12	-16/12	5/12			
4	55/24	-59/24	37/24	-9/24		
5	1901/720	-2774/720	2616/720	-1274/720	251/720	
6	4277/1440	-7923/1440	9982/1440	-7298/1440	2877/1440	-475/1440

The multistep formulas are usually applied in tandem as predictor-corrector methods. The method used to integrate the equations of motion throughout this thesis was the sixth-order Adams-Bashforth formula as the predictor:

$$y_{i+1}^0 = y_i + h\left(\frac{4277}{1440}f_i - \frac{7923}{1440}f_{i-1} + \frac{9982}{1440}f_{i-2} - \frac{7298}{1440}f_{i-3} + \frac{2877}{1440}f_{i-4} - \frac{475}{1440}f_{i-5}\right) \tag{5.71}$$

and the sixth-order Adams-Moulton formula as the corrector:

$$y_{i+1} = y_i + h\left(\frac{475}{1440}f_{i+1} + \frac{1427}{1440}f_i - \frac{798}{1440}f_{i-1} + \frac{482}{1440}f_{i-2} - \frac{173}{1440}f_{i-3} + \frac{27}{1440}f_{i-4}\right) \quad (5.72)$$

Multistep methods are, in general, better than one-step methods, but they are non-self-starting, therefore, the first steps of the integration must be done by one-step method; in our simulations the Runge-Kutta-Gill method was used for these first steps. Table 5.3 summarizes the methods discussed in this Section.

Table 5.2: Coefficients for Adams-Moulton formula.

Order	β_0	β_1	β_2	β_3	β_4	β_5
2	1/2	1/2				
3	5/12	8/12	-1/12			
4	9/24	19/24	-5/24	1/24		
5	251/720	646/720	-264/720	106/720	-19/720	
6	475/1440	1427/1440	-798/1440	482/1440	-173/1440	27/1440

Table 5.3: Comparison of different numerical methods.

Method	Type	Local error	Global error	P/C*
Euler	One-step	$O(h^2)$	$O(h)$	No
Heun	One-step	$O(h^3)$	$O(h^2)$	Yes
Midpoint	One-step	$O(h^3)$	$O(h^2)$	No
4th-order Runge-Kutta	One-step	$O(h^5)$	$O(h^4)$	No
6th-order Adams-Bashforth-Moulton	Multistep	$O(h^7)$	$O(h^6)$	Yes

*Predictor-corrector method.

4. SAMPLING OF INITIAL CONDITIONS

Before the integration of the equations of motion, the initial coordinates and momenta must be selected.[4] This initial sampling depends on the type of process that is being simulated, the type of coordinates of the system, the Hamiltonian that describes the system, the introduction of quantum

effects and the number of atoms and the geometry of the molecules that are colliding.

In this thesis, inelastic collisions of polyatomic molecules with an F-SAM surface are the process of interest. Therefore, we focus our attention on the sampling of initial condition only for this sort of event, and in particular, Monte Carlo selection of Cartesian coordinates will be discussed. We split the sampling in three categories: sampling of initial coordinates and momenta for the polyatomic molecule, for the surface and sampling of parameters which depend on both the molecule and the surface.

4.1 Polyatomic molecule sampling

The normal-mode and rigid-rotor models were employed for vibrational and rotational degrees of freedom, respectively, for selecting the initial coordinates and momenta of the polyatomic molecule.

The vibrational Hamiltonian for a system of n normal modes is given by

$$H = E_{vib} = \sum_{i=1}^{n} E_i = \sum_{i=1}^{n} \frac{P_i^2}{2} + \frac{\omega_i^2 Q_i^2}{2} \tag{5.73}$$

where the first term is the kinetic energy and the second term is the potential energy. Q_i and P_i are the normal-mode coordinates and momenta, ω_i is the angular frequency and E_i represents the vibrational energy of each normal mode.

In normal-mode sampling specific energies E_i or quantum numbers v_i are assigned to each normal-mode according to:

$$E_i = \left(v_i + \frac{1}{2}\right)\hbar\omega_i \tag{5.74}$$

where the angular frequency ω_i is related with the vibrational frequency ν_i by $\omega_i = 2\pi\nu_i$. Once the vibrational energy is selected, normal-mode coordinates Q_i and momenta P_i are computed by:

$$Q_i = A_i \cos(\omega_i t) \tag{5.75}$$

$$P_i = \dot{Q}_i = -A_i \omega_i \sin(\omega_i t) \tag{5.76}$$

where A_i is the amplitude that is given by

$$A_i = \frac{(2E_i)^{1/2}}{\omega_i} \tag{5.77}$$

Since each time has equal probability during a vibrational period, random Q_i and P_i can be selected by

$$Q_i = A_i \cos(2\pi R_i) \tag{5.78}$$

$$P_i = \dot{Q}_i = -A_i\, \omega_i \sin(2\pi R_i) \tag{5.79}$$

with R_i being a random number ranging between 0 and 1.

On the other side, the classical rotational energy is given by

$$E_{rot}\,(j) = \frac{j_x^2}{2I_x} + \frac{j_y^2}{2I_y} + \frac{j_z^2}{2I_z} \tag{5.80}$$

where j is the angular momentum with components j_x, j_y and j_z, and I_x, I_y and I_z are the principal moments of inertia of the molecule. The rotational energy is chosen from a thermal distribution assuming that the molecule is a symmetric top, that is:

$$I_x < I_y = I_z \;\text{ or }\; I_x = I_y < I_z \tag{5.81}$$

The component j_z of the total angular momentum is sampled from its classical Boltzmann distribution:

$$P(j_z) = e^{-j_z^2/(2I_z k_B T)} \tag{5.82}$$

where $P(j_z)$ is generated by the von Neumann rejection technique, and then, j_z is calculated. The rejection procedure is performed as follows. When a random number is generated, the probability of obtaining a value x_i is given by

$$P(x_i) = \left(1 - \sum_{j=1}^{i-1} x_j^2 - x_i^2\right)^{(2n-i-2)/2} \tag{5.83}$$

This means that the probability of obtaining x_i depends on the values x_j that are being generated previously. From equation 5.83 it is easy to see that the most probable value of x_i is zero, for which

$$P^0(x_i) = \left(1 - \sum_{j=1}^{i-1} x_j^2\right)^{(2n-i-2)/2} \tag{5.84}$$

In the first step, the first value of x_i, that is x_1, is generated between 0 and 1, and this value is accepted if

$$\frac{P(x_1)}{P^0(x_1)} > R \tag{5.85}$$

where R is other random number. If x_1 does not fulfill the condition 5.85, new x_1 and R are generated. This process is repeated until x_1 is accepted. In subsequent steps the procedure is the same except that x_i is sampled in the range $0 < x_i < r_i$, with r_i given by

$$r_i = \left(1 - \sum_{j=1}^{i-1} x_j^2\right)^{1/2} \tag{5.86}$$

The total angular momentum j is sampled by the cumulative distribution function formula

$$j = (j_z^2 - 2I_x k_B T \ln(1-R))^{1/2} \tag{5.87}$$

with R being a random number. The components j_x and j_y are found from the next equations:

$$j_x = (j^2 - j_z^2)^{1/2} \sin(2\pi R) \tag{5.88}$$

$$j_y = (j^2 - j_z^2)^{1/2} \cos(2\pi R) \tag{5.89}$$

For linear molecules, as CO_2 (Chapters 6, 7 and 8), NO (Chapter 9) and $SiNCS^+$ (Chapter 11) , the x-axis defines the molecular axis, and therefore $j_x = 0$, the total angular momentum j is sampled from equation 5.87, and the components j_y and j_z are given by

$$j_y = j \sin(2\pi R) \tag{5.90}$$

$$j_z = j \cos(2\pi R) \tag{5.91}$$

Once normal-mode coordinates Q_i and momenta P_i were selected randomly, these must be transformed to Cartesian coordinates q_i and momenta p_i to integrate the equations of motion. The relations between normal and Cartesian coordinates and momenta are

$$q = q_0 + M^{-1/2} L Q \tag{5.92}$$

$$p = M^{1/2} L P \tag{5.93}$$

where q and p are the matrixes of Cartesian coordinates and momenta, Q and P are the matrixes of normal-mode coordinates and momenta, q_0 is the matrix of equilibrium Cartesian coordinates, M is a diagonal matrix whose elements are the atomic masses, and L is the matrix of normal-mode eigenvectors which arises by diagonalizing the mass-weighted Cartesian force constant matrix B:[35]

$$BL = L\Lambda \tag{5.94}$$

where Λ is the diagonal matrix which contains the eigenvalues λ_i that are related to the vibrational frequencies ν_i by

$$\nu_i = \frac{\sqrt{\lambda_i}}{2\pi} \tag{5.95}$$

Since normal modes are approximate, a spurious angular momentum j_s arises from the Cartesian/nomal coordinate transformation. This spurious angular momentum for a molecule of N atoms is given by

$$j_s = \sum_{i=1}^{N} r_i \times m_i \dot{r}_i \tag{5.96}$$

where m_i is the mass of the ith atom and r_i its position vector. This spurious angular momentum must be taken into account when the desired angular momentum j_0 is added to the molecule:

$$j_0 = j + j_s \tag{5.97}$$

Now, the internal energy E of the molecule is calculated with the Cartesian coordinates q_i and momenta p_i and compared with the intended energy E^0.

$$E = T + V \tag{5.98}$$

where

$$T = \frac{1}{2} M \tilde{q} \dot{q} \tag{5.99}$$

and the potential energy V is determined from the potential analytical function used for the simulation. If they do not agree within some acceptance criterion, the Cartesian coordinates and momenta are scaled according to

$$q_i^{'} = q_i^0 + \left(q_i - q_i^0\right)\left(\frac{E^0}{E}\right)^{1/2} \tag{5.100}$$

$$p_i^{'} = p_i \left(\frac{E^0}{E}\right)^{1/2} \tag{5.101}$$

where q_i^0 are the equilibrium Cartesian coordinates and $q_i^{'}$ and $p_i^{'}$ are the scaled Cartesian coordinates and momenta whose internal energy agrees with the intended internal energy E^0.

Another way of selecting the energy of the normal modes is the local-mode sampling, in which an individual normal mode is excited. The first step is to choose Cartesian coordinates and momenta, which correspond to the zero-point energy, that is $v_i = 0$. This step is performed as in the normal-mode sampling described above by equations 5.78 and 5.79. Then, a particular bond is excited to a local mode state v by adding more energy to the bond so that the

Einstein-Brillouin-Keller (EBK) semiclassical quantization condition is accomplished:

$$\oint p_r dr = \left(v + \frac{1}{2}\right) h \tag{5.102}$$

This means that the total bond energy given by

$$E_r = \frac{p_r^2}{2\mu} + V_{Morse}(r) \tag{5.103}$$

must be equal to the energy of the quantum level v of a Morse oscillator given by

$$E(v) = \left(v + \frac{1}{2}\right)\hbar\omega - \left(v + \frac{1}{2}\right)^2 \hbar\omega\chi_e \tag{5.104}$$

where p_r is the bond radial momentum given by $p_r = \mu\dot{r}$, with μ and r being the reduced mass and the separation for the two atoms constituting the bond, ω is the harmonic frequency and χ_e is the anharmonic correction. The cyclic integral in equation 5.102 denotes integration over one vibrational period.

For diatomic molecules, as NO in Chapter 9, Cartesian coordinates and momenta can be chosen according to given vibrational and rotational quantum numbers v and J. The vibration-rotational energy E_{vr} of a diatomic molecule is given by

$$E_{vr} = \frac{p_r^2}{2\mu} + \frac{J(J+1)\hbar^2}{2\mu r^2} + V(r) \tag{5.105}$$

Cartesian coordinates and momenta can be selected from this energy; a more detailed description can be found in the reference 4.

4.2 Surface sampling

The initial coordinates and momenta of the F-SAM surface may be selected using the procedures explained above for polyatomic molecules. But, in general, if the surface has low force constants, and therefore low frequencies, its normal modes may displace far from the equilibrium position, and the sampling techniques seen above, that are based on the harmonic oscillator, are not suitable for choosing the initial conditions.

In these cases, the initial conditions can be selected from a molecular dynamics simulation[36,37] in which the velocities are scaled to obtain the structure corresponding to the temperature of interest. Initially, the velocities of the surface atoms are selected from the Maxwell-Boltzmann distribution:

$$P(v_i) = v_i^2 e^{-\frac{m_i v_i^2}{2k_B T_s}} \tag{5.106}$$

where T_s is the surface temperature and m_i and v_i are the masses and velocities of each atom. Once the initial coordinates and momenta are known, a molecular dynamics simulation is performed in order to the surface achieves a structure according to the T_s temperature. During the dynamics the velocities are scaled to correct the deviations from the equilibrium structure:

$$v_i^{new} = v_i^{old} \left(\frac{T_s}{T_a}\right)^{1/2} \tag{5.107}$$

where v_i^{new} is the scaled velocity for the ith atom, v_i^{old} is the velocity atom before scaling, T_s is the desired surface temperature and T_a is the actual temperature. The coordinates and momenta can be calculated at each step from the atom velocities.

The F-SAM surface used in the simulations of this thesis is formed by 1475 atoms. The size of the surface for a more realistic model, which tries to mimic a bulk material, should be composed by much more atoms (may be the Avogadro number of atoms) to describe a real surface. But performing a simulation with such number of atoms is unworkable and the use of a small model is necessary. Such small systems contain a large number of atoms or molecules that lie on the surface of the system. For instance, for 1000 molecules arranged in a $10 \times 10 \times 10$ cube, no less than 488 molecules appear on the cube faces. The chemical environment of atoms or molecules that appears on the surface of the system is different from that of the molecules staying inside the system. Therefore molecules on the surface will experience different forces from molecules in the bulk. If the objective of the simulation is to describe the behaviour of a bulk system, small models will not be reliable because the number of molecules on the surface and that inside the system is similar to each other, unlike the real system, where most of the atoms are in the bulk.

This uncorrected behaviour can be avoided using periodic boundary conditions (PBC).[36,37] Suppose that the bulk material can be represented by N atoms confined to a volume V. The volume V is called primary cell; it is representative of the bulk material to the extent that the bulk is assumed to be composed of the primary cell surrounded by exact replicas of itself. These replicas are called image cells. Each image cell contains N atoms, which are images of the atoms in the primary cell. Thus the primary cell is imagined to be periodically replicated in all directions to form a macroscopic sample of the substance of interest, so that the positions and momenta of the primary atoms

are also replicated. In our case, the PBC are applied in the x and y directions at which the F-SAM grows, being z the direction normal to the surface.

Now, to discuss how the positions and momenta in image cells are related to those of the atoms in the primary cell, we introduce the following notation. A reference frame is assigned to each cell, and it is located in a corner of the cell. The frame in the primary cell is called primary frame, and the others are image frames. Figure 5.5 shows this situation for 2 dimensions.

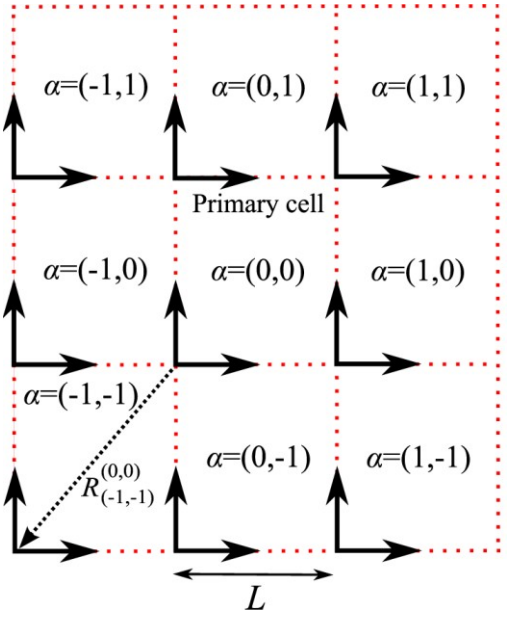

Figure 5.5: PBC for a 2 dimensional system.

In D dimensions each unit cell can be identified by a D-dimensional α vector, called cell translation vector, whose components are either signed integers or zero. For example, the primary cell for 2 dimensions in Figure 5.5 has $\alpha = (0,0)$; the cell located inmediatly to the right has $\alpha = (1,0)$. The origin of a reference frame in any image cell α can be located with respect to the primary frame $(0,0)$ by a vector $R^{\alpha}_{(0,0)}$ where

$$R^{\alpha}_{(0,0)} = L\alpha \tag{5.108}$$

where L is the length of each cell. For instance, the vector $R^{(0,0)}_{(-1,-1)}$ relates the reference frame of the cell $\alpha = (-1,-1)$ with the primary cell as seen in Figure 5.5.

Each image of an atom i occupies the same position with respect to its image frame as atom i occupies with respect to the primary frame, that is:

$$r_{i(0,0)}^{(0,0)} = r_{i(\alpha)}^{(\alpha)} \tag{5.109}$$

Moreover, each image of i has the same momentum as i,

$$p_{i(0,0)}^{(0,0)} = p_{i(\alpha)}^{(\alpha)} \tag{5.110}$$

Cells are separated by open boundaries, that is, atoms and images can freely enter or leave any cell. But the number of atoms in each unit cell is always N because when an atom i leaves the primary cell, an image of i simultaneously enters the primary cell through an opposite cell.

During the simulation we need store only the positions of N atoms in the primary cell. Positions of images can be computed, when needed, by coordinate transformation. Thus, for square unit cells of edge L, an image atom of i in a cell α is located with respect to the primary cell by

$$r_{i(\alpha)}^{(0,0)} = r_{i(\alpha)}^{(\alpha)} + R_{\alpha}^{(0,0)} \tag{5.111}$$

where $r_{i(\alpha)}^{(0,0)}$ is the position of the image of atom i in the image cell α with respect to the primary frame $(0,0)$, $r_{i(\alpha)}^{(\alpha)}$ is the position of the image of i in the image cell α with respect to its reference frame α, and $R_{\alpha}^{(0,0)}$ is a vector which relates the primary frame with the image frame as Figure 5.6 shows.

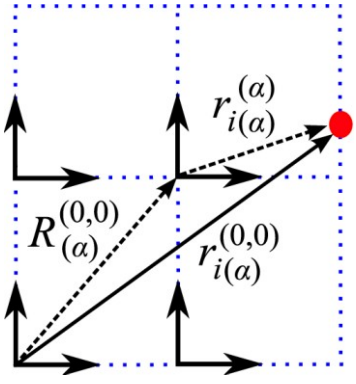

Figure 5.6: Position vector defining an image atom.

Replacing equations 5.109 and 5.108 into equation 5.111 gives

$$r_{i(\alpha)}^{(0,0)} = r_{i(0,0)}^{(0,0)} + L\alpha \tag{5.112}$$

This means that to compute the position $r_{i(\alpha)}^{(0,0)}$ of an image, we need only the position of the atom i in the primary cell $r_{i(0,0)}^{(0,0)}$ and the cell translation vector α.

Once we know how to determine the position of atoms in primary and image cells, the calculation of the potential energy is straightforward. For just N atoms in the primary cell, the pairwise potential energy, called V_{pc}, is

$$V_{pc} = \frac{1}{2}\sum_{i}\sum_{j\neq i} V\left(r_{ij\,(0,0)}^{(0,0)}\right) \tag{5.113}$$

where V is the two-body potential between two molecules or atoms i and j in the primary cell and r_{ij} is the separation between these two particles. The factor of $1/2$ is introduced for counting each interaction only once. Now, if image atoms are taken into account, the potential energy is given by

$$V = \frac{1}{2}\sum_{\alpha}\sum_{i}\sum_{j\neq i} V\left(r_{ij\,(0,0)}^{(0,0)} - \alpha L\right) \tag{5.114}$$

with $V\left(r_{ij\,(0,0)}^{(0,0)} - \alpha L\right)$ being the pairwise potential between all particles of the system in primary and image cells, and $r_{ij} - \alpha L = r_i - \left(r_j + \alpha L\right)$ is the separation between two any particles.

Now consider any one atom m in the primary cell. Its potential energy is

$$V_m = \frac{1}{2}\sum_{\alpha}\sum_{j\neq m} V\left(r_{mj\,(0,0)}^{(0,0)} - \alpha L\right) \tag{5.115}$$

and any image of atom m has the same potential energy. For example, if we consider the image atom m' having $\alpha = (1,1)$, its potential energy is

$$V_{m'} = \frac{1}{2}\sum_{\alpha}\sum_{j\neq m'} V\left(r_{m'j\,(1,1)}^{(1,1)} - \alpha L\right) \tag{5.116}$$

but according to 5.109 we get

$$V_{m'} = \frac{1}{2}\sum_{\alpha}\sum_{j\neq m'} V\left(r_{mj\,(0,0)}^{(0,0)} - \alpha L\right) \tag{5.117}$$

and therefore

$$V_m = V_{m'} \tag{5.118}$$

This means that the force or the potential energy felt by any image m' is the same as that felt by the primary atom m. Thus, image atoms in image cells follow trajectories that are exact duplicates of those followed by the atoms in the primary cell.

In a system having periodic boundaries, any atom that leaves the primary cell is replaced by the image that simultaneously enters the primary

cell. For example, if atom i moves from the primary cell to cell α, an image enters the primary cell from image cell $-\alpha$. Thus, the position of atom i is transformed by

$$r_{i(0,0)}^{(0,0)} \Rightarrow r_{i(-\alpha)}^{(0,0)} = r_{i(0,0)}^{(0,0)} - L\alpha \tag{5.119}$$

and according to 5.110 the momentum p_i is unaffected by the translation in position:

$$p_{i(0,0)}^{(0,0)} \Rightarrow p_{i(-\alpha)}^{(0,0)} = p_{i(0,0)}^{(0,0)} \tag{5.120}$$

Equations 5.119 and 5.120 define the periodic boundary conditions.

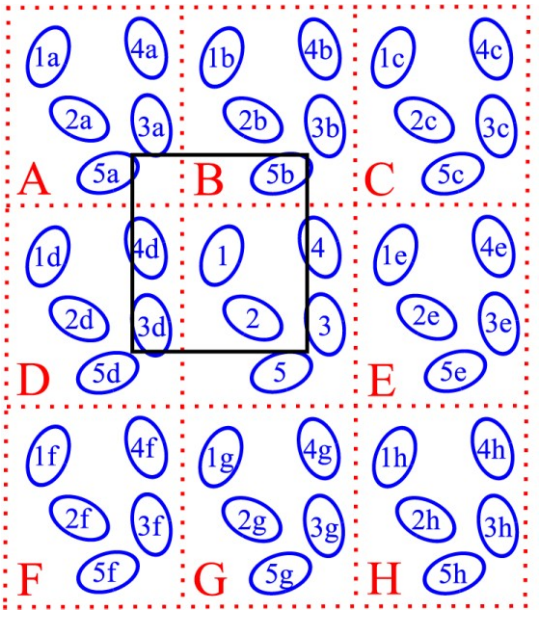

Figure 5.7: PBC for a 2 dimensional system.

The PBC allows us to replicate the primary cell throughout space to form an infinite lattice. The potential energy involving a molecule m can be calculated by equation 5.115, assuming pairwise additivity. But if all possible interactions in the infinite number of cells are included, we have an infinite number of terms in the potential, and of course, they are impossible to calculate in practice. We must make some type of approximation to compute the total potential. In works involved in this thesis the minimum image convention was used;[36,38,39] it works as follows. Consider particle 1 to rest at the center of a region which has the same size and shape as the basic simulation box, as Figure 5.7 shows. Particle 1 interacts with all particles whose centers lie within this region, that is with the closest $N-1$ particles. For example, in Figure 5.7

particle 1 interacts with particles 2, 3d, 4d and 5b. In this approximation, the calculation of the intermolecular potential energy involves $\frac{1}{2}N(N-1)$ two-body terms.

4.3 Gas/surface sampling

Once the initial conditions for the projectile and the surface have been defined, one must chose some parameters which depend on both the gas and the surface. The relative orientation of the gas with respect to the surface is chosen by randomly rotating its axis through Euler angles. Figure 5.8 displays the definition of these angles.

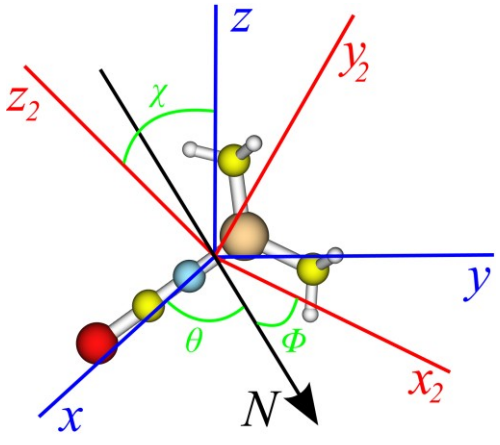

Figure 5.8: Definition of Euler angles.

The initial position of the molecule is defined by the axis x, y and z whose origin is in the center of mass of the molecule. These axis are rotated to define a new axis x_2, y_2 and z_2 which define the new orientation of the molecule. Both set of axis are related by the Euler angles as follows. The vector N is defined as the intersection formed by the planes xy and x_2y_2. θ is the angle formed by the x-axis and the vector N; ϕ is the angle between the x_2-axis and the vector N; and χ is the angle formed by the z-axis and the z_2-axis. These angles θ, ϕ and χ are chosen randomly within the ranges $0 \leq \theta \leq 2\pi$, $0 \leq \phi \leq 2\pi$ and $0 \leq \chi \leq \pi$ to generate a new orientation of coordinates q_{new} from the old orientation of coordinates q_{old}. The relation between new and old coordinates is given by the Euler matrix[36] E as

$$q_{new} = Eq_{old} \tag{5.121}$$

where

$$E = \begin{pmatrix} \cos\theta\cos\phi - \sin\theta\cos\chi\sin\phi & \sin\theta\cos\phi + \cos\theta\cos\chi\sin\phi & \sin\chi\sin\phi \\ -\cos\theta\sin\phi - \sin\theta\cos\chi\cos\phi & -\sin\theta\sin\phi + \cos\theta\cos\chi\cos\phi & \sin\chi\cos\phi \\ \sin\theta\sin\chi & -\cos\theta\sin\chi & \cos\chi \end{pmatrix} \quad (5.122)$$

Once the molecule was oriented one must chose the point where the projectile center of mass is going to collide on the surface. This aiming point A was randomly selected by

$$A = R_1 u + R_2 v \quad (5.123)$$

where R_1 and R_2 are random numbers and u and v are vectors determined from the Cartesian coordinates of the terminal carbon atoms for three chains at a central region of the surface as can be seen in Figure 5.9.

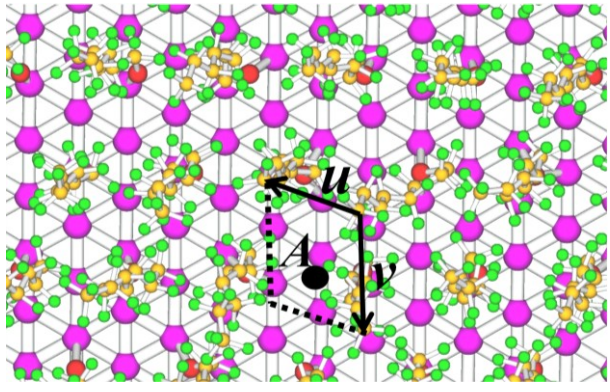

Figure 5.9: Selection of the aiming point.

5. ANALYSIS OF FINAL CONDITIONS

As seen in previous sections, classical trajectory simulations are carried out by selecting initial coordinates and momenta and solving numerically the Hamilton equations of motion. Once the reactive or unreactive process finish or the simulation time elapsed, the result of the trajectory is a set of final coordinates and momenta of the products. One can calculate classically many properties of the system from these final coordinates and momenta.[40] Here, the computation of the most common properties will be discussed, but many others can be calculated as will be seen in subsequent chapters.

Suppose the following process

$$A + B \longrightarrow C + D \quad (5.124)$$

where the products C and D may be different compounds from A and B, or the same species but with different energy as in the unreactive collisions studied throughout this thesis.

The product relative velocity is the difference between the velocities of the centers of mass of molecules C and D. The center of mass position and velocity of product D is given by

$$Q_D = \frac{\sum_{i=1}^{n_d} m_i q_i}{M_D} \tag{5.125}$$

$$\dot{Q}_D = \frac{\sum_{i=1}^{n_d} m_i \dot{q}_i}{M_D} \tag{5.126}$$

where n_D is the number of atoms of product D, m_i and q_i are the mass and the coordinates of each atom and M_d is the total mass of molecule D. The coordinates Q_D denotes any of the three coordinates of the center of mass, that is, X_D, Y_D or Z_D, and q_i denotes any coordinate of atom i, that is, x_i, y_i and z_i. For example, the X component of the center of mass position is computed as

$$X_D = \frac{\sum_{i=1}^{n_d} m_i x_i}{M_D} \tag{5.127}$$

The product relative velocity is the time derivative of the vector R defining the separation between the center of mass of C and D:

$$\begin{aligned} R &= (X_D - X_C)\hat{\imath} + (Y_D - Y_C)\hat{\jmath} + (Z_D - Z_C)\hat{k} \\ &= R_x\hat{\imath} + R_y\hat{\jmath} + R_z\hat{k} \end{aligned} \tag{5.128}$$

and

$$v_{rel} \equiv \dot{R} = \dot{R}_x\hat{\imath} + \dot{R}_y\hat{\jmath} + \dot{R}_z\hat{k} \tag{5.129}$$

with $\hat{\imath}$, $\hat{\jmath}$ and $\hat{k}$ being unit vectors in x, y and z directions. The product relative translational energy is given by

$$E_{rel} = \frac{\mu_{CD}\dot{R} \cdot \dot{R}}{2} \tag{5.130}$$

where μ_{CD} is the reduced mass of CD.

The evaluation of the rotational and vibrational energy requires the coordinates and velocities of each atom in the molecule in the center of mass frame. The coordinates and velocities of the atoms of D in the D center of mass frame, denote by prime, are given by:

$$x_i^{'} = x_i - X_D \tag{5.131}$$

$$\dot{x}_i^{'} = \dot{x}_i - \dot{X}_D \tag{5.132}$$

The internal energy of molecule D is the sum of kinetic energy T_D and potential energy V_D:

$$E_{int,D} = T_D + V_D \tag{5.133}$$

The potential energy is easily determined from the potential energy function used for the simulation, and the kinetic energy is

$$T_D = \sum_{i=1}^{n_d} \frac{m_i\left(\dot{x}_i'^2 + \dot{y}_i'^2 + \dot{z}_i'^2\right)}{2} \tag{5.134}$$

The rotational angular momentum j of the product D is the sum of the angular momenta j_i of the individual atoms of D rotating about the D center of mass:

$$j_D = \sum_{i=1}^{n_D} j_i = j_x\hat{\imath} + j_y\hat{\jmath} + j_z\hat{k} \tag{5.135}$$

The atomic angular momenta j_i are given by

$$j_i = m_i r_i' \times \dot{r}_i' = j_{xi}\hat{\imath} + j_{yi}\hat{\jmath} + j_{zi}\hat{k} \tag{5.136}$$

where r_i' defines the position of atom i with respect to the D center of mass:

$$r_i' = x_i'\hat{\imath} + y_i'\hat{\jmath} + z_i'\hat{k} \tag{5.137}$$

and x_i', y_i' and z_i' are determined by equation 5.131. The total angular momentum L of the $C + D$ products is

$$L = j_C + j_D + l \tag{5.138}$$

where j_C and j_D are computed by equation 5.135 and l is the orbital angular momentum due to the angular (orbital) motion of C with respect to D and is determined by

$$l = \mu_{CD} R \times \dot{R} \tag{5.139}$$

with R and $\dot{R}$ defined in equations 5.128 and 5.129.

The internal energy can be calculated by equations 5.133 and 5.134, but we can also evaluate rotational and vibrational energy separately:

$$E_{int,D} = E_{vib,D} + E_{rot,D} \tag{5.140}$$

Because of vibrational-rotational coupling, the rotational and vibrational energies will fluctuate as the molecule vibrates. An instantaneous rotational energy may calculated by

$$E_{rot,D} = \frac{1}{2}\omega_D j_D \tag{5.141}$$

where j_D is the rotational angular momentum of D (equation 5.135) and ω_D is the angular velocity of D, determined from

$$\omega_D = I_D^{-1} j_D \tag{5.142}$$

with I_D being the moment of inertia tensor for D. Inserting $E_{rot,D}$ into equation 5.140 allows to calculated the vibrational energy $E_{vib,D}$.

Many other properties can be evaluated from coordinates and momenta, but in general, they are derived from those shown here.

REFERENCES

(1) Bunker, D. L. *J. Chem. Phys.* **1962**, *37*, 393-403.
(2) Bunker, D. L. *J. Chem. Phys.* **1964**, *40*, 1946-57.
(3) Bunker, D. L.; Pattengill, M. *J. Chem. Phys.* **1968**, *48*, 772-6.
(4) Peslherbe, G. H.; Wang, H.; Hase, W. L. In *Monte Carlo Methods in Chemical Physics*; Ferguson, D. M., Siepmann, J. I., Thrular, D. G., Eds.; John Willey & Sons: New York, 1999; Vol. 105.
(5) Thrular, D. G.; Muckerman, J. T. In *Atom-Molecule Collision Theory*; Bernstein, R. B., Ed.; Plenum Press: New York, 1979.
(6) Levine, R. D. *Molecular Reaction Dynamics*; Cambridge University Press: New York, 2005.
(7) Mayne, H. R. In *Dynamics of Molecules and Chemical Reactions*; Wyatt, R. E., Zhang, J. Z. H., Eds.; Marcel Dekker, Inc.: New York, 1996.
(8) Steinfeld, J. I.; Francisco, J. S.; Hase, W. L. *Chemical Kinetics and Dynamics*; Prentice-Hall, Inc.: New Jersey, 1989.
(9) Houston, P. L. *Chemical Kinetics and Reaction Dynamics*; McGraw-Hill Higher Education: New York, 2001.
(10) Helgaker, T.; Uggerud, E.; Jensen, H. J. A. *Chem. Phys. Lett.* **1990**, *173*, 145-50.
(11) Uggerud, E.; Helgaker, T. *J. Am. Chem. Soc.* **1992**, *114*, 4265-8.
(12) Bueker, H.-H.; Helgaker, T.; Ruud, K.; Uggerud, E. *J. Phys. Chem.* **1996**, *100*, 15388-15392.
(13) Millam, J. M.; Bakken, V.; Chen, W.; Hase, W. L.; Schlegel, H. B. *J. Chem. Phys.* **1999**, *111*, 3800-3805.
(14) Doubleday, C., Jr.; Bolton, K.; Peslherbe, G. H.; Hase, W. L. *J. Am. Chem. Soc.* **1996**, *118*, 9922-9931.
(15) Doubleday, C., Jr.; Bolton, K.; Hase, W. L. *J. Phys. Chem. A* **1998**, *102*, 3648-3658.
(16) Warshel, A.; Levitt, M. *J. Mol. Biol.* **1976**, *103*, 227-49.
(17) Henriksen, N. E.; Hansen, F. Y. *Theories of Molecular Reaction Dynamics*; Oxford University Press: New York, 2008.
(18) Zhang, D. H.; Zhang, J. Z. H. In *Dynamics of Molecules and Chemical Reactions*; Wyatt, R. E., Zhang, J. Z. H., Eds.; Marcel Dekker, Inc: New York, 1996.
(19) Alexander, W. A.; Morris, J. R.; Troya, D. *J. Phys. Chem. A* **2009**, *113*, 4155-4167.
(20) Alexander, W. A.; Troya, D. *J. Phys. Chem. C* **2011**, *115*, 2273-2283.
(21) Bosio, S. B. M.; Hase, W. L. *J. Chem. Phys.* **1997**, *107*, 9677-9686.
(22) Day, B. S.; Morris, J. R.; Troya, D. *J. Chem. Phys.* **2005**, *122*, 214712/1-214712/12.
(23) Gibson, K. D.; Isa, N.; Sibener, S. J. *J. Chem. Phys.* **2003**, *119*, 13083-13095.

(24) Isa, N.; Gibson, K. D.; Yan, T.; Hase, W.; Sibener, S. J. *J. Chem. Phys*. **2004**, *120*, 2417-2433.

(25) Martinez-Nunez, E.; Rahaman, A.; Hase, W. L. *J. Phys. Chem. C* **2007**, *111*, 354-364.

(26) Tasic, U.; Troya, D. *Phys. Chem. Chem. Phys*. **2008**, *10*, 5776-5786.

(27) Yan, T.; Hase, W. L. *Phys. Chem. Chem. Phys.* **2000**, *2*, 901-910.

(28) Yan, T.; Hase, W. L. *J. Phys. Chem. A* **2001**, *105*, 2617-2625.

(29) Yan, T.; Hase, W. L. *J. Phys. Chem. B* **2002**, *106*, 8029-8037.

(30) Yan, T.; Hase, W. L.; Barker, J. R. *Chem. Phys. Lett.* **2000**, *329*, 84-91.

(31) Yan, T.; Isa, N.; Gibson, K. D.; Sibener, S. J.; Hase, W. L. *J. Phys. Chem. A* **2003**, *107*, 10600-10607.

(32) Chapra, S. C.; Canale, R. P. *Numerical Methods for Engineers: With Software and Programming Aplications* 4ed.; McGraw-Hill Higher Education: New York, 2002.

(33) Gerald, C. F.; Wheatley, P. O. *Análisis Numérico con Aplicaciones*; 6 ed.; Pearson Eduacion: Naucalpan de Juárez, 2000.

(34) Butcher, J. C. *Numerical Methods for Ordinary Differential Equations*; 2 ed.; John Willey & Sons: Chichester, 2008.

(35) Requena Rodríguez, A.; Zúñiga Román, J. *Espectroscopía*; Pearson Prentice Hall: Madrid, 2004.

(36) Allen, M. P.; Tildesley, D. J. *Computer Simulation of Liquids*; Oxford University Press: New York, 1987.

(37) Haile, J. M. *Molecular Dynamics Simulations: Elementary Methods*; John Wiley & Sons: New York, 1992.

(38) Wheeler, D. R.; Fuller, N. G.; Rowley, R. L. *Mol. Phys.* **1997**, *92*, 55-62.

(39) Alejandre, J.; Tildesley, D. J.; Chapela, G. A. *J. Chem. Phys.* **1995**, *102*, 4574-83.

(40) Hase, W. L. In *Encyclopedia of Computational Chemistry*; Von Ragué Schleyer, P., Ed.; John Willey & Sons: Chichester, 1998; Vol. 1, p 399-402.

Chapter 6

Dynamics of CO_2/F-SAM: Influence of Collision Energy, Mass and Surface Model

1. INTRODUCTION

Investigations of energy transfer and collisional accommodation between a gas and a liquid surface are of fundamental importance in acquiring a thorough comprehension of heterogeneous chemical phenomena at the molecular level. Over the last decades, advances in experimental techniques have allowed experimentalists to investigate in detail the dynamics of collisions of gases with liquid surfaces and characterize the role of important parameters, such as the mass, structure and temperature of the surface, collision energy, or impact orientation.[1-21] The quantity measured in scattering of atoms from liquid surfaces is the translational energy distribution, $P(E_f)$, of the scattered atoms, which may be determined for different polar and azimuthal angles.[3,4,20] For the scattering of a molecule such as CO_2 one may also determine its final rotational energy distribution, $P(J)$, as well as its final vibrational energies.[15-18,21]

The $P(E_f)$ and $P(J)$ distributions are often bimodal, with a low energy component that is well fit by the Boltzmann distribution for desorption at the surface temperature. It has been suggested that this component represents trapping desorption (TD) events in which the projectile may physisorb, or penetrate into the bulk liquid, and reach thermal accommodation with the surface. The high energy component of the distribution is associated with impulsive scattering (IS), for which the projectile rebounds immediately from the surface, so that the time scale of the collision is very short and insufficient for thermal equilibration with the surface. Though this is an attractive surface model, chemical dynamics simulations of projectile scattering indicate that the scattering may often be considerably more complex; e.g. direct events without trapping on the surface may scatter with a low energy Boltzmann component, often at the surface temperature, and the low energy Boltzmann component for physisorption events may have a temperature higher than that at the surface.[22-25] In addition, the forms of $P(E_f)$ and $P(J)$ may be considerably different, illustrating different collision dynamics for translational and rotational energy transfer.

One of the gas-liquid systems that has been experimentally investigated in great detail is CO_2 scattering from perfluoropolyether (PFPE).[15-18] In these experiments, carried out by Nesbitt and co-workers, supersonic jet-cooled molecular beams of CO_2 impinged on a freshly formed liquid surface of PFPE in vacuum, and the nascent internal-state distributions of the scattered CO_2 molecules were probed by high-resolution direct infrared absorption spectroscopy and laser dopplerimetry. They investigated the role of collision energy, incident angle, and surface temperature, and found that the CO_2 rotational and translational distributions are well described by the above TD+IS

model, with the IS component having a Boltzmann temperature much higher than the surface temperature. The fraction of each component was found to depend significantly on collision energy and incident angle.[16,17] Also, the size of the TD component and the rotational/translational temperature of the IS component were observed to increase with surface temperature.[18]

Classical chemical dynamics simulations help to interpret experimental observations and provide additional insights into the scattering dynamics of gases with surfaces. Simulations of carbon dioxide scattering off a perfluorinated alkanethiol [$CF_3(CF_2)_7S$] self-assembled monolayer (F-SAM) on gold, using an explicit atom (EA) model potential for the surface, gave results in quite good agreement with the scattering experiments of CO_2 + liquid PFPE, though surfaces of different nature were involved in the simulations and experiments.[18,24] This suggests that both the F-SAM and PFPE surfaces behave in similar ways in terms of energy transfer. Cooks and co-workers[26] observed similar translational to vibrational (T-V) energy transfer conversion efficiencies and, moreover, similar ion-surface reactions for both PFPE and F-SAM surfaces. These results, together with the observation of Ramasamy and Pradeep[27] that the terminal $–CF_3$ groups primarily constitute the surface of PFPE, suggest that energy transfer between the projectile and the surface is controlled by the chemical nature of the outermost layer of the surface and not by the detailed structure of the interfacial material. It is also worth mentioning that molecular dynamics simulations of long chain alkanes indicate that the liquid surface is mostly composed of the chain ends.[28] All these data strongly support the proposal that results of chemical dynamics simulations of energy transfer in collisions of gases with F-SAMs may be directly compared with the corresponding experimental information obtained for a liquid PFPE surface, provided initial conditions are chosen for the trajectories in accord with the experimental conditions. There are, however, some differences between the simulation and the experimental results, concerning the directions of the scattered CO_2 molecules, which result from the ordered structure of the F-SAM surface, as compared to the PFPE surface, and are discussed later in the paper.

The present work complements our previous simulations of CO_2 scattering off the F-SAM,[24] considering now the additional collision energies of 1.6, 4.7, 7.7 kcal/mol and several aspects that were not investigated before. These include the influence of mass effects in the energy transfer process and the performance of a united-atom (UA) model for the F-SAM surface, in which the CF_3 and CF_2 units are represented as single pseudoatoms. This model was previously used in Ar + F-SAM simulations,[29] and it is of special interest to investigate its quality and reliability, given that this model may be very useful for large scale computations since it reduces the CPU time considerably in comparison with the explicit-atom (EA) model. A thorough comparison is

made between our CO_2 + F-SAM scattering simulations and the CO_2 + PFPE scattering experiments. Firstly, the rotational quantum number J distributions of the scattered CO_2 molecules obtained in this study are compared with the available experimental data. Secondly, from the projections of the velocity distributions of the scattered CO_2 molecules onto the surface plane, a translational temperature is extracted as a function of the rotational quantum number J. Experimentally, this temperature is obtained from the Doppler widths of IR laser absorption profiles of the scattered carbon dioxide molecules.

2. COMPUTATIONAL DETAILS

2.1 Potential energy surfaces

As in the previous work,[24] the potential energy function employed to study the dynamics of inelastic collisions of CO_2 with the F-SAM surface comprises a potential for CO_2 (V_{CO_2}), the surface potential (V_{surf}) and a CO_2/F-SAM interaction term ($V_{CO_2,surf}$):

$$V = V_{CO_2} + V_{surf} + V_{CO_2,surf} \tag{6.1}$$

We used two different models for the surface. In the explicit-atom (EA) model all atoms are treated explicitly, whereas in the united-atom (UA) model the CF_3 and CF_2 units are represented as single pseudoatoms and therefore the total number of interactions is dramatically diminished, which results in a factor of ~3 decrease in CPU time per trajectory. For both models, the F-SAM surface consists of 48 chains of $CF_3(CF_2)_7S$ radicals adsorbed on a single layer of 225 (196 in the UA model) constrained Au atoms. The details of these models were described elsewhere,[24,29] and for simplicity they are not given here. Figure 6.2 depicts a snapshot of the EA model of the surface after a collision with the CO_2 molecule, as well as the definition of the axes used in the simulations.

The CO_2/F-SAM interaction function ($V_{CO_2,surf}$) for the UA model was derived from a fit of the Buckingham expression to a potential, $V_{av}(R)$, obtained by isotropically averaging the EA interactions in the $CO_2\cdots CF_4$ system:

$$V_{av}(R) = \frac{1}{n}\sum_{k=1}^{n}\sum_{i,j} V_R\left(r_{i,j};\theta_k,\phi_k,\chi_k\right) \tag{6.2}$$

where R is the C···C separation, n is the number of random orientations of CF_4 (defined in terms of the Euler angles θ_k, ϕ_k and χ_k) for a given distance R, and $V_R(r_{i,j};\theta_k,\phi_k,\chi_k)$ is the EA potential energy of CO_2···CF_4. At constant R, the value of this potential energy varies with the orientation of CF_4, which determines the $r_{i,j}$ distances (i stands for C or F in CF_4 and j for C or O in CO_2). $V_{av}(R)$ is plotted in Figure 6.1 as circles for two different orientations of the CO_2 molecule with respect to CF_4. All points in the figure were considered in the fitting to the Buckingham potential

$$V(R) = Ae^{-BR} + \frac{C}{R^D} \tag{6.3}$$

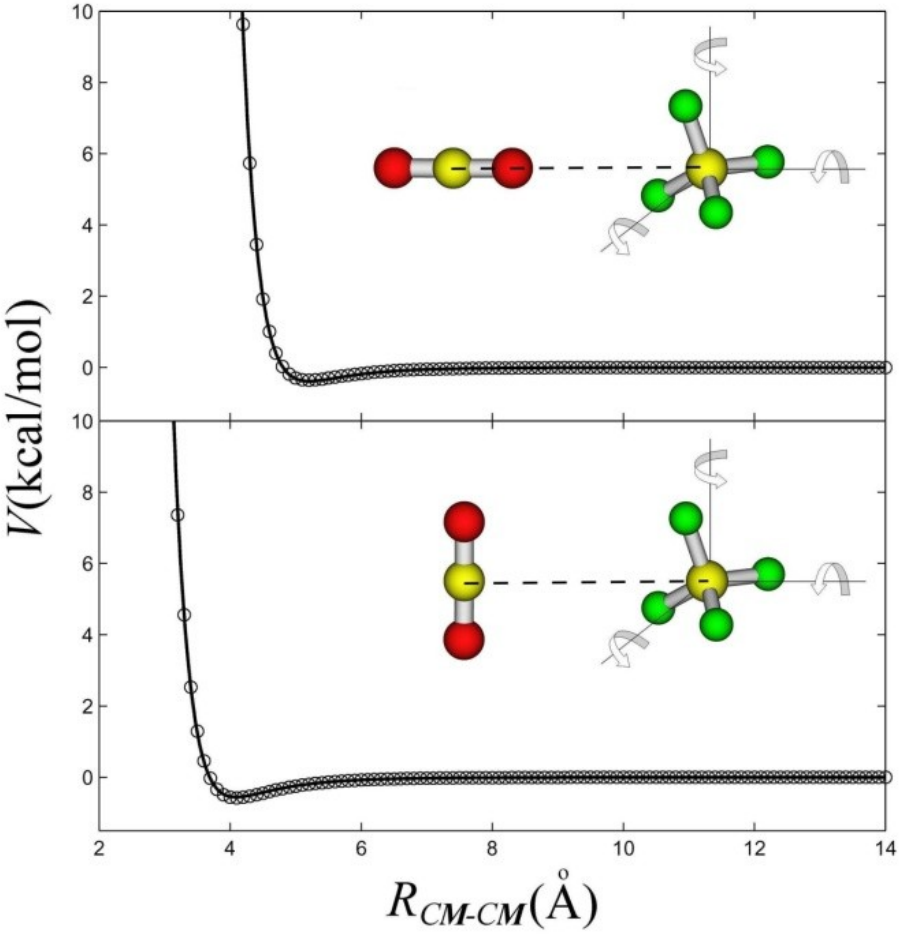

Figure 6.1: The two orientations between CO_2 and CF_4 used to calculate the UA model interaction potential between CO_2 and the F-SAM surface.

Table 6.1: Parameters[a] of the CO_2/F-SAM Interaction Potential.

UA model				
	A	B	C	D
C···CF_4	14557336.665	4.562231	- 20182460694.28	20
O···CF_4	1473656.5293	3.806771	- 11730.83989144	7
EA model				
	A	B	C	D
C···C	7560.1542982	2.913320	- 502887.9228984	15
C···F	54318.344110	3.998996	- 1759.413466311	8
O···C	23100.485102	3.243885	- 1398.683812882	6
O···F	75993.648886	4.183596	- 578.2202760926	7

[a]Units are such that the potential energy is in kcal/mol and R in Å.

The parameters were obtained using a nonlinear least-squares program. To improve the computational efficiency of the simulations the value of the exponent D was rounded off to the nearest integer. After that, the remaining parameters A, B and C were fit again fixing the value of D. The results of the fitting for the UA model are shown as a black line in Figure 6.1 and the parameters collected in Table 6.1.

2.2 Trajectory simulations

The initial conditions of the trajectories were selected to model as accurately as possible the experimental conditions for CO_2 + PFPE. The angle with respect to the surface normal (z axis in Figure 6.2) for the CO_2 projectile, the incident polar angle (θ_i), was 0º. As in previous simulations,[24] the aiming points ($\vec{A}$) on the surface at which the CO_2 center-of-mass impacts were randomly selected by

$$\vec{A} = R_1\vec{u} + R_2\vec{v} \tag{6.4}$$

where the vectors $\vec{u}$ and $\vec{v}$ are determined from the Cartesian coordinates of the terminal carbon atoms for three chains at the corner of the unit cell, and R_1 and R_2 are two freshly generated random numbers. We used periodic boundary conditions and the image vector convention[30] to represent a larger surface, thus avoiding possible complications that may appear in collisions resulting in multiple CO_2 encounters with the surface.

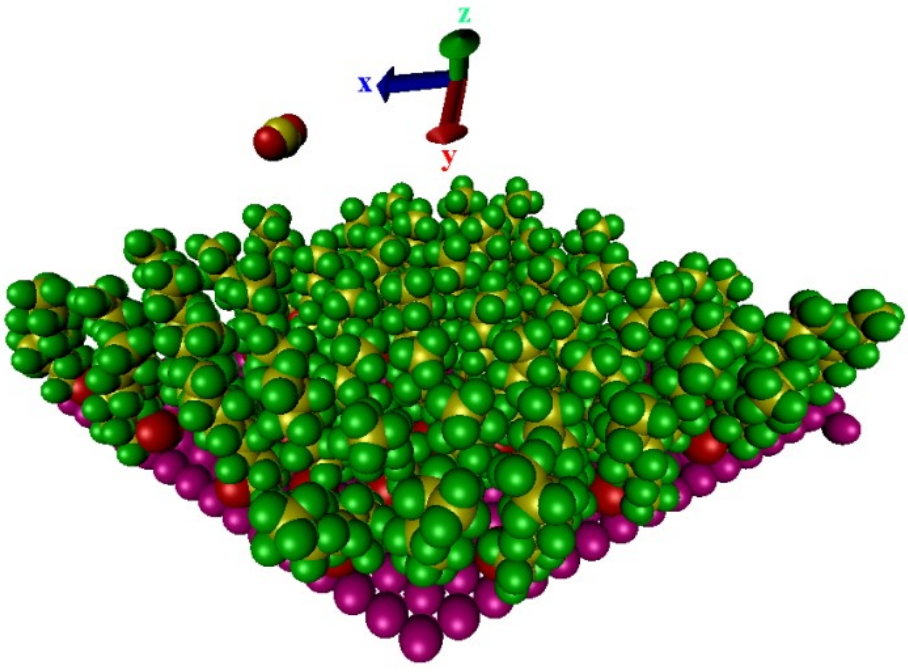

Figure 6.2: Snapshot of the EA model of the surface after a collision with CO_2, including the orientation of the axes considered in the present study.

The simulations were carried out with the VENUS05 program,[31] at collision energies (E_i) of 1.6, 4.7, 7.7, and 10.6 kcal/mol, and using both the UA and EA models; at E_i = 10.6 kcal/mol only the UA model was used because the simulations with the EA model were already carried out in previous work.[24] These collision energies are the same as those used in the CO_2 + PFPE experiments, and so the present study complements our previous simulations at the collision energies of 3.0, 10.6, and 20.0 kcal/mol using the EA model.[24] The initial separation between CO_2 and the surface aiming point was 25 Å (37Å above the gold atoms). The integration of the classical equations of motion was performed with a fixed step size of 0.3 fs using the Adams-Moulton algorithm. Prior to propagation of the first trajectory, a molecular dynamics simulation was performed for 2 ps to ensure thermal relaxation of the F-SAM surface at 300 K. The structure thus obtained was used later as the initial structure of a 100 fs equilibration run before the second trajectory. This process was repeated before initiation of each trajectory.

Trajectories were stopped when the distance between CO_2 and the surface was 30 Å or when 150 ps elapsed. Then, the following properties were evaluated from the atomic Cartesian coordinates and momenta: the final translational and internal energy of CO_2, the final internal energy of the surface, the residence time of CO_2 (τ_{res}) on/in the surface, and the angular distributions

of the scattered CO_2 atoms. Ensembles of 2000 trajectories were considered in these calculations in order to attain reasonable statistics.

Table 6.2: Percentages of trajectories that did not desorb ("incomplete" trajectories) within the simulation time of 150 ps.

E_i (kcal/mol)	Model	
	EA	UA
1.6	3.0	38.5
4.7	2.5	30.1
7.7	1.6	23.3
10.6	0.0	22.9

For some trajectories the CO_2 molecule did not desorb during the 150 ps integration time. The percentages of these "incomplete" trajectories are collected in Table 6.2 for each energy and model. Almost all of the incomplete trajectories correspond to penetrating trajectories (see below for a description of the different trajectory types). The percentages of incomplete trajectories decrease with the incident energy, which is consistent with a reduction in the percentage of penetrating trajectories with collision energy (see below). In addition the percentage of incomplete trajectories is much higher for the UA model. For the incomplete trajectories, the final CO_2 translational, vibrational, and rotational energies were sampled from 300 K Boltzmann distributions and the scattering angle θ_f was randomly sampled from a cosine distribution. This is a reasonable approach because after 150 ps the CO_2 molecule is expected to reach thermal equilibrium with the F-SAM surface, so that the ensuing desorbing process will presumably proceed statistically.

3. RESULTS

3.1 Trajectory types

Figure 6.3 shows plots of the height of the CO_2 center-of-mass above the Au(111) surface as a function of time for the different trajectory types. Trajectories which move below the dashed line, which denotes the intermediate height (11.6 Å) between the average height of the C atoms of the $-CF_3$ groups and that of their adjacent $-CF_2$ groups at 300 K are identified as penetrating.[24] As seen in the plots, direct trajectories have only one inner turning point (ITP) in their perpendicular motion, whereas physisorption occurs when the molecule undergoes two or more ITPs. The time scales for both processes differ significantly, although as will be discussed later there is an important fraction of physisorbing trajectories that have just a few ITPs, and therefore their time

scale is similar to that of direct trajectories. There are two types of penetrating trajectories: those that penetrate directly the surface (direct-penetration) and those that penetrate the surface after the molecule has performed several ITPs on the surface (physisorption-penetration). The time scales of the three different trajectory types (direct, physisorption, and penetration) are very different as can be seen in the plots, with the average time scale for penetrating trajectories an order of magnitude higher than those for direct trajectories.

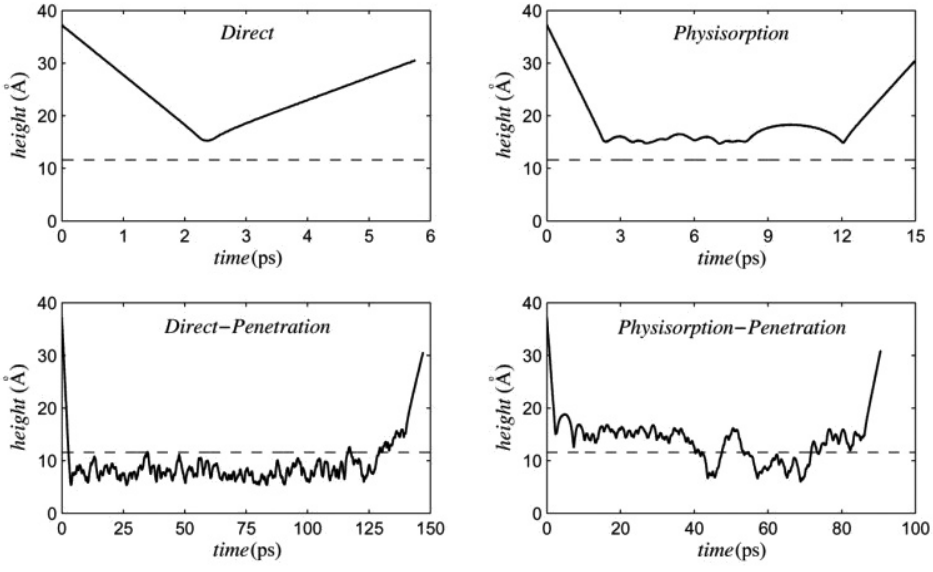

Figure 6.3: Variation of the CO_2 center-of-mass height with respect to the gold surface as a function of time for the different trajectory types. The plots are for typical trajectories using the EA model of the surface and E_i = 4.7 kcal/mol.

The percentage of each trajectory type as a function of the incident collision energy is shown in Figure 6.4 for each surface model. The figure also collects the previous simulation results at E_i = 3.0, 10.6, and 20.0 kcal/mol for the surface EA model.[24] As seen in the plots, the percentages of trajectory types obtained with the EA surface model differ significantly from those determined with the UA model, although there are several trends that are followed by the two surface models. For example, in both cases the percentage of direct trajectories increases and the percentage of penetrating trajectories decreases with collision energy. However, the percentage of penetrating trajectories calculated with the UA model is much higher than that obtained with the EA model. Two different types of penetration trajectories were found in this study: direct-penetration, for which CO_2 molecules penetrate directly the surface and physisorption-penetration, where physisorption occurs before penetration.

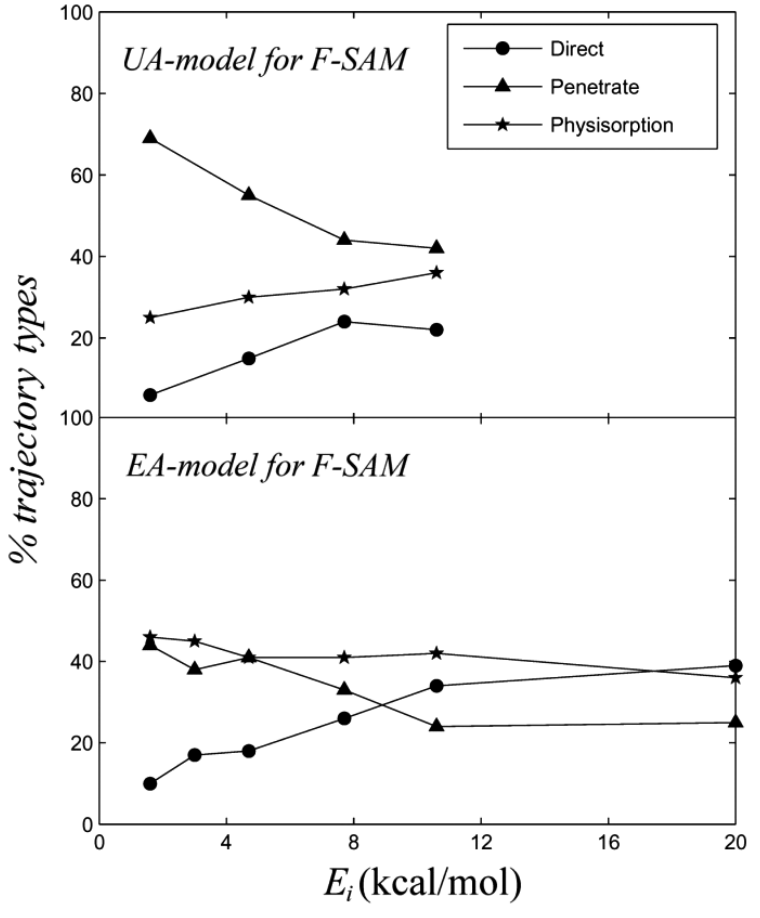

Figure 6.4: Percentages of different trajectory types as a function of collision energy.

Figure 6.5 shows the percentages of direct-penetration and physisorption-penetration for both surface models as a function of collision energy. In general, the percentage of physisorption-penetration is much higher than that of direct-penetration, particularly for the UA model. On the other hand, for the UA model the percentage of physisorption-penetration increases with collision energy and the percentage of direct-penetration decreases, whereas the contrary occurs for the EA model. Actually, for the EA model at E_i = 20 kcal/mol, the percentage of direct-penetration is higher than that of physisorption-penetration. The reason for disagreement between the two surface models will be discussed in detail in a separate Section below.

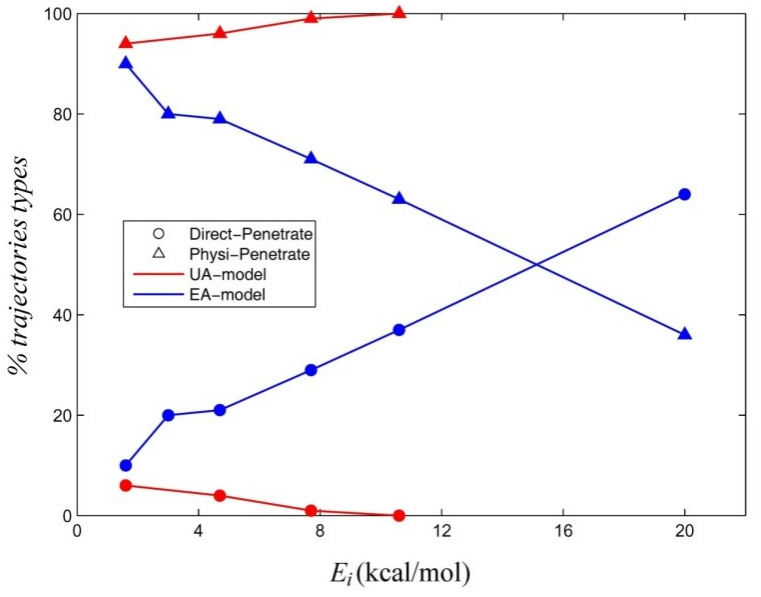

Figure 6.5: Percentages of direct-penetration and physisorption-penetration trajectories as a function of collision energy.

3.2 Residence times

As in previous work,[24] the residence time is defined as the difference in time between the first and the last ITPs in the perpendicular motion of the CO_2 center-of-mass. With this definition, only penetrating and physisorbing trajectories have residence times. As found before,[24] the average residence times of penetrating trajectories are higher than those of physisorbing trajectories. At E_i = 10.6 kcal/mol, the difference between the corresponding averages is 27.0 ps for the EA surface model and 44.4 ps for the UA model. The difference is much higher for the UA model because the residence-time distributions of penetrating trajectories are much broader than those calculated with the EA model (see Figure 6.6). In fact, the average residence times of the physisorbing trajectories, as well as their distributions, are very similar for the EA and UA models (both show a maximum close to τ = 0, and then each decreases monotonically with τ). Additionally, for the EA model the average residence times decrease with collision energy, whereas for the UA model the average values of the penetrating trajectories do not follow this trend.

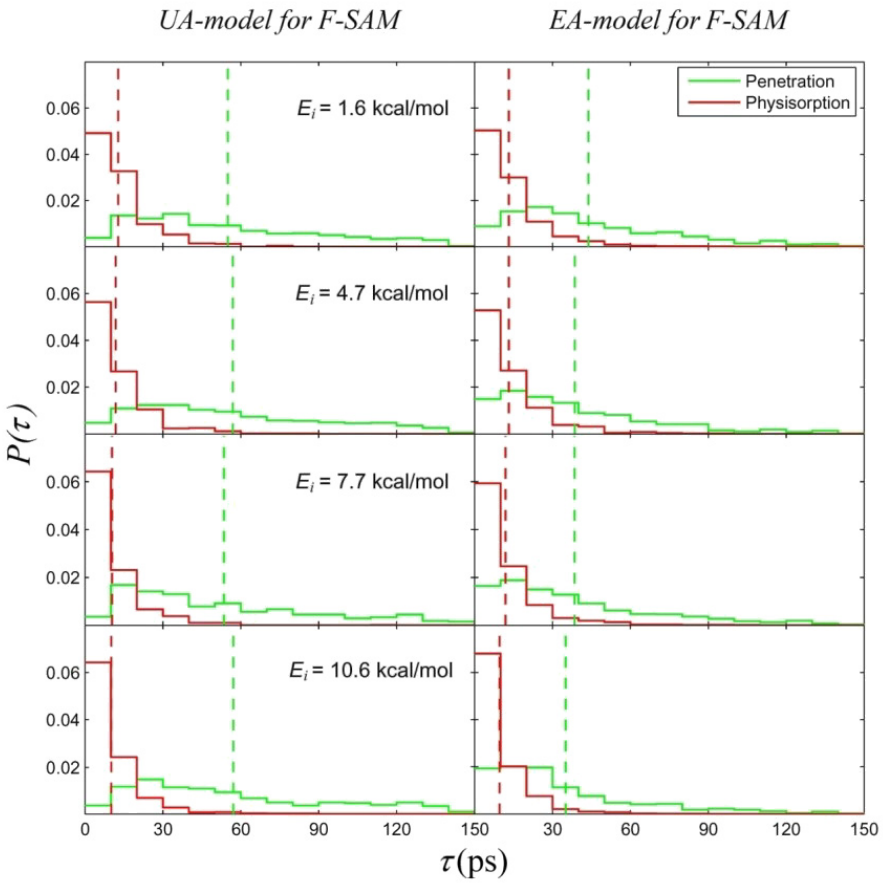

Figure 6.6: Distributions of residence times for physisorbing and penetrating trajectories for different collision energies. The vertical dashed lines show the average values.

3.3 Energy transfer

Collisions of the CO_2 molecules with the F-SAM surface result in variations in the CO_2 translational energy from E_i to a final value E_f, as well as in changes in the internal energy of CO_2, ΔE_{int}, and the surface energy, ΔE_{surf}; i.e.

$$E_i = E_f + \Delta E_{int} + \Delta E_{surf} \tag{6.5}$$

Figure 6.7 gives a graphical presentation of the average percentages of E_i that go to E_f, ΔE_{int}, and ΔE_{surf}. As seen in the plots, the variations for all trajectory types follow the same pattern. In particular for ΔE_{int}, the results for all trajectory types are very similar, whereas for ΔE_{surf} and E_f there is more scattering in the results, especially at the highest energies and for the EA model. The change in the internal energy of the CO_2 molecule (ΔE_{int})

comprises a change in the vibrational and rotational energies. As in the previous simulations there is a leakage of zero-point energy from CO_2 of approximately 0.3 kcal/mol, which has been attributed to excitation of the vibrational angular momentum states of the CO_2 molecule after collision with the surface.[24] Therefore, most of the change in the internal energy of the projectile comes from rotational excitation and this excitation is relatively less important as the collision energy increases. Also seen in Figure 6.7 is the result that the percentage of energy transferred to the projectile's internal degrees of freedom (ΔE_{int}) does not strongly depend on the collision energy E_i, while the percentage of energy transferred to the surface ΔE_{surf} and that transferred to the translational energy of the projectile increases and decreases, respectively.

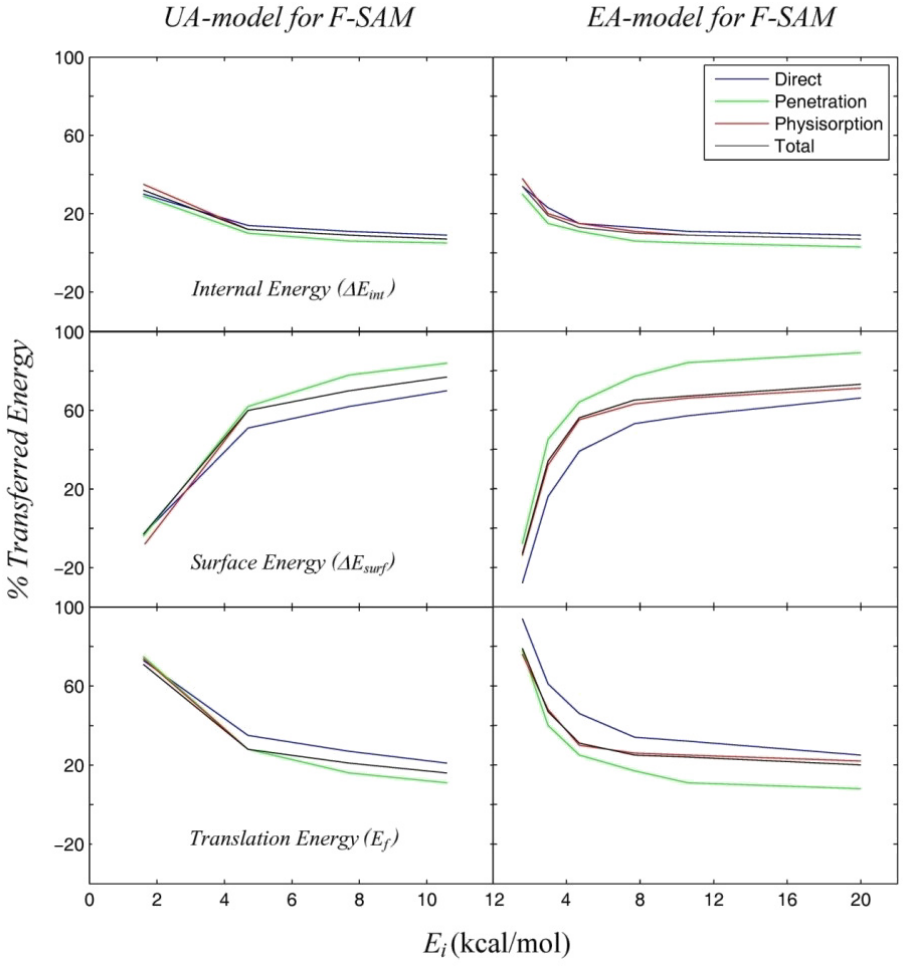

Figure 6.7: Average percentages of different energies ΔE_{int} , ΔE_{surf} and E_f as a function of collision energy for the different trajectory types.

The same result has been observed in previous studies,[32-35] and may be interpreted in terms of an approximate model successfully applied to collisions of gly_2-H^+ and ala_2-$H^+$with an F-SAM surface.[35] This model is used in the present study to analyze the energy transfer efficiencies in collisions of CO_2 with F-SAM.

The model is based on the adiabaticity parameter, ξ,[36] which is given by

$$\xi = \frac{t_c}{t_v} \tag{6.6}$$

where t_c represents the duration of the collision, which is inversely proportional to the collision velocity (v_i), and t_v is an effective vibrational period for the surface modes receiving the energy transfer. Thus, ξ is inversely proportional to the collision velocity. The average probability of energy transfer to the surface depends on ξ according to[36]

$$P_{surf}\,(E_i) = \frac{\langle \Delta E_{surf} \rangle}{E_i} = P_0 e^{-\xi} = P_0 e^{-\frac{b}{v_i}} \tag{6.7}$$

where P_0 is the limiting, small ξ, probability of energy transfer and b is a fitting parameter.

Following previous work on collisions of gly_2-H^+ and ala_2-H^+ with an F-SAM surface, we used equation 6.7 to model the percentage of energy transferred to the F-SAM upon collision with CO_2 molecules, where b and P_0 are the adjustable parameters. The fitting is shown in Figure 6.8a and the parameters are P_0 = 1.17 and b = 797 m/s. As found before for gly_2-H^+ and ala_2-H^+ colliding with an F-SAM, P_0 is greater than unity, which is unrealistic. It has been suggested[35] that it is more appropriate to express the adiabaticity parameter, ξ, as b/E_i instead of b/v_i. The fitting for $\xi = b/E_i$ is shown in Figure 6.8b. As can be seen, it is apparent that the fitting is much better for $\xi = b/E_i$than for $\xi = b/v_i$, and P_0 is now 0.86 (which is a realistic value) and b = 2.46 kcal/mol. The limiting energy transfer to the surface (P_0) at high energy is 86%, a value very close to the value of ~90% obtained for gly_2-H^+ and ala_2-H^+ colliding perpendicularly with F-SAM.

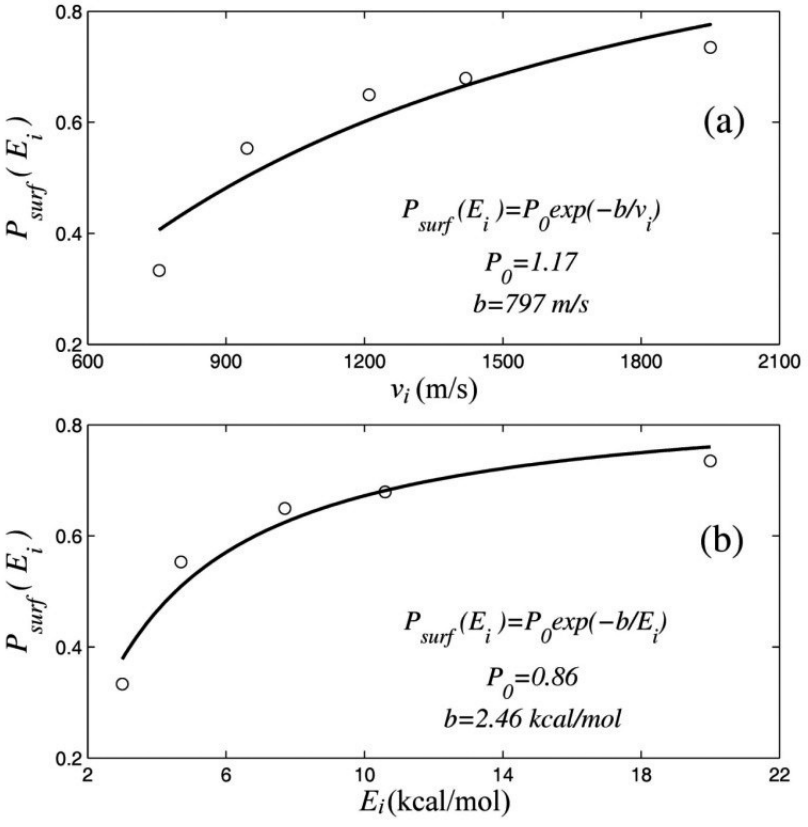

Figure 6.8: Fits of equation 6.7 to (a) the average energy transferred to the surface. In (b) the adiabaticity parameter was substituted by b/E_i instead of b/v_i.

3.4 Rotational energy distributions

The distributions of the rotational quantum number J of the scattered CO_2 molecules are shown in Figure 6.9 as histograms. Each of the distributions obtained in our simulations was fit to the sum of two components: low-temperature (LT) and high-temperature (HT):

$$P(J) = \alpha_{LT} P_{LT}(J) + (1 - \alpha_{LT}) P_{HT}(J) \tag{6.8}$$

and each of the normalized components reads

$$P_X(J) = \frac{(2J+1)e^{-E_{rot}/k_B T_{rot}(X)}}{Q_{rot}(X)} \tag{6.9}$$

with X = LT or HT. The results of the fits are collected in Tables 6.3 and 6.4 for the UA and EA models, respectively. In some cases, the distributions were fit to a single Boltzmann distribution and α_{LT} = 1, with the only variable being the rotational temperature. For the rest of the distributions the rotational temperature of the LT component was fixed to 300 K and only α_{LT} and

T_{rot} (HT) were allowed to vary during the fittings; these LT and HT components are depicted in Figure 6.9 by lines in blue and red, respectively. This procedure is the same as that used by Nesbitt and co-workers in their experimental investigations of CO_2 + PFPE scattering dynamics,[15-18] when they referred to the LT and HT components as TD and IS, respectively.

Table 6.3: Parameters for the bimodal Boltzmann fits to the *P*(*J*) distributions for the UA model.[a]

E_i (kcal/mol)		α_{LT}	T_{rot} (LT)	T_{rot} (HT)
Total trajectories				
1.6	Sim.	1	282 ± 5	-
	Exp.[b]	0.92 ± 0.12	298	330 ± 100
4.7	Sim.	1	290 ± 6	-
	Exp.	0.76 ± 0.07	298	520 ±60
7.7	Sim.	0.89 ± 0.03	300	1025 ± 326
	Exp.	0.64 ± 0.06	298	600 ± 80
10.6	Sim.	0.85 ± 0.03	300	1073 ± 315
	Exp.	0.54 ± 0.03	298	710 ± 60
Direct trajectories				
1.6		1	287 ± 20	-
4.7		1	275 ± 15	-
7.7		0.58 ± 0.10	300	723 ± 168
10.6		0.59 ± 0.08	300	864 ± 198
Penetrating trajectories				
1.6		1	279 ± 5	-
4.7		1	284 ± 7	-
7.7		1	293 ± 7	-
10.6		1	291 ± 9	-
Physisorption trajectories				
1.6		1	287 ± 12	-
4.7		1	305 ± 9	-
7.7		0.90 ± 0.05	300	1205 ± 882
10.6		0.78 ± 0.07	300	800 ± 273

[a]The *P*(*J*) distributions are bimodal and fit with a low temperature (LT) component for thermal accommodation at the surface and a high temperature (HT) component. [b]Experimental values from ref.[16]

In general the results obtained with the UA model (Table 6.3) are different from those obtained with the EA model of the surface (Table 6.4). For the penetrating trajectories and for both models α_{LT} = 1 and the temperatures are close to 300 K, with slightly higher temperatures for the EA model of the surface. For direct and physisorption trajectories α_{LT} < 1 for the highest

collision energies, even for the UA model, although α_{LT} is always higher for the UA model than for the EA model. When all the trajectories are considered, single Boltzmann fits with α_{LT} = 1 are obtained with the UA model for the two lowest collision energies, whereas with the EA model two Boltzmann components were obtained for all collision energies investigated.

Table 6.4: Parameters for the bimodal Boltzmann fits to the *P*(*J*) distributions for the EA model.[a]

E_i (kcal/mol)		α_{LT}	$T_{rot}(LT)$	$T_{rot}(HT)$
Total trajectories				
1.6	Sim.	0.83 ± 0.24	300	430 ± 230
	Exp.[b]	0.92 ± 0.12	298	330 ± 100
4.7	Sim.	0.74 ± 0.13	300	520 ± 154
	Exp.	0.76 ± 0.07	298	520 ±60
7.7	Sim.	0.67 ± 0.08	300	597 ± 112
	Exp.	0.64 ± 0.06	298	600 ± 80
10.6	Sim.	0.52 ± 0.06	300	712 ± 78
	Exp.	0.54 ± 0.03	298	710 ± 60
Direct trajectories				
1.6		0.94 ± 0.13	300	120 ± 193
4.7		0.78 ± 0.14	300	713 ± 408
7.7		0.29 ± 0.15	300	585 ± 88
10.6		0.46 ± 0.06	300	933 ± 133
Penetrating trajectories				
1.6		1	310 ± 9	-
4.7		1	302 ± 10	-
7.7		1	293 ± 11	-
10.6		1	313 ± 13	-
Physisorption trajectories				
1.6		0.80 ± 0.20	300	500 ± 285
4.7		0.35 ± 0.36	300	452 ± 108
7.7		0.64 ± 0.08	300	692 ± 134
10.6		0.24 ± 0.14	300	566 ± 71

[a]The *P*(*J*) distributions are bimodal and fit with a low temperature (LT) component for thermal accommodation at the surface and a high temperature (HT) component. [b]Experimental values from ref.[16]

A possible model for the transfer of rotational energy to CO_2 is that low values of J are associated with collisions in which CO_2 bounces multiple times at the surface, with multiple ITPs, and becomes thermally accommodated with the surface. To investigate this idea, the average number of ITPs, i.e. $\langle N_{ITPs} \rangle$, was calculated versus J for J in ΔJ = 10 intervals. These distributions

are depicted in Figure 6.10 for the EA model of the surface. For the lowest collision energy $\langle N_{ITPs} \rangle$ is nearly independent of J, except for the highest J. To fit the distributions a model based on an average (constant) value for the number of ITPs for each component of the $P(J)$ distribution was used:

$$N_{ITPs}(J) = \frac{1}{P(J)}\left(\langle N_{ITPs}(LT)\rangle P_{LT}(J) + \langle N_{ITPs}(HT)\rangle P_{HT}(J)\right) \quad (6.10)$$

Where $\langle N_{ITPs}(LT)\rangle$ and $\langle N_{ITPs}(HT)\rangle$ are the average number of ITPs for the LT and HT components, respectively. Using the above equation to fit the distributions (the fits are shown in Figure 6.10), the average number of ITPs for the LT component is 15-18 and that for the HT component is close to 0. The origin of the different dynamics for low and high E_i is uncertain and is an important topic for future studies.

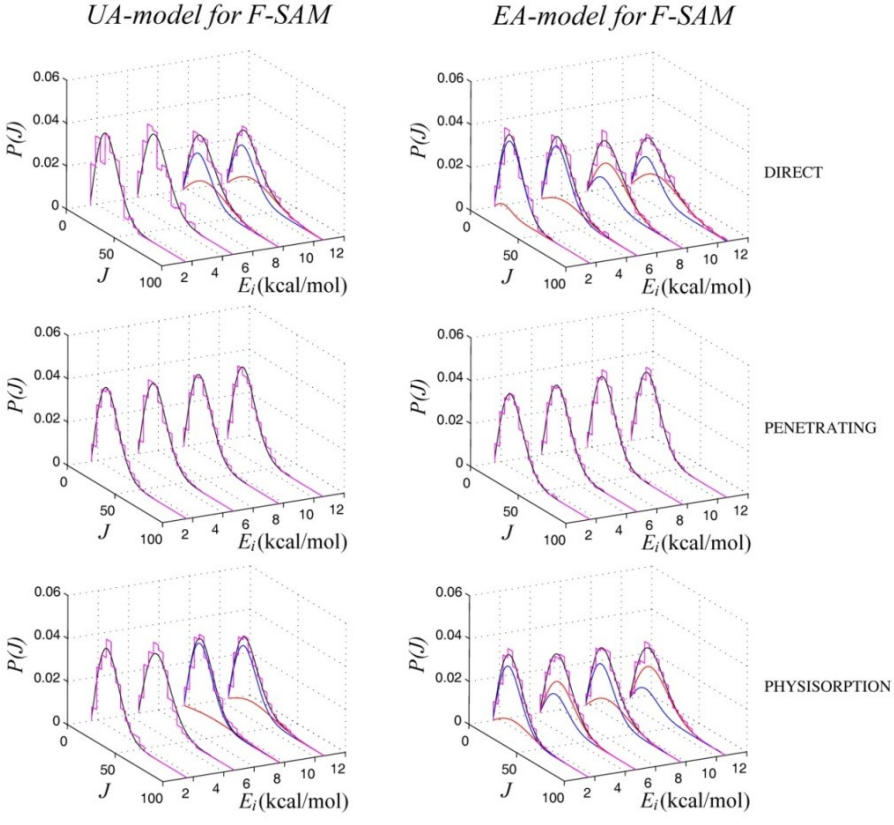

Figure 6.9: Distributions of the CO_2 rotational quantum number for different trajectory types as a function of the collision energy. Lines in black are fits to equation 6.8 (see text). When $\alpha_{LT} < 1$, the LT and HT components are shown by lines in blue and red, respectively.

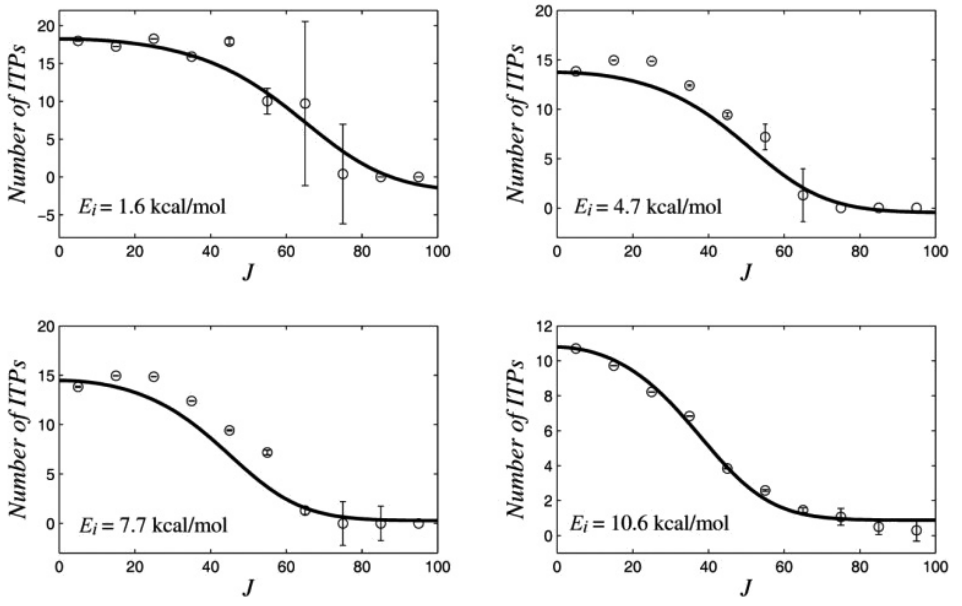

Figure 6.10: Distributions of inner turning points as a function of J for the different collision energies and for the EA model (circles) and fits of equation 6.10 to the distributions (solid lines).

3.5 Translational energy distributions

The final translational energy distributions $P(E_f)$ of the scattered CO_2 molecules are depicted in Figure 6.11 for both the UA and EA models of the surface and for different trajectory types. Usually,[3,4,12,37-45] in analyses of experiments the fraction of TD is identified as the fraction of the translational energy distribution of the scattered species, $P(E_f)$, that can be fit to a Maxwell-Boltzmann distribution for thermal desorption;[46] i.e.

$$P(E_f) = \frac{1}{(k_B T_s)^2} E_f e^{-\frac{E_f}{k_B T_s}} \tag{6.11}$$

where k_B is Boltzmann's constant, E_f is the final translational energy of the scattered gas particle, and T_s is the surface temperature. The remaining higher energy component of the distribution is then assigned to inelastic scattering (IS). However, as will be discussed below, there are uncertainties in this approach; for instance, classical trajectory simulations of Ne scattering off SAMs adsorbed on Au(111) have shown that a Boltzmann component in $P(E_f)$ does not necessarily arise from a trapping desorption intermediate.[22,23,47,48] Therefore, in the present study we did not fit our $P(E_f)$ distributions to equation 6.11. The following two-temperature Boltzmann distribution was used instead:

$$P(E_f) = \frac{\alpha_{LT}}{\left(k_B T_{trans}\,(LT)\right)^2} E_f\, e^{-\frac{E_f}{k_B T_{trans}\,(LT)}} + \frac{(1-\alpha_{LT})}{\left(k_B T_{trans}\,(HT)\right)^2} E_f\, e^{-\frac{E_f}{k_B T_{trans}\,(HT)}} \quad (6.12)$$

where, as in the $P(J)$ distributions, LT and HT are the low-temperature and high-temperature components of the distribution. The results of these fits can be compared directly with those to the $P(J)$ distributions.

The $P(E_f)$ distributions corresponding to direct trajectories in Figure 6.11 can not be fit with equation 6.12; the lines in black for these trajectories are fits obtained using the method of Legendre moments.[49] In contrast, the distributions of physisorption and penetration trajectories are fit by equation 6.12. The results of the fits are collected in Table 6.5. Penetration trajectories have $P(E_f)$ distributions that are very well fit with α_{LT} = 1, with temperatures close to the surface temperature of 300 K for all incident energies. For physisorption trajectories at E_i of 7.7 and 10.6 kcal/mol, α_{LT} is in the range 0.30-0.52 with the temperatures of the HT component being in the range (491-847 K). For those cases in which α_{LT} is less than unity, the blue lines in Figure 6.11 give the LT component and the lines in red correspond to the HT component.

Table 6.5: Parameters for the Boltzmann fits to the $P(E_f)$ distributions.

E_i (kcal/mol)	United Atom Model			Explicit Atom Model		
	α_{LT}	$T_{trans}(LT)$	$T_{trans}(HT)$	α_{LT}	$T_{trans}(LT)$	$T_{trans}(HT)$
Total trajectories						
1.6	1	292±1	-	0.91±0.01	300	533±31
4.7	1	326±1	-	0.61±0.01	300	484±8
7.7	0.68±0.01	300	630±22	0.34±0.01	300	593±5
10.6	0.70±0.01	300	686±13	0.34±0.00	300	861±6
Penetrating trajectories						
1.6	1	290±1	-	1	310±1	-
4.7	1	293±2	-	1	313±1	-
7.7	1	284±1	-	1	326±1	-
10.6	1	280±2	-	1	305±1	-
Physisorption trajectories						
1.6	1	293±1	-	0.99±0.00	300	1354±478
4.7	1	331±1	-	0.71±0.03	300	502±26
7.7	0.41±0.01	300	491±6	0.39±0.01	300	658±8
10.6	0.52±0.01	300	567±12	0.30±0.00	300	847±5

In general, the $P(E_f)$ distributions of physisorption trajectories and those of all the trajectories (total) are very similar to each other. The $P(E_f)$ distributions of penetrating trajectories peak at smaller E_f. The distributions of direct trajectories are broader and peak at much higher E_f. On the other hand, the $P(E_f)$ distributions for the EA model of the surface are much broader than those for the UA model, which is consistent with the fact that the UA model leads to more energy transfer to the surface, as indicated above, and to a lesser percentage of the high energy component in comparison with the EA model.

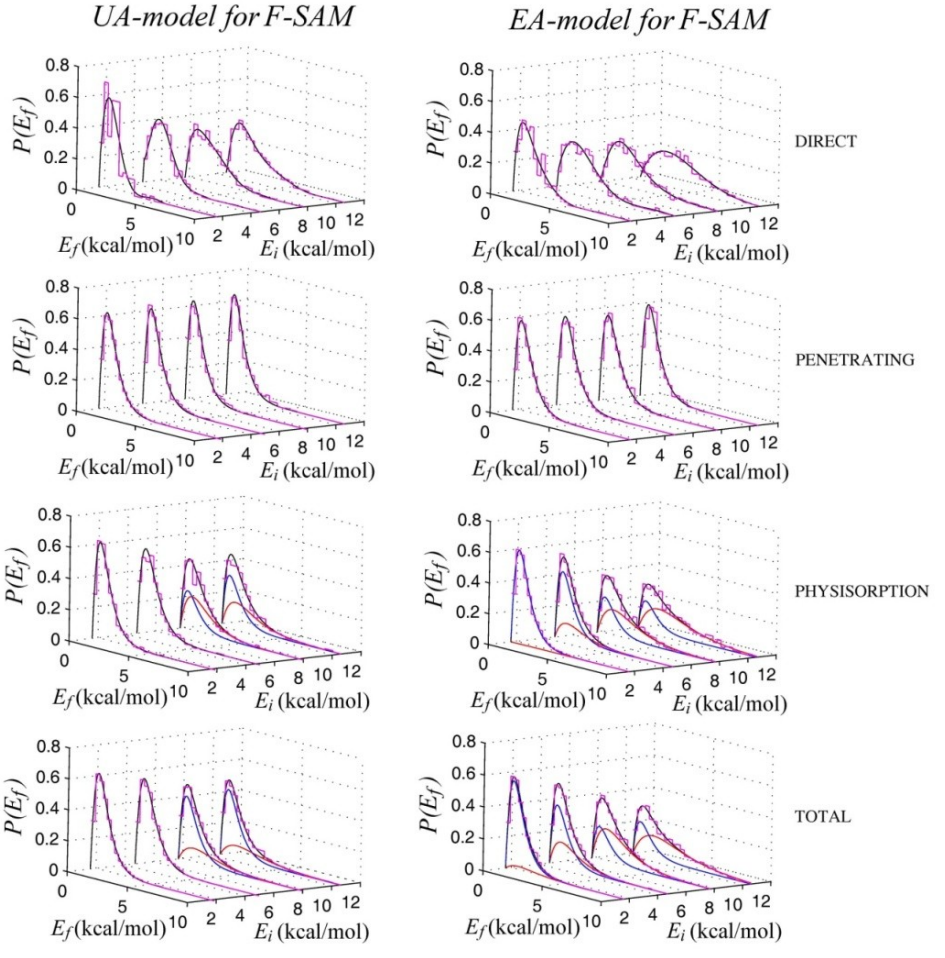

Figure 6.11: Distributions of the translational energy of the scattered CO_2 molecules for the different trajectory types as a function of collision energy. Histograms are the simulation results and lines are fits to Maxwell-Boltzmann distributions (see text) except for direct trajectories where the lines are Legendre fits.

3.6 Percentages of low-temperature and high-temperature

Figure 6.12 compares the fraction of LT extracted from the $P(E_f)$ distributions, $\alpha_{LT}(E_f)$, with those obtained from the analysis of the $P(J)$ distributions, $\alpha_{LT}(J)$, and with the sum of penetration and physisorption trajectories for both the UA and EA models. In general, the three fractions decrease with increasing collision energy. Exceptions occur for the UA model, as $\alpha_{LT}(E_f)$ and the sum of penetration and physisorption trajectories increase for the highest energy. In addition, the LT component becomes considerably less important at the highest E_i for the EA model.

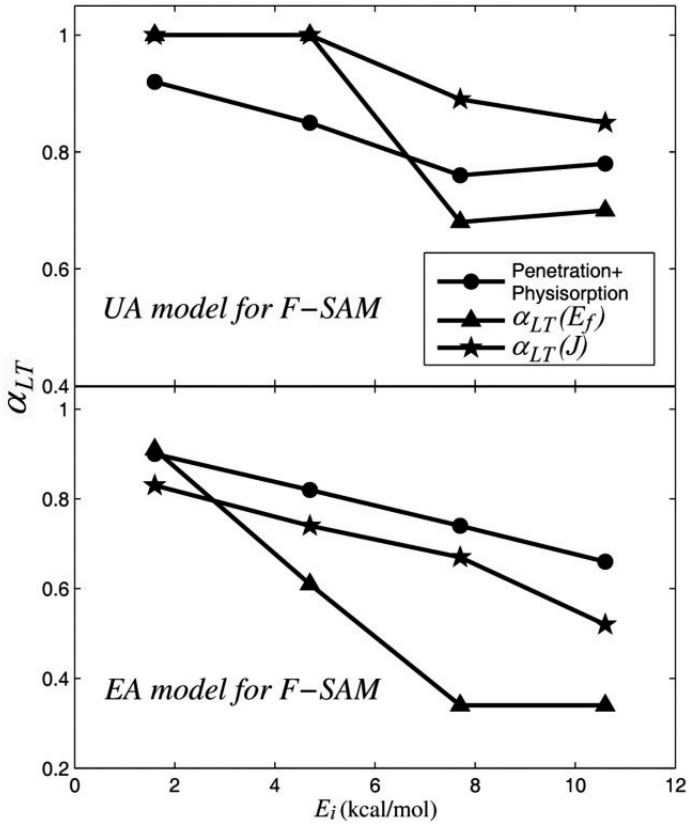

Figure 6.12: Variation of the trapping-desorption coefficients as a function of collision energy. These coefficients were obtained from the rotational and translational distributions and are compared in the figure with the sum of penetration and physisorption trajectories.

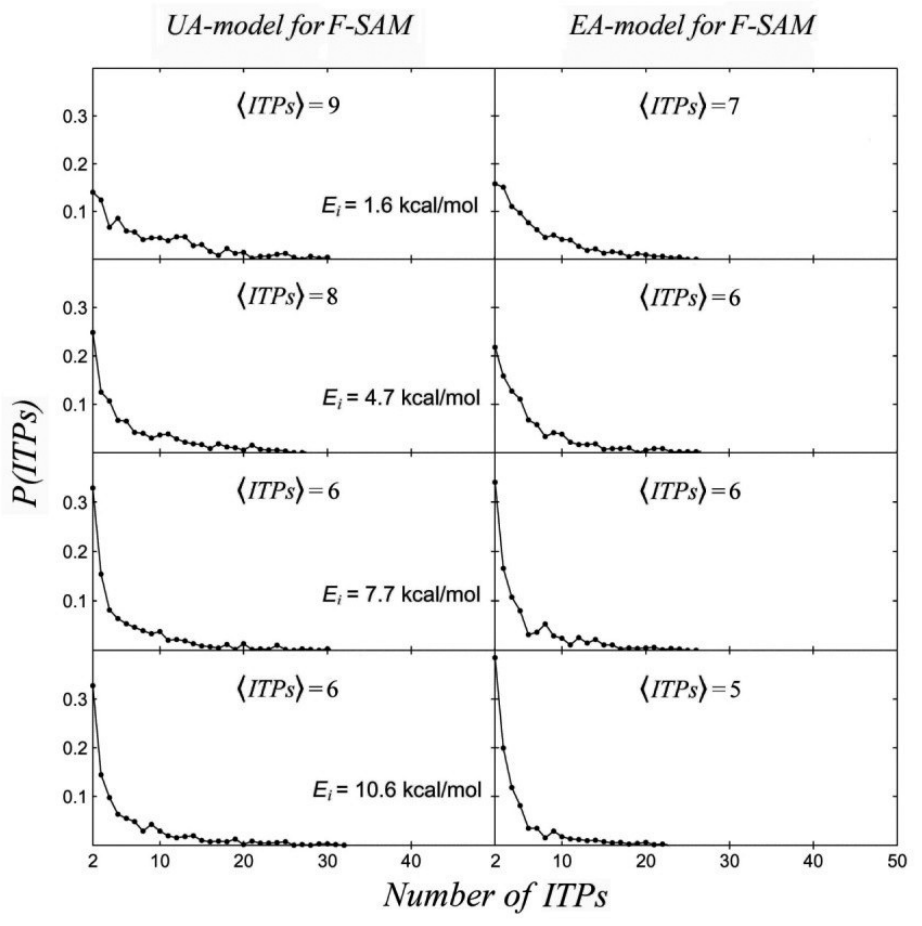

Figure 6.13: Distributions of inner turning points for physisorption trajectories as a function of collision energy.

For Ar scattering off an F-SAM surface,[29] we previously found that α_{LT} (denoted as α_{TD} in that paper) is not equivalent to either the fraction of physisorption or penetration events, or their combination. This is also observed in the present work. In a previous study of Ne scattering off SAMs by Hase and co-workers,[22,47,48] a fraction of trajectories associated with the Boltzmann component in the $P(E_f)$ distributions were found to be direct, which, to some extent, may explain the differences in Figure 6.12. Additionally, a fraction of trajectories associated with the high temperature component can be formed by physisorption trajectories as well. Figure 6.13 shows the distributions of ITPs for physisorption trajectories. As seen in the figure, all distributions peak at ITPs = 2, which means that a significant fraction of physisorption trajectories may not be completely thermalized, and therefore these trajectories could be associated to the LT component. The distributions of ITPs become narrower as

the collision energy increases, and an important number of physisorption trajectories have only just a few ITPs. The distributions of number of ITPs as a function of collision energy are similar for the EA and UA models, although the percentages of physisorption trajectories obtained with both models differ significantly from each other.

3.7 Scattering angle distributions

For each collision energy, we analyzed the distributions of the angles formed between the final CO_2 center-of-mass velocity vector and the surface normal (θ_f). These scattering angle distributions, $P(\theta_f)$, are displayed in Figure 6.14. The average values of the scattering angles are collected in Table 6.6. The dashed line in each plot of the figure is the expected distribution for random scattering ($\sin\theta\cos\theta$).[47] In only one plane perpendicular to the surface, the random distribution would be given by $\cos\theta$.[50] If we analyze separately direct, physisorbing, and penetrating trajectories, we observe clear differences between the corresponding distributions. The distributions for penetrating trajectories are more random and are in excellent agreement with the random scattering model. In contrast, the distributions for direct scattering are shifted towards lower θ_f and those for physisorption (shifted towards higher θ_f). This tendency becomes more pronounced as the collision energy increases.

The result that the physisorption trajectories do not follow a $\sin\theta\cos\theta$ distribution can be explained by the fact that, as shown above (see Figure 6.13), a significant fraction of them have a small number of ITPs, which means that the time period of interaction with the surface is relatively small and insufficient for complete thermalization. Actually, we found here and in previous work[29] that if we increase the minimum number of ITPs in the criterion for identifying a trajectory as being of the physisorption type, the average scattering angle decreases approaching the average value of 45º for random scattering.

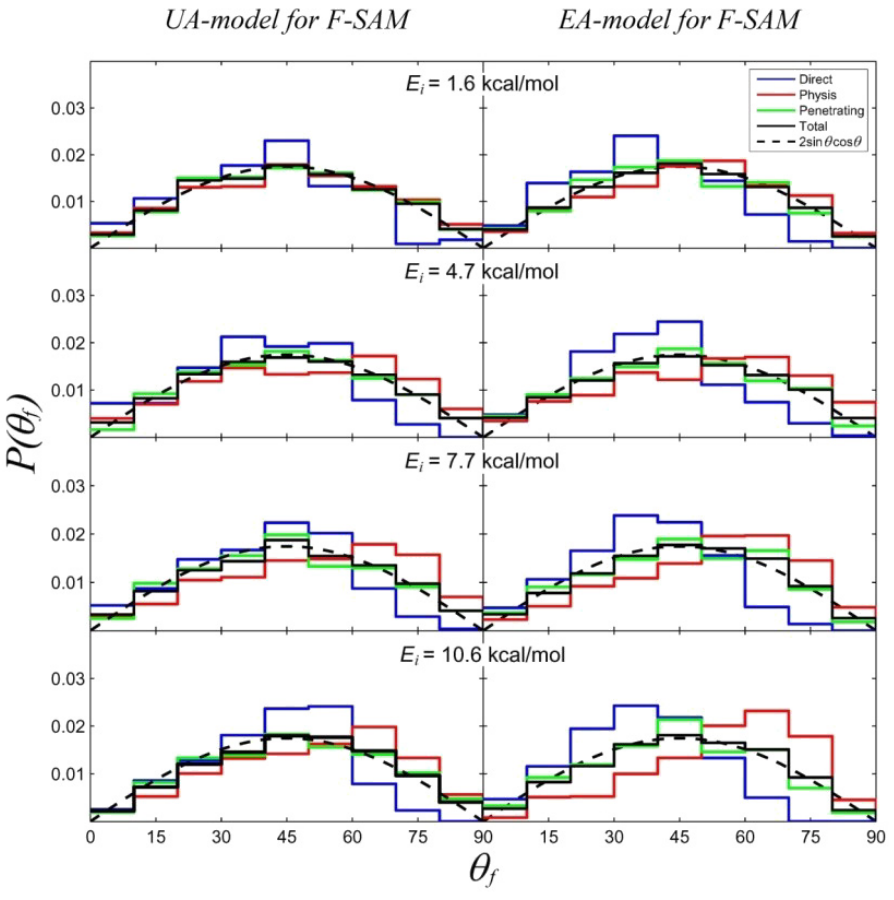

Figure 6.14: Distributions of the scattering angle as a function of the collision energy for the different trajectory types.

It is instructive to analyze whether the CO_2 molecules scatter preferentially with their angular momentum perpendicular (cartwheel type) or parallel (helicopter type) to the surface normal. Figure 6.15 shows the distributions of the angle β formed by the angular momentum of scattered CO_2 and the surface normal. All the distributions peak at or near 90 degrees, that is, CO_2 scatters preferentially in a cartwheel fashion for all collision energies, trajectory types, and surface models. The vast majority of trajectories have β values in the interval 30-150º. For a CO_2 molecule to scatter in a helicopter fashion, the collision with the surface would produce a torque in the molecule with a direction parallel to the surface normal, which is very unlikely to occur. The distributions obtained with the UA model are slightly broader than those obtained with the EA model.

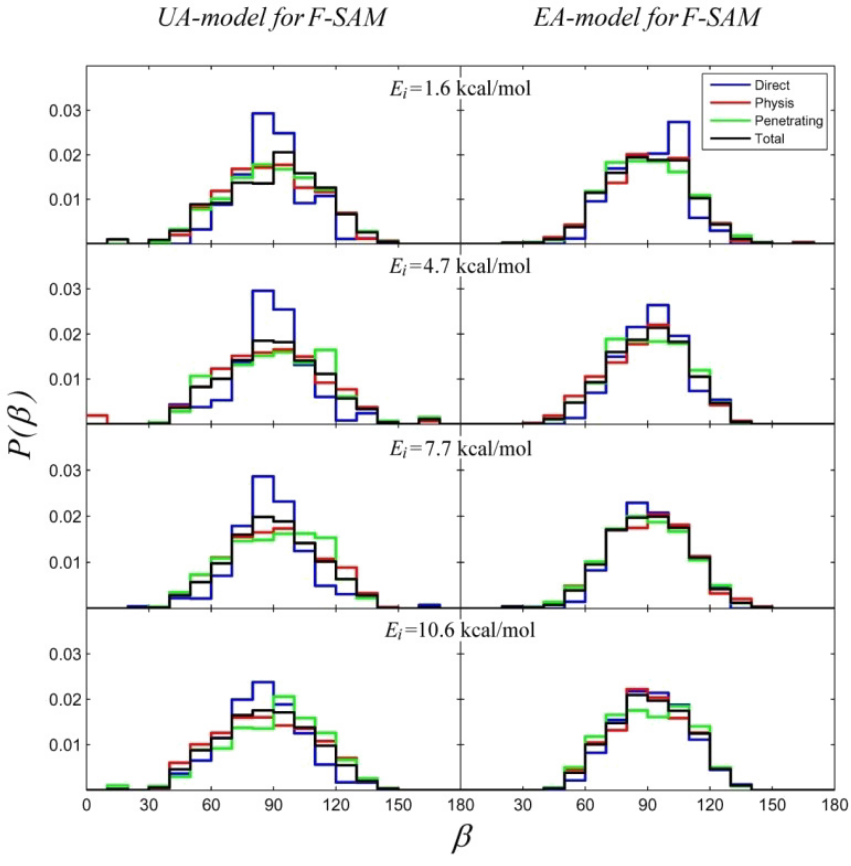

Figure 6.15: Distributions (per solid angle) of the angle formed by the angular momentum of the scattered CO_2 molecules and the surface normal (z axis in Figure 6.2) for the different trajectory types as a function of the collision energy.

Table 6.6: Average scattering angles for different trajectory types.

E_i (kcal/mol)	Direct	Penetrating	Physisorption	Total
United Atom Model				
1.6	39.4	45.8	46.4	45.6
4.7	38.8	45.7	48.1	45.4
7.7	40.4	45.2	51.5	46.1
10.6	41.4	47.0	51.0	47.3
Explicit Atom Model				
1.6	36.7	43.6	46.8	44.4
4.7	38.0	44.6	49.9	45.6
7.7	37.1	45.0	51.9	45.8
10.6	35.6	44.1	54.7	45.8

3.8 Mass and surface stiffness effects

The importance of the mass ratio in gas-surface scattering dynamics is well documented.[50-52] Previous simulations and experiments show that hydrogenated H-SAM absorbs more energy than does the fluorinated F-SAM surface.[29,40,53] In addition, results of energy transfer in Ar + H-SAM simulations[53] agree very well with those for Ar + H/F-SAM simulations,[29] where the potential energy function is that for the F-SAM surface but the masses correspond to those of the H-SAM (with H instead of F atoms). This result indicates that it is the mass, rather than the particular details of the potential energy function, that dominates the process of energy transfer to the SAM surface.

To further investigate mass effects in collisions of gases with SAMs, we carried out two additional simulations at E_i = 10.6 kcal/mol, using the EA potential function. In the first simulation, the mass of the fluorine atoms was replaced by that of hydrogen, and in the second one by the mass of chlorine. These simulations will be identified as CO_2 + H/F-SAM and CO_2 + Cl/F-SAM, respectively, following the nomenclature used in our previous study.[29] Thus, the potential energy function and parameters were the same as for CO_2 + F-SAM, and the simulations only investigated a possible mass effect. The details of these simulations are the same as those described above for CO_2 + F-SAM except that the step size for the integration of the trajectories was decreased to 0.15 fs in the CO_2 + H/F-SAM simulations in order to achieve good energy conservation.

The percentage of energy transferred to the surface is 83% in the CO_2 + H/F-SAM simulations, 67% in CO_2 + F-SAM, and 59% in CO_2 + Cl/F-SAM. These results reproduce the experimental and simulation findings[40,53] that the hydrogenated SAM absorbs more energy than does the fluorinated one, and in turn, the F-SAM absorbs more energy than does the chlorinated surface. Additionally, our simulation results indicate that a small percentage of the initial collision energy is transferred to the CO_2 internal degrees of freedom: 3% in the CO_2 + H/F-SAM simulations, 9% in CO_2 + F-SAM, and 10% in CO_2 + Cl/F-SAM. Most of the energy is transferred to the surface vibrational modes and, particularly, to the inter-chain modes of the surface, as shown in previous studies.[23,54-56] Because of the heavy mass of the alkyl chains in Cl/F-SAM and F-SAM as compared to that in H/F-SAM, the chains in the latter surface may be more mobile, which facilitates energy transfer upon collision. This effect, of decreased collisional energy transfer with decrease in surface flexibility, is consistent with a study of the Ne + H-SAM system in which energy transfer for a harmonic, single potential energy minimum model of the H-SAM was compared with that for the complete anharmonic surface model.[23] Energy

transfer is less efficient for the former surface. This effect is also seen in comparing energy transfer in collisions of Ar with the H-SAM and OH-SAM. Because of hydrogen bonding the latter is less mobile.[24]

3.9 Comparison between the EA and UA models

In this study, differences between the simulation results obtained using the UA and EA models are significant and more pronounced that those found in our previous study of Ar + F-SAM collisions.[29] In the present investigation, the residence times of penetrating trajectories calculated with the UA model are markedly higher than those obtained with the EA model. Although the percentages of direct and physisorption trajectories are more or less similar in both models, the percentage of penetrating trajectories is substantially higher for the UA model of the surface (see Figure 6.4). For the Ar + F-SAM study, the percentages of different trajectories were essentially similar for both models at the incident energy of 100 kJ/mol although the differences for E_i = 50 kJ/mol were significant.[29]

As in previous studies of the Ar + F-SAM[29] and Ne + H-SAM systems,[48] energy transfer for the EA model is less efficient than for the UA model. Specifically, energy transferred to the EA surface was approximately 12% (10%) smaller than that transferred to the UA surface in Ar + F-SAM and Ne + H-SAM, respectively. In our CO_2 + F-SAM simulations the amount of energy transferred to the EA surface is 8-13% smaller than that in the UA model for E_i between 4.7 and 10.6 kcal/mol, in agreement with the results obtained in the Ar + F-SAM and Ne + F-SAM simulations. As mentioned above, energy is transferred preferentially to the inter-chain modes, and therefore the relatively less rigid structure of the UA model, which allows more conformational changes, explains why this model absorbs more collision energy than does the EA model. An increase in the nonbonded interactions between the chains in the UA model should make the chains less loosely packed, decreasing the efficiency of energy transfer to the surface. Work in our group is directed to improve the UA model of the F-SAM surface by modifying the inter-chain interactions. Specifically, we have modified the UA model of the surface to make it stiffer and comparable to the more realistic EA model. This work is in progress in our laboratory and preliminary simulations with new inter-chain interactions in the UA model show very good agreement with EA model results.[57]

3.10 Comparison with experiment

It is important to compare our results with experimental data of Nesbitt and co-workers.[15,16] The first comparison is for the rotational quantum number distributions $P(J)$ of the scattered CO_2 projectiles. In previous work,[24] the $P(J)$ distribution obtained in our simulations for E_i = 10.6 kcal/mol was compared with the experimental one, and here we extend our previous comparison to lower incident energies. The comparison of the simulation (solid lines) and experimental (circles) $P(J)$ distributions is shown in Figure 6.16 for the four different collision energies. The simulation results for the total trajectories compare very well with the experimental results of Nesbitt and co-workers,[16] particularly for the EA model of the surface. For the UA model some differences become apparent as the collision energy increases, which may be associated with the fact that for this model there is no HT component, which makes the distributions narrower than the experimental (and EA) ones.

Tables 6.3 and 6.4 compare the fits of equation 6.8 to the simulation and experimental results. Nesbitt and co-workers fixed the LT component to 298 K in their fits, as we did for the bimodal distributions (in our case the fixed surface temperature for the bimodal distributions was 300 K instead of 298 K). For the UA model, the $P(J)$ distributions for the two lowest energies are well fit by a single Boltzmann distribution at temperatures very close to the surface temperature of 300 K. This result contrasts with the experimental fits and those for the EA-model of the surface, for which at all E_i the $P(J)$ distributions are bimodal (see Table 6.4). For the lowest E_i the value of α_{LT} obtained in the fit to the experimental distribution is 0.92, which is somewhat higher than that calculated in the present work (0.83); the temperatures of the HT component obtained in the fits to the experimental and simulation results are 330 and 430, respectively. For the remaining collision energies, the fitting parameters obtained with the EA model are in excellent agreement with the experimental parameters. We notice there is a difference with respect to the fitting reported in the previous simulations at E_i = 10.6 kcal/mol.[24] In the present case, the low temperature was not considered as a variable in the fitting, it was rather kept fixed at the surface temperature of 300 K.

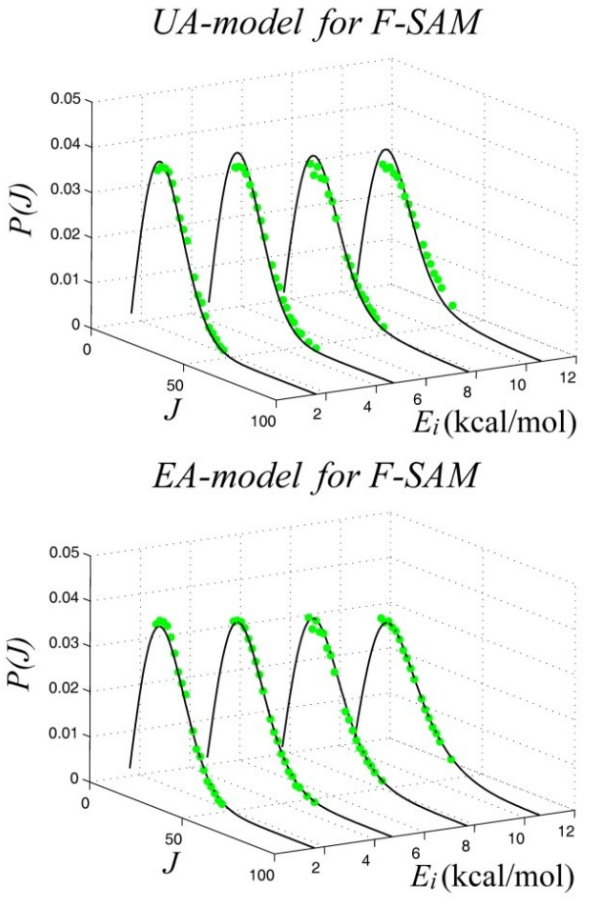

Figure 6.16: Distributions of the CO_2 rotational quantum number for total trajectories in comparison with the experimental results.[15]

The second comparison with experiment concerns the translational distributions of scattered CO_2. These were characterized and compared with the PFPE experimental results for E_i = 10.6 kcal/mol.[15] The high resolution detection scheme in the experiments measures CO_2 translational distributions parallel to the laser propagation direction. Each absorption profile reflects the distribution of velocities parallel to the surface. Explicitly, the Doppler profiles are fit to a Gaussian line shape to extract a characteristic translational temperature (T_{trans}) from the Doppler width, i. e.

$$\Delta\nu_D = 2\nu_0\sqrt{\frac{2\ln(2)k_B T_{trans}}{m_{CO_2}c^2}} \tag{6.13}$$

where ν_0 is the centerline rovibrational transition frequency of the asymmetric stretching mode in CO_2 (2419 cm^{-1} with our model potential), c is the speed of

light, k_B is the Boltzmann constant, and m_{CO_2} the mass of the CO_2 molecule. Because the scattering geometry is azimuthally symmetric about the surface normal, T_{trans} characterizes both the v_x and v_y velocity distributions of the scattered CO_2 molecule (see Figure 6.2 for the definition of the x and y axes). Results from the Dopplerimetry analysis are shown in Figure 6.17, where T_{trans} has been plotted as a function of J-state. Interestingly, the translational distributions broaden as J increases, which show the surface interactions that excite CO_2 into high rotational states also transfer energy into translation parallel to the surface. Such a single-temperature characterization of the absorption profiles has been extended with a two-temperature line shape model that incorporates low and high temperatures along with results from the two-temperature rotational state analysis. While details of the model and fits are presented elsewhere, we plot T_{trans} (LT), T_{trans} (HT) and fit results from a predicted line shape in Figure 6.17 to illustrate the two-channel dynamics within the translation of scattered CO_2.

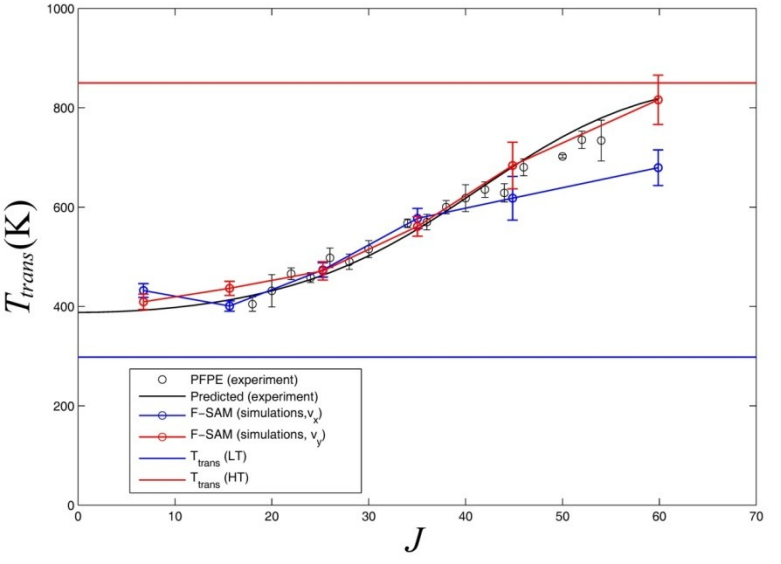

Figure 6.17: State-dependent translational energy distributions of scattered CO_2 for E_i = 10.6 kcal/mol. Circles in blue and red give the translational temperatures corresponding to the v_x and v_y velocity distributions, respectively, as calculated by the simulations (the lines are included for visual clarity). In the experiment,[15] a single-temperature line shape gives T_{trans} (J), shown as black circles, while a two-temperature line shape analysis affords T_{trans} (IS), which is represented by the red horizontal line. The black line is a single Gaussian fit for a reconstructed two-temperature line shape.[15]

To compare with experimental results, the velocity distributions from the CO_2 + F-SAMs simulations are characterized with a similar Dopplerimetry analysis. An accurate comparison with experimental measurements involves quantum state-dependent velocity distributions that correctly account for the absorption probability associated with the laser detection scheme. In other words, the scattered flux in the simulations must be converted into a density that is based on particular velocity components of each trajectory. J-state dependent velocity distributions are generated by first sorting trajectories into ΔJ = 10 groups, i.e. J = 0–10, 10–20, etc. Within each group, the trajectories are binned by either v_x or v_y to generate the respective velocity distribution. Instead of counting each trajectory equally within a given velocity bin, the key flux-to-density transformation weights each trajectory by the time the molecule would spend traversing across the laser beam, where the transit time is directly proportional to the probability of absorption. From the experiment configuration, we approximate the laser beam as a cylinder that passes directly above a large spot where the molecular beam strikes the surface. Based on this comparison, the transit time across the laser beam is proportional to $v_\perp^{-1}$, where $v_\perp^{-1} = \sqrt{v_x^2 + v_y^2}$ for v_y-distributions, and $v_\perp^{-1} = \sqrt{v_y^2 + v_z^2}$ for v_x-distributions. Resulting velocity histograms accurately simulate absorption profiles for scattered CO_2 that can be directly compared to the experimental Doppler profiles.

The density-based velocity distributions for the scattered trajectories once again are fit with a Gaussian line shape to extract T_{trans} along the x- and y-direction. Results of these fits are plotted in Figure 6.17 along with values for the CO_2 + PFPE experiment. Such a comparison shows nearly quantitative agreement between experiment and simulation results, where the translational distributions broaden with increasing rotational excitation. The minor discrepancy between the v_x- and v_y-distributions reflects the degree of order of the F-SAM surface, where the orientation of the terminal CF_3 group is different between the two directions. Such a difference is not to be expected for the PFPE liquid surface since the time-averaged motions of the surface groups randomly sample a variety of orientations. In parallel with the rotational state populations, the dynamics illustrated within the translation of scattered CO_2 appears to be nearly the same between the F-SAM and PFPE liquid surface, where dynamical motion of surface groups appear to be nearly the same between the two surfaces.

4. CONCLUSIONS

Classical trajectory calculations were carried out to further investigate the dynamics of collisions of CO_2 with an F-SAM on gold. The present study reports simulations for collision energies of 1.6, 4.7, 7.7, and 10.6 kcal/mol, and with the incident direction of the CO_2 molecules perpendicular to the surface. The results of these simulations are compared with experimental data obtained for collisions of CO_2 with liquid surfaces of PFPE. Although at first sight the structures of F-SAM and liquid PFPE may appear to be very different in nature, it has been shown that both surfaces exhibit similar energy transfer efficiencies as well as similar ion-surface reactions[25]. The simulations were performed with both an EA and UA model potential energy function for the F-SAM surface.

The calculations show significant differences between the results obtained with the EA model and those given by the UA model. For example, the percentage of penetrating trajectories predicted by the latter model is much higher than that calculated by the former, and the residence times of this trajectory type computed with the UA model are substantially longer than those calculated with the EA model. These results are associated with the fact that the UA model overestimates the efficiency of energy transfer in comparison with the EA model. Specifically, and in agreement with previous work on Ar + F-SAM and Ne + SAMs, the energy transferred to the UA surface is about 10% higher than that transferred to the EA surface. The reason for this is that the structure of the UA surface is less stiff than that of the EA surface, thus facilitating the transfer of collision energy to inter-chain modes. Our group is currently working on the refinement of the UA model of the F-SAM.[57] In particular, the representation of the nonbonded interaction terms in the new UA model, which have been shown to play a determinant role in energy transfer efficiencies in collisions of projectile gases with self-assembled monolayers, will be improved. As a reference, we will use the EA force field of F-SAM. As in the EA model, the improved UA force fields will employ Buckingham potentials, rather than the Lennard-Jones functions utilized in the original UA model. The parameterizations will be based on fits to potential energy curves of interacting fragments (e.g., $CF_3\cdots CF_3$ or $CF_2\cdots CF_2$), calculated with the EA force field. Preliminary results[57] shows that the new UA model agrees much better with the EA model (in terms of energy transfer efficiencies, *P(J)* and $P(E_f)$ distributions, etc…) for CO_2 scattering off an F-SAM surface.

The simulations corroborate the important role of the masses in the process of energy transfer. Changing the mass of the fluorine atoms by that of hydrogen or of chlorine, while keeping the parameters of the potential energy

functions unchanged in order to investigate pure mass effects, we find that the efficiency of energy transfer is highest when the mass is that of hydrogen. Specifically, for E_i = 10.6 kcal/mol, the percentage of energy transferred to the surface is 83% for CO_2 + H/F-SAM collisions (mass of F atoms replaced by that of H atoms), 67% for CO_2 + F-SAM, and 59% for CO_2 + Cl/F-SAM (mass of F atoms replaced by that of Cl atoms). This trend follows the observation that energy transfer for collisions with hydrogenated SAM is more efficient than for halogenated SAMs, and may be explained by the decrease in chain flexibility as the masses of the chain atoms increase.

The rotational quantum number distributions $P(J)$ of the scattered CO_2 molecules predicted by the simulations using the EA model are in very good agreement with the corresponding experimental distributions for CO_2 + PFPE. In general, the $P(J)$ distributions for the total trajectories are bimodal, with the percentage of high temperature increasing with collision energy. For the two lowest energies, the distributions obtained with the UA model do not follow this pattern and can be fit to a single Boltzmann expression. These UA distributions differ somewhat from the experimental ones, especially as the collision energy increases. The UA distributions are slightly narrower than the experimental and EA distributions because of the lack of the high temperature component.

The translational temperatures calculated by the simulations are in quantitative agreement with those extracted from the experimental measurements. In both cases, T_{trans} increases with J. However, minor differences appear between theoretical and experimental results, where the simulations predict distinct temperatures for the v_x and v_y components. This is a consequence of the ordered structure of the F-SAM surface, which makes the x and y directions non-equivalent. In liquid PFPE, however, the random motion of the surface groups, when averaged in time, makes the x and y directions equivalent.

REFERENCES

(1) Saecker, M. E.; Govoni, S. T.; Kowalski, D. V.; King, M. E.; Nathanson, G. M. *Science* **1991**, *252*, 1421.

(2) Kenyon, A. J.; McCaffery, A. J.; Quintella, C. M.; Zidan, M. D. *Chemical Physics Letters* **1992**, *190*, 55.

(3) Saecker, M. E.; Nathanson, G. M. *The Journal of Chemical Physics* **1993**, *99*, 7056.

(4) King, M. E.; Nathanson, G. M.; Hanning-Lee, M.; Minton, T. K. *Physical Review Letters* **1993**, *70*, 1026.

(5) Saecker, M. E.; Nathanson, G. M. *The Journal of Chemical Physics* **1994**, *100*, 3999.

(6) King, M. E.; Saecker, M. E.; Nathanson, G. M. *The Journal of Chemical Physics* **1994**, *101*, 2539.

(7) Nathanson, G. M.; Davidovits, P.; Worsnop, D. R.; Kolb, C. E. *J. Phys. Chem.* **1996**, *100*, 13007.

(8) King, M. E.; Fiehrer, K. M.; Nathanson, G. M.; Minton, T. K. *J. Phys. Chem. A* **1997**, *101*, 6556.

(9) Ringeisen, B. R.; Muenter, A. H.; Nathanson, G. M. *J. Phys. Chem. B* **2002**, *106*, 4988.

(10) Ringeisen, B. R.; Muenter, A. H.; Nathanson, G. M. *J. Phys. Chem. B* **2002**, *106*, 4999.

(11) Manning, M.; Morgan, J. A.; Castro, D. J.; Nathanson, G. M. *The Journal of Chemical Physics* **2003**, *119*, 12593.

(12) Nathanson, G. M. *Annual Review of Physical Chemistry* **2004**, *55*, 231.

(13) Zhang, J.; Garton, D. J.; Minton, T. K. *The Journal of Chemical Physics* **2002**, *117*, 6239.

(14) Kelso, H.; Kohler, S. P. K.; Henderson, D. A.; McKendrick, K. G. *The Journal of Chemical Physics* **2003**, *119*, 9985.

(15) Perkins Jr., B. G.; Haeber, T.; Nesbitt, D. J. *J. Phys. Chem. B* **2005**, *109*, 16396.

(16) Perkins Jr., B. G.; Nesbitt, D. J. *J. Phys. Chem. B* **2006**, *110*, 17126.

(17) Perkins Jr., B. G.; Nesbitt, D. J. *J. Phys. Chem. A* **2007**, *111*, 7420.

(18) Perkins Jr., B. G.; Nesbitt, D. J. *J. Phys. Chem. B* **2008**, *112*, 507.

(19) Zolot, A. M.; Harper, W. W.; Perkins, B. G.; Dagdigian, P. J.; Nesbitt, D. J. *The Journal of Chemical Physics* **2006**, *125*, 021101.

(20) Garton, D. J.; Minton, T. K.; Alagia, M.; Balucani, N.; Casavecchia, P.; Volpi, G. G. *The Journal of Chemical Physics* **2000**, *112*, 5975.

(21) Perkins, B. G., Jr; Nesbitt, D. J. *Proc. Natl. acad. sci.* **2008**, *105*, 12684.

(22) Yan, T.; Hase, W. L.; Barker, J. R. *Chem. Phys. Lett.* **2000**, *329*, 84.

(23) Yan, T.; Isa, N.; Gibson, K. D.; Sibener, S. J.; Hase, W. L. *J. Phys. Chem. A* **2003**, *107*, 10600.

(24) Martínez-Núñez, E.; Rahaman, A.; Hase, W. L. *J. Phys. Chem. C* **2007**, *111*, 354.

(25) Tasic, U.; Day, B. S.; Yan, T.; Morris, J. R.; Hase, W. L. *J. Phys. Chem. C* **2008**, *112*, 476.

(26) Pradeep, T.; Miller, S. A.; Cooks, R. G. *J. Am. Soc. Mass Spectrom.* **1993**, *4*, 769.

(27) Ramasamy, S.; Pradeep, T. *J. Chem. Phys.* **1995**, *103*, 485.

(28) Harris, J. G. *J. Phys. Chem.* **1992**, *96*, 5077.

(29) Vazquez, S. A.; Morris, J. R.; Rahaman, A.; Mazyar, O. A.; Vayner, G.; Addepalli, S. V.; Hase, W. L.; Martinez-Nunez, E. *J. Phys. Chem. A* **2007**, *111*, 12785.

(30) Allen, M. P.; Tildesley, D. J. *Computer Simulation of Liquids*; Clarendon Press: Oxford, 1987.

(31) VENUS05 is an enhanced version of VENUS96, with additional algorithms. VENUS96 is available on the website cdssim.chem.ttu.edu and was initially released through the Quantum Chemistry Program Exchange (QCPE) Bulletin **1996**, *16*, 671.

(32) Meroueh, O.; Hase, W. L. *J. Am. Chem. Soc.* **2002**, *124*, 1524.

(33) Wang, J.; Meroueh, S. O.; Wang, Y.; Hase, W. L. *Int. J. Mass. Spectr.* **2003**, *230*, 57.

(34) Song, K.; Meroueh, O.; Hase, W. L. *J. Chem. Phys.* **2003**, *118*, 2893.

(35) Yang, L.; Mazyar, O. A.; Lourderaj, U.; Wang, J.; Rodgers, M. T.; Martinez-Nunez, E.; Addepalli, S. V.; Hase, W. L. *J. Phys. Chem. A* **2008**, *(submitted)*.

(36) Levine, R. D.; Bernstein, R. B. *Molecular Reaction Dynamics and Chemical Reactivity*; Oxford University Press: New York, 1987.

(37) Cohen, S. R.; Naaman, R.; Sagiv, J. *Phys. Rev. Lett.* **1987**, *58*, 1208.

(38) Paz, Y.; Naaman, R. *J. Chem. Phys.* **1991**, *94*, 4921.

(39) Day, B. S.; Morris, J. R. *J. Phys. Chem. B* **2003**, *107*, 7120.

(40) Gibson, K. D.; Isa, N.; Sibener, S. J. *J. Chem. Phys.* **2003**, *119*, 13083.

(41) Day, B. S.; Shuler, S. F.; Ducre, A.; Morris, J. R. *J. Chem. Phys.* **2003**, *119*, 8084.

(42) Hwang, G. S.; Anderson, C. M.; Gordon, M. J.; Moore, T. A.; Minton, T. K.; Giapis, K. P. *Phys. Rev. Lett.* **1996**, *77*, 3049.

(43) Minton, T. K.; Giapis, K. P.; Moore, T. *J. Phys. Chem. A* **1997**, *101*, 6549.

(44) Hurst, J. E.; Becker, C. A.; Cowin, J. P.; Janda, K. C.; Wharton, L.; Auerbach, D. J. *Phys. Rev. Lett.* **1979**, *43*, 1175.

(45) Rettner, C. T.; Schweizer, E. K.; Mullins, C. B. *J. Chem. Phys.* **1989**, *90*, 3800.

(46) Grimmelmann, E. K.; Tully, J. C.; Cardillo, M. J. *J. Chem. Phys.* **1980**, *72*, 1039.

(47) Yan, T.; Hase, W. L. *Phys. Chem. Chem. Phys* **2000**, *2*, 901.

(48) Yan, T.; Hase, W. L. *J. Phys. Chem. B* **2002**, *106*, 8029.
(49) Aoiz, F. J.; BanÌfares, L. *J. Phys. Chem.* **1996**, *100*, 18108.
(50) Goodman, F. O.; Wachman, H. Y. *Dynamics of Gas-Surface Scattering*; Academic Press: New York, 1976.
(51) Harris, J. Mechanical Energy Transfer in Particle-Surface Collisions. In *Dynamics of Gas-Surface Interactions*; Rettner, C. T., Ashfold, M. N. R., Eds.; Royal Society of Chemistry: Cambridge, U. K., 1991.
(52) Szabo, T. J.; Siavosh-Haghighi, A.; Adams, J. E. *J. Phys. Chem. B* **2006**, *110*, 1319.
(53) Day, B. S.; Morris, J. R.; Troya, D. *J. Chem. Phys.* **2005**, *122*, 214712.
(54) Isa, N.; Gibson, K. D.; Yan, T.; Hase, W.; Sibener, S. J. *J. Chem. Phys*. **2004**, *120*, 2417.
(55) Yan, T.; Hase, W. L. *J. Phys. Chem. A* **2001**, *105*, 2617.
(56) Yan, T.; Hase, W. L.; Tully, J. C. *J. Chem. Phys*. **2004**, *120*, 1031.
(57) Nogueira, J. J.; Martinez-Nunez, E.; Vazquez, S.; *J. Phys. Chem. C* **2009**, *113*, 3300.

Chapter 7

Dynamics of CO_2/F-SAM: United Atom Models

1. INTRODUCTION

Self-assembled monolayers (SAMs) of organic molecules chemisorbed on solid surfaces have attracted much attention due to their wide potential for technological and biological applications.[1] One of the interesting features of SAMs is that they exhibit a highly order and well-characterized structure, which makes them convenient materials for investigating the dynamics of collisions of gases with organic surfaces. Computer simulations involving SAMs usually employ models based on molecular mechanics force fields,[2-23] which are basically of two types: all-atom (AA) models, where all atoms are taken into account in the force field, and united-atom (UA) models, in which specific groups of atoms (e.g., $-CH_3$, and $-CH_2-$ in alkyl chains) are regarded as single pseudo-atoms. Clearly, the number of interactions in the force field decreases substantially in the latter approach, thus reducing the CPU time in the simulations. Therefore, the development of accurate UA force fields of SAMs is important for practical applications of molecular dynamics simulations.

In recent classical trajectory simulations of Ar scattering off a perfluorinated octanethiol self-assembled monolayer (F-SAM) surface,[18] we observed discrepancies between the results obtained with AA and UA models of the F-SAM. For example, there is a difference in the percentages of direct trajectories that are direct scattering at an incident energy of 12 kcal/mol with the AA and UA models. In addition, at this collision energy, the energy transfer to the AA surface is 12% less efficient than that to the UA surface.[18] Similar results (differences of about 10% in energy transfer efficiencies) were also found in CO_2 + F-SAM[24] and Ne + alkyl thiolate SAM simulations.[8] These discrepancies in energy transfer efficiencies calculated with the UA and AA models have been explained on the basis of a less stiff structure of the UA model, which allows the surface to absorb the collision energy more easily by conformational changes.[8] The van der Waals interactions between the chains in the monolayer determine the density and stiffness of the models used to represent the surfaces. A decrease in the nonbonded interactions between the chains makes them more loosely packed, which results in an increase in the energy transfer efficiency due to the lower barrier for conformational changes. In fact, it was shown that increasing the surface density of an alkanethiolate SAM leads to a decrease in the energy transfer in collisions with projectile Ar atoms.[15,25]

Additionally, trajectory calculations of Ar colliding with an isolated chain of F-SAM showed that energy transfer is ≈9% less efficient when the isolated chain is represented by the UA model.[18] A similar trend was found for

collisions of Ar atoms with the simple molecule C_2F_6, using the AA and UA force fields. These tests corroborate that, to a large extent, the inter-chain interactions are responsible for the differences between the results obtained with the UA and AA models of the surface.

The AA model of the F-SAM surface employed in previous simulations[17,18,22,26] is based on a force field of perfluoroalkanes developed by fits to ab initio data.[27] Nonbonded interactions in this force field are represented by two-body Buckingham potentials. The repulsion parameters were fitted to model interaction energies of the CF_4 dimer calculated at the Hartree-Fock level. The dispersion parameters were approximated by the London formula,[28] employing the dipole polarizability and ionization potential of carbon and fluorine atoms, and subsequently scaled by the same factor in order to reproduce the density of C_7F_{16} liquid at 298 K. On the other hand, the UA model of the F-SAM uses parameters taken from various force fields.[2,29-33] The van der Waals interactions in the current UA model of F-SAM are described by Lennard-Jones 6-12 potentials, with parameters adjusted to reproduce the vapor pressure and saturated liquid density of perfluorohexane.[33]

In the present paper, we focus on the improvement of the current UA model, taking as a test system CO_2 + F-SAM, which has been extensively studied in recent years by Nesbitt, Hase, and their co-workers.[17,26,34-38] Actually, the experimental investigations were performed with perfluoropolyether (PFPE) liquid surfaces, rather than with F-SAM surfaces. However, it was found that the surface of PFPE is essentially constituted by terminal $–CF_3$ groups,[39] and that both type of surfaces (PFPE and F-SAM) exhibit similar translational to vibrational energy transfer efficiencies as well as similar ion-surface reactions.[40] These observations suggest that energy transfer in gas-surface collisions is mostly controlled by the chemical nature of the outermost layer of the surface and not by the structure of the interfacial material. Consequently, results of simulations of collisions of CO_2 molecules with F-SAM surfaces can be directly compared with experimental data on CO_2 + PFPE, provided the initial conditions in the simulations are correctly selected in order to mimic the experiments.

Since the results of CO_2 + F-SAM simulations performed with the AA force field are, in general, in good agreement with experiment,[24,26,34,35] and nonbonded interactions between the chains of the F-SAM play a critical role in the energy transfer upon collisions with the projectile gas, our strategy here was to refine the van der Waals terms in the UA force field by fits to AA interaction potentials, as described in the next section. After the reparameterization process, we performed classical trajectory simulations on CO_2 + F-SAM, using the UA approach and at collision energies considered in previous experimental CO_2 + PFPE scattering experiments,[34,35] specifically, 10.6 and 7.7 kcal/mol.

Several UA parameterizations will be discussed, which, in general, improve the performance of the current UA model.

2. COMPUTATIONAL DETAILS

2.1 Potential energy surfaces

The potential energy surface for the system is:

$$V = V_{CO_2} + V_{UA-FSAM} + V_{inter} \tag{7.1}$$

where V_{CO_2} is the potential for carbon dioxide, $V_{UA-FSAM}$ is the united-atom potential for the F-SAM surface, and V_{inter} is the interaction potential between CO_2 and the surface. The potential function for the CO_2 molecule, V_{CO_2}, was obtained in previous work,[17] and consists of a sum of harmonic functions for the two stretchings and the bending, with force constants adjusted to reproduce the experimental vibrational frequencies and the zero-point energy of the molecule.[41-43]

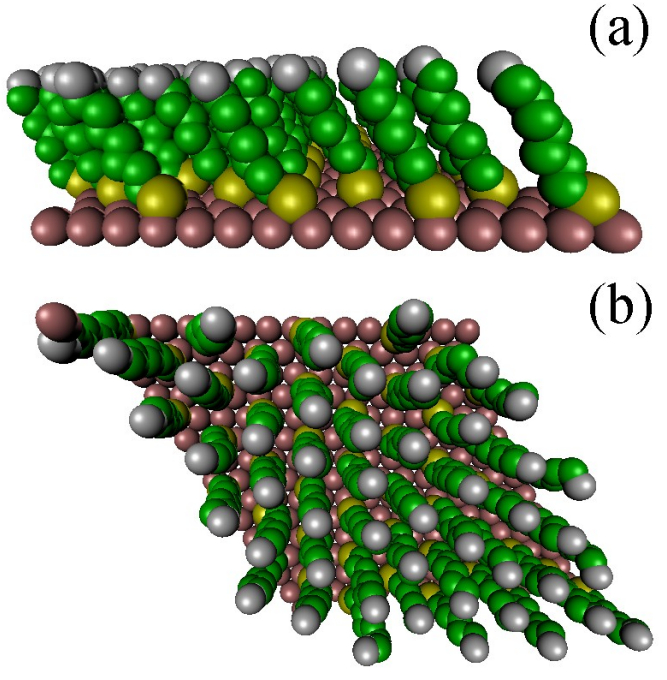

Figure 7.1: (a) A side view and (b) a top view of the united atom model for the F-SAM used in this work.

The F-SAM surface comprises 48 chains of perfluorinated octanethiol radicals adsorbed on a single layer of 196 frozen Au atoms (see Figure 7.1). As mentioned before, in the UA approach the CF_3 and CF_2 units are represented as single (pseudo) atoms. The S atoms of the $CF_3(CF_2)_7S$ chains are located 1.931 Å above the Au(111) surface[2] in close-packed rows rotated 30º from the close-packed rows of gold atoms,[44] resulting in a closest neighbor chain-chain distance of 5.776 Å. In all the UA models presented in this work, the potential energy function is written as sums of nonbonded interactions, $V^{NB}(r_{ij})$, bond stretchings, $V^{S}(r_{ij})$, bendings, $V^{B}(\theta_{ijk})$, and torsions, $V^{T}(\varphi_{ijkl})$:

$$V_{UA-FSAM} = \sum_{i<j} V^{NB}(r_{ij}) + \sum_{i,j} V^{S}(r_{ij}) + \sum_{i,j,k} V^{B}(\theta_{ijk}) + \sum_{i,j,k,l} V^{T}(\varphi_{ijkl}) \tag{7.2}$$

The stretching and bending interactions for atoms i, j, and k are represented by harmonic functions

$$V^{S}(r_{ij}) = 0.5k^{S}_{\alpha\beta}(r_{ij} - r^{0}_{\alpha\beta})^2 \tag{7.3}$$

$$V^{B}(\theta_{ijk}) = 0.5k^{B}_{\alpha\beta\gamma}(\theta_{ijk} - \theta^{0}_{\alpha\beta\gamma})^2 \tag{7.4}$$

where $r^{0}_{\alpha\beta}$ is the equilibrium bond length for atom types α and β (CF_3 and CF_2 united atoms, S, and Au), $\theta^{0}_{\alpha\beta\gamma}$ is the equilibrium bond angle for atom types α, β, and γ, and $k^{S}_{\alpha\beta}$ and $k^{B}_{\alpha\beta\gamma}$ are the stretching and bending force constants, respectively. Torsional terms are given by cosine series

$$V^{T}(\varphi_{ijkl}) = \sum_{n} 0.5k^{T}_{n,\alpha\beta\gamma\delta}\{1 - \cos(n\varphi - \varphi^{0}_{n,\alpha\beta\gamma\delta})\} \tag{7.5}$$

where $k^{T}_{n,\alpha\beta\gamma\delta}$ and $\varphi^{0}_{n,\alpha\beta\gamma\delta}$ are torsional parameters.

As mentioned above, the objective of this paper is to devise new UA models for the F-SAM surface that reproduce the results of CO_2 + F-SAM simulations using the more realistic AA model, which were found to be in good agreement with experimental results on CO_2 + liquid PFPE.[17,24,34,35] For this purpose, we first modified the nonbonded terms of the original UA model, hereinafter called UA0. In particular, in UA0 the nonbonded interactions are represented by Lennard-Jones 6-12 potentials

$$V^{NB}_{UA0}(r_{ij}) = \frac{A_{\alpha\beta}}{r_{ij}^{12}} + \frac{B_{\alpha\beta}}{r_{ij}^{6}} \tag{7.6}$$

The values of the force-field parameters employed in UA0 were taken from the literature[2,29-33] and are collected in Table 7.1.

Table 7.1: Parameters employed in the potential energy surface of the UA0 model for the F-SAM.

Bond force-filed parameters			
Bond Type[a]	k^s(mdyn/Å)	r^0 (Å)	
Au–S	2.8	[b]	
S–CF_2	5.7	1.82	
CF_2–CF_2 , CF_2–CF_3	3.51[c]	1.53[d]	
Bond angle force-field parameters			
Bend Type[e,f]	k^B (mdyn Å/rad^2)	θ^0 (deg)	
S–CF_2–CF_2 , CF_2–CF_2–CF_2, CF_2–CF_2–CF_3	0.863	114.6	
Torsion force-field parameters			
Torsional Type[e,f]	n	k^T (kcal/mol)	φ^0(deg)
S–CF_2–CF_2–CF_2	1	7.08471554	0.0
CF_2–CF_2–CF_2–CF_2	2	4.208465094	0.0
CF_2–CF_2–CF_2–CF_3	3	5.462568782	0.0
	4	2.953659654	0.0
	5	1.726793568	0.0
	6	1.726793568	0.0
	7	0.2560869246	–180.0
Nonbonded force-field parameters			
UA Pair [f]	A[g]	B[g]	
CF_2···CF_2	77172756.95	–7633.897037	
CF_3···CF_3	24370344.30	–2410.704328	
CF_2···CF_3 [h]	50771550.62	–5022.300682	

[a]Ref [2]. [b]Equilibrium distances between the S atoms and the corresponding three closest Au atoms are different for all S atoms in the unit cell.[44] [c]Refs[29,30]. [d]Ref[31]. [e]Ref[32]. [f]Ref[33]. [g]Units are such that the potential energy is in kcal/mol and r in Å. [h]Taken as the arithmetic mean of the parameters for CF_2···CF_2 and CF_3···CF_3 interactions.

As in the AA force field, the nonbonded interactions in the models proposed here [UAX (X = 1-5, where X represents the variations of defining the nonbonded interactions)] are represented by Buckingham functions:

$$V_{UAX}^{NB}(r_{ij}) = \sum_{i>j} A_{\alpha\beta}\, exp(-B_{\alpha\beta}\, r_{ij}) + \frac{C_{\alpha\beta}}{r_{ij}^{D_{\alpha\beta}}} \qquad (7.7)$$

Parameters $A_{\alpha\beta}$, $B_{\alpha\beta}$, $C_{\alpha\beta}$, and $D_{\alpha\beta}$ were determined by fits of equation 7.7 to UA potentials, $V_{UA,av}^{NB}(r_{ij})$, obtained by isotropically averaging the AA interactions (using the AA force field) between two model fragments as explained below. Details of the AA force field of the F-SAM are reported in the literature,[17,18,27] and for simplicity they are not given in the present paper.

The ordering of models UA1-UA3 follows the degree of generality employed in the derivation of the nonbonded parameters. In UA1 we considered the perfluoropropane dimer as a model to calculate averaged nonbonded interaction energies by the formula

$$V_{UA1,av}^{NB}(r_{ij}) = \frac{1}{N}\sum_{k=1}^{N}\sum_{l>m} V^{EA}(r_{lm};\alpha_{1,k},\alpha_{2,k},\alpha_{3,k},\alpha_{4,k}) \qquad (7.8)$$

where N is the number of configurations of the dimer, for a given intermolecular distance, obtained by random internal rotations of the four terminal CF_3 groups ($\alpha_{1,k}$, $\alpha_{2,k}$, $\alpha_{3,k}$, and $\alpha_{4,k}$ are the dihedral angles), and $V^{EA}(r_{lm};\alpha_{1,k},\alpha_{2,k},\alpha_{3,k},\alpha_{4,k})$ is the AA potential energy of the perfluoropropane dimer. At a given intermolecular distance, the value of the AA potential energy varies with the orientations of the methyl groups and with the relative orientation of the backbones of the dimer (see Figure 7.2 for the three orientations considered here), which determine the r_{lm} distances (l and m stand for C or F in each octafluoropropane molecule). We considered $N = 10^4$ different configurations for each backbone orientation and intermolecular distance. We selected octafluoropropane because it is the simplest molecule containing both CF_3 and CF_2 united atoms. In the three configurations (see Figure 7.2), straight lines crossing the terminal and central C atoms in each molecule are parallel between each other (upper line in the molecule on the left is parallel to the lower line in the molecule on the right, and vice versa), and the six C atoms are in the same plane. In each configuration, all distances and bending angles are fixed to the equilibrium values of the chains in F-SAM. The potential energies depicted in Figure 7.2 (as well as in Figures 7.3-7.6) correspond to the total nonbonded interaction energies averaged over all rotational space spanned by the arrows shown in the figure.

In the remaining UA models (UA2-UA5), CF_x fragments (with x = 2, 3), instead of the octafluoropropane dimer, were employed to obtain averaged nonbonded interaction energies between the united atoms. The differences between these models lie in the way in which the fragments are randomly rotated to obtain the averaged interaction potential, as detailed below. As above, the CF_x fragments are rotated and translated with the intramolecular equilibrium distances and angles kept fixed and equal to the corresponding reference values (r^0 and θ^0) in the F-SAM. A general equation can be written for the averaged nonbonded interactions in the UAX (X=2-5) models:

$$V_{UAX,av}^{NB}(r_{ij}) = \frac{1}{N}\sum_{k=1}^{N}\sum_{l>m} V^{EA}(r_{lm};\theta_k,\varphi_k,\chi_k) \qquad (7.9)$$

where N is the number of random orientations of the CF_x fragments (x = 2, 3), defined in this case in terms of the Euler angles θ_k, φ_k, and χ_k, for a given center-of-mass distance between both fragments, and $V^{EA}(r_{lm};\theta_k,\varphi_k,\chi_k)$ is the AA potential energy for the interaction between them. At a given center-of-mass distance, the value of this AA potential energy varies with the relative orientation of the CF_x fragments, which determines the r_{lm} distances (l and m stand for C or F in each CF_x fragment).

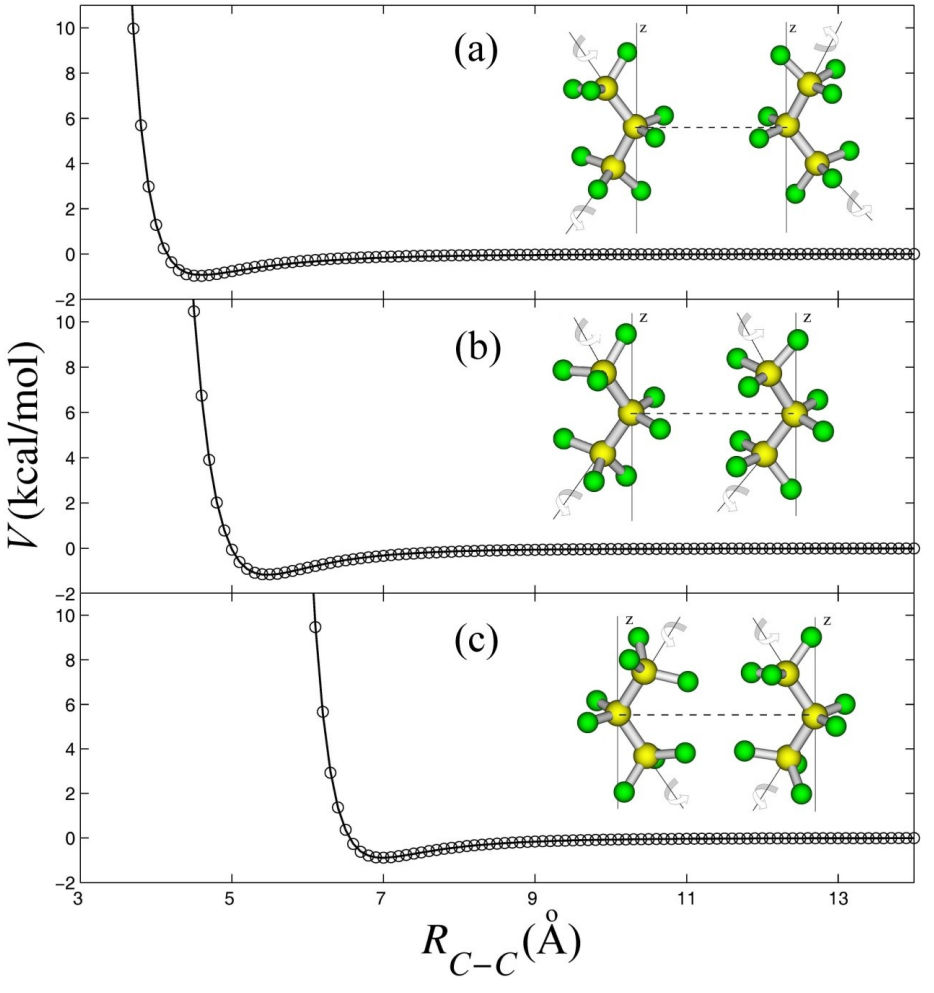

Figure 7.2: Different backbone orientations of the octafluoropropane dimer used to derive the Buckingham parameters for the UA1 model. The fits are also shown in the figure. The average potential energy is plotted against the distance between the two middle carbon atoms.

In UA2, CF_3 and CF_2 are randomly rotated about the corresponding z axes, as shown graphically in Figure 7.3. For CF_3, the z axis is defined as the

C_{3v} symmetry axis; for CF_2, it is defined as the axis perpendicular to the molecular plane passing through the center of mass of the fragment. In UA2, only θ_k varies with k; φ_k, and χ_k are kept constant for each configuration k. For the $CF_3\cdots CF_3$ and $CF_2\cdots CF_2$ interactions, the relative orientations of the fragments are shown in Figures 7.3a and 7.3c, respectively; the z coordinate of each atom remains constant for the different configurations. However, for the $CF_3\cdots CF_2$ interactions we picked configurations where the center of masses of both fragments lie along the z axis. These orientations were chosen to mimic, in a rough way, the actual orientations of the fragments in the chains, wherein all CF_3 fragments have approximately the same height and are above CF_2 fragments.

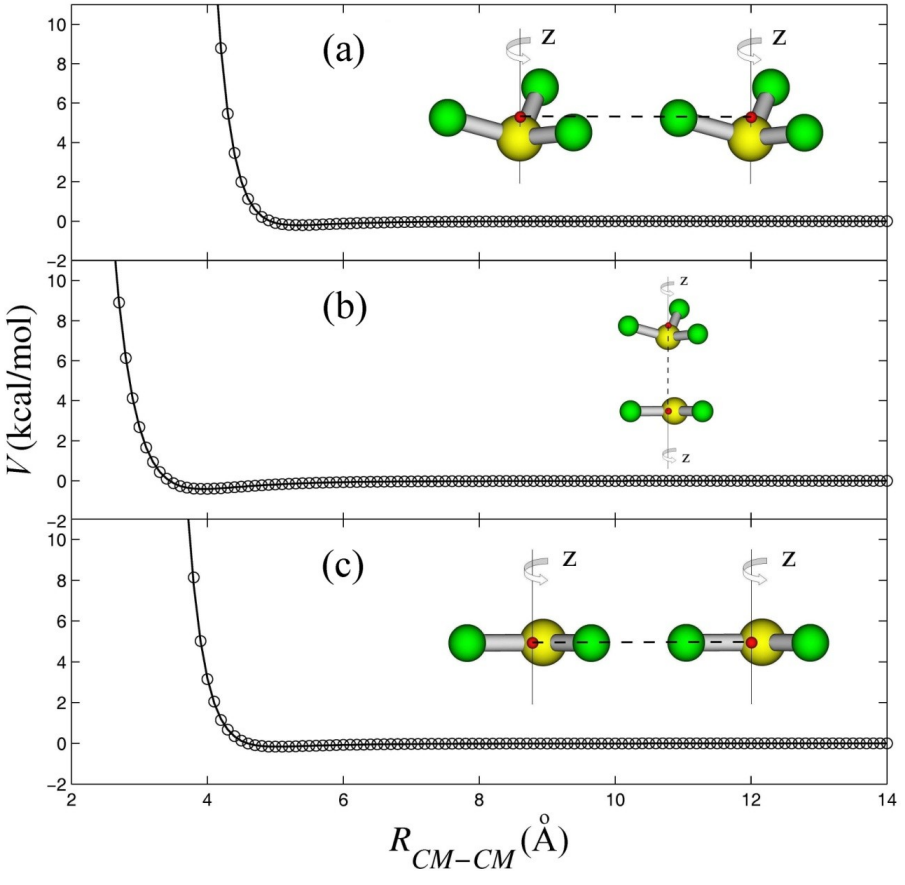

Figure 7.3: Different orientations of the CF_3 and CF_2 units considered to derive the UA2 parameters. The potential energy is averaged over all rotational space spanned by the arrows. The fits are also shown in the figure. See text.

In UA3, both CF_3 and CF_2 groups are randomly rotated in three dimensions with the Euler angles θ_k, φ_k, and χ_k changing from configuration to configuration (see Figure 7.4). Notice that in this case the relative orientations between the fragments depicted in Figure 7.4 are not relevant at all, since we are isotropically averaging in three dimensions the interaction between fragments. Conceptually, this is perhaps the most straightforward approach for parameterizing the UA nonbonded interaction terms from the AA force field.

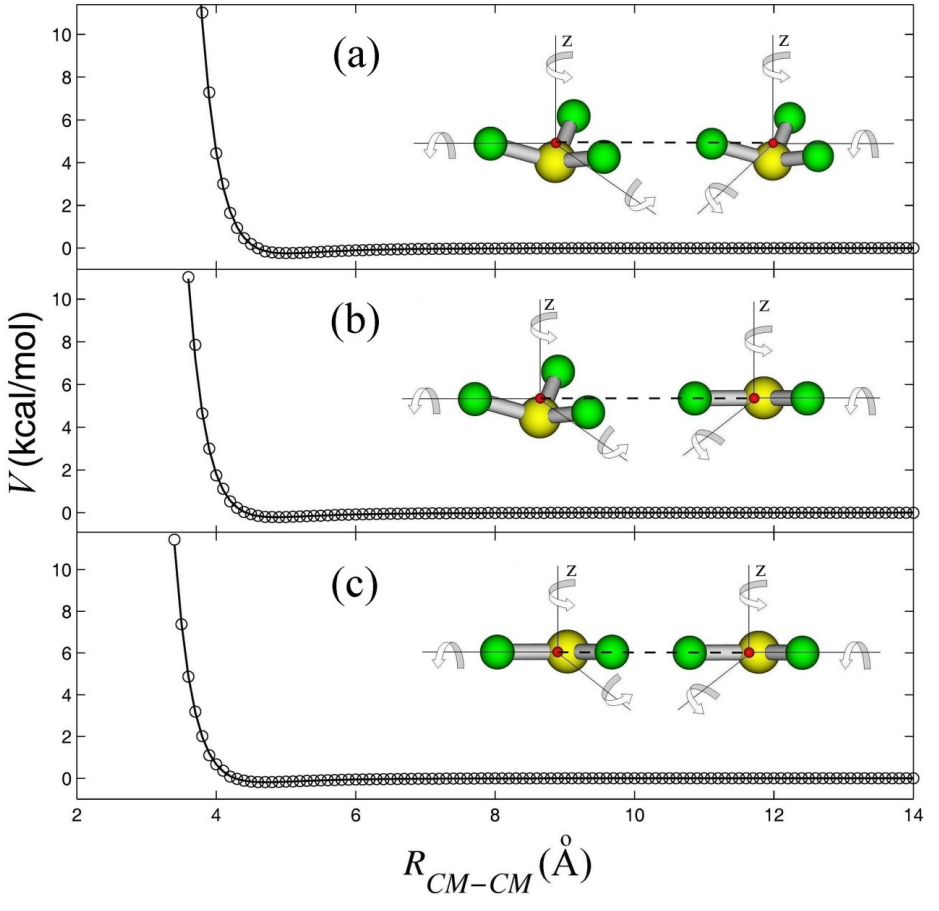

Figure 7.4: Same as Figure 7.3 but for model UA3.

We finally devised an intermediate situation between UA2 and UA3, called united atom model 4 (UA4). In UA4, CF_3 is rotated in three dimensions as in UA3, whereas the CF_2 fragment is rotated only in one dimension as in UA2. The parameters for the $CF_3\cdots CF_3$ and $CF_2\cdots CF_2$ potentials are, therefore, the same as those for the corresponding potentials in models UA3 and UA2,

respectively. However, the parameters for the $CF_3\cdots CF_2$ interaction potential are new, as it is the definition for the relative orientations considered for these two fragments (see Figure 7.5). Model UA5 has the same F-SAM potential as UA4, the only difference being the CO2···F-SAM interactions as indicated in the next section.

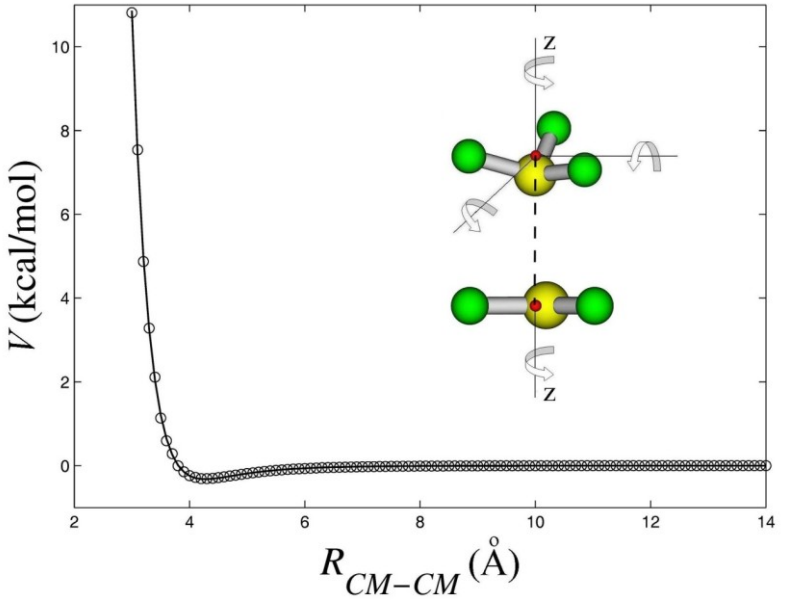

Figure 7.5: Orientations between the CF_3 and CF_2 units considered to derive UA4 parameters for the $CF_3\cdots CF_2$ nonbonded interaction. The potential energy is averaged over all rotational space spanned by the arrows.

In models UA2-5 we took $N = 10^6$ different configurations for each center-of-mass distance. For each configuration of fragment A, fragment B was randomly rotated 10^3 times, and this process was repeated 10^3 times. The values obtained in the fittings of the parameters of equation 7.7 to the averaged potential functions of equations 7.8 and 7.9 are collected in Table 7.2, and the fittings are shown graphically in Figures 7.2-7.5. The table also shows the root-mean-square (rms) error of the fittings, being always lower than 0.08 kcal/mol except for model UA1, which has an rms deviation of 0.7 kcal/mol.

For all UA models considered in this work, nonbonding interactions between united atoms that belong to the same chain and are separated by less than four bonds were not included in the potential energy evaluation. Additionally, a spherical potential truncation at 13.5 Å and no tail corrections were used in the calculations.

In the UA models proposed in this work, the potential function that represents the interaction between CO_2 and the F-SAM surface (V_{inter}) is similar to equation 7.7. For UA0, the parameters were obtained elsewhere[24] from a fit to the following isotropically averaged potential, $V_{inter,av}(R)$, for CO_2 interacting with CF_4

$$V_{inter,av}(R) = \frac{1}{N}\sum_{k=1}^{N}\sum_{i>j} V_R(r_{ij};\theta_k,\varphi_k,\chi_k) \qquad (7.10)$$

where R is the $CO_2\cdots CF_4$ center-of-mass separation, N is the number of random orientations of CF_4 (defined in terms of the Euler angles θ_k, φ_k, and χ_k) for a given distance R, and $V_R(r_{ij};\theta_k,\varphi_k,\chi_k)$ is the potential energy of $CO_2\cdots CF_4$ calculated with the AA force field reported in previous work.[17] At constant R, the value of this potential energy varies with the r_{ij} distances (i stands for C or O in CO_2 and j for C or F in CF_4), which depend on the orientation of CF_4. These interaction parameters, presented in Table 7.3, are also used for models UA1 and UA5.

Table 7.2: Nonbonded force field parameters of the UAX (X = 1-4) models.[a]

Method	UA pair	*A*	*B*	*C*	*D*[b]	*RMSE*
UA1	$CF_3\cdots CF_3$	413023385.27	–4.074900	–7263.719	6	7.0E–01
	$CF_3\cdots CF_2$	26857.072893	–2.335955	–4991.516	6	
	$CF_2\cdots CF_2$	227688835.59	–4.533048	–3145.234	6	
UA2	$CF_3\cdots CF_3$	314220864.33	–4.099903	–47883.79	7.147589	3.4E–02
	$CF_3\cdots CF_2$	51017.215363	–2.962870	–3313.338	6.040752	1.1E–02
	$CF_2\cdots CF_2$	23257894.246	–3.882012	–6757.211	6.357618	2.3E–02
UA3	$CF_3\cdots CF_3$	11566182.518	–3.586044	–80017.08	7.537772	6.4E–02
	$CF_3\cdots CF_2$	8866827.3575	–3.723713	–11412.60	6.606797	3.0E–02
	$CF_2\cdots CF_2$	3033095.0023	–3.614947	–9420.006	6.655372	3.2E–02
UA4	$CF_3\cdots CF_3$	11566182.518	–3.586044	–80017.08	7.537772	6.4E–02
	$CF_3\cdots CF_2$	231948.11944	–3.147010	–14924.21	6.907105	7.6E–02
	$CF_2\cdots CF_2$	23257894.246	–3.882012	–6757.211	6.357618	2.3E–02

[a]Units are such that the potential energy is in kcal/mol and r in Å. [b]For UA1, this parameter was fixed to 6.

For models UA2-UA4, we followed a similar procedure, but in this case we considered the CF_3 and CF_2 fragments, rather than CF_4, which led to different set of parameters for $CO_2\cdots CF_3$ and $CO_2\cdots CF_2$ interactions. As for $CO_2\cdots CF_4$,[24] two different orientations of the CO_2 molecule, depicted in Figure 7.6, were taken into account. The fittings are shown in this figure and the parameters are collected in Table 7.3.

Table 7.3: Parameters[a] of the Buckingham potentials used in models UA2, UA3, and UA4 for interactions CO_2···CF_3 and CO_2···CF_2. The last two rows show the interaction potential parameters used in UA0, UA1, and UA5.[b]

	A	*B*	*C*	*D*	*RMSE*
C···CF_3	2532156.6553	3.952849	–11703187.74	12.75851	9.3E–02
O···CF_3	1043242.8642	3.777613	–9431.277512	6.977135	
C···CF_2	369109.78034	3.521648	–267864.8086	10.22270	9.0E–02
O···CF_2	581486.99085	3.672064	–13074.50051	7.305438	
C···CF_4	14557336.665	4.562231	–20182460694.28	20	2.6E–01
O···CF_4	1473656.5293	3.806771	–11730.83989144	7	

[a]Units are such that the potential energy is in kcal/mol and r in Å. [b]Derived in a separate work.[24]

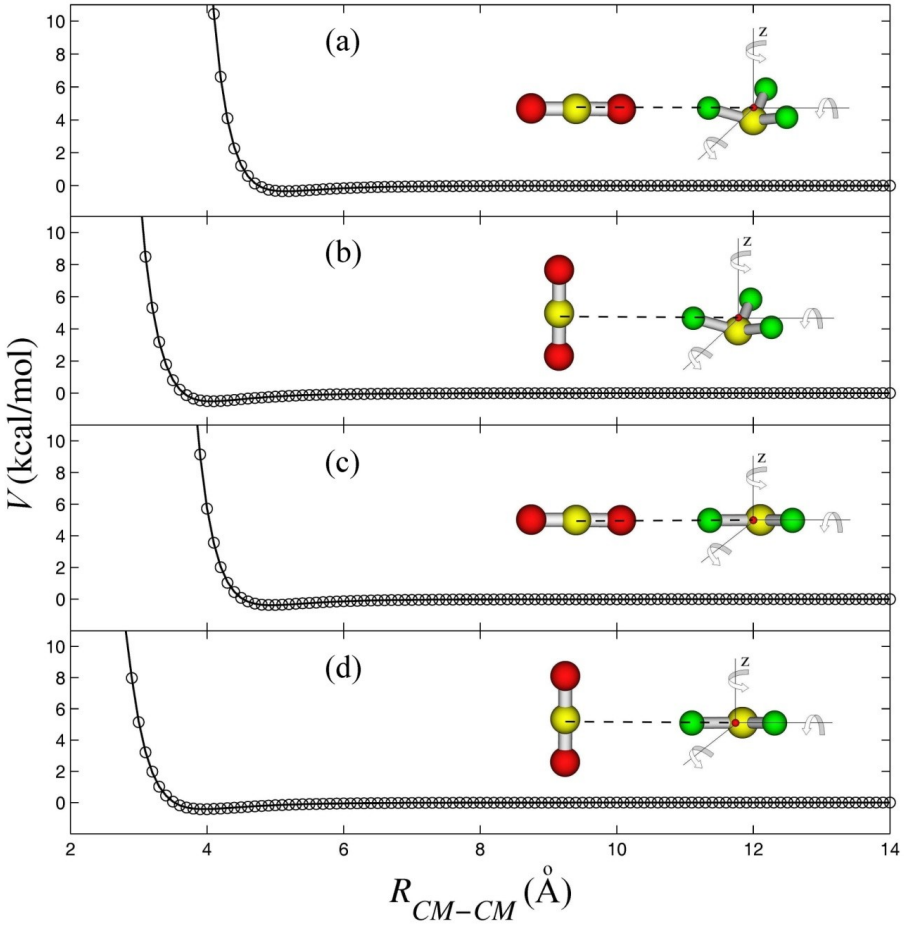

Figure 7.6: Different orientations between CO_2 and the CF_3 and CF_2 units considered to develop the intermolecular interaction potentials for models UA2, UA3, and UA4. The potential energy is averaged over all rotational space spanned by the arrows.

2.2 Trajectory simulations

Initial conditions were selected as in our previous CO_2 + F-SAM simulations[17,24] using the VENUS05 computer program; these conditions mimic the experimental conditions of Nesbitt and co-workers in their CO_2 + PFPE scattering experiments.[34,35] A quasi-classical sampling[45] was employed for carbon dioxide to add zero point energy to its vibrational modes and to sample its rotational degrees of freedom according to a Boltzmann distribution at a temperature of 15 K. The angle with respect to the surface normal, (i.e., the incident angle) for the CO_2 molecule was zero degrees. The collision energies, E_i, investigated were 10.6 and 7.7 kcal/mol. For the latter energy, we only employed the UA3 and UA4 models, which give the best performances for E_i = 10.6 kcal/mol. As mentioned in the Introduction, these collision energies were also selected in previous scattering experiments of CO_2 + liquid PFPE.[34,35] The center of mass of CO_2 was randomly thrown towards a point in the central unit cell of the F-SAM surface as described in previous work.[17] Periodic boundary conditions and the image vector convention were utilized in order to represent a larger surface.[46]

In each trajectory, the initial separation between the CO_2 center of mass and the surface aiming point was 25 Å, and that between CO_2 and the gold atoms was ≈38 Å. Ensembles of 2000 trajectories were integrated with a fixed step size of 0.3 fs using the Adams-Moulton algorithm implemented in VENUS05. Before initiating the first trajectory, a molecular dynamics simulation was performed during 2 ps for the F-SAM surface to reach thermal relaxation at a temperature of 300 K. The structure thus obtained was subsequently employed as the initial structure of a 100 fs equilibration run before the start of the second trajectory. This process was repeated before the beginning of each trajectory. At the end of each trajectory, the final translational, vibrational, and rotational energy of CO_2 were calculated from the atomic Cartesian coordinates and momenta. The CO_2 rotational quantum number J was also determined from the CO_2 rotational angular momentum. The maximum integration time for a trajectory was 150 ps. For a small number of trajectories (see below) the CO_2 molecule did not desorb within this time limit. For these trajectories, the final CO_2 velocity and the rotational quantum number J were randomly assigned from a 300 K Boltzmann distribution. This statistical assignment is reasonable because after a long period of time, such as more than 150 ps, the CO_2 molecule is expected to reach thermal equilibrium with the F-SAM surface.

3. RESULTS

3.1 Structure of the surface

The structures of the F-SAM surfaces in all models considered here are similar to each other. The only difference refers to the tilt angle, that is, the angle that forms the chains with respect to the vertical (see Figure 7.1). An average tilt angle of 14º was previously calculated for the AA model,[17] which compares very well with the experimental estimation of 12 ± 2º.[44] In the present study, this average tilt angle was also computed (the angle was averaged for several snapshots of the surface during the molecular dynamics equilibration run), obtaining 9º for UA0, 7º for UA1, 8º for UA2, and 10º for UA3 and UA4. Among the UA models investigated in this work, the values for UA3 and UA4 (for the F-SAM, UA5 is equal to UA4) give the best comparison with experiment.

3.2 Trajectory types

As in previous simulations of collisions of CO_2 with F-SAM surfaces, the present results exhibit three different types of trajectories: *direct*, *physisorbing*, and *penetrating* trajectories. We define a direct trajectory as that having only one inner turning point (ITP) in their motion perpendicular to the surface plane. A penetrating trajectory occurs when the CO_2 molecule approaches the gold surface by less than 11.6 Å, which is the intermediate average height between that of the C-atoms of the $–CF_3$ terminal groups and that of their adjacent $–CF_2–$ groups. We consider a physisorbing trajectory as one in which the CO_2 molecule rebounds several times (i.e., there is more that one ITP), without penetration into the monolayer. Both physisorption and penetration have frequently been classified as trapping desorption.[47-49]

Table 7.4 shows the percentages of different trajectory types calculated with the UAX (X = 1-5) force fields for an incident energy of 10.6 kcal/mol. The results are compared with previous values for the AA and UA0 models of the F-SAM.[17,24] As seen in the table, the UA0 model predicts too much penetration (42%) as compared with the AA model (24%). The new UA models reduce the percentage of penetrating trajectories, but in some cases (for UA1, UA2, and UA3) the percentage is too low (10-14%) in comparison with the reference value provided by the AA simulations (24%). In general, models UA4 and UA5 give the best agreement with the AA results, although significant discrepancies are still apparent.

Table 7.4: Percentages of different trajectory types.[a]

Model	Direct	Penetration	Physisorption
		E_i = 10.6 kcal/mol	
AA	34	24	42
UA0	22	42	36
UA1	49	10	41
UA2	60	11	29
UA3	46	14	40
UA4	42	18	40
UA5	36	29	35
		E_i = 7.7 kcal/mol	
AA	26	33	41
UA0	24	44	32
UA3	46	22	32
UA4	30	24	46

[a]Values for AA and UA0 were taken from refs[17,24].

In addition, we found in previous work[24] that the UA0 model leads to incomplete trajectories, that is, trajectories in which the CO_2 molecule does not desorb within the 150 ps of integration time. Incomplete trajectories were not observed in the simulations performed with the AA model.[17] The percentages of incomplete trajectories calculated with the UA0 model at 7.7 and 10.6 kcal/mol were, in both cases, about 23%. This result of incomplete trajectories, as well as that of large percentages of penetrating trajectories, is a consequence of the higher efficiency of energy transfer to the surface in the UA model, as discussed elsewhere.[18,24] With our new models UA1, UA2, and UA4, the percentage of incomplete trajectories is lower than 2% (6% for UA3 and 4% for UA5), which approaches the AA results.

For each trajectory, we evaluated a phenomenological residence time (τ) as the difference between the times of the last and first ITPs in the perpendicular motion of the CO_2 molecule. According to this definition, only trajectories involving trapping-desorption will have non-zero residence times. The average residence times obtained in this work with all UA models of the F-SAM are collected in Table 7.5, along with our preceding results determined with the AA and UA0 models.[17,24] As seen in the table, the average times for penetrating trajectories calculated with the UA models proposed here decrease significantly with respect to the UA0 values, leading to better agreement with the AA results. The best performance is achieved with UA4. For physisorbing trajectories, all the force fields predict average residence times of 8-10 ps in the simulations carried out at the collision energy of 10.6 kcal/mol.

Table 7.5: Average residence times (in ps).[a]

Model	Penetration	Physisorption
	E_i = 10.6 kcal/mol	
AA	35.1	9.6
UA0	57.1	10.1
UA1	38.3	9.1
UA2	35.0	7.8
UA3	36.6	8.3
UA4	33.1	9.5
UA5	49.7	9.3
	E_i = 7.7 kcal/mol	
AA	38.5	11.9
UA0	53.5	10.4
UA3	43.0	8.5
UA4	34.4	9.7

[a]Values for AA and UA0 were taken from refs[17,24].

3.3 Energy transfer efficiencies

Energy conservation leads to a simple relationship between the following quantities: the initial and final translational energies of carbon dioxide, E_i and E_f, respectively, the change in the vibrational energy of the F-SAM surface, ΔE_{surf}, and the change in the internal energy of CO_2, ΔE_{int},

$$E_i = E_f + \Delta E_{int} + \Delta E_{surf} \tag{7.11}$$

The average values of ΔE_{surf}, ΔE_{int}, and E_f are presented in Table 7.6. Following the trends found in previous studies of projectile gases colliding with SAM surfaces, most of the incident energy goes to the surface's vibrational modes. For total trajectories, the average energy transferred to the surface with the UA0 force field (77% of E_i) is substantially higher than that transferred with the AA model of F-SAM (67%). The new UA models, and particularly UA3 (68%), UA4 (70%), and UA5 (70%), give percentages in better agreement with the AA results. The vibrational modes of CO_2 are not excited, and in fact there is a slight decrease of 0.3 kcal/mol in its vibrational energy; this result has already been discussed and explained in terms of energy transfer to the vibrational angular momentum states of the CO_2 molecule.[17]

We also analyzed the energy transfer efficiencies for the different trajectory types. For penetrating trajectories, all UA models lead to results in good agreement with the AA model, whereas for direct and physisorbing trajectories important differences are found. For direct trajectories, again models UA3, UA4, and UA5 give the best performance in comparison with the reference AA model. For physisorbing trajectories, UA4 is not as good as UA3

and UA5. All in all, for energy transfer efficiencies the results obtained with model UA3 are in best agreement with the AA calculations, but the performances of the UA4 and UA5 force fields are only slightly inferior. We notice that there may be some cancellation of errors when the comparisons are made for total trajectories, especially for those models for which the percentages of the different trajectory types are not accurately predicted.

Table 7.6: Average energy transferred in collisions of CO_2 with F-SAM at E_i = 10.6 kcal/mol.[a]

	AA[b]	UA0[b]	UA1	UA2	UA3	UA4	UA5
Direct							
$\langle \Delta E_{int} \rangle$	1.2 (11)	1.0 (10)	1.6 (15)	1.6 (15)	1.2 (11)	1.2 (11)	1.3 (13)
$\langle \Delta E_{vib} \rangle$	–0.2	–0.2	–0.2	–0.1	–0.2	–0.2	–0.2
$\langle \Delta E_{rot} \rangle$	1.4	1.2	1.8	1.7	1.4	1.4	1.5
$\langle \Delta E_{surf} \rangle$	6.0 (57)	7.4 (69)	5.0 (47)	5.3 (50)	6.7 (63)	6.7 (63)	6.5 (61)
$\langle E_f \rangle$	3.4 (32)	2.2 (21)	4.0 (38)	3.7 (35)	2.7 (26)	2.7 (26)	2.8 (26)
Penetration							
	AA	UA0	UA1	UA2	UA3	UA4	UA5
$\langle \Delta E_{int} \rangle$	0.5 (5)	0.5 (5)	0.5 (5)	0.5 (5)	0.7 (7)	0.5 (5)	0.5 (5)
$\langle \Delta E_{vib} \rangle$	–0.5	–0.5	–0.4	–0.4	–0.4	–0.4	–0.4
$\langle \Delta E_{rot} \rangle$	1.0	1.0	0.9	0.9	1.1	0.9	0.9
$\langle \Delta E_{surf} \rangle$	8.9 (84)	9.0 (85)	8.9 (84)	8.8 (83)	8.5 (80)	8.9 (84)	8.8 (83)
$\langle E_f \rangle$	1.2 (11)	1.1 (10)	1.2 (11)	1.3 (12)	1.4 (13)	1.2 (11)	1.3 (12)
Physisorption							
	AA	UA0	UA1	UA2	UA3	UA4	UA5
$\langle \Delta E_{int} \rangle$	1.0 (9)	0.8 (7)	1.3 (12)	1.3 (13)	1.0 (10)	1.0 (9)	1.0 (9)
$\langle \Delta E_{vib} \rangle$	–0.2	–0.2	–0.2	–0.2	–0.2	–0.2	–0.2
$\langle \Delta E_{rot} \rangle$	1.2	1.0	1.5	1.5	1.2	1.2	1.2
$\langle \Delta E_{surf} \rangle$	7.0 (66)	8.1 (77)	6.3 (59)	6.8 (64)	7.4 (70)	7.7 (73)	7.6 (72)
$\langle E_f \rangle$	2.6 (25)	1.7 (16)	3.0 (29)	2.5 (23)	2.2 (20)	1.9 (18)	2.0 (19)
Total							
	AA	UA0	UA1	UA2	UA3	UA4	UA5
$\langle \Delta E_{int} \rangle$	0.9 (9)	0.8 (7)	1.4 (13)	1.4 (13)	1.0 (10)	1.0 (10)	1.0 (10)
$\langle \Delta E_{vib} \rangle$	–0.3	–0.3	–0.2	–0.2	–0.2	–0.2	–0.3
$\langle \Delta E_{rot} \rangle$	1.2	1.1	1.6	1.6	1.2	1.2	1.3
$\langle \Delta E_{surf} \rangle$	7.2 (67)	8.1 (77)	5.8 (55)	6.1 (58)	7.2 (68)	7.5 (70)	7.5 (70)
$\langle E_f \rangle$	2.5 (24)	1.7 (16)	3.4 (32)	3.1 (29)	2.4 (22)	2.1 (20)	2.1 (20)

[a]Values in parenthesis are the percentages of the initial collision energy transferred to the specific degrees of freedom. [b]Results for AA and UA0 were taken from refs[17,24].

3.4 Rotational and translational energy distributions

The rotational quantum number J of a scattered CO_2 molecule is obtained from its rotational angular momentum j from the relationship

$$j = \sqrt{J(J+1)}\hbar \tag{7.12}$$

Distributions of rotational quantum number J, $P(J)$, of the scattered CO_2 molecules are depicted in Figure 7.7 as fits to two Boltzmann distributions with a low-temperature (LT) and a high-temperature (HT) components:

$$P(J) = \alpha_{LT} P_{LT}(J) + (1 - \alpha_{LT}) P_{HT}(J) \tag{7.13}$$

where each of the normalized components reads

$$P_X(J) = \frac{(2J+1)\mathrm{e}^{-\frac{E_{rot}}{kT_{rot}(X)}}}{Q_{rot}(X)} \tag{7.14}$$

with X = LT or HT. In the experimental investigations on CO_2 + liquid PFPE,[26,34-38] these two components were assigned to trapping-desorption (TD) and inelastic scattering (IS) mechanisms, respectively. Following previous work,[24] the LT component was fixed to the surface temperature (300 K), and so the fits were conducted by only varying α_{LT} and $T_{rot}(HT)$. The results of the fits are gathered in Table 7.7.

Table 7.7: Parameters for the Boltzmann fits to the $P(J)$ distributions.[a]

	E_i = 10.6 kcal/mol		
Model	α_{LT}	$T_{rot}(LT)$	$T_{rot}(HT)$
AA	0.52 ± 0.06	300	712 ± 78
UA0	0.85 ± 0.03	300	1073 ± 315
UA1	0.29 ± 0.04	300	828 ± 50
UA2	0.19 ± 0.04	300	773 ± 43
UA3	0.55 ± 0.04	300	873 ± 83
UA4	0.57 ± 0.04	300	807 ± 90
UA5	0.55 ± 0.04	300	821 ± 81
Experiment[b]	0.54 ± 0.03	298	710 ± 83
	E_i = 7.7 kcal/mol		
AA	0.67 ± 0.08	300	597 ± 112
UA0	0.85 ± 0.03	300	1025 ± 326
UA3	0.61 ± 0.13	300	595 ± 145
UA4	0.67 ± 0.06	300	689 ± 119
Experiment[b]	0.64 ± 0.06	298	600 ± 80

[a]Values for AA and UA0 were taken from refs[17,24]. [b]Experimental values from refs.[34,35]

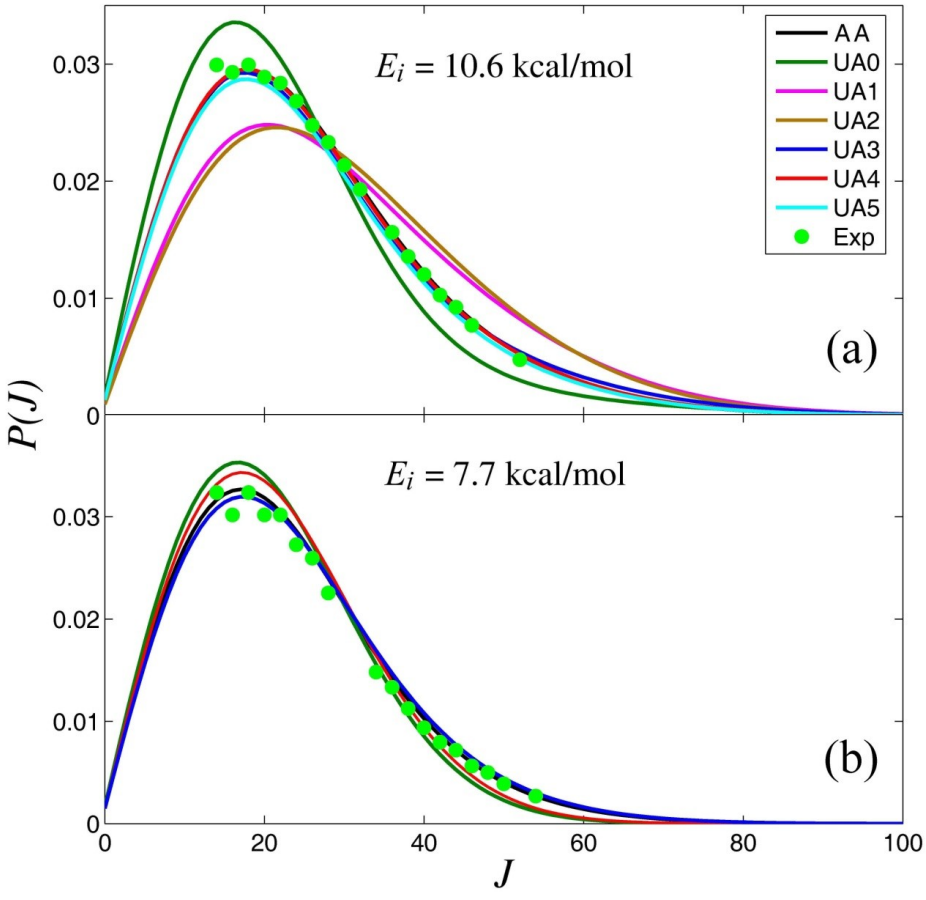

Figure 7.7: Rotational quantum number distributions of scattered CO_2 molecules obtained with several models of the F-SAM in comparison with the experimental distributions.[34,35] (a) E_i = 10.6 kcal/mol and (b) E_i = 7.7 kcal/mol. The AA and UA0 distributions are taken from previous work.[17,24]

The $P(J)$ distributions obtained with the UA models, for E_i = 10.6 kcal/mol, are also compared in Figure 7.7 with the AA distribution[17] and with the experimental data on CO_2 + liquid PFPE.[34,35] It is clear that the UA3, UA4, and UA5 models substantially improve the performance of the original UA0 force field. In fact, the distributions obtained with these three new models essentially match the distribution predicted with the AA force field, and, moreover, they are in very good agreement with the experimental results.[34,35] On the other hand, it is apparent that the UA1 and UA2 distributions are significantly hotter than that obtained with the reference force field (i.e., the AA model); this could be anticipated from the data on energy transfer collected in Table 7.6, which, for UA1 and UA2, show significant rotational excitation

for carbon dioxide. These conclusions can also be inferred from the values of the parameters of the Boltzmann fits, listed in Table 7.7, although the comparison through a graphical representation of the distributions is more straightforward.

The translational energy distributions, $P(E_f)$, of the scattered CO_2 molecules were first fitted by the method of Legendre moments,[50,51] and the results are represented graphically in Figure 7.8. Then, and following an approach parallel to that for rotational distributions, we fitted the above $P(E_f)$ distributions to two Maxwell-Boltzmann components:

$$P(E_f) = \frac{\alpha_{LT}}{\left(k_B T_{trans}\,(LT)\right)^2} E_f\, e^{-E_f/k_B T_{trans}\,(LT)} + \frac{(1-\alpha_{LT})}{\left(k_B T_{trans}\,(LT)\right)^2} E_f\, e^{-E_f/k_B T_{trans}\,(HT)} \tag{7.15}$$

where, again, LT and HT refer to low-temperature (fixed at 300 K) and high-temperature, respectively. The parameters of these fits are listed in Table 7.8. For the collision energy of 10.6 kcal/mol, it is clear from Figure 7.8 that the UA3 model leads to the best agreement with the AA distribution. The UA2, UA4, and UA5 distributions agree fairly well with the AA distribution, but those calculated with the UA0 and UA1 force fields show considerable disagreement with the reference distribution. These conclusions may also be drawn from a comparison between the parameters obtained in the Maxwell-Boltzmann fits (Table 7.8), although in this case some care must be exercised. For example, it is evident that the UA0 distribution, with α_{HT} = 0.30 (α_{HT} = 1−α_{LT}) and $T_{trans}\,(HT)$ = 686 K, is significantly cooler than the AA distribution, which has α_{HT} = 0.48 and a corresponding temperature of 712 K. And, on the other hand, the UA1 distribution [α_{HT} = 0.85 and $T_{trans}\,(HT)$ = 990 K] is substantially hotter than the reference distribution. Again, these results may be anticipated from a comparison of the energy transfer data reported in Table 7.6. Specifically, the average translational energy of scattered CO_2 molecules calculated with the UA0 model is 0.8 kcal/mol smaller than that predicted with the AA force field, whereas the value computed with the UA1 model is 0.9 kcal/mol larger than the reference value.

It is worth noting that fittings of the type described in this section have frequently been reported in experimental studies and, for the particular case of rotational distributions, the LT and HT components have been ascribed to TD and IS mechanisms, respectively.[26,34-38] On the other hand, the translational energy distributions of scattered projectiles have often been fitted to a single Maxwell-Boltzmann component (or low-energy component), associated with the fraction of TD, and the remaining higher-energy component

was attributed to inelastic scattering.[10,47-49,52-59] It has also been shown that allowing the temperature of the low-energy component of $P(E_f)$ to vary in the fits may lead to an "effective" temperature that is significantly higher than the surface temperature, which was interpreted in terms of thermalization with a subset of surface vibrational modes.[11] In the present paper, as well as in previous work,[24] we found that the $P(E_f)$ distributions of scattered CO_2 molecules may be well-fitted by two Maxwell-Boltzmann components. Interestingly, the fractions of the LT and HT components (i.e., α_{LT} and α_{HT}) determined in the $P(J)$ fits differ substantially from the corresponding fractions obtained in the $P(E_f)$ fits (see Tables 7.7 and 7.8). Furthermore, the fractions of the LT components do not correspond to either the fraction of penetrating or physisorbing trajectories, or their sum. Significant discrepancies are also found between the high temperatures calculated from the $P(J)$ fits, T_{rot} (HT), and the corresponding quantities determined from the $P(E_f)$ fits, T_{trans} (HT). Because of these discrepancies, we recommend using the terms low-temperature and high-temperature for the two Boltzmann components. In addition, these results suggest that assignments of the LT and HT components to TD and IS mechanisms should be taken with caution.

Table 7.8: Parameters for the Boltzmann fits to the $P(E_f)$ distributions.[a]

	E_i = 10.6 kcal/mol		
Model	α_{LT}	T_{trans} (LT)	T_{trans} (HT)
AA	0.34 ± 0.00	300	861 ± 6
UA0	0.70 ± 0.01	300	686 ± 13
UA1	0.15 ± 0.00	300	990 ± 8
UA2	0.23 ± 0.01	300	857 ± 8
UA3	0.26 ± 0.00	300	688 ± 4
UA4	0.28 ± 0.02	300	606 ± 12
UA5	0.33 ± 0.01	300	629 ± 7
	E_i = 7.7 kcal/mol		
AA	0.34 ± 0.01	300	593 ± 5
UA0	0.68 ± 0.01	300	630 ± 22
UA3	0.28 ± 0.02	300	606 ± 12
UA4	0.59 ± 0.01	300	581 ± 3

[a]Values for AA and UA0 were taken from refs[17,24].

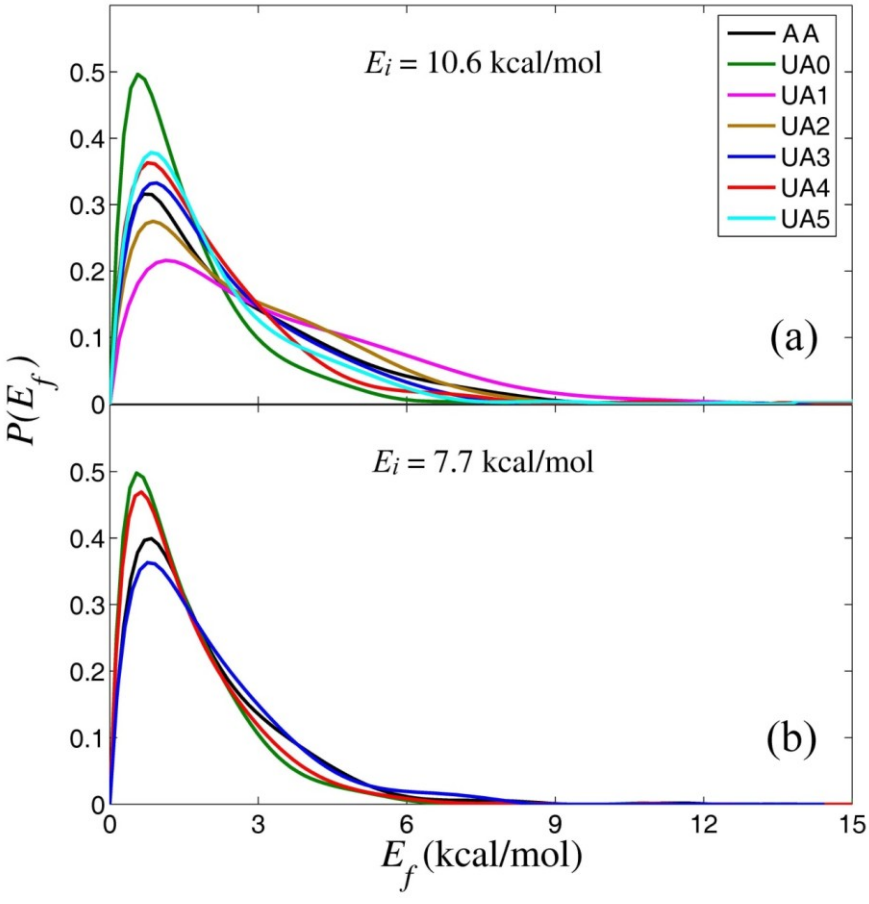

Figure 7.8: Translational energy distributions of scattered CO_2 molecules predicted with several models of the F-SAM. (a) E_i = 10.6 kcal/mol and (b) E_i = 7.7 kcal/mol. The AA and UA0 distributions are taken from previous work.[17,24]

3.5 Comparison with the simulation results at E_i = 7.7 kcal/mol

Taking all the above comparisons into account, it is apparent that, among the united-atom models proposed in this work, the UA3 and UA4 force fields give the best performances. In order to judge the consistency of these two models, we carried out additional CO_2 + F-SAM simulations at the incident energy of 7.7 kcal/mol. The percentages of trajectory types at this incident energy are collected in Table 7.4. As can be seen, the UA3 force field gives the worse agreement with the reference values given by the simulations performed with the AA model. In particular, the percentage of direct trajectories predicted with this force field (46%) is markedly higher than that computed with the AA approach (26%). In addition, the performance of the UA4 force field is not superior to that of the UA0 model. These results contrast with those obtained at

the highest energy investigated (10.6 kcal/mol), for which it was clear that UA3 and UA4 were better than UA0.

As shown in Table 7.5, the average residence times of penetrating trajectories calculated with the UA3 and UA4 models (43.0 and 34.4 ps, respectively, at E_i = 7.7 kcal/mol) are in better agreement with the AA value (38.5 ps) than is the UA0 result (53.5 ps). The values of the average residence times for physisorbing trajectories are quite similar among each other, following the trend observed at E_i = 10.6 kcal/mol.

We pointed out in a previous section that, at the incident energy of 10.6 kcal/mol, energy transfer efficiencies are best calculated with the UA3 force field. The data reported in Table 7.9 show the same trend for E_i = 7.7 kcal/mol, although the differences between values calculated with the various force fields are not substantial. For example, for total trajectories, the amounts of energy transferred to the surface calculated with the UA3 (4.9 kcal/mol) and UA4 (5.2 kcal/mol) force fields are closer to the AA result (5.0 kcal/mol) than is that computed with the original UA0 model (5.4 kcal/mol).

Figure 7.7 shows the CO_2 rotational distributions, $P(J)$, calculated at the collision energy of 7.7 kcal/mol, and compares them with those evaluated at E_i = 10.6 kcal/mol. As expected, decreasing the incident energy leads to cooler distributions, manifested by lower populations of high J levels and a shortening of the tail of the distribution. However, for the distributions calculated with a given model, the most probable value of J remains essentially unchanged. The variations in the rotational distributions due to a decrease in the incident energy are more apparent when one compares the parameters of the Boltzmann fits, which are collected in Table 7.7. For instance, the high-temperature component obtained with the AA model at E_i = 10.6 kcal/mol contributes 48% to the total distribution and its temperature is 712 K, whereas at E_i = 7.7 kcal/mol the percentage of this component is only 33% and its temperature 597 K (see Table 7.7). The latter percentage is the same as that calculated with the UA4 force field, but the temperature is significantly higher (689 K). The percentage obtained with UA3 (39%) is somewhat higher than the reference value (33%), but the temperature of this component (595 K) is very close to the AA result. As a consequence, the UA3 rotational distribution is in better agreement with the AA distribution (as well as with the experimental data) than is the UA4 distribution (see Figure 7.7). The UA0 distribution shows the largest deviation with respect to the AA distribution. Its high-temperature component is quite small (15%) and the associated temperature is too high (1025 K).

As expected, decrease in the incident energy also leads to a contraction of the translational energy distributions of the scattered CO_2 molecules. This can be shown in Figure 7.8, which depicts the $P(E_f)$

distributions calculated with the AA, UA0, UA3, and UA4 force fields for E_i = 7.7 and 10.6 kcal/mol. As for the $P(J)$ distributions, the maxima of the distributions obtained with each model at the two collision energies do not change appreciably. As for the highest collision energy investigated, the calculations at E_i = 7.7 kcal/mol indicate that the UA3 force field leads to the best agreement for translational energy distributions. This is clearly seen from the figure and from a comparison between the parameters of the Maxwell-Boltzmann fits listed in Table 7.8.

Table 7.9: Average energy transferred in collisions of CO_2 with F-SAM at E_i = 7.7 kcal/mol.[a]

Direct				
	AA[b]	UA0[b]	UA3	UA4
$\langle \Delta E_{int} \rangle$	1.0 (13)	0.9 (11)	0.8 (10)	0.9 (12)
$\langle \Delta E_{vib} \rangle$	–0.2	–0.1	–0.2	–0.1
$\langle \Delta E_{rot} \rangle$	1.2	1.0	1.0	1.0
$\langle \Delta E_{surf} \rangle$	4.1 (53)	4.8 (62)	4.4 (57)	4.6 (59)
$\langle E_f \rangle$	2.6 (34)	2.0 (27)	2.5 (33)	2.2 (29)
Penetrate				
	AA	UA0	UA3	UA4
$\langle \Delta E_{int} \rangle$	0.4 (6)	0.5 (6)	0.5 (7)	0.6 (8)
$\langle \Delta E_{vib} \rangle$	–0.5	–0.5	–0.5	–0.3
$\langle \Delta E_{rot} \rangle$	0.9	1.0	1.0	0.9
$\langle \Delta E_{surf} \rangle$	6.0 (77)	6.1 (80)	5.9 (76)	5.9 (77)
$\langle E_f \rangle$	1.3 (17)	1.1 (14)	1.3 (17)	1.2 (15)
Physisorption				
	AA	UA0	UA3	UA4
$\langle \Delta E_{int} \rangle$	0.8 (11)	0.7 (9)	0.8 (10)	0.8 (10)
$\langle \Delta E_{vib} \rangle$	–0.2	–0.2	–0.2	–0.2
$\langle \Delta E_{rot} \rangle$	1.0	0.9	1.0	1.0
$\langle \Delta E_{surf} \rangle$	4.9 (63)	5.4 (70)	5.1 (66)	5.4 (70)
$\langle E_f \rangle$	2.0 (26)	1.6 (21)	1.8 (24)	1.5 (20)
Total				
	AA	UA0	UA3	UA4
$\langle \Delta E_{int} \rangle$	0.8 (10)	0.7 (9)	0.8 (10)	0.8 (10)
$\langle \Delta E_{vib} \rangle$	–0.3	–0.3	–0.2	–0.2
$\langle \Delta E_{rot} \rangle$	1.1	1.0	1.0	1.0
$\langle \Delta E_{surf} \rangle$	5.0 (65)	5.4 (70)	4.9 (63)	5.2 (68)
$\langle E_f \rangle$	1.9 (25)	1.6 (21)	2.0 (27)	1.7 (22)

[a]Values in parenthesis are the percentages of the initial collision energy transferred to the specific degrees of freedom. [b]Results for AA and UA0 were taken from refs[17,24].

3.6 CPU times

Finally, it is of interest to compare the performance of the different surface models in terms of CPU time. The total CPU time for a batch of trajectories depends very much on the total integration time of the trajectories, which varies with the particular force field employed for the simulations. This is because the different UA models give different percentages for the distinct trajectory types, which have very different integration times. Therefore, to make a direct comparison between models, relative CPU times are calculated as the total CPU time for a batch of trajectories run with a given model divided by the total integration time. The AA model is 5.2 times slower than the UA0 model and 3.1 times slower than the UAX models (with X = 1-5). The simulations with UA0 are 1.7 times faster than those with UAX models. This difference comes from the distinct nonbonded interaction potentials used in both cases: UA0 employs Lennard-Jones terms, which are faster than the Buckingham potentials used in the UAX models. Besides this, the best UA force fields, namely, UA3 and UA4, are still more than 3 times faster than the AA one for CO_2 + F-SAM simulations, with only small loss of accuracy in the results. These force fields will be very useful for future simulations involving very large species, such as peptide ions (as in soft-landing studies), because the number of intermolecular, two-body interaction terms increases significantly with the number of atoms, so that the pseudo-atom approach becomes more convenient.

4. CONCLUSIONS

A united-atom force field for F-SAM surfaces was refined in various ways in order to improve the representation of the nonbonded interaction terms, which have been shown to play a determinant role in energy transfer efficiencies in collisions of projectile gases with self-assembled monolayers. As a reference, we used an all-atom force field of F-SAM, which has been successfully applied to CO_2 + F-SAM and other related systems.[17,18,22,24] As in the AA model of the F-SAM, the proposed UA force fields employ Buckingham potentials, rather than the Lennard-Jones functions utilized in the original UA model (referred to as UA0). The parameterizations were based on fits to potential energy curves of interacting fragments (e.g., $CF_3\cdots CF_3$ or $CF_2\cdots CF_2$), calculated with the AA force field. The performances of the UA models developed in the present study (UAX, X = 1-5) were assessed by comparisons of several properties calculated for collisions of CO_2 with F-SAM, using as a reference the results of simulations carried out with the AA force field.

Among the UA models proposed in this work, UA3 gives the best results for energy transfer efficiencies and for rotational and translational distributions of the scattered CO_2 molecules. It is especially remarkable that the simulations performed with this force field at the collision energies of 7.7 and 10.6 kcal/mol predict $P(J)$ distributions in very good agreement with the AA distributions and with the experimental distributions observed for collisions of CO_2 with liquid PFPE.[34,35] The only weakness of the UA3 force field lies in its predictions for percentages of distinct types of trajectories. Particularly, the UA3 force field underestimates the probability of penetrating trajectories in comparison with the reference values provided by the AA model. The UA4 force field predicts percentages in better agreement with the AA results, but its performance for energy transfer efficiencies and for rotational and translational distributions of CO_2 is rather inferior to that of UA3. On the other hand, the parameterization strategy used to derive UA3 seems to be the more straightforward among those followed in the present work. For all these reasons, we recommend the UA3 force field for simulations of collisions of gases with F-SAM surfaces, especially when large species are involved such as in soft-landing studies of peptide ions with F-SAMs. Finally, we notice that the UAX models proposed in this study were refined in order to reproduce energy transfer properties associated with collisions of gases with F-SAMs. It may be of interest to test the performance of some of these force fields (e.g., UA3 and UA4) for calculating thermodynamic properties such as the density of liquid perfluoroalkanes.

REFERENCES

(1) Love, J. C.; Estroff, L. A.; Kriebel, J. K.; Nuzzo, R. G.; Whitesides, G. M. *Chemical Reviews* 2005, *105*, 1103.
(2) Bosio, S. B. M.; Hase, W. L. *J. Chem. Phys.* 1997, *107*, 9677.
(3) Yan, T.; Hase, W. L. *Phys. Chem. Chem. Phys* 2000, *2*, 901.
(4) Yan, T.; Hase, W. L.; Barker, J. R. *Chem. Phys. Lett.* 2000, *329*, 84.
(5) Li, G.; Bosio, S. B. M.; Hase, W. L. *J. Mol. Struc.* 2000, *556*, 43.
(6) Meroueh, O.; Hase, W. L. *Phys. Chem. Chem. Phys* 2001, *3*, 2306.
(7) Yan, T.; Hase, W. L. *J. Phys. Chem. A* 2001, *105*, 2617.
(8) Yan, T.; Hase, W. L. *J. Phys. Chem. B* 2002, *106*, 8029.
(9) Song, K.; Meroueh, O.; Hase, W. L. *J. Chem. Phys.* 2003, *118*, 2893.
(10) Gibson, K. D.; Isa, N.; Sibener, S. J. *J. Chem. Phys.* 2003, *119*, 13083.
(11) Yan, T.; Isa, N.; Gibson, K. D.; Sibener, S. J.; Hase, W. L. *J. Phys. Chem. A* 2003, *107*, 10600.
(12) Isa, N.; Gibson, K. D.; Yan, T.; Hase, W.; Sibener, S. J. *J. Chem. Phys.* 2004, *120*, 2417.
(13) Troya, D.; Schatz, G. C. *J. Chem. Phys.* 2004, *120*, 7696.
(14) Day, B. S.; Morris, J. R.; Troya, D. *J. Chem. Phys.* 2005, *122*, 214712.
(15) Day, B. S.; Morris, J. R.; Alexander, W. A.; Troya, D. *J. Phys. Chem. A* 2006, *110*, 1319.
(16) Tasic, U. S.; Yan, T.; Hase, W. L. *J. Phys. Chem. B* 2006, *110*, 11863.
(17) Martínez-Núñez, E.; Rahaman, A.; Hase, W. L. *J. Phys. Chem. C* 2007, *111*, 354.
(18) Vazquez, S. A.; Morris, J. R.; Rahaman, A.; Mazyar, O. A.; Vayner, G.; Addepalli, S. V.; Hase, W. L.; Martinez-Nunez, E. *J. Phys. Chem. A* 2007, *111*, 12785.
(19) Yamamoto, H.; Watanabe, T.; Ohdomari, I. *J. Chem. Phys.* 2008, *128*, 164710.
(20) Lane, J. M. D.; Chandross, M.; Lorenz, C. D.; Stevens, M. J.; Grest, G. S. *Langmuir* 2008, *24*, 5734.
(21) Lane, J. M. D.; Chandross, M.; Stevens, M. J.; Grest, G. S. *Langmuir* 2008, *24*, 5209.
(22) Yang, L.; Mazyar, O. A.; Lourderaj, U.; Wang, J.; Rodgers, M. T.; Martínez-Núñez, E.; Addepalli, S. V.; Hase, W. L. *J. Phys. Chem. C* 2008, *112*, 9377.
(23) Mar, W.; Klein, M. L. *Langmuir* 1994, *10*, 188.
(24) Nogueira, J. J.; Vázquez, S. A.; Mazyar, O. A.; Hase, W. L.; Perkins Jr., B. G.; Nesbitt, D. J.; Martínez-Núñez, E. *J. Phys. Chem. A* 2009, 113(16), 3850-3865.

(25) Day, B. S.; Morris, J. R. *J. Chem. Phys.* 2005, *122*, 234714.
(26) Perkins Jr., B. G.; Nesbitt, D. J. *J. Phys. Chem. B* 2008, *112*, 507.
(27) Borodin, O.; Smith, G. D.; Bedrov, D. *J. Phys. Chem. B* 2002, *106*, 9912.
(28) Stone, A. J. *The Theory of Intermolecular Forces*; Oxford University Press: New York, 1996.
(29) Weiner, S. J.; Kollman, P. A.; Case, D. A.; Singh, U. C.; Ghio, C.; Alagona, G.; ProfetaJr, S.; Weiner, P. *J. Am. Chem. Soc.* 1984, *106*, 765.
(30) Brooks, B. R.; Bruccoleri, R. E.; Olafson, B. D.; States, D. J.; Swaminathan, S.; Karplus, M. *J. Comput. Chem.* 1983, *4*, 187.
(31) Hariharan, A.; Harris, J. G. *J. Chem. Phys.* 1994, *101*, 4156.
(32) Cui, S. T.; Siepmann, J. I.; Cochran, H. D.; Cummings, P. T. *Fluid Phase Equilib.* 1998, *146*, 51.
(33) Cui, S. T.; Cochran, H. D.; Cummings, P. T. *J. Chem. Phys. B* 1999, *103*, 4485.
(34) Perkins Jr., B. G.; Haeber, T.; Nesbitt, D. J. *J. Phys. Chem. B* 2005, *109*, 16396.
(35) Perkins Jr., B. G.; Nesbitt, D. J. *J. Phys. Chem. B* 2006, *110*, 17126.
(36) Perkins Jr., B. G.; Nesbitt, D. J. *J. Phys. Chem. A* 2007, *111*, 7420.
(37) Perkins, B. G.; Nesbitt, D. J. *J. Phys. Chem. A* 2008, *112*, 9324.
(38) Perkins Jr, B. G.; Nesbitt, D. J. *Proc. Natl. Acad. Sci. USA* 2008, *105*, 12684.
(39) Ramasamy, S.; Pradeep, T. *J. Chem. Phys.* 1995, *103*, 485.
(40) Pradeep, T.; Miller, S. A.; Cooks, R. G. *J. Am. Soc. Mass Spectrom.* 1993, *4*, 769.
(41) Davies, P. R.; Orville-Thomas, W. J. *J. Mol. Struc.* 1969, *4*, 163.
(42) Person, W. B.; Zerbi, G. *Vibrational Intensities in Infrared and Raman Spectroscopy* 1982.
(43) Shimanouchi, T. *Table of Molecular Vibrational Frequencies, Consolidated Volume 1*; NSRDS NBS-39, U.S. Department of Commerce: Washington, DC, 1972.
(44) Liu, G. Y.; Fenter, P.; Chidsey, C. E. D.; Ogletree, D. F.; Eisenberger, P.; Salmeron, M. *J. Chem. Phys.* 1994, *101*, 4301.
(45) Peslherbe, G. H.; Wang, H.; Hase, W. L. *Adv. Chem. Phys.* 1999, *105*, 171.
(46) Allen, M. P.; Tildesley, D. J. *Computer Simulation of Liquids*; Clarendon Press: Oxford, 1987.
(47) Nathanson, G. M. *Annu. Rev. Phys. Chem.* 2004, *55*, 231.
(48) Hurst, J. E.; Becker, C. A.; Cowin, J. P.; Janda, K. C.; Wharton, L.; Auerbach, D. J. *Phys. Rev. Lett.* 1979, *43*, 1175.
(49) Rettner, C. T.; Schweizer, E. K.; Mullins, C. B. *J. Chem. Phys.* 1989, *90*, 3800.
(50) Aoiz, F. J.; Herrero, V. J.; Sáez-Rábanos, V. *J. Chem. Phys.* 1992, *97*, 7423.

(51) Aoiz, F. J.; Bañares, L.; Herrero, V. J. *J. Chem. Soc., Faraday Trans*. 1998, *94*, 2483.

(52) Cohen, S. R.; Naaman, R.; Sagiv, J. *Phys. Rev. Lett.* 1987, *58*, 1208.

(53) Paz, Y.; Naaman, R. *J. Chem. Phys.* 1991, *94*, 4921.

(54) Day, B. S.; Shuler, S. F.; Ducre, A.; Morris, J. R. *J. Chem. Phys*. 2003, *119*, 8084.

(55) Day, B. S.; Morris, J. R. *J. Phys. Chem. B* 2003, *107*, 7120.

(56) Saecker, M. E.; Nathanson, G. M. *J. Chem. Phys*. 1993, *99*, 7056.

(57) Hwang, G. S.; Anderson, C. M.; Gordon, M. J.; Moore, T. A.; Minton, T. K.; Giapis, K. P. *Phys. Rev. Lett*. 1996, *77*, 3049.

(58) Minton, T. K.; Giapis, K. P.; Moore, T. *J. Phys. Chem. A* 1997, *101*, 6549.

(59) King, M. E.; Nathanson, G. M.; Hanning-Lee, M.; Minton, T. K. *Phys. Rev. Lett.* 1993, *70*, 1026.

Chapter 8

Dynamics of CO_2/F-SAM: Vibrational Angular Momentum

1. INTRODUCTION

Experimental studies of interactions between a gas and a liquid surface have provided us with fundamental knowledge of the scattering mechanism.[1-14] Recently, Nesbitt's group has investigated in detail the dynamics of collisions of CO_2 with liquid surfaces.[15-22] Distributions of the scattered CO_2 molecules for the vibrational, rotational and translational degrees of freedom help elucidate the scattering mechanism, for example, whether it is dominated by thermal-desorption (TD) or by higher energy, non-thermal desorption. In particular, Nesbitt and co-workers studied the stereodynamics,[15,18,19] the influence of the incident angle,[16,20] of the collision energy,[21] and of the surface temperature,[17] on the collision dynamics of CO_2 with perfluoropolyether (PFPE) and with perfluorinated alkanethiol self-assembled monolayers (F-SAM) on gold using dynamics simulations.

The results of Nesbitt and co-workers on the CO_2 + PFPE scattering dynamics provide evidence for nonthermal scattering dynamics. In particular, the CO_2 rotational distributions are consistent with two different mechanisms: a thermal desorption (TD) Boltzmann component in which the scattered molecules become accommodated with the 298 K surface temperature and a component with much higher energies and a Boltzmann temperature of ~ 750 K.[22] The experimental results also show that CO_2 scatters off the liquid surface in both the ground (00^00) state and the first excited (01^10) bend state, with vibrational temperatures T_{vib} in the range 200-300 K, i.e., much colder than T_{rot}, and below the liquid surface temperature of 298 K. The inefficient warming of the CO_2 bend mode is in accordance with standard theories of energy transfer among different degrees of freedom, whereby impulsive collisions can impart considerable additional energy into translation and rotation, while the vibrational states with much larger energy spacings remain largely unpopulated. In contrast to rotation and translation motion, the bend vibrational mode of CO_2 appears to be largely decoupled from the surface, at least on time scales sampled under the experimental scattering conditions. To reach equilibrium, CO_2 must remain on the surface sufficiently long to exchange 667 cm^{-1} (1.9 kcal/mol) of energy into and/or out of the bending vibrational manifold. Similar results were found in experimental studies of acetylene (C_2H_2) scattering from LiF(100).[23] The results indicate that acetylene largely retains its vibrational energy throughout the scattering event and the time required to completely relax the vibrations of acetylene was much longer than needed to translationally accommodate the molecules with the surface. No experimental or theoretical studies of vibrational relaxation have been performed for CO_2 physisorbed on a PFPE liquid or similar surface. Therefore,

it would be of interest to carry out dynamics simulations of vibrational energy accommodation in collisions of CO_2 with PFPE or F-SAM.

We have studied the dynamics of collisions of CO_2 with F-SAM[24,25] and compared the simulation results with those obtained by Nesbitt and co-workers in their experiments of CO_2 scattering off a liquid PFPE surface.[22] The simulations identify three different trajectory types, i.e. those that penetrate the surface, physisorb on the top of the surface, and those that directly scatter without penetration or physisorption. Of these trajectory types only those that penetrate are accommodated with the 298 K surface temperature. The calculated CO_2 rotational energy distribution is in near quantitative agreement with experiment and may be fit by a sum of Boltzmanns as is done experimentally. However, an analysis of the trajectories indicates that the low temperature, 298 K, Boltzmann component is comprised of all three trajectory types. The translational energy distribution of the scattered CO_2 molecules is also determined from the simulations and it may not be fit by the sum of two Boltzmanns as is possible for the rotational energy distribution.

Although the surfaces used in the experiments and in the simulations are different, experiment and simulations predict similar internal energy distributions of the scattered CO_2 molecules. This suggests that F-SAM can be used as a model surface in energy transfer studies of CO_2 scattering off a liquid PFPE surface. The use of F-SAM as a model for liquid PFPE to study the scattering dynamics of CO_2 molecules is further supported by work done in Cooks' group,[26] who observed similar energy transfer efficiencies and ion-surface reactions for both PFPE and F-SAM, and by Ramsamy and Pradeep,[27] who observed that the surface of PFPE is primarily formed by the terminal $-CF_3$ groups.

In the present work, chemical dynamics simulations of CO_2 in the ground (00^00) and first excited (01^10) bend states scattering from F-SAM are performed to study vibrational relaxation/warming of the bend vibrational mode in the scattering process. Comparisons are made with the available experimental rovibrational CO_2 distributions of the scattered molecules at two incident energies, 1.6 and 10.6 kcal/mol.[21,22] Our goal is to study in detail the exchange of energy into and/or out of the bending vibrational manifold and to determine the time scale for vibrational energy accommodation.

2. COMPUTATIONAL DETAILS

2.1 Potential energy surface

The potential function for the system has been described previously,[25] and comprises an intramolecular potential for carbon dioxide, V_{CO_2}, a potential for the F-SAM, V_{surf}, and the interaction between both, V_{CO_2-surf}:

$$V = V_{CO_2} + V_{surf} + V_{CO_2-surf} \tag{8.1}$$

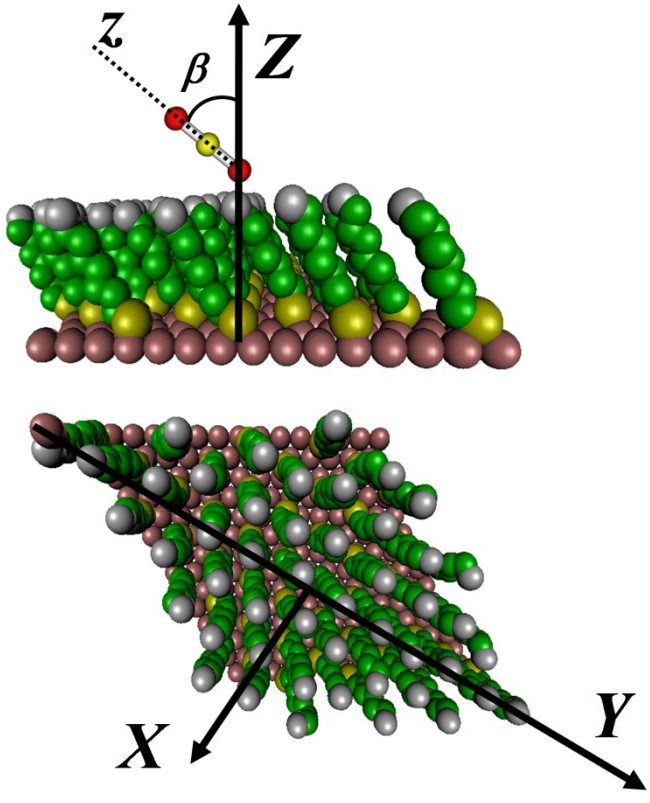

Figure 8.1: UA model of the F-SAM with the 48 chains and the definition of the coordinates and angles used in this study.

In previous work,[28] several united atom (UA) models for the F-SAM were developed, where the CF_3 and CF_2 groups are treated as single pseudo-atoms. With this simplification the total number of interaction sites diminishes dramatically with respect to the all atom (AA) model,[24,25] which results in a substantial decrease in CPU time. Among the UA models proposed in our previous work[28], UA3 gives the best results for energy transfer efficiencies and

for rotational and translational distributions of the scattered CO_2 molecules. The good performance of UA3 alongside with the considerable save in CPU time (simulations using the UA models of the F-SAM are ~3 times faster than those using the corresponding AA models) made it our choice for the simulations presented in this paper.

As in previous computational studies,[24,25,28] the F-SAM surface consists of 48 chains of $CF_3(CF_2)_7S$ radicals adsorbed on a single layer of 196 constrained Au atoms. The potentials for CO_2, for the surface and the interaction between both are described in previous work[28] and for simplicity there are not given here. Figure 8.1 shows the 48 UA chains that make up the model for our F-SAM with the definition of the coordinates and angle used below. In particular, X and Y define the surface plane, Z is the surface normal and β is the angle formed between the O–O direction (z) and the Z-axis.

2.2 Trajectory simulations

Carbon dioxide molecules collide with the surface perpendicularly (along the Z-axis) with incident energies of 1.6 and 10.6 kcal/mol. The dynamics of CO_2 scattering from PFPE at both incident energies were investigated experimentally.[21] The projectiles are aimed randomly at a point in the unit cell on the surface as described in detail in previous work.[25] The initial separation between CO_2 and the surface aiming point was 25 Å (37 Å above the gold atoms). Prior to the propagation of the first trajectory, a molecular dynamics simulation was performed for 2 ps to ensure thermal relaxation of the F-SAM surface at 298 K. The structure thus obtained was used later as the initial structure of a 100 fs equilibration run before the second trajectory. This process was repeated before initiation of each trajectory. Periodic boundary conditions and the image vector convention[29] were used to represent a larger surface, thus avoiding possible complications that may appear in collisions resulting in multiple CO_2 encounters with the surface. Trajectories were stopped when the distance between CO_2 and the surface was 30 Å or when 150 ps elapsed. The Adams-Moulton algorithm was employed to integrate the trajectories with a fixed step size of 0.3 fs. With this step size the energy conservation was better than five significant figures. For each of the initial conditions batches of 5000 trajectories were run with VENUS05.[30]

2.2.1 Internal energy sampling of CO_2

The aim of this work is to obtain an insight into the vibrational activation/relaxation processes of vibrationally cold/excited carbon dioxide colliding with an F-SAM. The lowest frequency mode of CO_2 is the degenerate

bend modes ($\tilde{\nu}$ = 667 cm^{-1}). Excitations of the degenerate bends thus provide a good opportunity to investigate vibrational energy transfer between carbon dioxide and the surface. In addition, Nesbitt and co-workers in their experiments of CO_2 scattering off PFPE[21] reported vibrational temperatures of the incident beam of the order of ~200 K, which populates the first excited bend state (01^10) of CO_2. The vibrational state of carbon dioxide is denoted as (n_1,N^L,n_3), where n_1, N, n_3 and L are the symmetric stretch, the degenerate bends, the asymmetric stretch, and the vibrational angular momentum quantum numbers, respectively.

In the present work, chemical dynamics simulations were performed for the two lowest bend states of CO_2, (00^00) and (01^10). Since we are only interested in the CO_2 bend energy, and the vibrational quantum numbers of the stretchings (n_1 and n_3) are zero, the notation (N^L) instead of ($0N^L0$) will be used throughout the paper for simplicity. Therefore, according to the vibrational frequencies of our model potential[25] the symmetric and asymmetric stretching modes have energies of 1.81 and 3.46 kcal/mol, respectively.

The sampling of vibrational angular momentum states for linear molecules has been presented elsewhere,[31] and is already one of the standard options of VENUS05. Briefly, the sampling assumes the harmonic oscillator and separable rotation-vibration model, for which the total energy for a linear molecule's pair of normal-mode degenerate bends is

$$E_{bend} = \left(n_a + \frac{1}{2}\right)h\upsilon + \left(n_b + \frac{1}{2}\right)h\upsilon = (N+1)h\upsilon \qquad (8.2)$$

where the n's are the bends' vibrational quantum numbers and $N = n_a + n_b$. Each value of N is associated with $N + 1$ degenerate energy levels and wave functions $\boldsymbol{\Psi}(n_a,n_b)$ corresponding to different possible combinations of n_a and n_b. The vibrational angular momenta for the states are $j_z = L\hbar$, (z is the axis of the molecule) with $L = N, N-2, \ldots -(N-2), -N$. By changing the difference in the phase of the two degenerate bends, a given vibrational angular momentum quantum number L can be selected. Details of this algorithm have been given previously[31]. The initial rotational quantum number J was set to 0 in our calculations.

Some of the initial bend energy of CO_2 could flow to the symmetric stretch due to the strong coupling between both modes. This energy flow is expected to be fast in comparison with the time needed to reach the F-SAM surface (~2.5 ps at E_i = 10.6 kcal/mol).[24] To investigate intramoleclar vibrational energy transfer in our model for CO_2, the average bending and stretching energies for ensembles of 100 trajectories were calculated as a function of time. Figure 8.2a shows these average mode energies for the (0^0)

and (1^1) states. The bend energies show fluctuations due to energy transfer processes between the various modes of the molecule, although the time averaged value is conserved in the time scale shown in the figure. The Fourier transform (FT) of the average bend energies yield a spectrum that contains bands at frequencies corresponding to the mode-to-mode rate coefficients.[32] Figure 8.2b shows the FT of the corresponding energies in panel a. The FT of the (0^0) state shows only one band at 5.1 ps^{-1}, which corresponds to the rate at which the energy is being transferred between the bending mode and the symmetric stretch. For the (1^1) state there is an additional band with very low intensity at 52.9 ps^{-1} that involves the rotation about the molecular axis, initially excited in the (1^1) state. The two mode-to-mode energy transfer rates 5.1 ps^{-1} and 52.9 ps^{-1} correspond to very short time scales of 0.2 and 0.02 ps, respectively; much shorter than the time needed for CO_2 to reach the F-SAM (at least 2.5 ps).

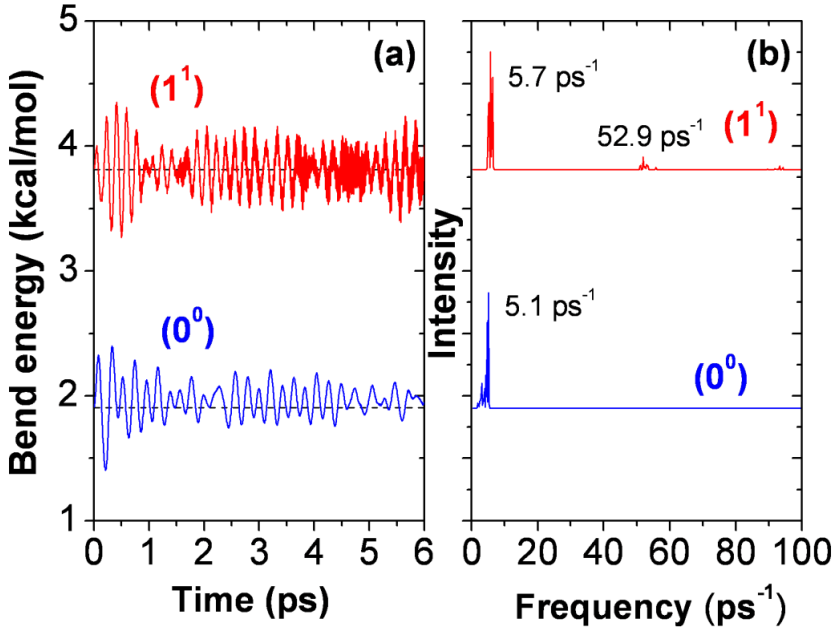

Figure 8.2: (a) Average bend energies vs time for an ensemble of 100 trajectories of CO_2 in the (0^0) and (1^1) bend states (blue and red lines, respectively). (b) Fourier transforms of the average bend energies of plot (a) for the corresponding initial states.

Although the average vibrational bend energy is conserved for several ps for an ensemble of trajectories as seen above, this may not be the case for individual trajectories. In particular, Figure 8.3 shows, for an individual trajectory, the bending and symmetric stretching energies and the rotational

energy about the molecular axis for the (0^0) and (1^1) states of CO_2. As seen in the figure, the initial energy of the (0^0) state (1.9 kcal/mol) is not conserved for this trajectory and it drops to an average value of 1.0 kcal/mol; the energy difference of 0.9 kcal/mol between the initial and the time averaged value is transferred to the symmetric stretch. For the (1^1) state there is also a drop in the bending energy although in this case it only represents ~20% of its initial value (the initial bending energy is 3.8 kcal/mol and the average value after several ps is 3.0 kcal/mol). For the (1^1) state, excitation of the vibrational angular momentum is conserved, which prevents a dramatic energy flow to the stretching mode as occurred for the (0^0) state. The non-conservation of the mode energies poses an important complication in the present study.

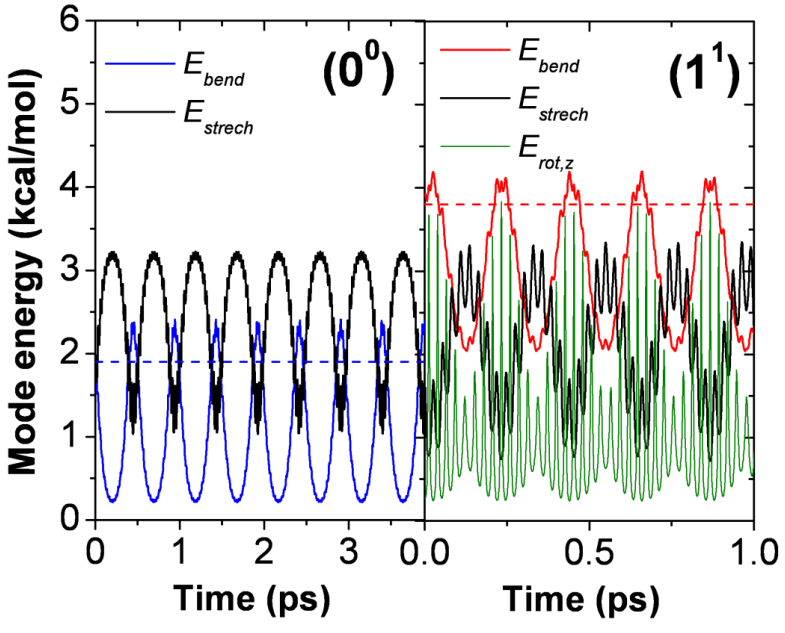

Figure 8.3: Mode energies for individual trajectories of CO_2 in their (0^0) and (1^1) bend states. Black lines correspond to the symmetric stretch energies, blue and red lines to the bend energies in the (0^0) and (1^1) states, respectively, and the green line is the rotational energy about the molecular axis (z).

The unphysical bend energy leakage can be largely attenuated by selecting only those trajectories that conserve their time averaged mode energies within a reasonable percentage of the initial value. Ensembles of 10^5 trajectories were run to investigate the conditions for which the (0^0) and (1^1) bend states conserve their energy. The trajectories that conserved their bend energies were found to fulfill a particular relationship between the phases of the stretching and bending normal modes. In particular, it was found that when the

phase of the bending mode α_b and that of the stretching α_s follow this relationship:

$$\alpha_s = (a - n)\pi + b\alpha_b \tag{8.3}$$

The conservation of the time averaged bending mode energy is within 3% of its initial value. The phases of both the bending and stretching modes are depicted in Figure 8.4 for those trajectories with (0^0) that conserve their bend energies. The quasiperiodic character of the CO_2 trajectories can be studied by the so-called Poincaré surface of section,[33] which is constructed by plotting simultaneous (θ, $d\theta/dt$) values whenever the trajectory crosses a given line ($R_{\mathrm{CO}} = R_{\mathrm{CO}}^{eq}$ in our case). The resulting points provide snapshots of the underlying phase space orbits. Figure 8.5 shows the Poincaré surfaces of section for four different CO_2 trajectories, for the (0^0) bend state, with time averaged bend mode energies of 0.8, 1.3, 1.9 and 2.7 kcal/mol. The integration time was 50 ps and, since the asymmetric stretching is not coupled with the other modes, it was given no energy in these simulations. Our calculations confirm that all trajectories with the same time averaged bend mode energies have the same Poincaré surfaces of section. The Poincaré surfaces of section for those trajectories that conserve their initial energy in the bend mode (1.9 kcal/mol) are distorted eights, whereas trajectories with different time averaged bend mode energies give rise to different patterns as seen in the figure. All trajectories are quasiperiodic for the (0^0) bend state but the initial phase differences between the bending and the stretching give rise to different bend mode energies and phase space orbits.

For the (1^1) state a similar behavior of the stretching and bending phases was found and the results of the fits of equation 8.3 to the trajectory points are collected in Table 8.1. In the fittings the values of a were fixed and b and n were optimized. First, for each initial bend state, six initial fits were done for each group of points in Figure 8.4. Then, using the average values of b, equation 8.3 was refit to the trajectory data, fixing now both a and b, and optimizing the values of n. The percentage of trajectories that conserve their initial energies is 3% and 10% for the (0^0) and (1^1) states, respectively. Therefore, the algorithm that selects vibrational angular states for linear molecules in VENUS[31] was modified for CO_2 to restrict the phases of the symmetric stretch according to equation 8.3. In a section below, the use of equation 8.3 to select the initial normal mode phases of the CO_2 molecules is discussed in more detail.

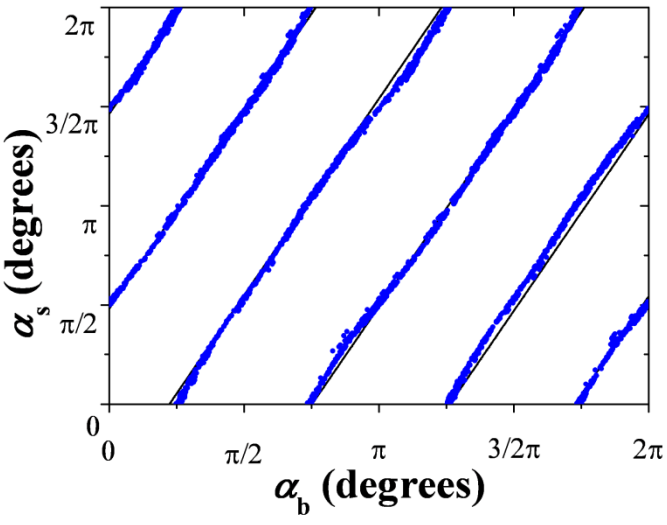

Figure 8.4: Correlations between the phase of the stretching mode (α_s) and that of the bending mode (α_b) for the trajectories that conserve their average bend energy within 3% of its initial value in the (0^0) state.

Table 8.1: Parameters obtained in the fits of equation 8.3 to the trajectory data that show the relationship between the phases of the stretching and bending modes for trajectories that conserve their bend energies.

CO_2 bend state	a	b[a]	n[b]
(0^0)	1.5	1.982 ± 0.008	0.003 ± 0.009
			1.016 ± 0.001
			1.977 ± 0.002
			2.985 ± 0.002
			3.945 ± 0.002
			4.929 ± 0.003
(1^1)	1.6	2.016 ± 0.009	0.055 ± 0.003
			0.055 ± 0.00
			1.985 ± 0.003
			2.925 ± 0.003
			3.973 ± 0.002
			4.886 ± 0.006

[a]The reported errors for b are the average errors of each of the fits in the first fitting (see text). [b]Each value of n corresponds to the different lines of Figure 8.4.

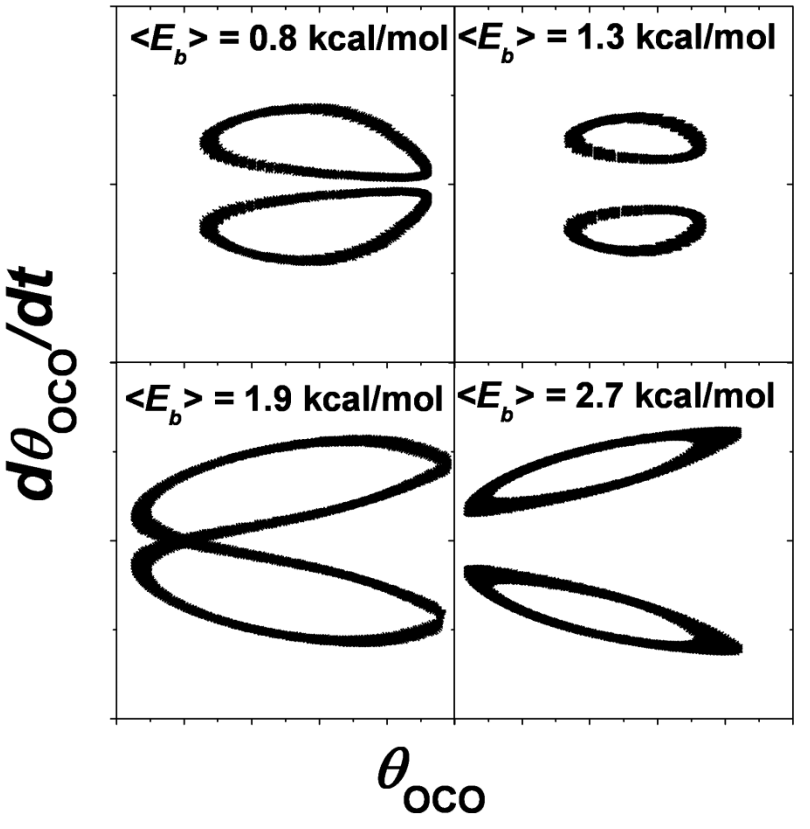

Figure 8.5: Poincaré surfaces of section (for $d\theta/dt$ vs θ, where θ is the OCO angle) calculated for four different CO_2 trajectories with $N = 0$ and $L = 0$. The symmetric stretching contains the zero-point energy and the asymmetric stretch has no energy. The total integration time was 50 ps. The surfaces-of-section were obtained for $R_{\mathrm{CO}} = R_{\mathrm{CO}}^{eq}$.

2.2.2 Determination of the final CO_2 energies and ro-vibrational states

From the final coordinates and momenta of CO_2, internal (rotational and vibrational) and bend mode energies can be obtained. The procedure to calculate the internal energies is standard in VENUS05. Since the internal coordinates do not depend on the molecular frame, they can be employed to calculate the bend energy as described by Wilson *et al.*[34] In particular, for CO_2 the bend energy can be calculated from the values of its angle θ and its time derivative $d\theta/dt$ as:

$$E_{bend} = \frac{1}{2} f_\theta (\theta - \theta_e)^2 + \frac{1}{2} \frac{m_O m_C R_e^2}{2m_C + 4m_O} \dot{\theta}^2 + \frac{j_z^2}{2I_z} \qquad (8.4)$$

where m_O, m_C and R_e are the masses of the oxygen and carbon atoms, and the CO equilibrium distance, respectively; f_θ is the bending force constant and I_z the moment of inertia about the molecular axis.

A real value for the bend vibrational state N can be determined by equating equation 8.2 to the classical determination of the bending energy (equation 8.4) and L and J can be determined from the relationships $j_z = L\hbar$ and $j = \sqrt{J(J+1)}\hbar$, respectively. The usual procedure to get integer values (quantum numbers) from the above classical actions consists in rounding the real values to the nearest integer [hereinafter called histogram binning (HB)], so that each trajectory will contribute 0 or 1 to the probability to end in a given quantum number. Some years ago, Bonnet and Rayez[35,36] proposed the use of Gaussian functions centered in the integer values (quantum numbers) to get more reliable distributions in the products. Gaussian binning (GB) was found to be superior than HB in predicting reactive cross sections and product energy distributions for a number of processes.[37-40] In the GB, each trajectory will contribute to the probability of every quantum number n but will contribute more for values of the classical actions close to n. In the present work, the final N and L quantum numbers of CO_2 were assigned according to both the HB and the GB. The full-width-half maximum (FWHM) of the Gaussian functions was 0.5 in the GB. Previous studies by Aoiz and co-workers[37-40] used narrower Gaussian functions. However, decreasing the FWHM of the Gaussians is not possible in our study due to poor statistics around the (1^1) state. For an accurate analysis of our trajectory results using GB, the total number of trajectories should be significantly increased. For this reason, the results obtained in this study with GB should be taken with caution and regarded only as an alternative to HB.

3. RESULTS

3.1 Bend energy transfer

The distributions of the final bend energies $P(E_b)$ of the scattered CO_2 molecules are depicted graphically in Figure 8.6 for both the (0^0) and (1^1) initial states at the two incident energies studied here. The colored areas in the figure represent the distributions for the different trajectory types. The percentages of (direct, penetration and physisorption) trajectories for the (0^0) initial state are (14, 33 and 53) and (46, 14 and 40) at E_i = 1,6 and E_i = 10.6 kcal/mol, respectively. These values are the same for the bend excited state. The differences in the percentages of the trajectory types as a function of incident energy have been discussed in detail previously.[24]

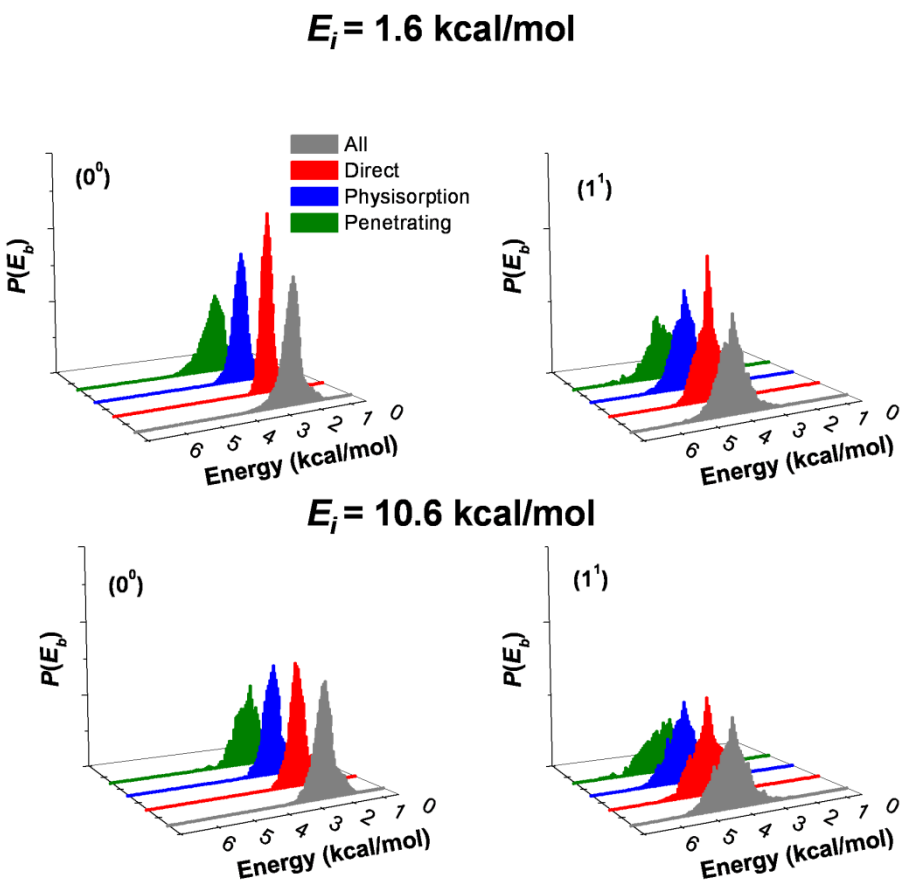

Figure 8.6: Distributions of the bend energy $P(E_b)$ for the different trajectory types at the incident energies and initial bend states studied here. The energy is calculated according to equation 8.4 and therefore refers to the bottom of the well.

In addition, Table 8.2 collects the full-width at half maximum (FWHM) and the average bend energy $\langle E_b \rangle$. The $P(E_b)$ distributions for the (0^0) initial state at both incident energies are slightly hot with an average value of 2.0 kcal/mol (vs an initial bend energy of 1.9 kcal/mol). The (0^0) $P(E_b)$ distributions of the penetrating trajectories (green color) are broad with a FWHM of ~1.0 kcal/mol vs 0.6 kcal/mol obtained for the remaining trajectories (see Table 8.2). Additionally, the average value of the bend energy $\langle E_b \rangle$ of the penetrating trajectories (for the initial 0^0 state) is 2.1 kcal/mol vs 2.0 kcal/mol obtained for all trajectories. This indicates that bend energy transfer is more efficient for penetrating trajectories than for the remaining trajectories.

The $P(E_b)$ distributions found in our study for both incident energies are very similar except those for the direct trajectories at E_i = 1.6 kcal/mol, which are narrower than the others; For the initial (0^0) state, the FWHM is only

0.4 kcal/mol. Direct trajectories undertake only one inner turning point along the Z direction,[24] which inefficiently promotes vibrational energy transfer. In addition, at the lowest incident energy, energy transfer is inefficient by an impulsive mechanism as well, which explains the almost 100% adiabatic behavior of the bend energy for direct trajectories.

Table 8.2: Features of the final bend energy distributions $P(E_b)$ at the two incident energies studied here.

Initial state		Direct	Physisorption	Penetration	Total
E_i = 1.6 kcal/mol					
(0^0)	FWHM[a]	0.41 ± 0.00	0.53 ± 0.00	0.97 ± 0.02	0.57 ± 0.01
	$\langle E_b \rangle$[a]	1.95 ± 0.01	2.02 ± 0.01	2.12 ± 0.03	2.05 ± 0.01
(1^1)	FWHM[a]	0.69 ± 0.01	0.83 ± 0.01	1.34 ± 0.03	0.90 ± 0.01
	$\langle E_b \rangle$[a]	3.75 ± 0.02	3.74 ± 0.02	3.64 ± 0.04	3.72 ± 0.02
E_i = 10.6 kcal/mol					
(0^0)	FWHM[a]	0.59 ± 0.01	0.64 ± 0.01	1.02 ± 0.02	0.64 ± 0.01
	$\langle E_b \rangle$[a]	2.00 ± 0.01	2.02 ± 0.01	2.11 ± 0.04	2.02 ± 0.01
(1^1)	FWHM[a]	0.98 ± 0.02	1.05 ± 0.01	1.58 ± 0.03	1.06 ± 0.01
	$\langle E_b \rangle$[a]	3.73 ± 0.02	3.76 ± 0.02	3.63 ± 0.06	3.74 ± 0.02

[a]In kcal/mol. The FWHMs are obtained from fits of Gaussian functions to our $P(E_b)$ distributions. The reported errors are given for a 95% confidence limit.

The trajectories for the initial (1^1) state present broader distributions than those for the (0^0) state; the FWHMs for the (1^1) state are 0.2–0.5 kcal/mol higher than those for the (0^0) state. Additionally, the penetrating trajectories give rise to $P(E_b)$ distributions with a FWHM of 1.3 (1.6) for E_i = 1.6 kcal/mol (10.6 kcal/mol) (much higher than those for the remaining trajectories). The average values of the $P(E_b)$ distributions for the (1^1) state are about 3.7 kcal/mol for both incident energies. For the penetrating trajectories the average values of the distributions are lower than those for the remaining trajectories. As above, bend energy transfer is more efficient for penetrating trajectories.

In previous work, we had found that penetrating trajectories led to rotational and translational distributions of the scattered CO_2 molecules which could be fit by 298 K (the surface temperature) Boltzmann distributions.[24,25] This result indicates that the time scale involved in the penetration process is

long enough to ensure rotational and translational energy accommodation, which is in line with our conclusion that bend energy transfer is more efficient for penetrating trajectories. To investigate whether the time scale of penetration is also enough to attain vibrational energy accommodation, the dependence of the $P(E_b)$ distributions for the penetrating trajectories with the residence time was also analyzed. As in previous work,[24] the residence time τ is defined here as the difference between the first and the last inner turning points in the Z direction. Figure 8.7 shows the variation of $\langle E_b \rangle$ for the penetrating trajectories as a function of τ for the two incident energies and initial states. To obtain $\langle E_b \rangle$, the trajectories were sorted in different bins so that every bin has a similar number of trajectories. As seen in the figure, $\langle E_b \rangle$ increases as a function of τ for the (0^0) state, whereas it decreases for the excited state. The average bend energies follow the same behavior for both incident energies. As seen in the figure, the bend energy shows linear dependence on the residence time on the time interval studied here 0–120 ps. However, this linear dependence is very weak (the slopes of the fits are $\leq$ 0.002 kcal/mol/ps) and, it seems that the time scale needed for vibrational energy accommodation is very long. This will be discussed in detail below.

The dependence of the vibrational angular momentum, j_z, on τ was also studied here, although the plots are not shown for simplicity. The average vibrational angular momentum increases with τ for the (0^0) ensemble of trajectories and it decreases for the (1^1) trajectories, following the same behavior as the bend energy.

The dependence of the average bend energy on the angle β formed between the CO_2 molecular axis (z) and Z at the moment of impact (see Figure 8.1 for the definition) was also investigated. As seen in Figure 8.8, it was found that, for the (0^0) initial state at E_i = 10.6 kcal/mol, $\langle E_b \rangle$ increases with β for the direct trajectories. For the other incident energy and bend states no angle dependence was found. As above, to calculate $\langle E_b \rangle$ the trajectories were sorted in different bins so that every bin has similar number of trajectories. For perpendicular orientations of CO_2 with respect to the surface (β = 0º) there is negligible excitation of the bend mode, whereas for β = 90º (with the CO_2 molecular axis lying on the XY plane) there is maximum excitation of the bend mode. This behavior can be explained on the basis of the hard-cube model[41] for gas-surface energy transfer, which rests on the assumption that the tangential component of momentum of the gas is conserved during collision with the surface, or, in other words, that the forces between the gas and the surface lie along the Z axis. Thus, in collisions with β = 0º the forces exerted on the molecule lie along the molecular axis, which is perpendicular to the bend mode eigenvector, whereas for β = 90º the forces exerted on the molecule are parallel

to the bend mode eigenvector, making excitation of the bend mode possible, provided the forces on the different atoms are different. This effect is not seen for E_i = 1.6 kcal/mol, because the magnitude of the forces is much smaller than for E_i = 10.6 kcal/mol. Hynes and co-workers found, in their study on the vibrational relaxation of the C–Cl bond of methyl chloride in water, that orientation of the water molecules with respect to the C–Cl bond is crucial and only those molecules that collide perpendicular to the C–Cl bond contribute significantly to the relaxation of the bond.[42]

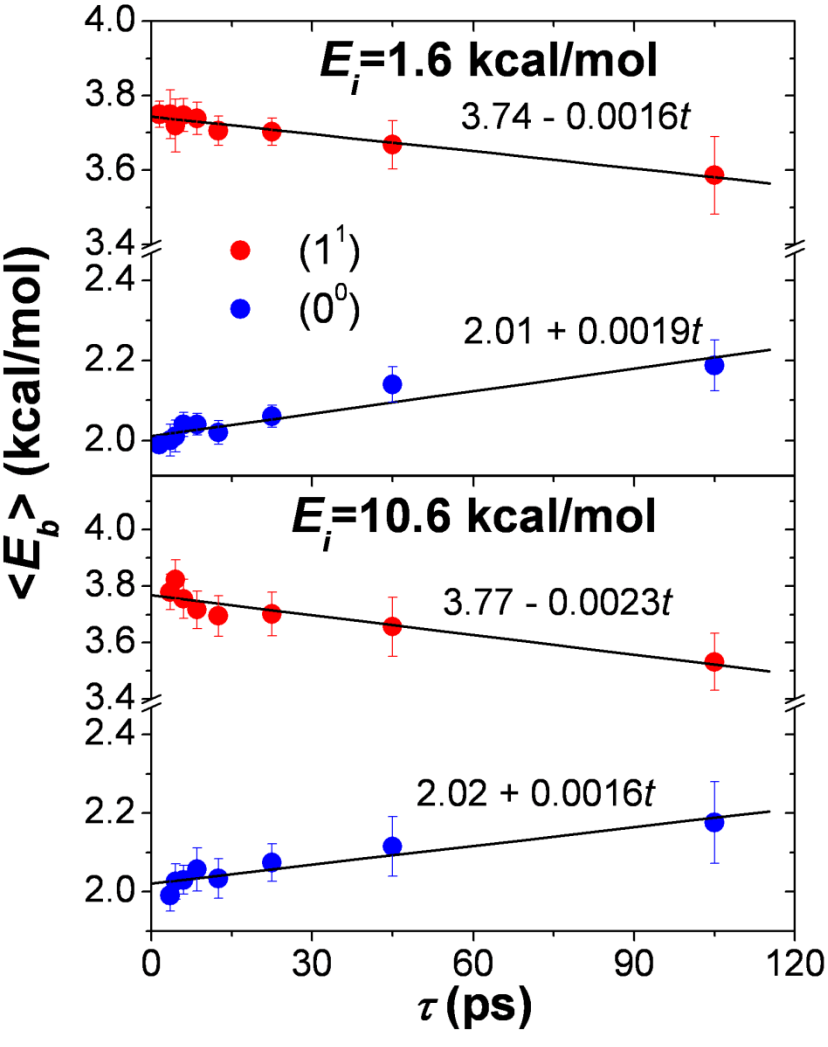

Figure 8.7: Variation of the average bend energies $\langle E_b \rangle$ vs residence time (τ) for the incident energies and initial bend states studied here.

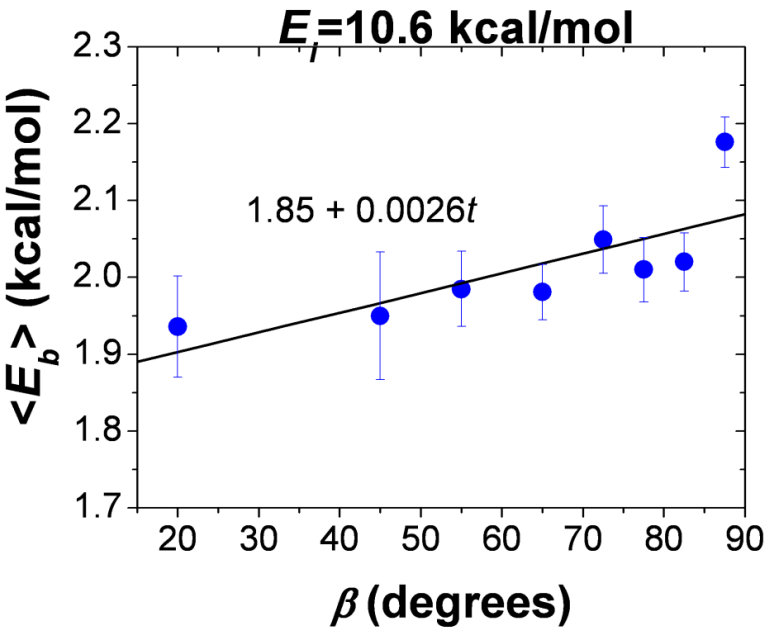

Figure 8.8: Variation of the average bend energies $\langle E_b \rangle$ vs the angle β, formed between the CO_2 molecular axis (z) and Z (see Figure 8.1), for the incident energies and initial bend states studied here.

3.2 Comparison with experiment

The simulation results of the present study are compared in this section with recent experimental work in Nesbitt's group for CO_2 scattering off PFPE.[21,22] In previous work, we have already shown that F-SAM is a very good model for PFPE to study the scattering dynamics of carbon dioxide.[24,25]

To carry out a detailed comparison between our simulations and the experiments, one has to take into account that the simulations provide flux distributions, where each trajectory has the same weight, and the 3D scattering space has no restrictions. However, in the experimental measurements, the concentration of CO_2 molecules in the laser volume (density) rather than flux is determined. In addition, the experimental laser geometry is very important because some projectiles scattering off the surface might not cross the laser beam depending on their final scattering and azymuthal angles.

Therefore, in order to make a rigorous comparison between simulations and experiments, the laser geometry has to be taken into account and flux-to-density transformations have to be made beforehand. The laser geometry employed by Perkins and Nesbitt,[21,22] is depicted in the cartoon of Figure 8.9, where the laser beam is assumed to be parallel to the X-axis. In particular, the laser beam is passed above a spot where the molecular beam

strikes the surface. The spot is represented in the figure as a circle of 2.5 cm of diameter and the laser is about 0.5 cm above the surface. Assuming uniform coverage over the collision area, only those CO_2 molecules that fulfill the following relationship between their scattering θ and azymuthal χ angles:

$$\chi < \arcsin\left(\frac{2.5}{tan\theta}\right) \tag{8.5}$$

will reach the laser beam and be detected. Therefore in our comparison of the trajectory results with the experiments only those trajectories that fulfill equation 8.5 are counted.

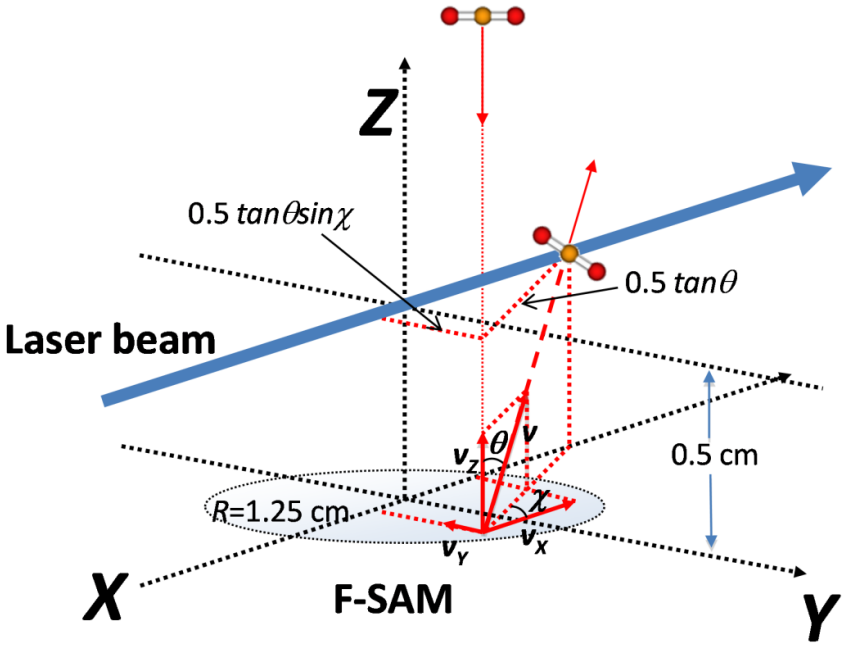

Figure 8.9: Laser beam geometry used in the experiments of Nesbitt and co-workers.[21,22] The laser propagation is assumed to be along the X-axis and passes 0.5 cm above the F-SAM surface. The scattering (θ) and azymuthal (χ) angles serve to sort the molecules according to whether they cross the laser beam and should be included in the analysis or not.

Additionally, the probability of absorption is proportional to the time that the molecule would spend traversing the laser beam. To carry out the flux-to-density transformation the laser beam is assumed to be a cylinder of diameter D. The transit time τ across the laser beam can be therefore calculated according to:

$$\tau = \frac{D}{\sqrt{v_Y^2 + v_Z^2}} \tag{8.6}$$

Since D is constant for each trajectory, the weight of each individual trajectory is just τ/D. This flux-to-density transformation was found to provide very good results for the J-dependent translational energy distributions of CO_2.[24]

The first comparison between our simulations and the experiments concerns the distributions $P(J)$ of the rotational quantum number J of the CO_2 molecules ending in the (0^0) and (1^1) bend states. As in previous work,[24,25] the $P(J)$ distributions obtained in our simulations were fit to the sum of two components, low temperature (LT) and high temperature (HT):

$$P(J) = \alpha_{\mathrm{LT}} P_{\mathrm{LT}} + \alpha_{\mathrm{HT}} P_{\mathrm{HT}} \tag{8.7}$$

where each of normalized component is given by

$$P_X(J) = \frac{(2J+1)e^{-E_{rot}/kT_{rot}(\mathrm{X})}}{Q_{rot}(\mathrm{X})} \tag{8.8}$$

with X = LT or HT. The rotational temperature of the LT component was fixed to 298 K, with α_{LT} and T_{rot} (HT) being the only variable parameters during the fittings.

Figure 8.10 displays graphically the distributions calculated in this work in comparison with the experimental data (circles) for the final (0^0) and (1^1) states of CO_2. The simulation results correspond to the fits of equation 8.7 to the trajectory data for the two incident energies using both GB and HB. Nesbitt and co-workers found that the population of the final (1^1) state is only 0.03 that of the (0^0) state,[22] however both distributions are normalized to one for visual clarity. The difference in the population of the (0^0) and (1^1) states explains the scattering in the experimental data for the final (1^1) state. The general conclusion from the figure is that the differences between the HB and GB theoretical results are negligible and both results agree well with the experimental data. The percentages of LT and HT components and their associated temperatures are collected in Table 8.3 for each of the distributions. The theoretical distributions at E_i = 1.6 kcal/mol are all well fit by single Boltzmann distributions with temperatures very close to the surface temperature. The experimental distribution for the (0^0) final state gives essentially the same result. At the highest E_i, the distributions are bimodal with each component (LT and HT) contributing approximately 50%. The rotational temperature of the HT component in our distributions for the final (0^0) state is about 770–800 K, which agrees, within the errors of the fits, with the experimental value of 710 K ± 60 K. Both the (0^0) and (1^1) manifolds present very similar $P(J)$ distributions.

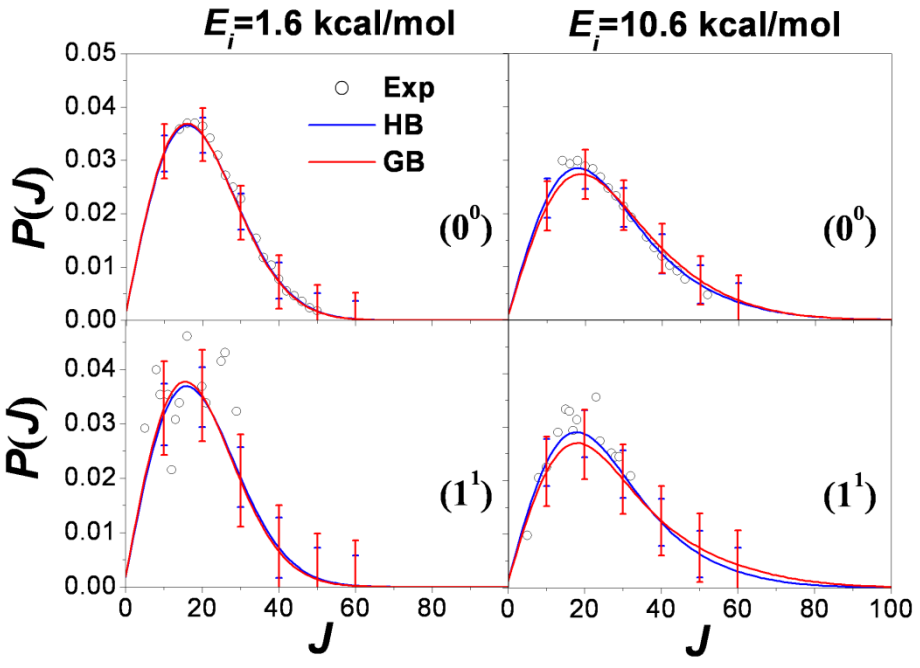

Figure 8.10: $P(J)$ distributions obtained in our simulations with HB and GB for the final (0^0) and (1^1) states of CO_2 compared with the experimental data (circles) at the two incident energies. The errors of the fits are given for the 95% confidence limits every 10 units.

The second comparison between our simulations and experiment concerns the population analysis of the (N^L) states of the scattered CO_2 molecules. The resulting percentages of molecules ending in a particular (N^L) state are collected in Tables 8.4 and 8.5 for E_i = 1.6 and 10.6 kcal/mol, respectively. The vibrational temperatures collected in the tables are "two-point" estimates using the (0^0) and (1^1) populations.

In all cases, HB and GB give similar results with the distributions obtained with HB being slightly hotter than those obtained with GB. For the trajectories with (1^1) initial bend states at both incident energies, the (2^2) state is populated after collision, but not the (2^0) state, which indicates that vibrational angular momentum is, in general, excited upon collisions with the F-SAM. This result has been already found in previous work and used to explain the apparent zero-point energy leakage of CO_2.[25]

All vibrational temperatures found in our simulations are near or below the surface temperature. To obtain vibrational temperatures from our simulations that can be compared with those obtained in the experiments, no more calculations are needed. In particular, the final bend state populations of

the trajectories with (0^0) and (1^1) initial bend states (see Tables 8.4 and 8.5) were weighted by the ratio of populations of both states obtained from the vibrational temperatures of the molecular beam: 255 and 190 K at E_i = 1.6 and 10.6 kcal/mol, respectively. The results collected in Tables 8.4 and 8.5 agree very well with the experimental data. In particular, at E_i = 1.6 kcal/mol the vibrational temperature obtained experimentally is 295 K, which compares quite well with the values obtained in our study of 262 and 272 K using GB and HB, respectively (see Table 8.4). At E_i = 10.6 kcal/mol the simulation results are 195 and 202 K for GB and HB, respectively, in comparison with a vibrational temperature of 230 K obtained experimentally (see Table 8.5). The vibrational temperature of the scattered CO_2 molecules obtained experimentally for the lowest incident energy (295 K) is higher than that obtained at the highest incident energy (230 K). However, the initial population of the (1^1) bend state at the lowest incident energy is higher than that for the highest incident energy due to different molecular beam conditions; the inefficient vibrational cooling in the experiments does not allow to draw a general conclusion.

Table 8.3: Parameters of the $P(J)$ distributions obtained in the fits to the trajectory data at E_i = 10.6 kcal/mol as a function of the final N^L state of CO_2.

Final State		α_{LT}	T_{rot} (LT)	T_{rot} (HT)
E_i = 1.6 kcal/mol				
(0^0)	HB	1	304 ± 5	-
	GB	1	299 ± 7	-
	Exp[a]	0.92 ± 0.12	298	330 ± 100
(1^1)	HB	1	299 ± 7	-
	GB	1	286 ± 1	-
E_i = 10.6 kcal/mol				
(0^0)	HB	0.52 ± 0.04	298	806 ± 64
	GB	0.42 ± 0.05	298	769 ± 67
	Exp[a]	0.54 ± 0.03	298	710 ± 60
(1^1)	HB	0.53 ± 0.05	298	773 ± 78
	GB	0.51 ± 0.05	298	980 ± 125

[a]From Ref.[21]

Table 8.4: Quantum distributions of the N^L states of scattered CO_2 obtained in our simulations at E_i = 1.6 kcal/mol in comparison with the experimental results.[a]

Initial state		(0^0)	(1^1)	(2^0)	(2^2)	T_{vib}
(0^0)	HB	98.3 ± 0.7	1.7 ± 0.7	0.0	0.0	202
		93.0 ± 2.8	*7.0 ± 2.8*	*0.0*	*0.0*	*292*
	GB	99.5 ± 0.6	0.5 ± 0.6	0.0	0.0	163
		97.0 ± 3.2	*3.0 ± 3.2*	*0.0*	*0.0*	*230*
(1^1)	HB	3.7 ± 1.1	94.7 ± 1.3	0.0	1.6 ± 0.8	
		12.1 ± 3.9	*83.3 ± 4.6*	*0.0*	*4.6 ± 2.8*	
	GB	1.8 ± 1.3	97.6 ± 1.5	0.0	0.6 ± 0.7	
		8.5 ± 6.6	*89.2 ± 7.3*	*0.0*	*2.3* ± 3.5	
Experimental conditions[b]	HB	94.1 ± 0.7	5.9 ± 0.7	0.0	0.0	277
		89.5 ± 2.9	*10.3 ± 2.8*	*0.0*	*0.2*	*337*
	GB	95.1 ± 0.6	4.9 ± 0.6	0.0	0.0	262
		93.1 ± 3.4	*6.8 ± 3.2*	*0.0*	*0.1*	*290*
	Exp[a]	92.8	7.2	-	-	295

[a]Values in italic are for the penetrating trajectories. [b]The vibrational temperature of the molecular beam is 255 K. The errors are given for the 95% confidence limits.

The final populations of the (0^0) and (1^1) states obtained for the direct and physisorption trajectories are very similar to those obtained for the whole set of trajectories. However, the distributions for the penetrating trajectories are markedly different and are also collected in Tables 8.4 and 8.5 for comparison. The vibrational distributions of the penetrating trajectories are hotter than those obtained for the remaining trajectories. In particular, the vibrational distribution of the penetrating trajectories for the initial (0^0) state at E_i = 1.6 kcal/mol obtained with HB gives a vibrational temperature of 292 K, very close to the surface temperature of 298 K, and the result for GB is 230 K. For the other trajectory types (direct and physisorption), vibrational energy accommodation does not take place in the time scales of these processes. In particular, for the initial (0^0) state, the direct trajectories at E_i = 10.6 kcal/mol (not shown in the tables) show a final population of the (0^0) state of 100% (99.9%) using HB(GB); for E_i = 1.6 kcal/mol the final population of the (0^0) state is 100% for both binning procedures. The results for the physisorption trajectories are almost identical to those obtained for the whole set of trajectories. The average

time scales for direct and physisorption trajectories are 0 and 10 ps, respectively.[24]

Table 8.5: Quantum distributions of the N^L states of scattered CO_2 obtained in our simulations at E_i = 10.6 kcal/mol in comparison with the experimental results.[a]

Initial state		(0^0)	(1^1)	(2^0)	(2^2)	T_{vib}
(0^0)	HB	99.4 ± 0.6	0.6 ± 0.6	0.0	0.0	164
		97.0 ± 3.8	*3.0 ± 3.8*	*0.0*	*0.0*	*230*
	GB	99.8 ± 0.5	0.2 ± 0.5	0.0	0.0	141
		98.0 ± 4.6	*2.0 ± 4.6*	*0.0*	*0.0*	*205*
(1^1)	HB	5.8 ± 1.6	92.1 ± 2.0	0.0	2.1 ± 1.3	
		20.6 ± 8.1	*75.9* ± 8.9	*0.0*	*3.5* ± 4.8	
	GB	2.9 ± 1.5	96.2 ± 1.9	0.0	0.9 ± 1.2	
		14.8 ± 10.3	*83.5 ± 11.2*	*0.0*	*1.7 ± 4.9*	
Experimental conditions[b]	HB	98.3 ± 0.6	1.7 ± 0.6	0.0	0.0	202
		96.1 ± 3.9	*3.9 ± 3.8*	*0.0*	*0.0*	*247*
	GB	98.6 ± 0.5	1.4 ± 0.5	0.0	0.0	195
		97.1 ± 4.7	*2.9 ± 4.6*	*0.0*	*0.0*	*227*
	Exp[a]	97.0	3.0	-	-	230

[a]Values in italic are for the penetrating trajectories. [b]The vibrational temperature of the molecular beam is 190 K. The errors are given for the 95% confidence limits.

Our simulation results agree with the experimental evidence of a lack of appreciable thermalization of the bend at E_i = 10.6 kcal/mol.[17] In order to quantify the time needed to achieve vibrational energy accommodation, Figure 8.11 shows the final populations of the (0^0) and (1^1) states of CO_2 for trajectories with initial (0^0) bend states at E_i = 1.6 kcal/mol as a function of the residence time for both HB and GB. The trajectories were sorted in different bins so that every bin has a similar number of trajectories. Although the HB vibrational distributions are slightly hotter than those obtained with GB, both distributions are very cold (with the final (0^0) state having a probability ≥ 99%) for residence times lower than 25 ps.

The vibrational temperatures calculated using the final populations of the (0^0) and (1^1) states are depicted graphically in Figure 8.12 as a function of the residence time at E_i = 1.6 kcal/mol. The behavior of the vibrational

temperature (T_{vib}) vs τ is asymptotic and the following equation fits reasonably the $T_{vib}(\tau)$ plots:

$$T_{vib}(\tau) = a \times \exp\left(-\frac{b}{\tau}\right) \tag{8.9}$$

As seen in Figure 8.12, the fitting of equation 8.9 to the HB temperatures is better than that to the GB temperatures. The value of parameter a, which is the limiting vibrational temperature for infinite residence time is 298 K for the GB temperatures (red circles) and 446 K for the HB temperatures (blue circles). The limiting vibrational temperature obtained with GB surprisingly coincides with the surface temperature and that obtained with HB is higher. The latter result is clearly in error due to the approximations used to obtain the vibrational populations and temperatures. Anyway, as seen in Figure 8.12, more than 50 ps are needed to reach vibrational temperatures close to the surface temperature (298 K). This time scale is an order of magnitude higher than that found by Hynes and co-workers in their study on the relaxation of the 670 cm^{-1} C−Cl vibration of CH_3Cl in water.[42] However, methyl chloride is a dipolar molecule in a polar solvent and the Coulombic solute-solvent interactions accelerate the relaxation of the C−Cl vibration.

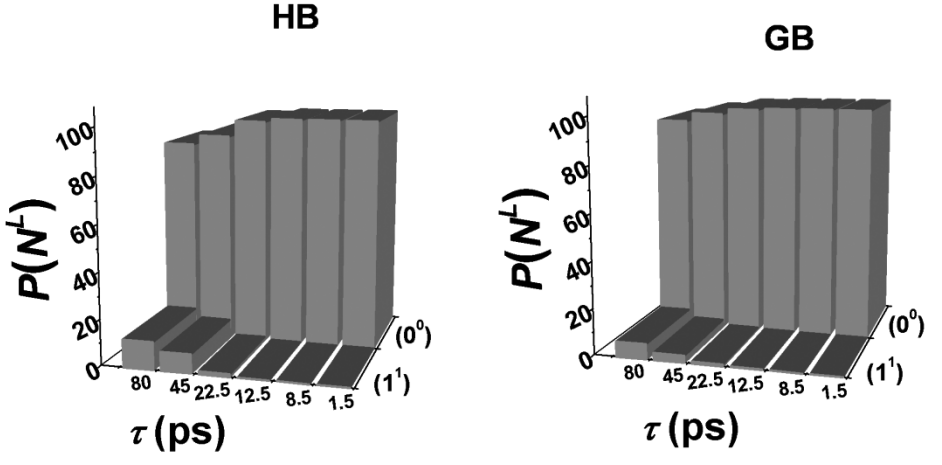

Figure 8.11: Distributions of the final (0^0) and (1^1) states as a function of residence time (τ) for the penetrating trajectories of the ensemble at E_i = 1.6 kcal/mol and (0^0) initial bend state.

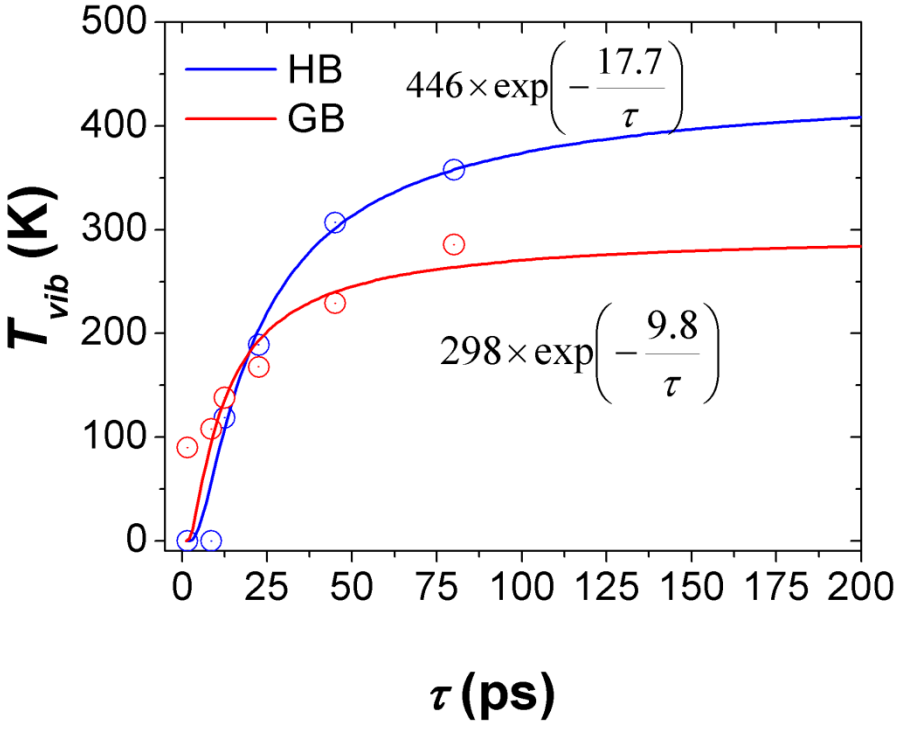

Figure 8.12: Dependence of the vibrational temperature (calculated from the (0^0) and (1^1) final populations of Figure 8.10) as a function of residence time (τ) using HB and GB.

3.3 Accuracy of the results and the surface model

The bend mode energies of the scattered CO_2 molecules may be affected, as the incoming ones, by the artificial bend energy leakage commented above. However, as seen in Figure 8.3, the drop of the bend mode energy occurs in the very first fs, after which the energy in the bend mode oscillates around a constant average value. This means that, for the scattered molecules, this unphysical bend-stretch energy flow takes place when the intermolecular forces are still playing an important role in the dynamics. For this reason, it is not possible to know the amount of bend energy that leaked to/from the stretch mode for the scattered molecules. On the other hand, the use of equation 8.3 to select the initial normal mode phases is intended to correct the unphysical energy flow due to the normal mode sampling. Since the sampling is not exact, the symmetric stretching is expected to receive some excitation in the process. The scattered molecules are free of this problem.

In order to investigate the effect of constraining the initial normal mode phases of the CO_2 molecules, an additional batch of 5000 trajectories was run using all CO_2 molecules (without selecting individual trajectories according

to equation 8.3) at E_i = 10.6 kcal/mol. The resulted populations of the final 0^0 and 1^1 bend mode states of CO_2 are 96.0 (99.4) and 4.0 (0.6) using HB (GB), which follow the same trend as those of Table 8.5: 99.4 (99.8) and 0.6 (0.2) using HB (GB). The bend mode states populations obtained when the normal mode phases are not restricted are slightly hotter than those obtained using equation 8.3 for the incoming CO_2 molecules. However, this does not change the main conclusion of the manuscript that vibrational energy exchange is very inefficient.

Finally, to make sure that the UA model used does not introduce any artifacts in the simulations, an explicit atom model for the surface was used[25] for a batch of additional 5000 trajectories at E_i = 10.6 kcal/mol. The results for the final 0^0 and 1^1 bend mode states of CO_2 are 96.0 (98.2) and 4.0 (1.8) using HB (GB), which compare reasonably well with the UA results of Table 8.5. Again the main conclusion of the present work does not depend on the model used for the surface.

4. CONCLUSIONS

Chemical dynamics simulations were performed to study the dynamics of ground state and vibrationally excited CO_2 scattering off an F-SAM. Two different bend states of carbon dioxide were studied, the ground-state and the (01^10) excited state at incident energies of 1.6 and 10.6 kcal/mol to compare with the experimental results of Nesbitt and co-workers.[21,22] The simulation results show that energy transfer to/from the bend energy is more efficient for penetrating trajectories than for the remaining types of trajectories at the two incident energies studied here. Collisions with the CO_2 molecular axis (z) perpendicular to the surface normal (Z) tend to excite the bend mode more than do collisions with both axes parallel. The vibrational temperatures obtained in our study from the final bending mode quantum numbers are below the surface temperature and agree reasonably well with those obtained experimentally. This result suggests that bend energy accommodation takes place on a time scale longer than involved in the collision process. An analysis of the vibrational temperatures as a function of residence time shows that the time scale needed to achieve bend energy accommodation is at least 50 ps.

Finally, the J quantum number distributions $P(J)$ of the scattered CO_2 molecules compare very well with experiment at the two incident energies and for both bend states (00^00 and 01^10). At the lowest incident energy the theoretical results are fit by a single Boltzmann distribution with temperatures close to 298 K, whereas at the highest incident energy the $P(J)$ are bimodal with approximately equal contribution of the low-temperature and high-

temperature components. The $P(J)$ distributions obtained in our study for both the ground state and first excited states of the bend mode of CO_2 are very similar to each other.

REFERENCES

(1) Saecker, M. E.; Govoni, S. T.; Kowalski, D. V.; King, M. E.; Nathanson, G. M. *Science* **1991**, *252*, 1421.
(2) Kenyon, A. J.; McCaffery, A. J.; Quintella, C. M.; Zidan, M. D. *Chem. Phys. Lett.* **1992**, *190*, 55.
(3) Saecker, M. E.; Nathanson, G. M. *J. Chem. Phys.* **1993**, *99*, 7056.
(4) King, M. E.; Nathanson, G. M.; Hanning-Lee, M. A.; Minton, T. K. *Phys. Rev. Lett.* **1993**, *70*, 1026.
(5) Saecker, M. E.; Nathanson, G. M. *J. Chem. Phys.* **1994**, *100*, 3999.
(6) King, M. E.; Saecker, M. E.; Nathanson, G. M. *J. Chem. Phys.* **1994**, *101*, 2539.
(7) Nathanson, G. M.; Davidovits, P.; Worsnop, D. R.; Kolb, C. E. *J. Phys. Chem.* **1996**, *100*, 13007.
(8) King, M. E.; Fiehrer, K. M.; Nathanson, G. M.; Minton, T. K. *J. Phys. Chem. A* **1997**, *101*, 6556.
(9) Ringeisen, B. R.; Muenter, A. H.; Nathanson, G. M. *J. Phys. Chem. B* **2002**, *106*, 4988.
(10) Ringeisen, B. R.; Muenter, A. H.; Nathanson, G. M. *J. Phys. Chem. B* **2002**, *106*, 4999.
(11) Manning, M.; Morgan, J. A.; Castro, D. J.; Nathanson, G. M. *J. Chem. Phys.* **2003**, *119*, 12593.
(12) Nathanson, G. M. *Ann. Rev. Phys. Chem.* **2004**, *55*, 231.
(13) Zhang, J.; Garton, D. J.; Minton, T. K. *J. Chem. Phys.* **2002**, *117*, 6239.
(14) Kelso, H.; Kohler, S. P. K.; Henderson, D. A.; McKendrick, K. G. *J. Chem. Phys.* **2003**, *119*, 9985.
(15) Perkins, B. G.; Nesbitt, D. J. *J. Phys. Chem. A* **2010**, *114*, 1398.
(16) Perkins, B. G.; Nesbitt, D. J. *J. Phys. Chem. A* **2009**, *113*, 4613.
(17) Perkins, B. G.; Nesbitt, D. J. *J. Phys. Chem. B* **2008**, *112*, 507.
(18) Perkins, B. G.; Nesbitt, D. J. *J. Phys. Chem. A* **2008**, *112*, 9324.
(19) Perkins, B. G.; Nesbitt, D. J. *Proc. Natl. Ac. Sci. USA* **2008**, *105*, 12684.
(20) Perkins, B. G.; Nesbitt, D. J. *J. Phys. Chem. A* **2007**, *111*, 7420.
(21) Perkins, B. G.; Nesbitt, D. J. *J. Phys. Chem. B* **2006**, *110*, 17126.
(22) Perkins, B. G.; Haber, T.; Nesbitt, D. J. *J. Phys. Chem. B* **2005**, *109*, 16396.
(23) Wight, A. C.; Miller, R. E. *J. Chem. Phys.* **1998**, *109*, 8626.
(24) Nogueira, J. J.; Vazquez, S. A.; Mazyar, O. A.; Hase, W. L.; Perkins, B. G.; Nesbitt, D. J.; Martinez-Nunez, E. *J. Phys. Chem. A* **2009**, *113*, 3850.
(25) Martínez-Núñez, E.; Rahaman, A.; Hase, W. L. *J. Phys. Chem. C* **2007**, *111*, 354.

(26) Pradeep, T.; Miller, S. A.; Cooks, R. G. *J. Am. Soc. Mass. Spectrom.* **1993**, *4*, 769.

(27) Ramasamy, S.; Pradeep, T. *J. Chem. Phys.* **1995**, *103*, 485.

(28) Nogueira, J. J.; Martinez-Nunez, E.; Vazquez, S. A. *J. Phys. Chem. C* **2009**, *113*, 3300.

(29) Allen, M. P.; Tildesley, D. J. *Computer Simulation of Liquids*; Clarendon Press: Oxford, 1987.

(30) VENUS; VENUS05 is a modified version of VENUS96. (a) Hase, W. L.; Duchovic, R. J.; Hu, X.; Komornicki, A.; Lim, K. F.; Lu, D.-h.; Peslherbe, G. H.; Swamy, K. N.; Vande Linde, S. R.; Varandas, A.; Wang, H.; Wolf, R. J. QCPE 1996, 16, 671. (b) Hu, X.; Hase, W. L.; Pirraglia, T. J. Comput. Chem. 1991, 12, 1014 ed.

(31) Lourderaj, U.; Martinez-Nunez, E.; Hase, W. L. *J. Phys. Chem. A* **2007**, *111*, 10292.

(32) Chang, X. Y.; Bintz, K. L.; Thompson, D. L.; Raff, L. M. *J. Phys. Chem.* **1994**, *98*, 6317.

(33) Child, M. S. *Semiclassical Mechanics with Molecular Applications*; Oxford University Press, 1991.

(34) Wilson, E. B.; Decius, J. C.; Cross, P. C. *Molecular Vibrations, The Theory of Infrared and Raman Vibrational Spectra*; McGraw-Hill, 1955.

(35) Bonnet, L.; Rayez, J. C. *Chem. Phys. Lett.* **2004**, *397*, 106.

(36) Bonnet, L.; Rayez, J. C. *Chem. Phys. Lett.* **1997**, *277*, 183.

(37) Banares, L.; Aoiz, F. J.; Honvault, P.; Launay, J. M. *J. Phys. Chem. A* **2004**, *108*, 1616.

(38) Banares, L.; Aoiz, F. J.; Honvault, P.; Bussery-Honvault, B.; Launay, J. M. *J. Chem. Phys.* **2003**, *118*, 565.

(39) Jambrina, P. G.; Aoiz, F. J.; Bulut, N.; Smith, S. C.; Balint-Kurti, G. G.; Hankel, M. *Phys. Chem. Chem. Phys.* **2010**, *12*, 1102.

(40) Brouard, M.; Burak, I.; Marinakis, S.; Minayev, D.; O'Keeffe, P.; Vallance, C.; Aoiz, F. J.; Banares, L.; Castillo, J. F.; Zhang, D. H.; Xie, D.; Yang, M.; Lee, S.-Y.; Collins, M. A. *Phys. Rev. Lett.* **2003**, *90*, 093201.

(41) Grimmelmann, E. K.; Tully, J. C.; Cardillo, M. J. *J. Chem. Phys.* **1979**, *72*, 1039.

(42) Whitnell, R. M.; Wilson, K. R.; Hynes, J. T. *J. Chem. Phys.* **1992**, *96*, 5354.

Chapter 9

Dynamics of NO/F-SAM: An Energy Transfer Model and Stereodynamics

1. INTRODUCTION

Considerable interest has been placed in the last two decades on the study of energy transfer in collisions of gas-phase species with self-assembled monolayers (SAMs)[1-34] and with liquid surfaces.[35-46] One of the signatures of the scattering mechanism is the final translational energy distribution of the projectile $P(E_f)$. Depending on the initial conditions and the particular system under study, the $P(E_f)$ distributions can be fit with a single Boltzmann distribution, they can also be bimodal (the most common case) or exhibit a more complicated shape. A simple gas-surface interaction model, which identifies each component of the distribution with a particular gas-surface interaction mechanism, has been used in many previous studies. In particular, the low energy component of the $P(E_f)$ distributions, which is, many times, well fit by a Boltzmann distribution at T_s (surface temperature), is associated with a *trapping desorption* (TD) mechanism, in which the projectile *physisorbs* or *penetrates* into the bulk of the liquid (or surface) reaching thermal accommodation. By contrast, according to this model the high energy component (usually fit to a Boltzmann distribution with a temperature higher than T_s) arises from an *impulsive scattering* (IS) mechanism, where the projectile immediately rebounds from the surface in such a short time scale that thermal equilibration with the surface does not take place.

Recent chemical dynamics simulations of gas-phase species scattering off SAM surfaces indicate that the scattering process may be considerably more complex. It was found that *direct* events, without trapping on the surface, may contribute to the low energy component, and, on the other hand, trajectories that *physisorb* or *penetrate* inside the monolayers may contribute to the high energy component.[5,9,17,20,47] In particular, in a recent CO_2 + a perfluorinated SAM (or F-SAM) dynamics study, the percentage of *penetrating* and *physisorption* events did not match the relative contribution of the low energy component of the $P(E_f)$ distribution, i.e., TD cannot be unambiguously identified with the low energy component of the $P(E_f)$ distribution.[5] Furthermore, the distributions of the rotational quantum numbers of the scattered CO_2 molecules $P(J)$ are also bimodal but the relative contribution of each component differs from those obtained for $P(E_f)$.[5]

An interesting aspect of the gas-surface dynamics is the energy transfer efficiencies to the various degrees of freedom of the molecule and to the surface. Previous simulation results of projectile ions + surface collisions show that the percentage (with respect to the collision energy) of energy transfer to the projectile's internal degrees of freedom does not depend much on the collision energy, while energy transfer to the surface increases.[7,31,48,49] A

model proposed previously[7] shows that the function $\exp(-b/E_i)$ fits reasonably well the average percentage energy transfer to the surface as a function of the collision energy E_i. This model predicts that the high E_i limiting energy transfer to the surface is ~90% for two protonated peptides scattering off an F-SAM.[7] The same model was employed by Morris and co-workers to obtain values for the high E_i limiting energy transfer to the surface of 89-98% for Ar and CO_2 scattering off several SAM surfaces.[34]

One of the projectiles that has attracted much attention in the last years is CO_2. The collision dynamics of CO_2 with F-SAM or similar surfaces has been studied by Nesbitt's group[35-43] and by our own group in collaboration with Hase's group.[4,5,9] Nesbitt's group analyzed in detail the influence of the incident angle, collision energy, and surface temperature on the scattering dynamics. Also the stereodynamics was studied in much detail.[39,43] Quite interestingly, they found that CO_2 scatters off the surface in a *helicopter* fashion for $J < 60$, whereas for the higher rotational states the molecule exhibits *cartwheel* rotational motion. On the other hand, Troya and co-workers found that *cartwheel* rotational motion is the preferred behavior for CO scattering off an F-SAM.[33] For both systems CO_2 + FSAM and CO + F-SAM, *cartwheel* motion has the same orientation of **J**, i.e., with *forward* (or *topspin*) sense of end-over-end tumbling.

In the present paper the collision dynamics of NO + F-SAM is studied by means of chemical dynamics simulations. As mentioned above, previous simulation results show that TD and IS are more complex mechanisms that cannot be rationalized in terms of different trajectory types. In the present paper a new scheme to sort the trajectories is presented, based on the assumption that thermal accommodation of the rotational degrees of freedom takes place after NO suffers a sufficiently large number of gentle "kicks" that produce deviations of the angular momentum vector.

Additionally, a new model of gas-surface energy transfer is presented here. The model is based on the adiabaticity parameter[50] and fits very accurately the NO + F-SAM simulation results. The stereodynamics of the NO + F-SAM collision dynamics is also studied in detail and compared with previous results on CO_2 + F-SAM[43] and CO + F-SAM.[33]

Finally, the pioneering work of Cohen *et al.* on the collision dynamics of He, Ar, O_2 and NO + SAM surfaces[1,2] also motivated the present study. Among the SAMs employed in their studies, they used perfluorinated acid ester (PFAE). This monolayer is entirely fluorinated over the outer eight carbons of the chain, exposing the $-CF_3$ groups, being therefore very similar to the F-SAM employed in our previous gas-surface simulations[3-9] and in the present study.

Therefore a direct comparison of the experimental and simulation results is possible, which serves to test the theoretical methods.

2. COMPUTATIONAL DETAILS

2.1 Potential energy surface

The potential energy function of the system consists of the F-SAM intramolecular interaction V_{surf}, the NO intramolecular interaction V_{NO}, and the interaction between NO and the surface $V_{\text{NO-surf}}$:

$$V = V_{\text{surf}} + V_{\text{NO}} + V_{\text{NO-surf}} \tag{9.1}$$

The intramolecular potential function for the F-SAM surface V_{surf} was explained in detail elsewhere.[8,9] The monolayer consists of 48 chains of $CF_3(CF_2)_7S$ radicals adsorbed on a single layer of 225 Au atoms, which are kept fixed during the dynamics simulations. An all-atom (AA) model was utilized, where every single atom constitutes an interaction site. This AA model is able to reproduce the 300 K structure of the surface, i.e., the monolayer forms a hexagonal close-packed structure with the nearest-neighbor direction rotated 30º with respect to the Au{111} lattice and the backbone of the $CF_3(CF_2)_7S$ moiety has a tilt angle with respect to the surface normal of ~ 12º.[9]

The NO intramolecular interaction energy contains only one term. For most of the simulations a simple harmonic potential V_{NO}^{harm} was employed. In one simulation that involves collisions of highly vibrationally excited NO molecules with the F-SAM (see section 2.2 below), the NO stretching interaction was modeled using a Morse expression V_{NO}^{Morse} :

$$V_{\text{NO}}^{harm} = \frac{k_s}{2}(r_0 - r)^2 \tag{9.2a}$$

$$V_{\text{NO}}^{Morse} = D_e\{1 - \exp[-\beta(r - r_0)]\}^2 \tag{9.2b}$$

where the force constant k_s is obtained from the harmonic oscillator relationship $k_s = 4\pi^2 c^2 \tilde{\nu}^2 \mu$, $\beta = (2\pi^2 c^2 \mu \tilde{\nu}^2 / D_e)^{1/2}$, c is the speed of light, μ is the reduced mass, D_e is the dissociation energy and $\tilde{\nu}$ is the vibrational frequency of the diatomic molecule (in wavenumbers). The CCSD(T)/aug-cc-pVDZ stretching frequency $\tilde{\nu}$ (scaled by 0.982) of 1978 cm^{-1} and equilibrium distance r_0 of 1.164 Å were employed. Finally, for the dissociation energy the experimental value 152.54 kcal/mol[51] was used.

In order to calculate the NO/F-SAM interaction potential $V_{\text{NO-surf}}$, single point energies were computed at the MP2/aug-cc-pVXZ (X = D, T, Q) and CCSD(T)/aug-cc-pVDZ levels of theory for ten different orientations

between the NO and CF_4 molecules (see Figure 9.1). Following the strategy of previous studies,[3,8,9,52-54] the carbon and fluorine atoms of CF_4 were regarded as representative of those in the F-SAM. The gas-surface interaction energies that this approach provides agree very well with those obtained using more realistic models for the F-SAM surface.[3] The MP2/aug-cc-pVXZ and CCSD(T)/aug-cc-pVDZ ab initio calculations include the counterpoise correction to account for the basis set superposition error (BSSE). Additionally, the MP2/aug-cc-pVXZ values were extrapolated to the complete basis set limit (CBS) using Peterson's prescription:[55]

$$E(n) = E_{\mathrm{CBS}} + A\exp\left[-(n+1)\right] + B\exp[-(n+1)^2] \qquad (9.3)$$

with $n = 2, 3, 4$ for X = D, T, Q, respectively, and $E(n)$ represents the MP2/aug-cc-pVXZ energy. In order to obtain more accurate energies, the focal-point approximation of Allen and co-workers[56] has been employed in this study. The method takes advantage of the fact that, usually, for large basis sets, the difference between the MP2 and CCSD(T) energies is independent of the basis set. In this work CCSD(T) energies at the CBS limit (here and after fp-CCSD(T)/CBS) were computed with the focal point approach.

Table 9.1: Parameters of the NO---CF_4 intermolecular analytical potential of equation 9.4.[a]

$i-j$	A_{ij}	B_{ij}	C_{ij}	D_{ij}	$E_{i,j}$	F_{ij}
N–C	1222.363	2.486	-	-	-	-
N–F	96826.251	4.000	99.622	5.200	5904.001	9.000
O–C	17873.835	3.594	-	-	90.262	8.997
O–F	114690.455	4.270	46.833	5.000	3540.142	9.000

[a]Units are such that potential energy is in kcal/mol and distance is Å.

The analytical function employed to fit to the fp-CCSD(T)/CBS interaction energies is a sum of two-body Buckingham potentials:

$$V_{\mathrm{NO-surf}} = \sum_{ij} A_{ij}\exp\left(-B_{ij}R_{ij}\right) - C_{ij}/R_{ij}^{D_{ij}} - E_{ij}/R_{ij}^{F_{ij}} \qquad (9.4)$$

where i and j represent each of the atoms of the NO and CF_4 molecules, respectively, R_{ij} is the $i-j$ interatomic distance and A_{ij}, B_{ij},…F_{ij} are the parameters. The fit was conducted with the help of a genetic algorithm.[57]

Figure 9.1 shows the results of the fit (solid line) for the ten NO---CF_4 orientations chosen in this study and the final two-body parameters are collected in Table 9.1. The root-mean-square error of the fit is 4×10^{-2} kcal/mol.

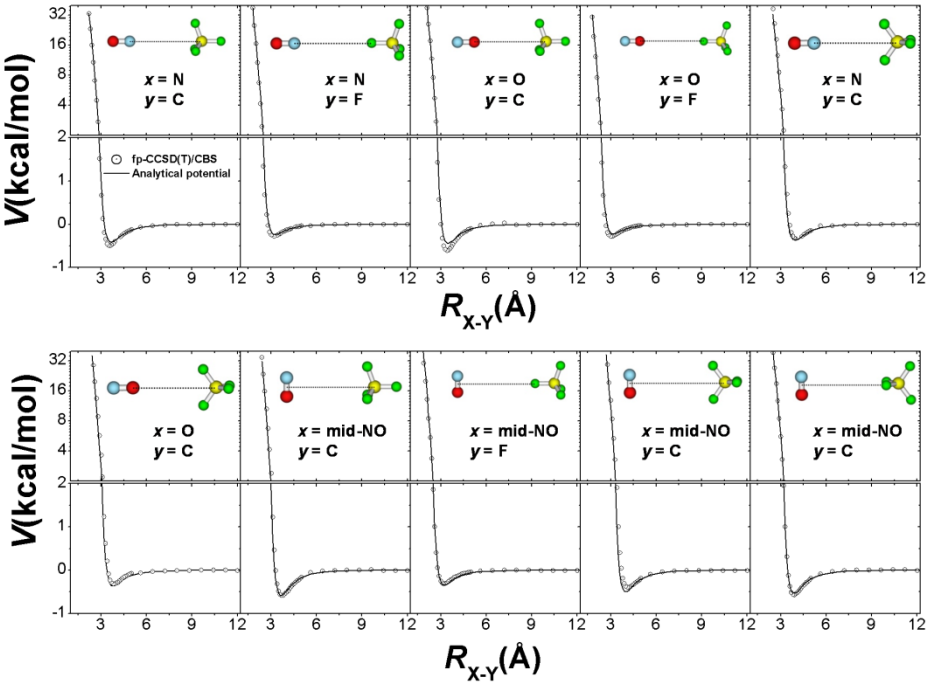

Figure 9.1: Analytical potential of equation 9.4 fitted to the fp-CCSD(T)/CBS ab initio calculations for the different configurations considered in this study to develop the NO + F-SAM interaction potential.

2.2 Chemical Dynamics Simulations

Ten different initial conditions (ICs) were considered for the simulations. The ICs differ from each other in the initial collision energy of the projectile E_i, the incident angle θ_i formed between the incident velocity and the surface normal, and the initial ro-vibrational state (v, J) of the NO molecule, where v and J are the NO vibrational and rotational quantum numbers, respectively. Details of each IC are collected in Table 9.2.

ICs 2-5 were selected to mimic the experimental conditions employed by Cohen *et al.* in their study of NO scattering off a perfluorinated acid ester (PFAE) monolayer.[1,2] The surface used in our simulations, F-SAM, consists of $CF_3(CF_2)_7S$ chains supported on Au{111}. The one employed in the experiments, PFAE, was prepared by self-assembling $CF_3(CF_2)_9(CH_2)_2OCO(CH_2)_8COOH$ chains on glass[2]. Both surfaces are

structurally similar, particularly the upper part of the monolayer. Previous work in our group, on the scattering dynamics of CO_2 + F-SAM,[5] suggests that energy transfer between the projectile and the surface is essentially controlled by the outermost layer of the surface (the $-CF_3$ groups) and not by the detailed structure of the interfacial material, which renders support for the comparison made here.

Table 9.2: Different initial conditions ICs considered in this work for the simulations.

IC	N_{traj} [a]	E_i [b]	θ_i	(v,J) [c]
1	6×10^3	1.0	0	(0, 6K)
2	6×10^3	3.2	0	(0, 6K)
3	6×10^3	4.6	0	(0, 6K)
4	6×10^3	6.7	0	(0, 6K)
5	6×10^3	10.6	0	(0, 6K)
6	6×10^3	40.0	0	(0, 6K)
7	6×10^3	10.6	0	(15, 0)
8	10^4	10.6	30	(0, 0)
9	10^4	10.6	30	(0, 30)
10	10^4	10.6	60	(0, 0)

[a]Number of trajectories. [b]In kcal/mol. [c]6 K means that J was taken from a 6 K Boltzmann distribution of rotational states.

ICs 1 and 6 were devised to investigate energy transfer efficiencies in a larger energy range. Additionally, different ro-vibrational states of the projectile were investigated in ICs 7 and 9 as well as different incident angles (ICs 8-10).

All the simulations of the present study have been carried out using the VENUS05[58] computer program. Ensembles of trajectories corresponding to the ICs of Table 9.2 were integrated with a fixed step size of 0.3 fs using the Adams-Moulton algorithm in VENUS05 for a total integration time of 90 ps. Before the beginning of each trajectory simulation, the surface was relaxed to a thermodynamic equilibrium structure by a 2 ps molecular dynamics simulation[59] in which the atomic velocities are scaled to obtain a surface temperature of 300 K. This structure was then used as the initial structure of a 100 fs equilibration run at the beginning of each trajectory. Periodic boundary conditions were also utilized to simulate a larger surface.[59] After the integration

of each trajectory, the surface energy, translational and internal energies, rotational angular momentum, orientation and velocity of the scattered NO molecule were calculated from the atomic Cartesian coordinates and momenta.

3. RESULTS

3.1 Collision types

Three collision types were found in our simulations. The different events were identified according to both the minimum height of the projectile center-of-mass above the Au{111} surface $h_{\mathrm{NO},min}$ and to the number of inner turning points nITPs in the direction perpendicular to the surface that the projectile experiences during the collision with the surface. According to the first criterion, the trajectories can be classified as *penetrating*, when $h_{\mathrm{NO},min}$ drops below a certain height h_p, defined as $0.5(\langle h_{\mathrm{CF_3}}\rangle + \langle h_{\mathrm{CF_2}}\rangle)$, where $h_{\mathrm{CF_3}}$ and $h_{\mathrm{CF_2}}$ are the heights of the CF_3 and adjacent CF_2 groups in the monolayer, and they can be calculated in a molecular dynamics simulation at 300 K; the value of h_p thus obtained is 11.6 Å. The trajectories were additionally sorted according to nITPs into two different subsets, i.e., those with $n\mathrm{ITPs} = 1$ and the remaining ones ($n\mathrm{ITPs} > 1$). The former type is called here *direct* collision and the latter *physisorption*. In previous work on the scattering dynamics of CO_2 + F-SAM,[5] it was found that in order to attain thermal accommodation of the CO_2 rotational degrees of freedom, at least 15 ITPs were needed. This means that, since the probability distribution plots of nITPs peak at $n\mathrm{ITPs} = 2$ and show exponential decay with average values of 5-9,[5] many of the CO_2 + F-SAM *physisorption* trajectories behave pretty much in the same way as the *direct* ones, and do not lead to thermal accommodation. This point is also discussed in this work below.

The percentages of the different trajectory types for the different ICs are plotted in Figure 9.2. As seen in Figure 9.2a, for ICs 1-5, the percentage of *direct* (*physisorption*) events increases (decreases) as a function of the collision energy, i.e., as it goes from IC 1 to IC 5, while the percentage of *penetration* remains almost constant. The percentages of trajectory types for ICs 7-10 are similar to those found for IC 5, except when the incident angle is 60º (IC 10), for which *physisorption* increases and the other two collision types decrease with respect to ICs 5 and ICs 7-9. Surprisingly, for IC 6 ($E_i = 40$ kcal/mol) there is a sharp increase in the percentage of *penetration* (it goes from 8% for IC 5 to 40% for IC 6) at the expense of a decrease in both *direct* trajectories and *physisorption*. These collision energy dependencies of the collision types contrast with previous CO_2 + F-SAM simulations, where the percentage of

penetration was shown to decrease with E_i.[5] The explanation for this discrepancy relies on the fact that there are two different types of *penetration*: (a) events where the projectile penetrates the F-SAM in the first collision (*direct penetration*) and (b) when the projectile penetrates after being physisorbed on top of the surface for a while (*physisorption penetration*). In the present NO + F-SAM simulations more than 84% of the *penetration* events turn out to be *direct*, whereas in CO_2 + FSAM *direct penetration* is much less important and ranges between 10% and 60%. When the percentage of *direct penetration* events was calculated as a function of E_i, this value increases for both projectiles NO and CO_2 scattering off F-SAM. Additionally, previous simulations in our research group on Ar scattering off an F-SAM go in the same direction, i.e., the percentage of *direct penetration* is 67% for $E_i = 12$ kcal/mol and 82% for $E_i = 24$ kcal/mol. However, overall *penetration* is much less important in NO + F-SAM than in CO_2 + FSAM. For NO + F-SAM, *penetration* accounts for less than 10% of the collision types for ICs 1-5 ($E_i \leq 10.6$ kcal/mol), while for CO_2 + F-SAM this *percentage* ranges from 20-45%, in the same energy range. Additionally, *penetration* in CO_2 + F-SAM is a much longer duration process than in NO + F-SAM. For CO_2 + F-SAM the probability density function of the *residence time* $P(\tau)$ inside the monolayer peaks at $\tau = 20 - 25$ ps and extends up to 140 ps for $E_i = 10.6$ kcal/mol,[9] while for NO + F-SAM $P(\tau)$ shows a sharp peak at $\tau = 0 - 10$ ps and the tail extends up to 60 ps, at the same collision energy (the plots are not shown here for simplicity). The strength of the gas-surface interaction conditions the shape of the *residence time* distributions, i.e., CO_2 interacts more strongly than NO with the F-SAM. In general, big charged molecules are expected to interact strongly with the F-SAM and provide a very high sticking probability as well as long *residence times*. By way of example, Cooks and co-workers conducted experimental studies on $(CH_3)_2SiNCS^+$ scattering off an F-SAM, and found that these cations remain trapped inside the monolayer for many hours.[60]

Although the frequency of *penetrating* collisions is low in our simulations, it is of interest to analyze the behavior of the projectile in the bulk of the monolayer. Figure 9.3 shows probability density plots as a function of the height of the projectile above the gold surface (h_{NO}), the angle formed between the O–N axis and the perpendicular to the surface (β), and the angle formed between the projection of the O–N axis onto the gold surface and the X axis (angle χ); the chains of the monolayer are tilted in the $+X$ direction (see the cartoon of Figure 9.3d). Panels (a) to (c) show probability functions depending on h_{NO} and β, whereas panels (d) to (f) depend on h_{NO} and χ. The results indicate that the projectile penetrates just a few Å inside the monolayer for the lowest collision energies, whereas for the highest E_i of 40 kcal/mol, NO penetrates deeper and there seems to be a stable region at around 3-4 Å above

the gold surface (see panels (c) and (f)). As the collision energy increases (from IC 1 to IC 6) the probability distributions become broader as the projectile has more energy to move around. In terms of the angle formed by the projectile with the normal there are two stable situations, drawn in a cartoon in Figure 9.3a. The maximum probabilities correspond to β angles that deviate from the 300 K equilibrium tilt angle of the F-SAM chains (~12º), i.e., the projectile and the chains are not arranged in a parallel fashion (see Figure 9.3a). This is due to the important number of interactions taking place between the projectile and the surface atoms, which make β to be higher than the tilt of the F-SAM chains (45º *vs* 12º). Quite interestingly, for low incident energies the most stable situation corresponds to an angle β of 45º, i.e., with the O atom pointing downwards, whereas for high incident energies the other orientation of β = 135º (O pointing upwards) is the most stable one.

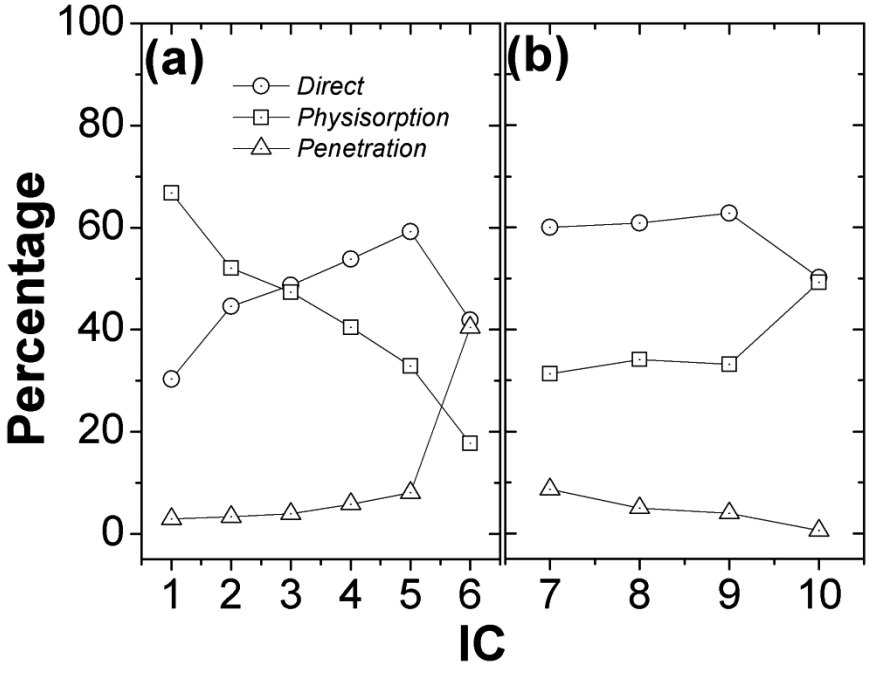

Figure 9.2: Percentages of the different collision events for the different initial conditions considered in this study.

When the orientation of the projectile inside the monolayer is analyzed in terms of the angle χ, four maxima are obtained for a given value of h_{NO}. In this case the plots (panels (d) to (f)) are symmetric for $\chi < 90º$ and $\chi > 90º$. The presence of the four peaks can be understood on the basis of the hexagonal package of the chains (see the cartoon of Figure 9.3d). In the

absence of a tilt angle, the four maxima would be of the same intensity as the three different grooves formed between the chains (green and red dashed lines in the cartoon) would be equally accessible. The green grooves (parallel to the X axis) lead to χ angles of 0º or 180º, and the red grooves accommodate the molecules inside them with theoretical χ angles close to 60º and 120º (the actual values of the angles corresponding to these peaks are 15º off the theoretical value obtained from the hexagonal package). But, there is a tilt in the chains along the $+X$ direction, which makes the $\chi = 0º$ or 180º orientation more easily for the projectile to achieve, as it can penetrate the monolayer along the perpendicular to the surface as it comes from the gas phase. However in order to penetrate the red grooves, the molecule has to enter skew, which explains the lower intensity of the peaks at around 45º and 135º.

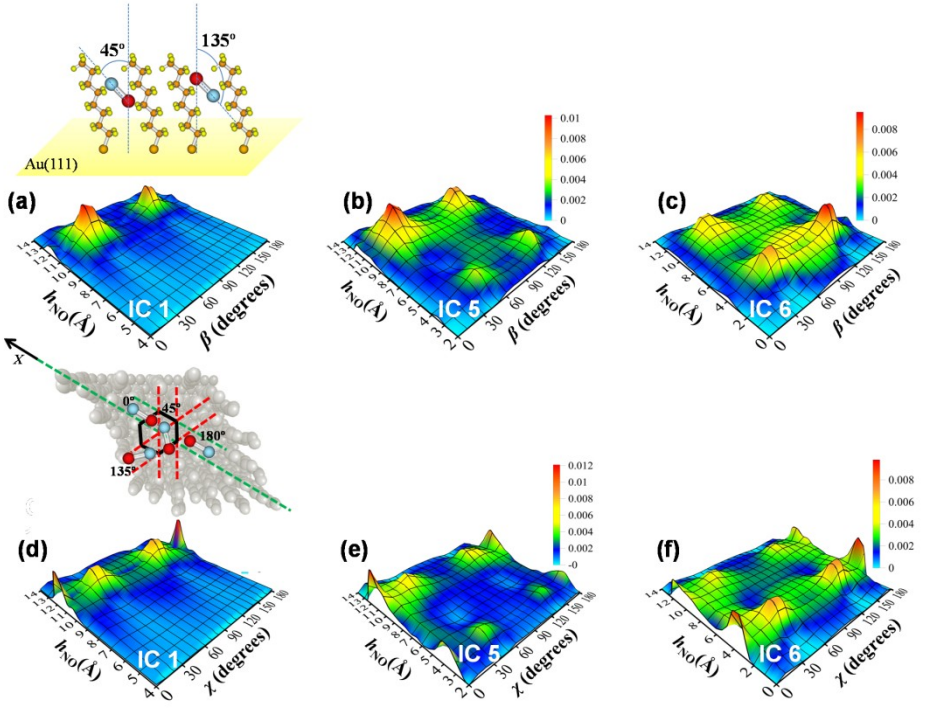

Figure 9.3: Probability density plots for the different configurations of the projectile inside the F-SAM. Panels (a), (b) and (c) display probability *vs* the height of the projectile above the gold surface h_{NO} and the angle β formed between the O–N direction and the perpendicular to the surface, for ICs 1, 5 and 6, respectively. Panels (d), (e) and (f) plot probability *vs* h_{NO} and the angle χ formed between the projection of the O–N direction onto the gold surface with the X axis (see the cartoon), for ICs 1, 5 and 6, respectively.

3.2 Rotational quantum number distributions

Energy conservation dictates that the initial collision energy E_i equals the sum of the final translational energy of the projectile E_f, and the changes in the internal ΔE_{int} and surface energies ΔE_{surf}

$$E_i = E_f + \Delta E_{int} + \Delta E_{surf} \quad (9.5)$$

For CO_2 + F-SAM, only rotational energy transfer contributed to ΔE_{int}, with the vibrational states being adiabatic.[4,5,9] In particular, CO_2 molecules initially excited to the (01^10) bend state, which is the lowest frequency mode of the molecule, preserve their initial excitation during the collision process in more than 90% of the collisions.[4] In the present study, when NO is vibrationally excited to $v = 15$ at $E_i = 10.6$ kcal/mol, 99.6% of the molecules scatter off the F-SAM without loss of vibrational energy, with 0.4% loosing only one quantum of vibration. This is an expected result on account of the previous behavior of the bend mode states of CO_2 and also due to the shorter interaction time in NO + F-SAM compared with CO_2 + F-SAM, and to the high NO stretching frequency. Multiquantum vibrational transitions are possible when NO collides against a gold surface, due to nonadiabatic coupling of nuclear motion to electronic excitations of the metal surface.[61,62]

Table 9.3: Parameters of the Boltzmann fits to the $P(J)$ distributions.

IC	α_{T_s} [a]	T
1	71 ± 8	104 ± 26
2	95 ± 2	38 ± 20
3	79 ± 11	993 ± 658
4	58 ± 9	875 ± 224
5	36 ± 6	935 ± 107
6	17 ± 2	1491 ± 74
7	36 ± 4	931 ± 73
8	34 ± 6	971 ± 112
9	0	-
10	28 ± 7	896 ± 98

[a]Expressed as percentage.

Figure 9.4 shows probability plots for the rotational quantum numbers J of the scattered molecules $P(J)$. As in previous work, the $P(J)$ values were fit to a sum of two Boltzmann distributions of rotational states at the temperatures T_s and T:

$$P(J) = \alpha_{T_s} \frac{hcB}{kT_s}(2J+1)e^{-\frac{hcBJ(J+1)}{kT_s}} + \left[1-\alpha_{T_s}\right]\frac{hcB}{kT}(2J+1)e^{-\frac{hcBJ(J+1)}{kT}} \quad (9.6)$$

where $T_s = 300$ K, and α_{T_s} and T are parameters in the fit. Table 9.3 collects the outcomes of the different fits. The histograms in Figure 9.4 are the simulation $P(J)$ results, the smooth black lines are the results of the fits, and the blue and red lines correspond to the first and second terms in equation 9.6, respectively. All simulation $P(J)$ results are well fit by equation 9.6 except those that resulted from IC 9.

The parameter α_{T_s} can be interpreted as the degree of thermal accommodation of the NO rotational degrees of freedom. Table 9.3 shows that α_{T_s} decreases with E_i (except for IC 1) and it becomes 0 for IC 9. These results indicate that thermalization of the rotational degrees of freedom is very efficient for IC 2. Actually, the average rotational energies of the scattered NO molecules for IC 2 is 0.61 kcal/mol, in close agreement with the theoretical value for a diatomic molecule that fully accommodates its rotational degrees of freedom ($RT_s = 0.6$ kcal/mol). The decrease of α_{T_s} with collision energy has also been found previously for CO_2 + F-SAM,[5] which correlates with the higher frequency of *direct* events (at high collision energies) that are not expected to be efficient attaining thermal accommodation. Some efforts have been unsuccessfully taken in the past to identify collision types with thermal accommodation mechanisms.[5,8,17,20] Intuitively, larger duration collisions, i.e., *physisorption* and *penetration*, might lead to thermal accommodation, while short *direct* events can be thought of processes that hardly achieve thermal accommodation. However, previous results show that α_{T_s} is not equivalent to either the fraction of *physisorption* or *penetration* events or to their sum in Ar + F-SAM[8] and CO_2 + F-SAM simulations.[5] Additionally, the thermal accommodation coefficients extracted from the Boltzmann fits of the $P(J)$ or the $P(E_f)$ distributions differ from each other in CO_2+F-SAM.[5] Furthermore, Hase and co-workers found that *direct* trajectories can also lead to thermal accommodation of the translational degrees of freedom in Ne scattering off a SAM surface.[16,17,19]

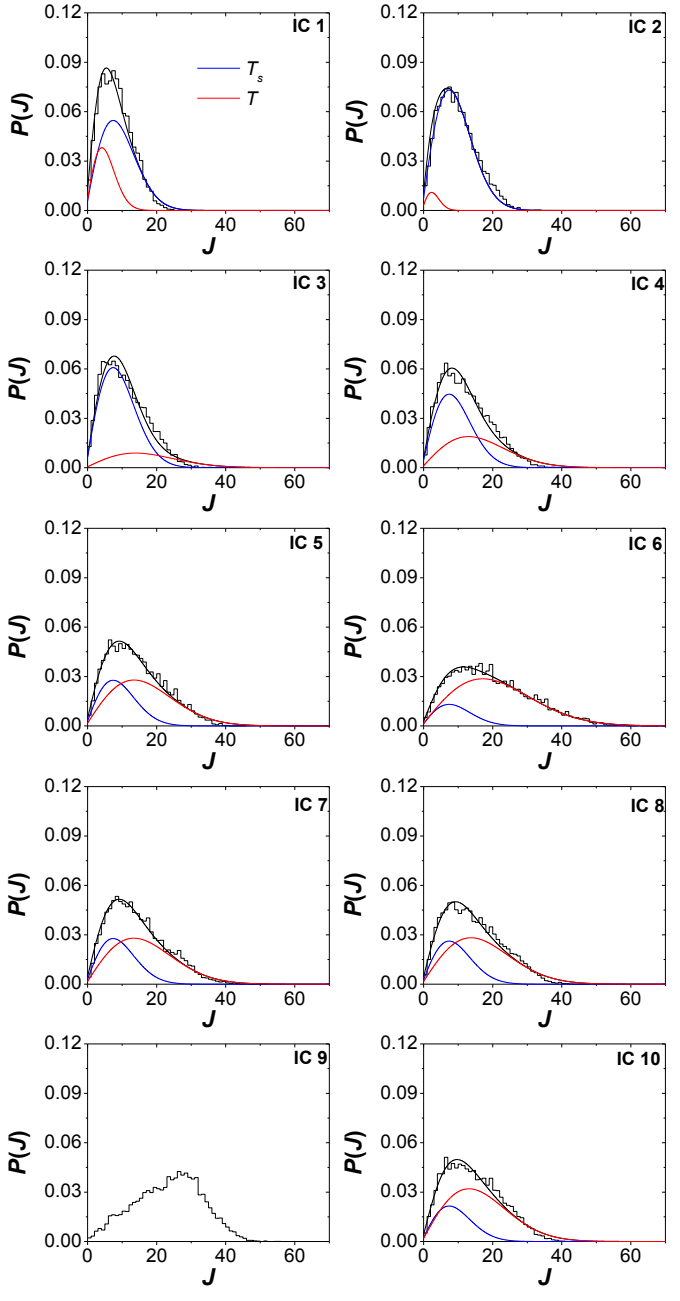

Figure 9.4: Probability density plots for the rotational quantum number J of the scattered NO molecules $P(J)$ for ICs 1-10. The histograms show the simulation results, the smooth black line is the fit to equation 9.6, and the red and blue lines are the first and second terms of the equation.

As seen in the previous section, the definition of the different collision mechanisms relies on counting the number of changes in the center-of-mass velocity vector of the projectile in the perpendicular axis (nITPs).

Figure 9.5a shows the percentages of trajectories with nITPs $> i$ (with $i = 1 - 4$) for the different ICs, in comparison with the values of α_{T_s} obtained from the fits to $P(J)$. The percentages of trajectories that fulfill the nITPs $> i$ criterion do not match the α_{T_s} pattern for the different ICs. In particular, two important features of the α_{T_s} histogram are not captured with the nITPs analysis, i.e., the sharp decrease as a function of E_i (from IC 1 to IC 6) and the fact that α_{T_s} vanishes for IC 9.

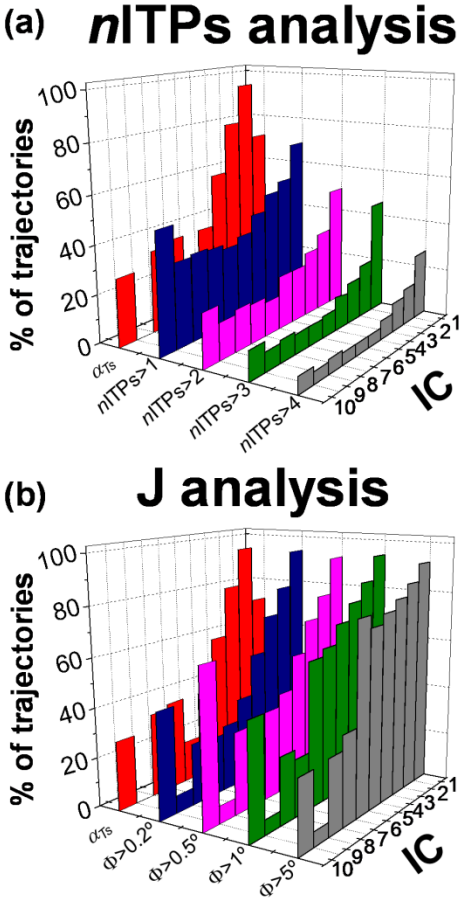

Figure 9.5: Percentages of trajectories that fulfill the (a) nITPs analysis and (b) the **J** analysis (see text), in comparison with the percentage of trajectories that thermalize rotation α_{T_s}, which was obtained from the $P(J)$ distributions.

Alternatively to the nITPs analysis, one may look at changes in the direction of the rotational angular momentum **J** of the NO molecule in the course of the dynamics. Particularly, Figure 5b shows the percentages of those trajectories that change the direction of **J** in two consecutive steps a minimum

angle of Φ degrees, at least n_Φ times along the trajectory. The angle Φ can be obtained from:

$$\Phi = \cos^{-1}\left(\frac{\mathbf{J}(t)\cdot\mathbf{J}(t-\tau)}{|\mathbf{J}(t)||\mathbf{J}(t-\tau)|}\right) \tag{9.7}$$

where $\mathbf{J}(t)$ is the rotational angular momentum of the molecule at time t, and τ is a time step of 30 fs. The values of n_Φ were optimized separately for ICs 1-6 and ICs 7-10, as they refer to different initial rotational excitations of the molecule; the optimized values are collected in Table 9.4. As seen in Figure 9.5b, the above **J** analysis sorts the trajectories in a way that resembles the α_{T_s} pattern for the different ICs, particularly when Φ is small.

Table 9.4: Optimized values of n_Φ for variations of **J** by an angle of at least Φ degrees.

Φ >	n_Φ	
	ICs 1-6	ICs 7-10
0.2	31	40
0.5	20	28
1	12	23
5	5	10

The **J** analysis presented in this paper is superior than the nITPs analysis predicting the kind of collision events that lead to thermal accommodation. The **J** analysis shows that thermalization occurs after the projectile suffers a minimum number of gentle "kicks" that induce a very small change in **J**. This mechanism explains both the decrease in the thermal accommodation as a function of E_i (from IC 1 to IC 6) and the lack of thermal accommodation obtained for rotationally excited NO + F-SAM (IC 9). The former occurs because the gas-surface interaction time decreases as E_i increases. Thus, for low E_i an important number of changes in the direction of **J** may take place, as the interaction time is long, even for *direct* events. Actually, for the lowest E_i, up to 86% of the *direct* trajectories contribute to thermal accommodation, according to the **J** analysis. This percentage diminishes to 18% for the highest collision energy (IC 6). The $\alpha_{T_s} = 0$ result for IC 9 can also be explained with the **J** analysis. When rotationally excited NO strikes the surface, the direction of **J** changes abruptly, i.e., on average the values of Φ are higher than those found for the other ICs, and a minimum number of moderate changes in **J** is not achieved by many trajectories.

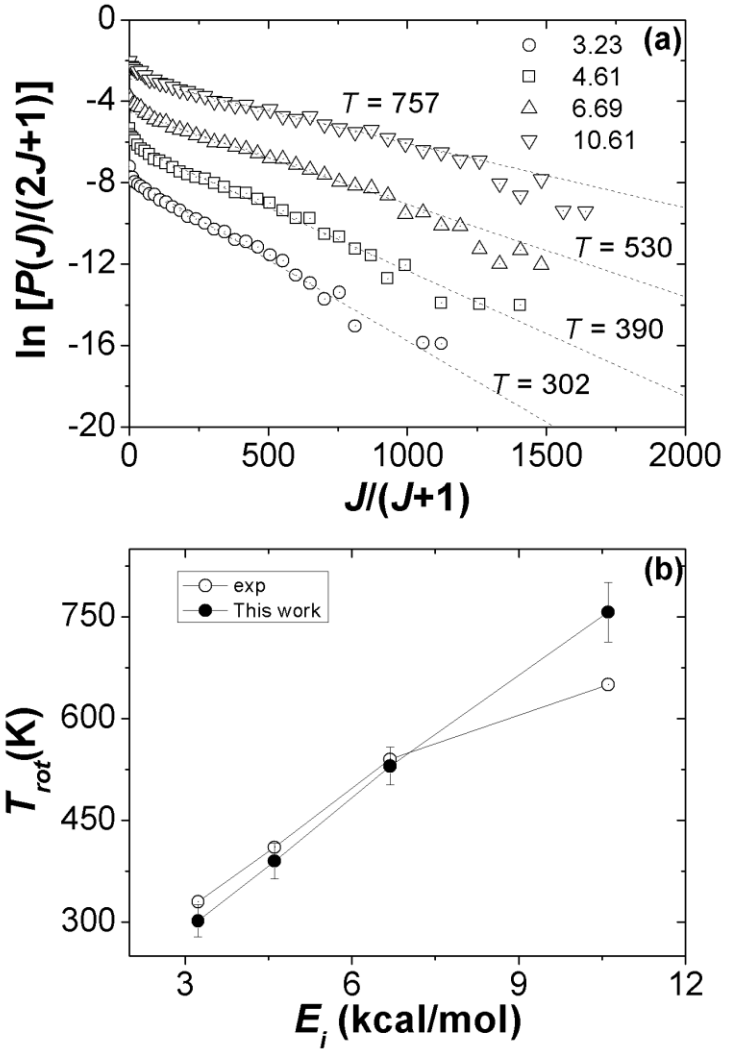

Figure 9.6: (a) Logarithmic linear plots (symbols) of the $P(J)$ distributions and fit (dotted lines) to extract the rotational temperatures, shown in panel (b) in comparison with experimental results.

Finally, the rotational energies of the scattered molecules obtained in our study are compared with those obtained in the experiments.[1] The first comparison concerns the experimental $P(J)$ distributions (see Figures 9.6a and 9.6b). In the experimental study the rotational quantum number distributions are presented as logarithmic plots (see Figure 7a of ref 1 and Figure 9.6a of this paper), alongside with linear least-squares fits to the high-J part of the distributions ($J > 10$) to extract the rotational temperatures T_{rot} from the slopes.[1] The values of T_{rot} obtained in the experimental study are in good agreement with those obtained here using the same procedure (see Figure 9.6b). An additional analysis was done in the experimental work that deals with the

probability δ of achieving 3.4 kcal/mol of rotational energy.[1] The experimental values of δ vary linearly with the incident velocity v_i. The slope of the experimental δ *vs* $1/v_i$ plot is -5.7×10^3 m/s (see Figure 9 of ref 1), which can be compared with the value $-(7.5\pm1.6)\times10^3$ m/s obtained here. The comparison presented here renders support for the quality of the results of the present study.

3.3 Translational energy distributions

If the NO translational degrees of freedom get fully accommodated as a consequence of the collisions with the F-SAM, a Boltzmann distribution of translational energies:

$$P^{Bolt}\left(E_f\right) = \frac{E_f}{(kT_s)^2} e^{-\frac{E_f}{kT_s}} \tag{9.8}$$

would fit the translational energy distributions of the scattered molecules. However, equation 9.8 only fits the $P(E_f)$ distributions for ICs 1-4 with temperatures different from T_s and being 268, 427, 542 and 779 K, respectively. The use of two Boltzmann components with different temperatures, either with one fixed at T_s and the other being a parameter or with both used as parameters, does not improve the fits. The temperature obtained for IC 1 (268 K) is the closest to T_s and indicates that, under these conditions ($E_i = 1$ kcal/mol), the degree of thermal accommodation of the translational degrees of freedom is the highest (among the ICs of this study). For IC 1 the average translational energy of the scattered molecules $\langle E_f \rangle$ is 1.07 kcal/mol, slightly lower than the theoretical value of 1.2 kcal/mol ($2RT_s$) for full thermal accommodation. For ICs 2-4, the distributions are hyperthermal with values of $\langle E_f \rangle \gg 2RT_s$. This indicates that, in comparison with the rotational degrees of freedom, for translation motion is harder to reach thermal equilibrium with the surface. Similar results have been obtained for CO_2 + F-SAM, where the values of α_{T_s} obtained from $P(E_f)$ were systematically lower than those obtained from $P(J)$.[5] For CO_2 + F-SAM, both $P(E_f)$ and $P(J)$ are fit to a sum of two Boltzmann components, with the contribution of the Boltzmann component at T_s being always above 0.5 for $E_i \leq 10.6$ kcal/mol, whereas for NO + F-SAM only the $P(J)$ distributions are fit to a couple of Boltzmann components. This result is a consequence of the stronger interaction of the CO_2 molecule *vs* NO with the F-SAM and the longer residence times, as indicated above.

3.4 Energy transfer

Assuming that rotation and vibration are uncoupled, ΔE_{int} can be written as:

$$\Delta E_{int} = \Delta E_{rot} + \Delta E_{vib} \tag{9.9}$$

where ΔE_{vib} and ΔE_{rot} are the changes in vibrational and rotational energies of NO, respectively. The average values of these quantities are shown in Figures 9.7a and 9.7b, respectively, as a function of the incident energy E_i. As seen in the figure, NO vibration is adiabatic in the energy range of this study, while rotational energy transfer increases with E_i.

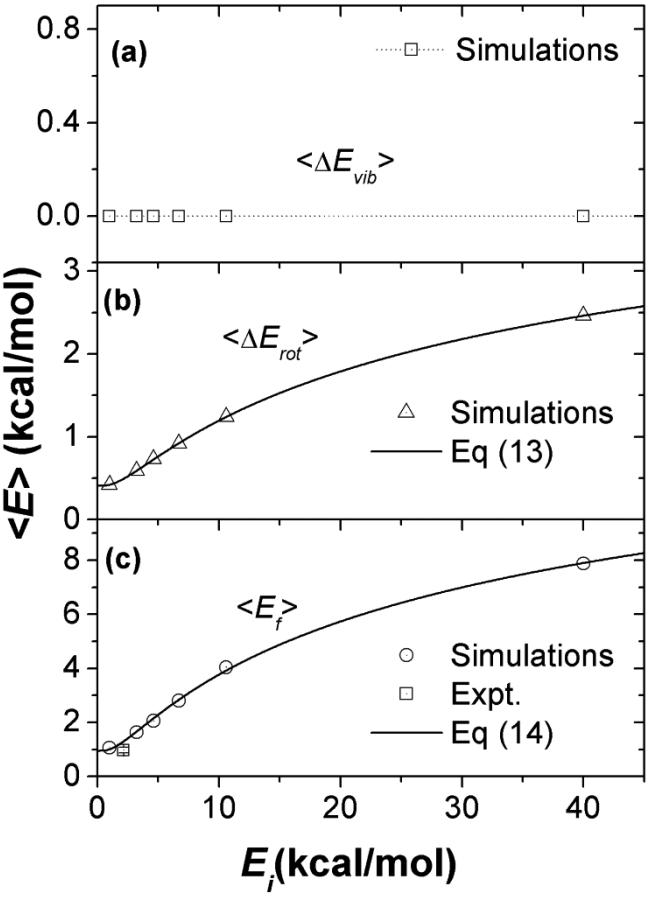

Figure 9.7: Average energy transfer to (a) vibrational, (b) rotational and (c) translational energy of the projectile as a function of the collision energy in the NO + F-SAM scattering process. Equations 9.13 and 9.14 are fit (solid lines) to the simulations results (symbols).

A simple model based on the adiabaticity parameter[50] can be used to rationalize the energy transfer efficiencies found in our NO + F-SAM simulations. The adiabaticity parameter is defined as[50]

$$\xi = \frac{\tau_c}{t_{rot\,(vib)}} \tag{9.10}$$

where τ_c is the duration of the collision process and $t_{rot\,(vib)}$ is the rotational(vibrational) period of the diatomic molecule, depending on whether rotational or vibrational energy transfer is treated. The collision time τ_c can be expressed as a/v_i, where a is the "range" of the intermolecular force, and v_i is the incident velocity of the projectile. The adiabaticity parameter is therefore inversely proportional to v_i

$$\xi = \frac{a}{v_i t_{rot\,,(vib)}} \tag{9.11}$$

In the adiabatic limit (ξ > 1), the average (rotational or vibrational) energy transfer decreases exponentially with ξ[50]

$$\langle \Delta E_{rot\,,vib} \rangle = \langle \Delta E_{rot\,,vib} \rangle^{sudden} \exp(-\xi) \tag{9.12}$$

where $\langle \Delta E_{rot\,,vib} \rangle^{sudden}$ is the average energy transfer in the sudden limit ($\xi = 0$). This model was proposed in the context of gas-phase atom + diatom collisions and it needs to be adapted to gas-surface collisions. The above equation predicts no average energy transfer in the limit of low incident velocities, which is not the case in gas-surface collisions because of thermal desorption. Therefore, the simplest adjustment needed in equation 9.12 is the inclusion of an additional constant term that would account for energy transfer in the $v_i \rightarrow 0$ limit.

As indicated above $\langle \Delta E_{vib} \rangle$ is zero in the energy range of our study, and higher collision energies would be needed to obtain nonzero vibrational energy transfer. However, the $\langle \Delta E_{rot} \rangle$ values increase significantly with the collision energy and equation 9.12 (adapted as indicated in the previous paragraph) can be used to model rotational energy transfer in NO + F-SAM:

$$\langle \Delta E_{rot} \rangle = \langle \Delta E_{rot} \rangle^{sudden} \times \exp\left(-\frac{b_{rot}}{\sqrt{E_i}}\right) + c_{rot}\, RT_s \tag{9.13}$$

where $\langle \Delta E_{rot} \rangle^{sudden}$ is the high-E_i limiting value for $\langle \Delta E_{rot} \rangle$ and b_{rot} is another parameter than contains a and t_{rot} in equation 9.11 and the mass of the projectile m. An additional parameter c_{rot} multiplying RT_s accounts for the degree of thermal accommodation in the $v_i \rightarrow 0$ limit.

As seen in Figure 9.7b, equation 9.13 reproduces very well the simulation results. The resulting fitting parameters are: $\langle \Delta E_{rot} \rangle^{sudden} = 5.35 \pm 0.02$ kcal/mol, $b_{rot} = 6.06 \pm 0.02$ (kcal/mol)$^{1/2}$ and $c_{rot} = 0.68 \pm 0.00$.

The average E_f values obtained in our work show a similar E_i dependence as $\langle \Delta E_{rot} \rangle$. For this reason the same exponential function (equation 9.12) was employed to fit $\langle E_f \rangle$, slightly adapted to account for the theoretical value $2RT_s$ (rather than RT_s) obtained for full accommodation of the translational degrees of freedom,

$$\langle E_f \rangle = \langle E_f \rangle^{sudden} \times \exp\left(-\frac{b_f}{\sqrt{E_i}}\right) + c_f (2RT_s) \tag{9.14}$$

As seen in Figure 9.7c, equation 9.14 is also able to reproduce the computed $\langle E_f \rangle$ values. The parameters obtained in the fit are: $\langle E_f \rangle^{sudden} = 17.08 \pm 0.61$ kcal/mol, $b_f = 5.69 \pm 0.24$ (kcal/mol)$^{1/2}$ and $c_f = 0.79 \pm 0.10$.

For completeness and to show the accuracy of our simulations, Figure 9.7c also shows an experimental result[2] (open square) that falls pretty close to the model results.

According to this model, both $\langle \Delta E_{rot} \rangle$ and $\langle E_f \rangle$ plateau at the limiting values of 5.5 and 18.0 kcal/mol, respectively. However, the absence of more data for high E_i precludes a definite conclusion about energy transfer efficiencies in the high-E_i regime. On the other hand, as state above, the exponential behavior of equation 9.12 is known to be valid in the adiabatic regime (low E_i values). For high E_i, the sudden limit is reached and the applicability of equation 9.12 is uncertain.

Energy transfer to the F-SAM surface has been studied in the past by Hase and co-workers[7] and Morris and co-workers[34] using Ar, CO_2, and peptides as projectiles. They obtained very high efficiencies of energy transfer to the surface in the high collision energy limit. When this efficiency is expressed as $\frac{\langle \Delta E_{surf} \rangle}{E_i}$ the limiting values they obtained in their systems range from 0.7 to 0.98. The model employed here for $\langle \Delta E_{rot} \rangle$ and $\langle E_f \rangle$ provides the following expression for $\frac{\langle \Delta E_{surf} \rangle}{E_i}$:

$$\frac{\langle \Delta E_{surf} \rangle}{E_i} = 1 - \frac{\langle \Delta E \rangle^{sudden} \times \exp\left(-\frac{b}{\sqrt{E_i}}\right) - c}{E_i} \tag{9.15}$$

Equations 9.5, 9.9, 9.13 and 9.14 were used to arrive at equation 9.15. The parameters in the equation are related to those of equations 9.13 and 9.14; $c = c_{rot} RT_s + c_f (2RT_s)$, $\langle \Delta E \rangle^{sudden} = \langle \Delta E_{rot} \rangle^{sudden} + \langle E_f \rangle^{sudden}$ and

$b \cong b_{rot} \cong b_f$. Equation 9.15 was fit to the simulation $\frac{\langle \Delta E_{surf} \rangle}{E_i}$ data obtaining the following fitting parameters: c = 1.42 ± 0.01, $\langle \Delta E \rangle^{sudden}$ = 24.5 ± 1.5 and b = 6.13±0.16. The fit is shown in Figure 9.8.

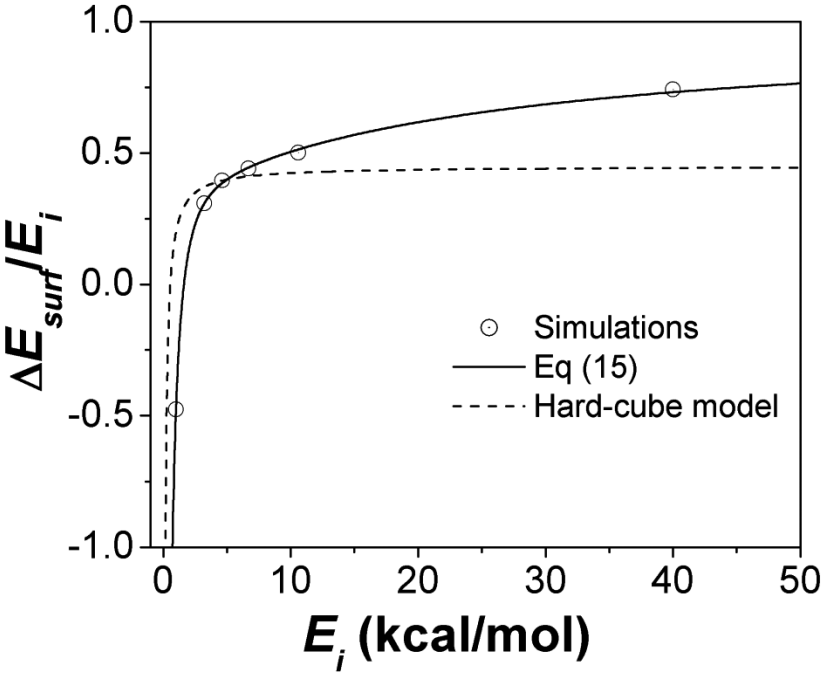

Figure 9.8: Average energy transfer to the surface, relative to the collision energy E_i as a function of E_i in the NO + F-SAM scattering process. Equation 9.15 and the hard-cube model are fit (solid and dashed lines, respectively) to the simulations results (circles).

It is instructive to compare the results of the model presented here with those obtained with other models. One of the most commonly used models to study energy transfer in gas-surface collisions is the hard-cube model.[63] According to the hard-cube model the energy transfer efficiency to the surface reads: [63]

$$\frac{\langle \Delta E_{surf} \rangle^{hc}}{E_i} = \frac{4\mu}{(\mu+1)^2} - \frac{\mu(2-\mu)}{(\mu+1)^2}\frac{2RT_s}{E_i} \tag{9.16}$$

where μ is m/M, with M being an effective surface mass. As seen in the figure the hard cube model is not able to reproduce the simulation data and the resulting value of μ is 0.15.

The model employed in the present paper predicts 100% efficiency of energy transfer to the surface at the high-E_i limit, i.e. $\frac{\langle \Delta E_{surf} \rangle}{E_i} = 1$ for $E_i \to \infty$. An additional fit was done with a constant term d included in the right-hand side of equation 9.15 to investigate possible deviations from the 100% efficiency in the $E_i \to \infty$ limit. The resulting fit provides a value of 0.00 for d, which corroborates the result. Previous studies showed limiting energy transfer efficiencies to the surface of 80-90% for peptides and CO_2 colliding with F-SAM surfaces.[5,7] However, these values were obtained using $\frac{\langle \Delta E_{surf} \rangle}{E_i} = a \times \exp(-b/E_i)$ to fit the simulation results. In fact, if equation 9.15, with an additional constant parameter to account for possible deviations from the 100% efficiency in the high E_i limit, is used instead to re-fit the CO_2 + F-SAM simulation results, a value of 1.02 ± 0.06 is obtained in the $E_i \to \infty$ limit. This result agrees with the value 1.00 found here for NO + F-SAM.

Experimental studies on rare gases scattering off gold and platinum surfaces[64] in the energy range 1-4000 eV point also to limiting efficiencies of 100% or close to 100% for energy transfer to the surface. Moreover, recent simulation results in our research group on Ar + F-SAM[65] show that equation 9.15 is able to fit the energy transfer efficiencies up to very high energies (1500 kcal/mol) with a value for $\frac{\langle \Delta E_{surf} \rangle}{E_i}$ in the high-E_i limit of 1.00 ± 0.01.

However, the highest E_i value in our NO + F-SAM simulation study was only 40 kcal/mol. Also, there is an uncertainty in the applicability of the model for high collision energies, which does not guarantee the correctness of equation 9.15 at very high E_i in NO + F-SAM. An additional factor that makes extrapolation to high collision energies uncertain is the fact that vibrational energy transfer is expected to occur at the highest energies, a process that will compete with energy transfer to the surface.

3.5 Stereodynamics

Alignment and orientation of the scattered NO molecules are studied in this Section. In particular the lowest tensor A_0, A_{1+} and A_{2+} alignment moments and the O_{1-} orientation moment of the **J** distribution are computed for ICs 8-10 as in previous work on CO_2 scattering off a liquid surface and F-SAM.[43] This allows us to make a direct comparison between the stereodynamics of the NO + F-SAM and CO_2 + F-SAM systems. The classical mechanical analogues of the A_0, A_{1+}, A_{2+} and O_{1-} moments are collected in Table 9.5; the Cartesian coordinate frame as well as the different limiting types of rotational motion are depicted graphically in the cartoon of Figure 9.9a. The z axis is perpendicular to the surface and the incident molecules move in the

positive x direction (xz plane). In our simulations the xz plane is not fixed as the azimuthal angle is randomly sampled between 0º and 360º for each trajectory.

Table 9.5: Lowest order orientation and alignment moments of the **J** distribution.

Moments	Classical mechanical value
A_0	$\langle 3J_z^2/\lvert\mathbf{J}\rvert^2\rangle - 1$
A_{1+}	$\langle 2J_xJ_z/\lvert\mathbf{J}\rvert^2\rangle$
A_{2+}	$\langle (J_x^2 - J_y^2)/\lvert\mathbf{J}\rvert^2\rangle$
O_{1-}	$\langle J_y/\lvert\mathbf{J}\rvert\rangle$

The values of the A_0 moment indicate whether **J** is preferentially perpendicular to the surface $A_0 > 0$, i.e., *helicopter* rotational motion, or if **J** is preferentially parallel to the surface $A_0 < 0$, i.e., *cartwheel* rotational motion. Analysis of the A_{2+} moments gives the relative contribution of in-plane (xz) and out-of-plane *cartwheel* behavior. The former occurs when A_{2+} is negative.

The O_{1-} moment is nonzero when the molecule scatters off the surface in a *cartwheel* fashion and there is a preferred orientation of **J** with respect to the y axis. In particular, O_{1-} is positive when the *cartwheel* rotation motion is such that NO spins with forward tumbling (*cartwheel topspin* motion).

Perkins and Nesbitt[43] and Troya and co-workers[33] have shown that the values of the orientation and alignment moments depend very strongly on the final angular momentum quantum number J for CO_2 + F-SAM and CO + F-SAM, respectively. Thus, in Figure 9.9b-d, the lowest alignment and orientation moments are depicted as a function of J for ICs 8-10. In most cases, these moments increase (or decrease) their values as J increases, i.e., alignment and orientation increase as J increases. This result can be understood in terms of the **J** analysis employed above to interpret the degree of thermal accommodation obtained from the $P(J)$ distributions. NO molecules have to suffer a minimum number n_Φ of gentle "kicks" that change slightly the direction of **J** (by an angle Φ), in order to randomize the direction of **J**. As discussed in previous sections, these events contribute mostly to the low-J part of the $P(J)$ distribution. Therefore, those NO molecules that scatter off the surface with low values of J will tend to randomize **J** and the degree of

alignment and orientation of **J** will be small. On the other hand, the molecules that scatter from the F-SAM rotationally excited will not randomize **J** completely and will give rise to alignment and orientation of **J**.

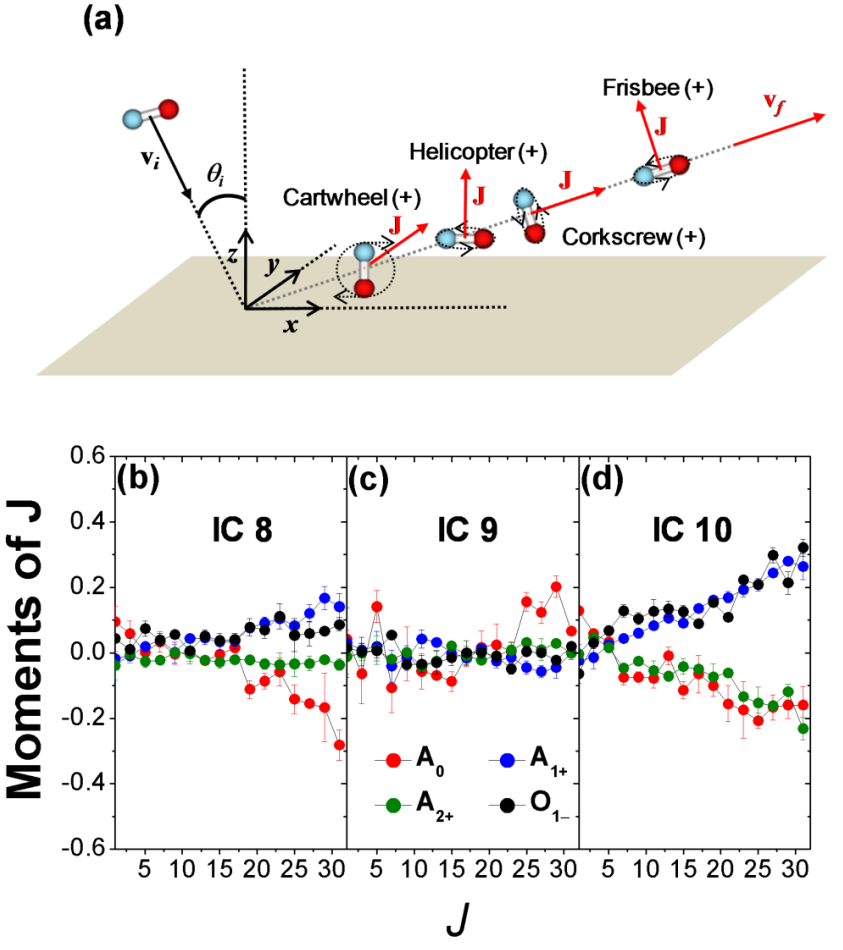

Figure 9.9: (a) Cartesian coordinate frame employed in the stereodynamics analysis and different rotational motions of the scattered projectile identified in the NO + F-SAM study. The lowest order orientation and alignment moments of the **J** distribution are plotted as a function of J, in panels: (b) for IC 8, (c) for IC 9 and (d) for IC 10.

The results of Figure 9.9b and 9.9d for IC 8 and 10, respectively, indicate that NO tends to scatter off the surface in a *cartwheel topspin* fashion when it is rotationally excited, because $A_0 < 0$ and O_{1-} is positive. This tendency is enhanced when the incident angle increases (for IC 10 when θ_i = 60º). Orientation of the angular momentum vector is analyzed in more detail in Figure 9.10, where probability distribution plots of the projections of **J** onto the $x, y,$ and z axes are shown for ICs 8-10. While the plots for the J_x and J_z projections are rather symmetric, the $P(J_y/|\boldsymbol{J}|)$ plots for ICs 8 and 10 peak

close to 1, as J increases, particularly for IC 10, indicating the preference for *cartwheel topspin* behavior or the scattered molecules. These results agree with the CO + F-SAM simulation study of Troya and co-workers[33] for similar initial conditions. The values of the A_0 moments for CO + F-SAM are –0.2 and –0.3 for θ_i of 30º and 60º, respectively, for $J > 20$, which compare well with the values of the present study that range from –0.1 to –0.3. The CO + F-SAM results of Troya and co-workers and our NO + F-SAM results contrast, however, with those for CO_2 + F-SAM, where a preference for *helicopter* behavior was found for $J < 60$ with *cartwheel* behavior arising for the higher J values.[43]

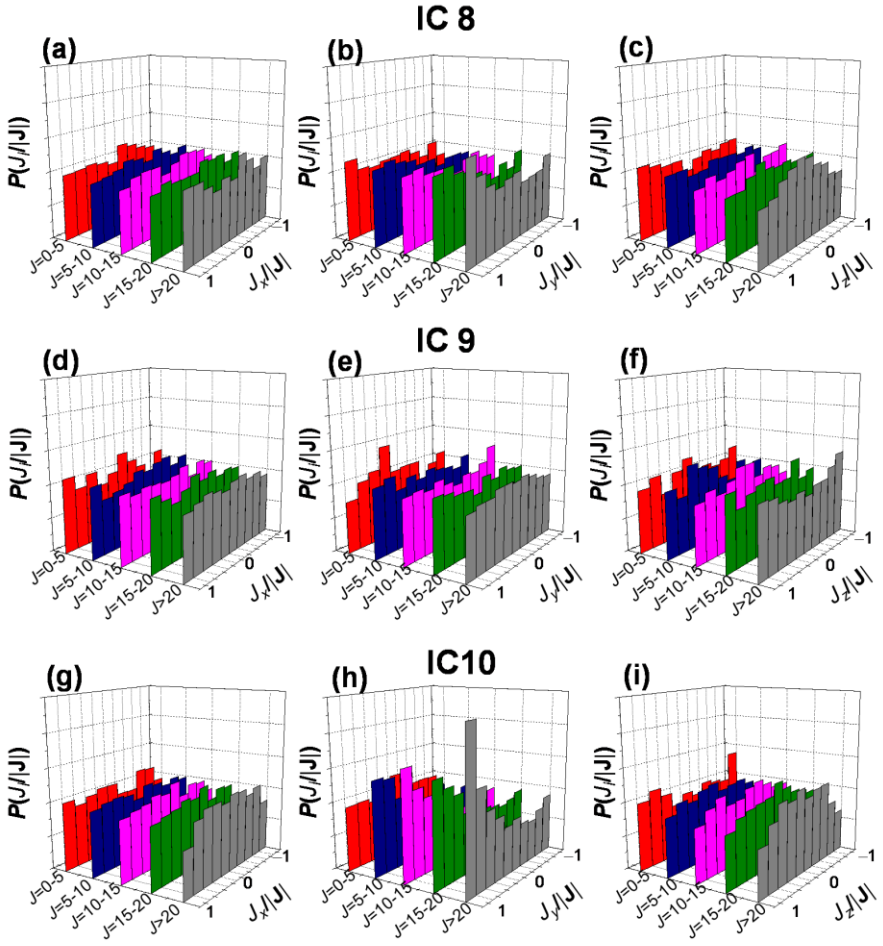

Figure 9.10: Probability density plots of the projection of the rotational angular momentum of the projectile **J** onto the three Cartesian axes defined in Figure 9.9a, as a function of the final values of J for IC 8 (panels (a), (b) and (c)), IC 9 (panels (d), (e) and (f)) and IC 10 (panels (g), (h) and (i)).

The negative values of the alignment A_{2+} moment indicate that *cartwheel* rotational motion takes place, primarily, in the xz plane for θ_i = 60º (IC 10), whereas for θ_i = 30º (IC 8) the xz and yz planes are equally probable for *cartwheel* behavior, as the values of A_{2+} are close to 0.

When rotationally excited NO molecules strike the F-SAM (IC 9) the behavior of the scattered species is different. In particular, all moments studied here are close to 0 for all J values, except A_0 that is slightly positive for $J > 25$, indicating *helicopter* behavior. This is an important difference with respect to the scattering of rotationally cold molecules colliding with F-SAM (ICs 8 and 10). Again, our result parallels those previously found by Troya and co-workers in their CO + F-SAM study.[33] The preference for *helicopter* rather than *cartwheel* behavior of the *rotationally* excited molecules was analyzed in detail in Troya's work.[33] Basically, rotationally excited molecules that strike the surface in a *helicopter* fashion tend to preserve their rotational excitation and conserve the alignment. On the other hand, those impinging the surface in a *cartwheel* fashion will deactivate more easily the initial rotational excitation, which will decrease *cartwheel* alignment.

Finally, the other two types of rotational motion of the scattered molecules shown in Figure 9.9a, *frisbee* and *corkscrew*, can only be examined by a further analysis of the projection of **J** onto the velocity of the scattering molecules $\mathbf{v}_f$. *Corkscrew* (+) and (–) behavior occurs when **J** and $\mathbf{v}_f$ are parallel and antiparallel to each other, respectively, and *frisbee* rotational motion takes place when both vectors are perpendicular to each other, with *frisbee* (+) defined as in Figure 9.9a. *Frisbee* and *cartwheel* behaviors can be distinguished from each other by adding a third vector that goes along the z axis and will be called **z** here. Thus, *frisbee* motion is defined when the angle formed between **J** and a vector perpendicular to **z** and $\mathbf{v}_f$ (defined here as $\mathbf{z} \times \mathbf{v}_f$) is 90º; when this angle is 0º (or 180º) the motion is pure *cartwheel* (+) [or (–)]. Figure 9.11 shows probability distribution plots for ICs 8-10 of the cosines of the following two angles: (1) the angle formed between $\mathbf{v}_f$ and **J** and (2) the one formed between $(\mathbf{z} \times \mathbf{v}_f)$ and **J**.

The results of Figure 9.11 indicate that *cartwheel* and *corkscrew* types of motion are slightly more probable than *frisbee* for all ICs. *Cartwheel topspin* is also more probable than *cartwheel backspin* for ICs 8 and 10, and both have the same probability for IC 9, which agrees with values of the O_{1-} moments seen before. *Corkscrew* motion has the same probability as *cartwheel* motion or slightly higher, particularly for ICs 9 and 10, with both orientations (+) and (–) being equally probable. The most (least) isotropic plot is that for IC 9 (IC 10) indicating less (more) orientation and alignment, in agreement again with the above analysis of the moments of the **J** distribution. Troya and co-

workers also found preference for both *cartwheel* and *corkscrew* behavior vs *frisbee* motion in their CO + F-SAM simulations.[33]

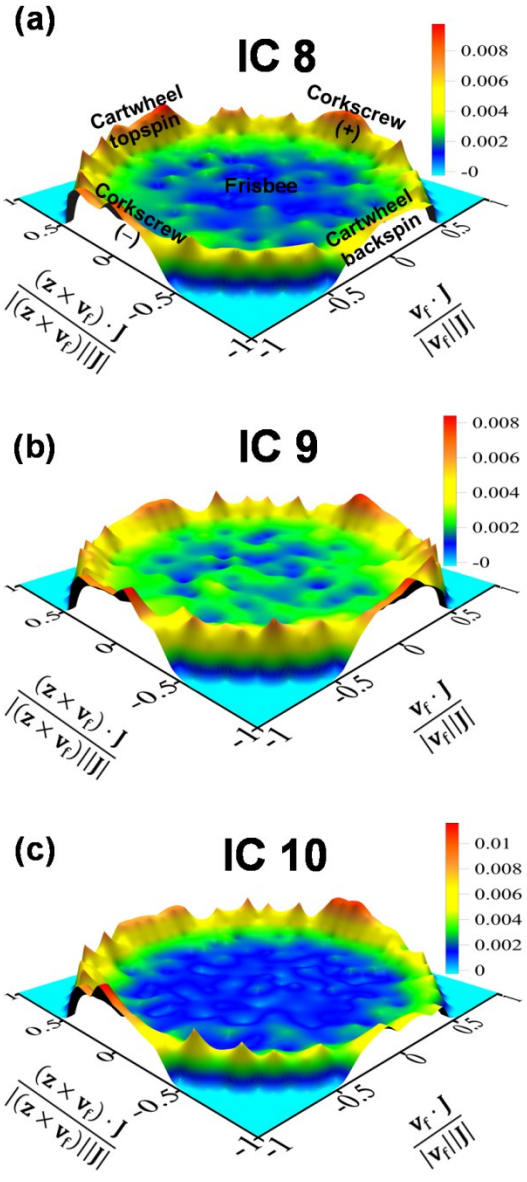

Figure 9.11: Probability density plots of the different rotational motions of the scattered NO molecules to distinguish amongst *frisbee*, *cartwheel* and *corkscrew* motions. The probability is calculated as a function of the cosines of the angles formed between $\mathbf{v}_f$ and **J,** and between $(\mathbf{z}\times\mathbf{v}_f)$ and **J**.

4. CONCLUSIONS

Chemical dynamics simulations were performed to study the collision dynamics of the NO + F-SAM system. A potential energy function for the interaction between the projectile and the surface was developed from a fit to high-level ab initio calculations. The simulations indicate that the scattered projectiles display non-Boltzmann $P(E_f)$ distributions for all ICs except 1-4, and $P(J)$ distributions modeled by a sum of two Boltzmann components, one of them with a temperature T_s, which indicates a higher degree of thermal accommodation of rotation *vs* translation. The same result was found previously for CO_2 + F-SAM. Thermal accommodation of the rotational degrees of freedom in NO + F-SAM can be understood in terms of a minimum number of moderate variations in the direction of the rotational angular momentum of the molecule **J** in the course of the dynamics. This type of analysis provides a much better metric than previously used analyses based on the variation of the center-of-mass velocity vector of the projectile in the perpendicular direction.

A new model that accounts for energy transfer to the various degrees of freedom of the molecule and the surface is presented in this paper. The model is based on the adiabaticity parameter and on an $\exp(-a/v_i)$ dependence of energy transfer with the collision velocity v_i. It reproduces very well the simulation data in the collision energy range employed in this study (from 1 to 40 kcal/mol) and predicts 100% efficiency of energy transfer to the surface in the high collision energy limit. However, the absence of more simulation results for higher energies, and the fact that the use of the exponential function is unclear for high energies, indicate that the result of the extrapolation should be taken with caution.

The stereodynamics of the title process was also investigated here. In agreement with previous results for the CO + F-SAM system, the two preferred rotational motions of the scattered molecules are *corkscrew* and *cartwheel*. For *corkscrew* motion, both orientations of **J** are equally probable, whereas for *cartwheel* motion, the *topspin* orientation clearly dominates, particularly for high rotational states. Orientation and alignment are enhanced for higher incident angles.

Finally, the available experimental data was compared with the present simulation results and good agreement was found in all cases, which supports the methods employed in the present paper.

REFERENCES

(1) Cohen, S. R.; Naaman, R.; Sagiv, J. *J. Chem. Phys.* **1988**, *88*, 2757.
(2) Cohen, S. R.; Naaman, R.; Sagiv, J. *Phys. Rev. Lett.* **1987**, *58*, 1208.
(3) Nogueira, J. J.; Sanchez-Coronilla, A.; Marques, J. M. C.; Hase, W. L.; Martinez-Nunez, E.; Vazquez, S. A. *Chem. Phys.* **2011 (in press)**.
(4) Nogueira, J. J.; Vazquez, S. A.; Lourderaj, U.; Hase, W. L.; Martinez-Nunez, E. *J. Phys. Chem. C* **2010**, *114*, 18455.
(5) Nogueira, J. J.; Vazquez, S. A.; Mazyar, O. A.; Hase, W. L.; Perkins, B. G.; Nesbitt, D. J.; Martinez-Nunez, E. *J. Phys. Chem. A* **2009**, *113*, 3850.
(6) Nogueira, J. J.; Martinez-Nunez, E.; Vazquez, S. A. *J. Phys. Chem. C* **2009**, *113*, 3300.
(7) Yang, L.; Mazyar, O. A.; Lourderaj, U.; Wang, J. P.; Rodgers, M. T.; Martinez-Nunez, E.; Addepalli, S. V.; Hase, W. L. *J. Phys. Chem. C* **2008**, *112*, 9377.
(8) Vazquez, S. A.; Morris, J. R.; Rahaman, A.; Mazyar, O. A.; Vayner, G.; Addepalli, S. V.; Hase, W. L.; Martinez-Nunez, E. *J. Phys. Chem. A* **2007**, *111*, 12785.
(9) Martínez-Núñez, E.; Rahaman, A.; Hase, W. L. *J. Phys. Chem. C* **2007**, *111*, 354.
(10) Paz, Y.; Naaman, R. *J. Chem. Phys.* **1991**, *94*, 4921.
(11) Day, B. S.; Shuler, S. F.; Ducre, A.; Morris, J. R. *J. Chem. Phys.* **2003**, *119*, 8084.
(12) Gibson, K. D.; Isa, N.; Sibener, S. J. *J. Chem. Phys.* **2003**, *119*, 13083.
(13) Day, B. S.; Morris, J. R. *J. Phys. Chem. B* **2003**, *107*, 7120.
(14) Isa, N.; Gibson, K. D.; Yan, T.; Hase, W.; Sibener, S. J. *J. Chem. Phys.* **2004**, *120*, 2417.
(15) Day, B. S.; Morris, J. R. *J. Chem. Phys.* **2005**, *122*, 234714.
(16) Yan, T.; Hase, W. L. *Phys. Chem. Chem. Phys* **2000**, *2*, 901.
(17) Yan, T.; Hase, W. L.; Barker, J. R. *Chem. Phys. Lett.* **2000**, *329*, 84.
(18) Yan, T.; Hase, W. L. *J. Phys. Chem. A* **2001**, *105*, 2617.
(19) Yan, T.; Hase, W. L. *J. Phys. Chem. B* **2002**, *106*, 8029.
(20) Yan, T.; Isa, N.; Gibson, K. D.; Sibener, S. J.; Hase, W. L. *J. Phys. Chem. A* **2003**, *107*, 10600.
(21) Day, B. S.; Morris, J. R.; Troya, D. *J. Chem. Phys.* **2005**, *122*, 214712.
(22) Day, B. S.; Morris, J. R.; Alexander, W. A.; Troya, D. *J. Phys. Chem. A* **2006**, *110*, 1319.
(23) Shuler, S. F.; Davis, G. M.; Morris, J. R. *J. Chem. Phys.* **2002**, *116*, 9147.
(24) Ferguson, M. K.; Lohr, J. R.; Day, B. S.; Morris, J. R. *Phys. Rev. Lett.* **2004**, *92*, 732011.

(25) Li, G.; Bosio, S. B. M.; Hase, W. L. *J. Mol. Struc.* **2000**, *556*, 43.
(26) Troya, D.; Schatz, G. C. *J. Chem. Phys.* **2004**, *120*, 7696.
(27) Tasic, U.; Yan, T.; Hase, W. L. *J. Phys. Chem. B* **2006**, *110*, 11863.
(28) Wainhaus, S. B.; Lim, H.; Schultz, D. G.; Hanley, L. *J. Chem. Phys.* **1997**, *106*, 10329.
(29) Schultz, D. G.; Wainhaus, S. B.; Hanley, L.; DeSainteClaire, P.; Hase, W. L. *J. Chem. Phys.* **1997**, *106*, 10337.
(30) Laskin, J.; Futrell, J. H. *J. Chem. Phys.* **2003**, *119*, 3413.
(31) Meroueh, O.; Hase, W. L. *J. Am. Chem. Soc.* **2002**, *124*, 1524.
(32) Troya, D.; Schatz, G. C. *Int. Rev. Phys. Chem.* **2004**, *23*, 341.
(33) Alexander, W. A.; Morris, J. R.; Troya, D. *J. Phys. Chem. A* **2009**, *113*, 4155.
(34) Lu, J. W.; Alexander, W. A.; Morris, J. R. *Phys. Chem. Chem. Phys.* **2010**, *12*, 12533.
(35) Perkins, B. G.; Haber, T.; Nesbitt, D. J. *J. Phys. Chem. B* **2005**, *109*, 16396.
(36) Perkins, B. G.; Nesbitt, D. J. *J. Phys. Chem. B* **2006**, *110*, 17126.
(37) Zolot, A. M.; Harper, W. W.; Perkins, B. G.; Dagdigian, P. J.; Nesbitt, D. J. *J. Chem. Phys.* **2006**, *125*.
(38) Perkins, B. G.; Nesbitt, D. J. *J. Phys. Chem. A* **2007**, *111*, 7420.
(39) Perkins, B. G.; Nesbitt, D. J. *Proc. Natl. Ac. Sci. USA* **2008**, *105*, 12684.
(40) Perkins, B. G.; Nesbitt, D. J. *J. Phys. Chem. A* **2008**, *112*, 9324.
(41) Perkins, B. G.; Nesbitt, D. J. *J. Phys. Chem. B* **2008**, *112*, 507.
(42) Perkins, B. G.; Nesbitt, D. J. *J. Phys. Chem. A* **2009**, *113*, 4613.
(43) Perkins, B. G.; Nesbitt, D. J. *J. Phys. Chem. A* **2010**, *114*, 1398.
(44) Los, J.; Gleeson, M. A.; Koppers, W. R.; Weeding, T. L.; Kleyn, A. W. *J. Chem. Phys.* **1999**, *111*, 11080.
(45) Koppers, W. R.; Beijersbergen, J. H. M.; Weeding, T. L.; Kistemaker, P. G.; Kleyn, A. W. *J. Chem. Phys.* **1997**, *107*, 10736.
(46) Koppers, W. R.; Gleeson, M. A.; Lourenço, J.; Weeding, T. L.; Los, J.; Kleyn, A. W. *J. Chem. Phys.* **1999**, *110*, 2588.
(47) Tasic, U.; Day, B. S.; Yan, T.; Morris, J. R.; Hase, W. L. *J. Phys. Chem. C* **2008**, *112*, 476.
(48) Wang, J.; Meroueh, S. O.; Wang, Y.; Hase, W. L. *Int. J. Mass. Spectr.* **2003**, *230*, 57.
(49) Song, K.; Meroueh, O.; Hase, W. L. *J. Chem. Phys.* **2003**, *118*, 2893.
(50) Levine, R. D. *Molecular Reaction Dynamics*; Cambridge University Press: Cambridge, 2005.
(51) Huber, K. P.; Herzberg, G. *Constants of Diatomic Molecules*; Van Nostrand: New York, 1979.
(52) Vayner, G.; Alexeev, Y.; Wang, J.; Windus, T. L.; Hase, W. L. *J. Phys. Chem. A* **2006**, *110*, 3174.
(53) Wang, J.; Hase, W. L. *J. Phys. Chem. B* **2005**, *109*, 8320.

(54) Alexander, W. A.; Troya, D. *J. Phys. Chem. A* **2006**, *110*, 10834.

(55) Peterson, K. A.; Woon, D. E.; DunningT.H, Jr. *J. Chem. Phys.* **1994**, *100*, 7410.

(56) East, A. L. L.; Allen, W. D. *J. Chem. Phys.* **1993**, *99*, 4638.

(57) Marques, J. M. C.; Prudente, F. V.; Pereira, F. B.; Almeida, M. M.; Maniero, A. M.; Fellows, C. E. *J. Phys. B: At. Mol. Opt. Phys.* **2008**, *41*, 85103.

(58) VENUS; VENUS05 is a modified version of VENUS96. (a) Hase, W. L.; Duchovic, R. J.; Hu, X.; Komornicki, A.; Lim, K. F.; Lu, D.-h.; Peslherbe, G. H.; Swamy, K. N.; Vande Linde, S. R.; Varandas, A.; Wang, H.; Wolf, R. J. QCPE 1996, 16, 671. (b) Hu, X.; Hase, W. L.; Pirraglia, T. J. Comput. Chem. 1991, 12, 1014 ed.

(59) Allen, M. P.; Tildesley, D. J. *Computer Simulation of Liquids*; Clarendon Press: Oxford, 1987.

(60) Miller, S. A.; Luo, H.; Pachuta, S. J.; Cooks, R. G. *Science* **1997**, *275*, 1447.

(61) Huang, Y.; Rettner, C. T.; Auerbach, D. J.; Wodtke, A. M. *Science* **2000**, *290*, 111.

(62) Shenvi, N.; Roy, S.; Tully, J. C. *Science* **2009**, *326*, 829.

(63) Grimmelmann, E. K.; Tully, J. C.; Cardillo, M. J. *J. Chem. Phys.* **1980**, *72*, 1039.

(64) Winters, H. F.; Coufal, H.; Rettner, C. T.; Bethune, D. S. *Phys. Rev. B* **1990**, *41*, 6240.

(65) Martinez-Nunez, E. *Unpublished results* **2011**.

Chapter 10

Intermolecular Potential Energy Curves for Silyl Ions/F-SAM

1. INTRODUCTION

More than one decade ago, Cooks and co-workers[1] described a method for preparing modified surfaces, in which intact polyatomic ions were deposited from the gas phase onto a self-assembled monolayer surface of fluorinated alkanethiols, $CF_3(CF_2)_7(CH_2)_2SH$, on a polycrystalline gold surface (F-SAM). This intact deposition of projectile ions impinging on surfaces at low collision energies (<100 eV) was referred to as soft-landing, and this process may occur with or without retention of the initial ion charge[2-4]. Experiments of soft-landing have involved a wide variety of projectile ions, including small and medium-size polyatomic ions,[1,5-12] clusters,[13-24] peptides,[11,23,25-30] proteins,[25,31,32] a nucleotide,[33] and intact viruses.[34,35] SAMs were used in many of these experiments because their well-characterized structure, controllable surface properties and biocompatibility make them convenient targets for biological and medical applications.[36]

Collisions of polyatomic ions with surfaces may lead to several physical and chemical processes that compete with soft-landing.[3] Examples are inelastic scattering of the projectile ion, surface-induced dissociation (SID), and reactive landing resulting in covalent modification of the surface. Experimental observations show that the efficiencies of these competing processes depend on the nature of the ion, the physical and chemical properties of the surface, the collision energy, and the incident angle. Soft-landing takes place when the amount of translational energy of the projectile ion that is transferred to the surface and to the internal degrees of freedom of the ion is such that there is insufficient recoil translational energy for the ion to escape from the surface attraction.

Silyl ions are among the smallest projectile ions selected by Cooks and co-workers for experiments of soft-landing.[1,5,12] They observed soft-landing for $(CH_3)_2SiNCS^+$, but not for the lighter H_2SiNCS^+ and $SiNCS^+$ ions, and found evidences that the $(CH_3)_2SiNCS^+$ projectiles trapped in the monolayer retain the charge. The analysis of the accumulated data for various classes of compounds led Cooks and co-workers to conclude that successful soft-landing of polyatomic ions is favored by relatively bulky steric groups. The inclusion of methyl groups in the silyl ion can be expected to increase the attractive intermolecular interaction with the monolayer, and may also facilitate entrapment of the ion within the F-SAM chains.[1,5]

Trajectory chemical dynamics simulations provide a valuable complement to experimental determinations, as they allow for the study of certain features that may be difficult, if not unfeasible, to be explored by experiment. Actually, classical trajectory calculations have been successfully

employed for the investigation of the dynamics of energy transfer of collisions of gases, including protonated peptide ions, with self-assembled monolayers.[37-60] These simulations are usually conducted using analytic potential energy functions of the molecular mechanics type, written as a sum of an intramolecular potential for the projectile gas (in case of polyatomics), an intramolecular potential for the SAM surface, and a gas/surface intermolecular potential. The gas/surface interaction term is frequently described by a sum of two-body functions based on the Buckingham potential,[61] which seems to be more realistic than the Lennard-Jones potential[62] from a physical point of view.[63] The latter, however, is commonly employed in molecular dynamics simulations due to its advantage in terms of CPU-time consumption. The parameters of these potential functions have been derived from fits to intermolecular potential energy curves (IPECs) obtained by high-level ab initio calculations for interaction between the gas and a model compound representing the SAM surface.

In previous studies, parameterizations of gas/F-SAM interaction potentials were carried out using the CF_4 molecule as a model of F-SAM surfaces.[48,64-66] A similar approach was followed for the development of interaction potentials of gases with self-assembled monolayers of alkanes (H-SAM), where CH_4 was utilized as a model of the surface.[37,41,44,47,49,55,58,66-68] These simplifications are made under the assumptions that the electron densities around the C and F(H) atoms in CF_4(CH_4) are similar to those in the fluorocarbon chains of F-SAM (alkane chains of H-SAM), and that non-additive effects, associated mainly with polarization interactions, are negligible. Calculations of quantum theory of atoms in molecules[69,70] predict a slight but significant variation of the atomic properties (e.g., partial charges) of the C and F or H atoms when going from CF_4 or CH_4 to long-chain perfluoroalkanes[71,72] or long-chain alkanes.[73-75] However, Troya and co-workers have shown that parameters of pair potentials derived from calculations on the Ar/CF_4 and Ar/CH_4 systems are transferable to Ar/C_2F_6 and Ar/C_2H_4,[68] thus suggesting that the differences between the electron densities in CF_4 and CH_4 with respect to those in long chains are not significant as far as interaction potentials are concerned. Also, parameterizations performed on the NH_4^+/CH_4 and $CH_3NH_3^+$/CH_4 systems led to essentially the same intermolecular potentials in the sense that NH_4^+ and the -NH_3^+ group of $CH_3NH_3^+$ behave the same way.[67]

In the first step of a typical parameterization, ab-initio IPECs are calculated for different orientations of the gas and CF_4 molecules, usually employing the supermolecule approach with frozen intramolecular geometries and correcting the energy for the basis set superposition error (BSSE) by the counterpoise method.[76,77] If the size of the projectile species is small, the molecular structure calculations may be performed using coupled cluster theory

with singles, doubles, and perturbative triples excitations [CCSD(T)],[78] together with one of the various schemes reported in the literature for extrapolating the total energy to the complete (one-electron) basis-set (CBS) limit.[79-88] However, as the size of the system increases, less expensive computational methods may be required as, for example, the focal point approach of Allen and co-workers.[89-91] With this approach, highly accurate energies obtained by second-order Møller-Plesset theory (MP2)[92,93] may be combined with coupled cluster energies to give approximations to CCSD(T)/CBS energies. For large systems, even this level of calculation may be computationally prohibitive, and the practical alternatives may be reduced to one of the new generation of density functional theory (DFT) methods[94] that have been adapted to describe long-range dispersion interactions (e.g., see Ref.[95]). In this case, however, it may be highly recommended to test the performance of the selected DFT method on the system under study or on related systems.

The main objective of the work reported in this paper was to develop accurate intermolecular potentials for interactions of $SiNCS^+$ and $(CH_3)_2SiNCS^+$ ions with F-SAM surfaces. An additional aim of our study was to assess the reliability of using CF_4 as a model of an F-SAM surface for parameterizations of intermolecular potentials. For these purposes, we performed molecular structure calculations to evaluate IPECs for different orientations of the silyl ion with respect to a CF_4 molecule and, separately, to a model of F-SAM composed by nine chains of perfluorobutane, which has a large enough size to ensure its validity. Pairwise potentials of the Buckingham and Lennard-Jones types were subsequently parameterized as described in Section 2.2.

2. COMPUTATIONAL DETAILS

2.1 Molecular structure methods

Except otherwise stated, all the molecular structure calculations were performed with the TURBOMOLE 5.10 program.[96] For the smallest system investigated here, $SiNCS^+/CF_4$, a series of scan calculations were performed for the relative orientations shown graphically in Figure 10.1. Two levels of theory were employed to compute the IPECs. One was the aforementioned focal point approach.[89-91] Specifically, we first carried out a series of MP2 calculations using the resolution of the identity (RI) approximation[97,98] and the correlation-consistent basis sets aug-cc-pV*X*Z, where X = D, T, and Q,[99] together with the corresponding auxiliary basis sets derived by Weigend et al.[100] The following scheme of Peterson and co-workers[88] was utilized to extrapolate to the CBS limit:

$$E(n) = E_{\text{CBS}} + A\, e^{-(n+1)} + Be^{-(n+1)^2} \quad (10.1)$$

where n = 2, 3, and 4 for the MP2 energies obtained with the DZ, TZ, and QZ basis sets, respectively. Then, CCSD(T)/CBS estimates were determined with the focal-point energy relationship:

$$\text{fp-CCSD(T)/CBS} = \text{MP2/CBS} + [\text{CCSD(T)/DZ} - \text{MP2/DZ}] \quad (10.2)$$

where fp stands for focal point and DZ refers to the aug-cc-pVDZ basis set. The interaction energies calculated with this approach were corrected for the BSSE using the counterpoise method.[76,77]

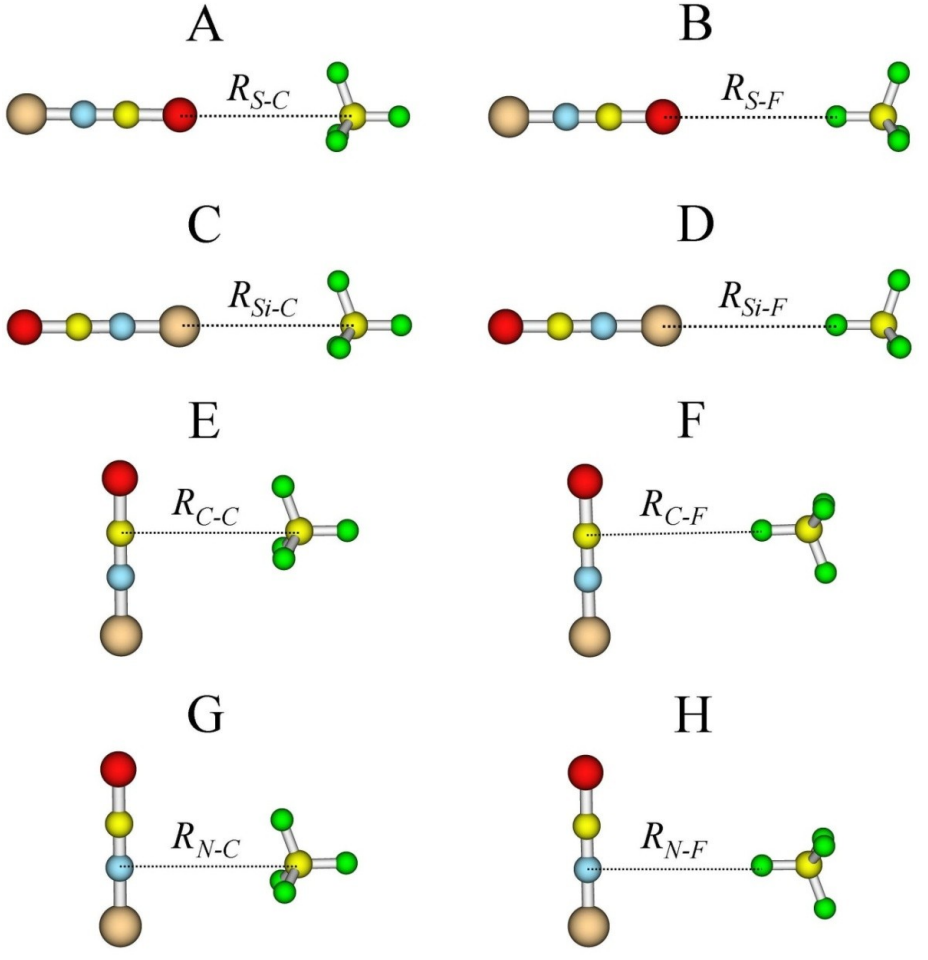

Figure 10.1: Orientations of $SiNCS^+$ and CF_4 selected for the calculation of intermolecular potential energy curves.

The second level of theory involved one of the DFT methods that include empirical, pairwise atomic dispersion corrections of the form $-C_6 r^{-6}$. Specifically, we used the B97-D method of Grimme[101,102] with the RI approximation[103] and with the TZVPP (orbital and auxiliary) basis sets included in the TURBOMOLE basis set library.[96] The interaction energies calculated at this level of theory were not corrected for the BSSE, thus following the recommendations reported in the literature.[101,102,104]

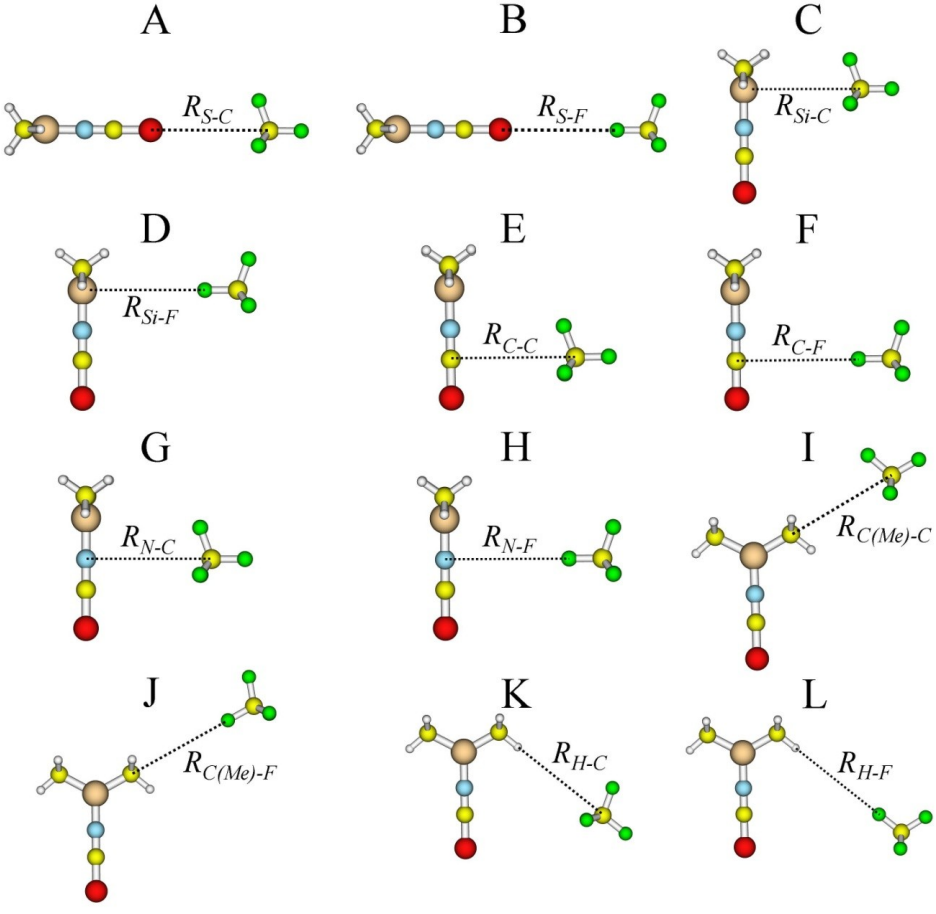

Figure 10.2: Orientations of $(CH_3)_2SiNCS^+$ and CF_4 selected for the calculation of intermolecular potential energy curves.

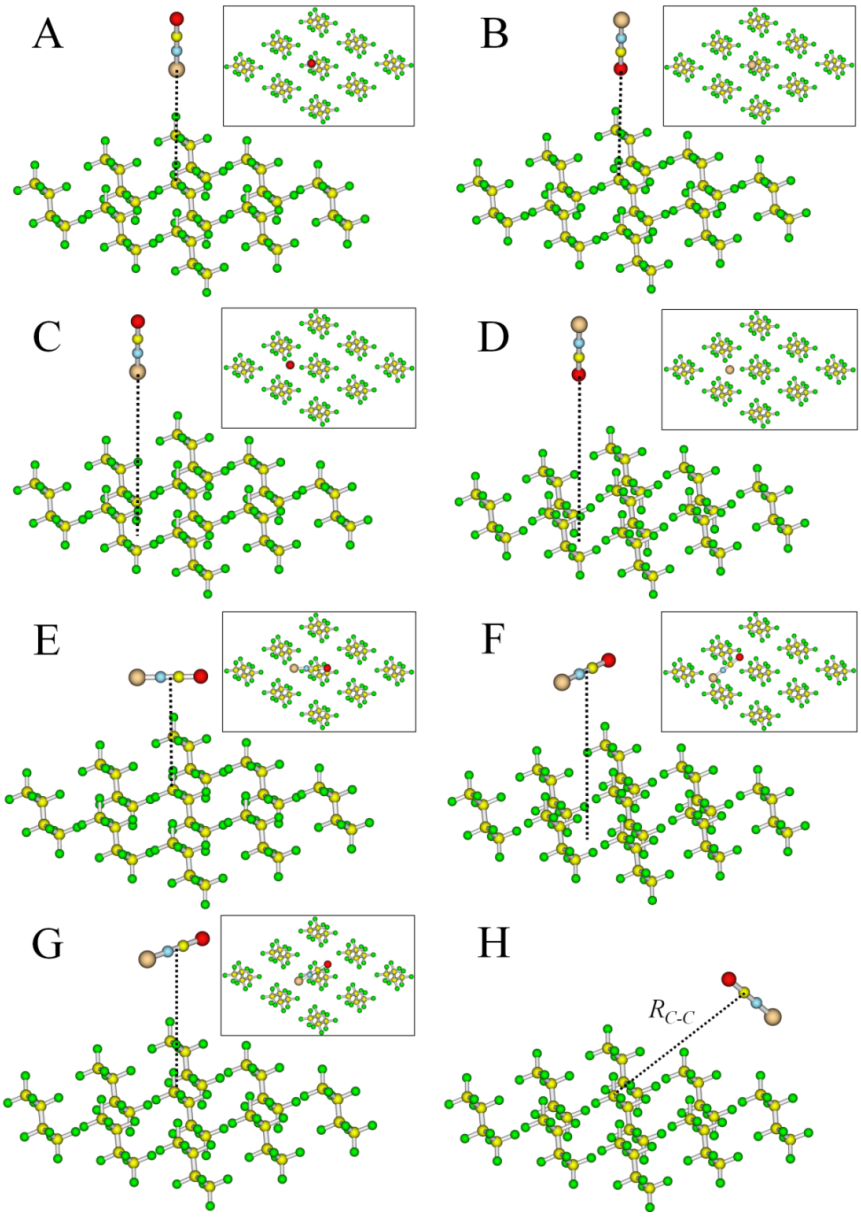

Figure 10.3: Orientations of $SiNCS^+$ and miniSAM selected for the calculation of intermolecular potential energy curves. Side and top views are shown for each orientation. The dotted lines indicate the direction of the scan axes.

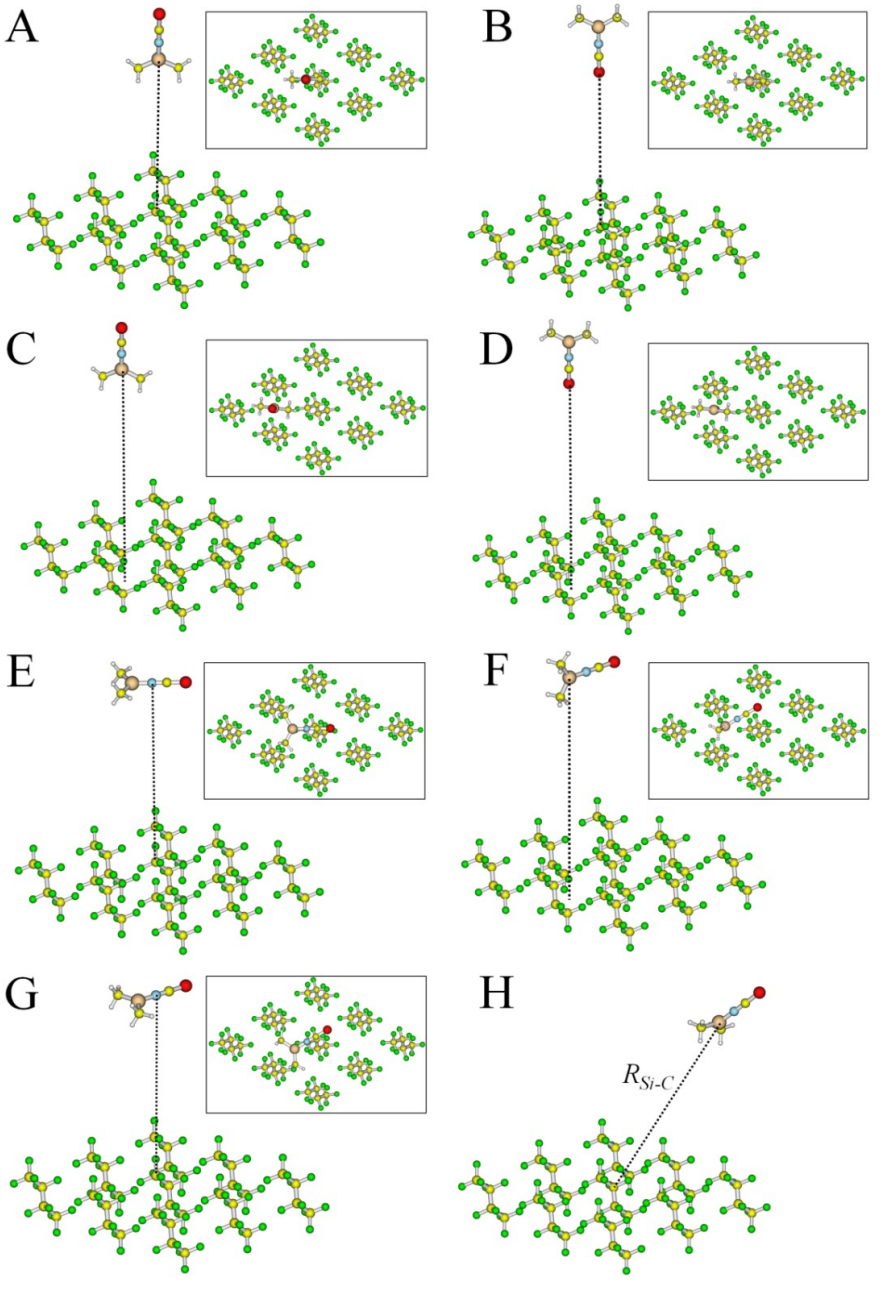

Figure 10.4: Orientations of $(CH_3)_2SiNCS^+$ and miniSAM selected for the calculation of intermolecular potential energy curves. Side and top views are shown for each orientation. The dotted lines indicate the direction of the scan axes.

As shown later in the paper, the IPECs calculated by B97-D were found to be in reasonably good agreement with the fp-CCSD(T) interaction curves. For this reason, only the DFT-D method was applied to the remaining model systems considered in this work. These are $(CH_3)_2SiNCS^+/CF_4$ as well as

$SiNCS^+$ and $(CH_3)_2SiNCS^+$ interacting (separately) with a model of F-SAM formed by nine chains of perfluorobutane, which, for the sake of simplicity and convenience, will be referred to as miniSAM. The orientations selected to calculate IPECs for $(CH_3)_2SiNCS^+/CF_4$ are detailed in Figure 10.2, while those considered for interaction curves of $SiNCS^+$ and $(CH_3)_2SiNCS^+$ with the miniSAM are depicted in Figures 10.3 and 10.4, respectively. The scan axis was considered to be perpendicular to the miniSAM, except for orientation H in Figures 10.3 and 10.4. In all the molecular structure calculations, the geometries of the $SiNCS^+$, $(CH_3)_2SiNCS^+$, and CF_4 molecules were constrained to their B97-D equilibrium values. For the geometry of the miniSAM, we used the equilibrium bond lengths and bond angles of a force field of perfluoroalkanes,[105] and the tilt angle and inter-chain separation determined from an optimization of an F-SAM, using the VENUS05 program[106,107] and a force field described in detail elsewhere.[48,105]

2.2 Analytical potentials and parameterization scheme

Two analytical potentials were considered in this paper to model the interaction between the silyl ion and CF_4 or the miniSAM. The first one is written as a sum of two-body Buckingham potentials[61] plus an additional term, which was necessary to include in order to increase the flexibility of the function:

$$V = \sum_i \sum_j \left\{ A e^{-Br_{ij}} - \frac{C}{r_{ij}^D} - \frac{E}{r_{ij}^F} \right\} \tag{10.3}$$

where the subscripts i and j refer to atoms of different interacting species. Parameters A to F were obtained by fits of the B97-D IPECs to this equation. Parameters D and F were treated as real numbers rather than as integers. The fits were conducted with the help of a genetic algorithm fully described in the literature.[108] Two different parameterizations were done. One, referred to as fit 1, was controlled by imposing the following constraints: $C \geq 0$, $E \geq 0$, $3 \leq D \leq 5$, and $5 \leq F \leq 7$. The constraints on D and F were established in order to avoid values that are too far from typical exponents for long-range interaction terms. The other parameterization, named fit 2, was guided without constraining the parameter limits. As shown later in this paper, the latter parameterization criterion leads to a set of parameters that are not transferable to the $SiNCS^+$/miniSAM system, and therefore that cannot model $SiNCS^+$/F-SAM interactions accurately.

The second potential function employed here to model the $SiNCS^+/CF_4$ interactions consists of a sum of Lennard-Jones type potentials

and electrostatic terms, that is, the common representation of nonbonded interactions in most force fields employed in molecular dynamics simulations:

$$V = \sum_i \sum_j \left\{ \frac{A}{r_{ij}^B} - \frac{C}{r_{ij}^D} + \frac{q_i q_j}{r_{ij}} \right\} \tag{10.4}$$

where parameters A and C are positive and q_i and q_j are the partial charges of atoms i and j obtained by B97-D/TZVPP calculations using the Merz-Singh-Kolman scheme,[109,110] which produces charges fitted to the electrostatic potential. These calculations were performed with the Gaussian 03 package.[111] To increase the flexibility of the function, parameter B was allowed to vary between 8.0 and 13.0, and D between 5.0 and 7.0. As discussed in the next Section, the potential function of equation 10.4 did not give a good representation of the intermolecular interactions in $SiNCS^+/CF_4$. Consequently, for the remaining systems investigated here, that is, $(CH_3)_2SiNCS^+/CF_4$, $SiNCS^+$/miniSAM, and $(CH_3)_2SiNCS^+$/miniSAM, we used equation 10.3 with the parameter constraints indicated above (i.e., fit 1). For the systems involving the miniSAM model, orientation H was not used for the parameterization but for a test of the reliability of the parameterized potential function. In addition, and in order to improve the fittings, two different types of C and F atoms in the perfluorobutane chains were considered and denoted by C_3 and F_3 (perfluoromethyl atoms), and C_2 and F_2 (perfluoromethylene atoms).

3. RESULTS

3.1 Molecular structure calculations

The IPECs calculated for the $SiNCS^+/CF_4$ system at the B97-D/TZVPP level of theory are compared in Figure 10.5 with those obtained by fp-CCSD(T) computations as described previously. The inset graphs, displaying the attractive wells in an expanded scale, show well depths in the range 0.8-2.8 kcal/mol. The most favorable orientation for attractive interaction is G, for which the fp-CCSD(T) and B97-D calculations give well depths of 2.4 and 2.8 kcal/mol, respectively, at R_{N-C} distances around 3.6 Å. In this orientation, the silyl ion approaches a face of CF_4 perpendicularly to the scan axis and with the N atom in line with the C-F bond that is parallel to that axis.

The differences between the IPECs obtained by the B97-D and the fp-CCSD(T) calculations are only apparent in the inset graphs. In general, the B97-D potential energy curves are slightly more attractive than those obtained by the fp-CCSD(T) calculations. The largest discrepancies (in absolute values) in the well depths occur for orientations G and C (0.4 kcal/mol in both cases); the latter corresponds to $SiNCS^+$ approaching perpendicularly to one face of the

CF_4 molecule and with Si as the attacking atom. On average, the relative deviation between the fp-CCSD(T) and the B97-D well depths is 17.8%. For the repulsive part, we calculated average relative deviations of 6.2% and 8.9% for the energy ranges 10-100 and 100-1500 kcal/mol, respectively. Although these deviations are significant, the quality of the B97-D IPECs, as compared with the fp-CCSD(T) curves, is satisfactory, at least from a semiquantitative point of view. Also, as shown later, the errors in the fittings, in the best cases, are rather close to these values. For these reasons, we only employed the B97-D method for the $(CH_3)_2SiNCS^+/CF_4$ system, as well as for the systems involving the miniSAM model and for the parameterizations of the analytical potentials.

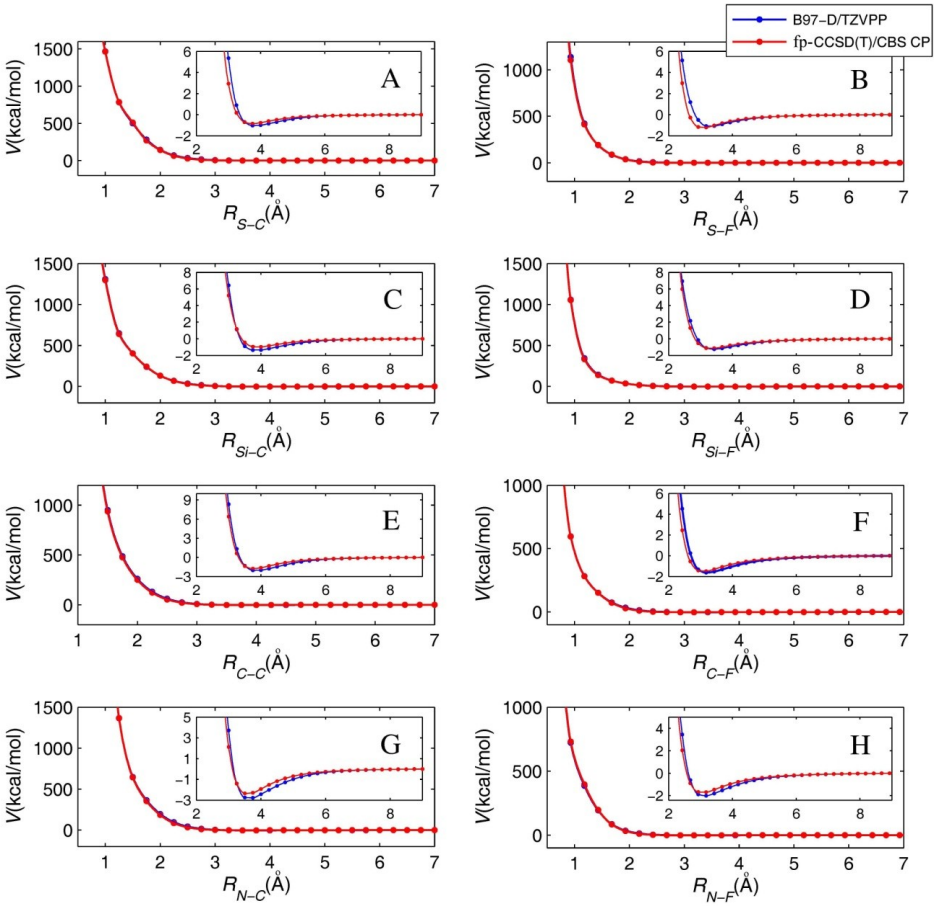

Figure 10.5: Comparison of the intermolecular potential energy curves of $SiNCS^+/CF_4$ calculated at the B97-D (blue circles) and fp-CCSD(T) (red circles) levels of theory. Lines are included for visual clarity.

Figure 10.6 depicts the B97-D potential energy curves for $(CH_3)_2SiNCS^+$ interacting with CF_4 in the 12 different orientations described in Figure 10.2. The most attractive interaction occurs for orientation G; this is one of the orientations in which $(CH_3)_2SiNCS^+$ approaches the CF_4 molecule with its symmetry axis perpendicularly to the scan axis. The well depth of the corresponding IPEC is 4.0 kcal/mol and the minimum is located at a N-C separation of 3.5 Å. Similarly, the IPECs of orientations C and D have well depths close to 4 kcal/mol. The IPECs of orientations A and B are very similar to those of the corresponding orientations (i.e., A and B) in the $SiNCS^+/CF_4$ system. This result could be anticipated because methyl groups are, in general, rather weak electron donors, and because in both orientations the silyl ion approaches the CF_4 molecule with its symmetry axis collinearly to one C-F bond and with the sulfur as the attacking atom.

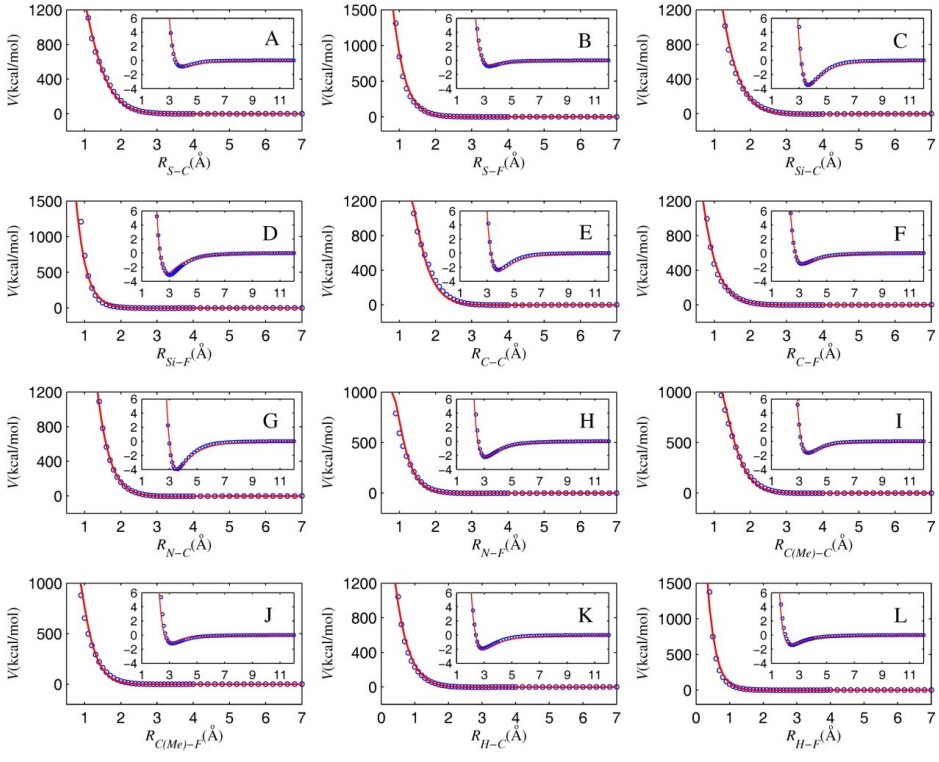

Figure 10.6: Intermolecular potential energy curves of $SiNCS^+/CF_4$ calculated at the B97-D/TZVPP level (open circles) and fit to equation 10.3 (red lines).

The IPECs obtained by the B97-D/TZVPP calculations for the $SiNCS^+$ and $(CH_3)_2SiNCS^+$ ions interacting with the miniSAM are shown in Figures 10.7 and 10.8, respectively. The intermolecular distance employed to

picture the IPECs in most plots (A-G, see also Figures 10.3 and 10.4) is defined as the distance between a selected atom of the silyl ion and the plane formed by the closest F-atom layer of the miniSAM. The selected atom is the one which is closest to the miniSAM, excluding hydrogen atoms in the case of $(CH_3)_2SiNCS^+$. For orientations in which the molecular axis of the silyl ion is perpendicular to the scan axis, all the atoms (except hydrogens) are at the same distance from the miniSAM. Negative values of R indicate penetration into the miniSAM. The distances used to depict the IPECs for orientation H in Figures 10.7 and 10.8 do not follow the above definition. In Figure 10.7, we considered the distance between the carbon atom of the silyl ion and the first carbon atom of the central chain of the miniSAM (see Figure 10.3), and in Figure 10.8 we used the distance between Si and the second C atom of the central chain (see Figure 10.4). As indicated before, we used the IPECs of orientation H for tests to assess the quality of the potentials but not for the fittings. For several orientations, the IPECs undulate in the region corresponding to negative values of R, which is associated with partial or even complete penetration of the silyl ion into the miniSAM structure. This type of behavior takes place especially in the $SiNCS^+$/miniSAM system because the shape of the ion facilitates the entrance into the miniSAM. For $(CH_3)_2SiNCS^+$, this feature occurs only for orientation D, in which the symmetry axis of the ion is collinear to the direction of attack and the sulfur atom approaches the surface first, so that partial penetration of the silyl ion into the surface is facilitated.

The well depths of the IPECs calculated at the B97-D/TZVPP level for the $SiNCS^+$/miniSAM system are in the range 2.8-8.8 kcal/mol. The highest depth (8.8 kcal/mol) is found for the test orientation H and occurs at a distance R_{C-C} of 6.6 Å. The IPEC of orientation C has also a substantial depth (7.9 kcal/mol at R = 1.4 Å). This orientation corresponds to $SiNCS^+$ directed toward a hole of the miniSAM, with the molecular axis collinear to the scan axis, and with Si as the attacking atom. Orientation D is similar, but the ion attacks the surface with the sulfur atom. The corresponding well depth is 4.6 kcal/mol (at R = 1.8 Å). Orientations E, F, and G, in which the ion approaches the surface with the molecular axis perpendicularly to the surface normal, have IPECs with depths in the range 6.6-6.9 kcal/mol and located at distances around 2.8 Å.

For $(CH_3)_2SiNCS^+$ interacting with the miniSAM, the B97-D calculations predict IPECs with well depths ranging from 2.2 kcal/mol, for orientation B, to 9.9 kcal/mol, for orientation E. Orientation G has also an IPEC with a significant depth (9.6 kcal/mol). Both orientations E and G involve configurations in which the ion approaches the surface with its symmetry axis perpendicular to the surface normal. According to the values of the calculated well depths it appears that the interaction between $(CH_3)_2SiNCS^+$ and the miniSAM in the attractive region is slightly stronger than that between $SiNCS^+$

and the miniSAM. This is qualitatively in line with the conclusion of Cooks and co-workers[1,5] mentioned in the Introduction, that inclusion of methyl groups increases the attractive intermolecular interaction with the monolayer. However, the differences in the strengths of the interactions of these two silyl ions with the miniSAM do not seem to be sufficiently marked to justify their different behavior for soft-landing observed experimentally.

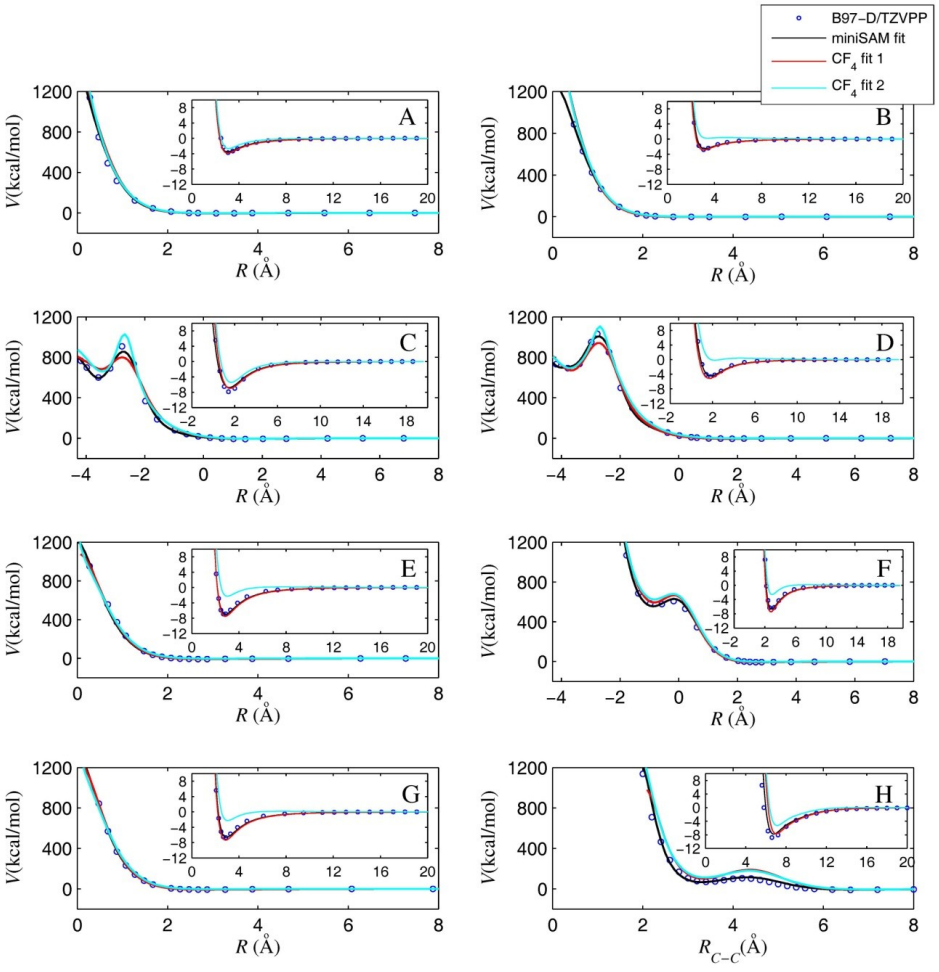

Figure 10.7: Intermolecular potential energy curves of $SiNCS^+$/miniSAM calculated at the B97-D/TZVPP level, fit to equation 10.3, and comparison with the IPECs obtained with equation 10.3 and the parameters listed in Table 10.1 (fit 1 for $SiNCS^+/CF_4$) and Table 10.2 (fit 2 for $SiNCS^+/CF_4$).

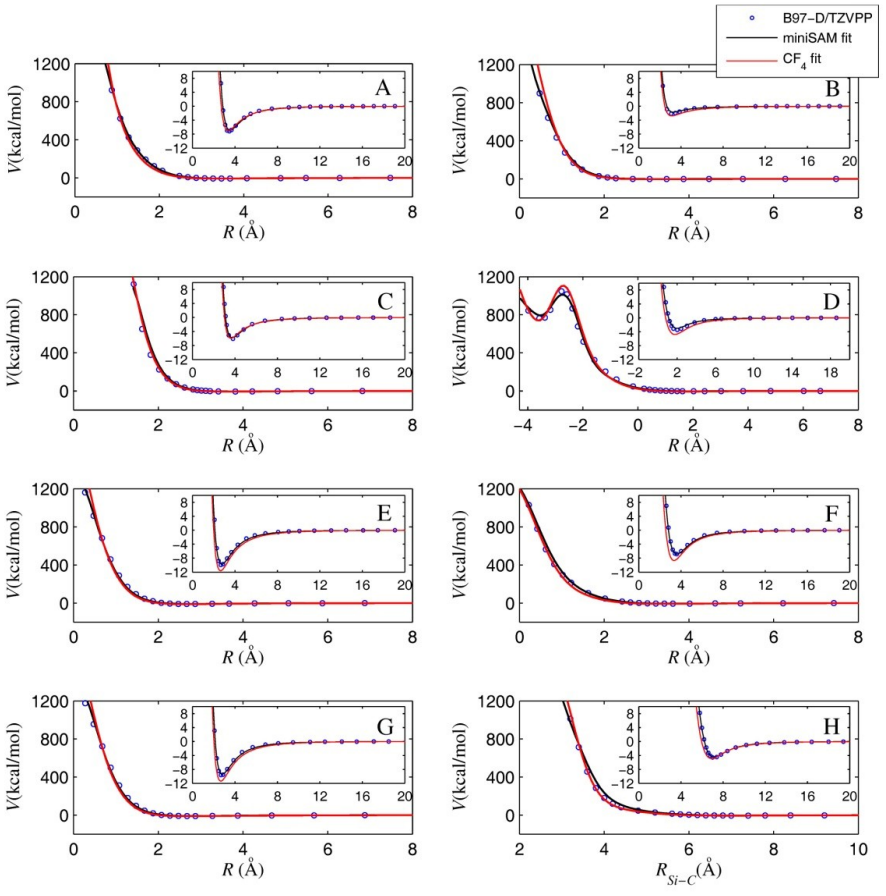

Figure 10.8: Intermolecular potential energy curves of $(CH_3)_2SiNCS^+$/miniSAM calculated at the B97-D/TZVPP level, fit to equation 10.3, and comparison with the IPECs obtained with equation 10.3 and the parameters listed in Table 10.5 (fit for $(CH_3)_2SiNCS^+/CF_4$).

3.2 Analytical potentials

The IPECs of the $SiNCS^+/CF_4$ system calculated at the B97-D/TZVPP level of theory were fitted to equations 10.3 and 10.4. The fits are shown graphically in Figure 10.9, in which the DFT data are represented as open circles. The solid lines in red correspond to the IPECs obtained with equation 10.3 and the parameters derived from fit 1, which are collected in Table 10.1. The lines in cyan were computed with the parameters derived from fit 2, which are listed in Table 10.2. The black lines are the interaction curves obtained from the fit to equation 10.4; the corresponding parameters are listed in Table 10.3 and the partial charges calculated with the Merz-Singh-Kolman approach[109,110] are shown in Figure 10.10. Errors associated with the fits were calculated as average values of energy deviations for the energy ranges of 10-

100 and 100-1500 kcal/mol, and for the well depths. The most remarkable result is that the latter potential energy function, that is, the combination of a Lennard-Jones type potential and an electrostatic term, is unable to accurately model the whole range of interaction energies investigated in this study. Specifically, the average errors for the well depths and for the energy ranges 10-100 and 100-1500 kcal/mol are 58.4%, 92.1%, and 58.6%, respectively. For fit 1, the average errors for the well depths and for the energy range 10-100 kcal/mol are about 9%, and that for the energy range 100-1500 kcal/mol is 6.2%. As seen in Table 10.3, the values of the parameters obtained for equation 10.4 correspond to limit values imposed in the parameterization procedure. Specifically, all *B* values are equal to 8, the lower limit considered in this work; all *C* values are zero, except for the N-C and C-C pair potentials but the associated *D* values are 5, which is the lower limit set for this exponent. This result suggests that there is an intrinsic limitation in the applicability of equation 10.4 to the systems investigated here. The performance of this type of potentials could be improved if an electrostatic damping factor is introduced to correct the unphysical behavior of the electrostatic term at short distances.[112] We notice that electrostatic damping factors are not used in most force fields implemented in molecular dynamics programs because the conditions employed in typical simulations do not lead to configurations of high energy repulsions. In fact, the usual force fields are parameterized to represent as accurately as possible the attractive regions only. Because potentials written in the form of equation 10.3 give good agreement with the B97-D IPECs, as shown in Figure 10.9, we decided to use them here rather than using potentials based on equation 10.4. It is interesting to note that the fit to equation 10.3 performed under the constraints detailed in Section 2.2 (i.e., fit 1) is practically as good as that conducted without constraints. The errors for fit 2 are only slightly (≈2%) smaller than those of fit 1. Also worth noting is the result that the fit made without constraints led to some parameters whose values are far from typical ranges of exponents in analytical functions representing intermolecular interactions. The most acute example is the value of 19.791 obtained for the *D* parameter corresponding to the S-F pair potential.

One of the objectives of this study was to test whether CF_4 can be used as a good model of an F-SAM surface for parameterization purposes. To this end, we calculated IPECs for the eight orientations of the $SiNCS^+$/miniSAM interacting system, using the analytical function given by equation 10.3 and the parameters listed in Tables 10.1 and 10.2, and we compared them with the IPECs predicted with the B97-D method, shown as open circles in Figure 10.7. Two remarkable results are apparent from this comparison. First, the parameters obtained from fit 1 (Table 10.1) are transferable to the $SiNCS^+$/miniSAM system, since the IPECs calculated with

them (red lines in Figure 10.7) agree reasonably well with the B97-D curves; the largest deviations (25.5%), obtained for the energy range 10-100 kcal/mol, are acceptable for qualitative or semiquantitative purposes. And second, the IPECs calculated with the parameters obtained from fit 2 in the $SiNCS^+/CF_4$ system (cyan lines) show significant disagreement with the B97-D curves. In particular, the average deviation for the well depths amounts 62.5%, whereas that for fit 1 is 8.4%. Therefore, for parameterization purposes, CF_4 may be used as a model of F-SAM, provided some care is taken in the parameterization conditions. For completeness, we fitted the B97-D curves calculated for the $SiNCS^+$/miniSAM system to equation 10.3, using the same constraints imposed in fit 1 for $SiNCS^+/CF_4$. The fit led to the set of parameters listed in Table 10.4 and the black lines depicted in Figure 10.7. For this fit, the largest average deviation (12.2%) was obtained for the energy range 10-100 kcal/mol. It can be seen that the IPECs computed with this potential agree quite well with those obtained with the set of parameters of Table 10.1 (red lines), derived using the $SiNCS^+/CF_4$ system. The most significant deviations appear in regions, at negative values of R, where undulations are exhibited.

Table 10.1. Parameters of equation 10.3 obtained from fit 1 for $SiNCS^+/CF_4$[a]

	A	*B*	*C*	*D*	*E*	*F*
Si-C	6538.188	2.434	-	-	-	-
Si-F	18138.253	3.131	-196.303	4.368	-	-
N-C	101627.865	4.648	-	-	-1466.543	5.908
N-F	33037.375	3.463	-113.072	5.000	-452.264	5.546
C-C	4463.786	2.274	-	-	-671.679	7.000
C-F	6979.581	3.018	-	-	-8.469	6.012
S-C	8789.758	2.525	-8.005	5.000	-49.946	5.215
S-F	27383.103	3.308	-163.076	4.652	-115.340	5.000

[a]The units are such that the potential is in kcal/mol and distances in Å.

Table 10.2. Parameters of equation 10.3 obtained from fit 2 for $SiNCS^+/CF_4$.[a]

	A	*B*	*C*	*D*	*E*	*F*
Si-C	11154.135	2.602	1693.381	11.737	-1767.434	8.623
Si-F	14675.277	2.966	299.087	13.523	-339.363	4.679
N-C	8259.926	4.153	2864.545	11.736	-729.107	5.456
N-F	23014.401	3.212	1055.419	5.765	-1493.217	5.302
C-C	16148.397	3.159	8807.686	4.860	-10507.434	5.179
C-F	10273.754	3.031	504.412	6.811	-688.895	5.936
S-C	184993.405	8.015	2379.662	4.972	-1783.814	6.017
S-F	33002.435	3.241	156.028	19.791	-667.150	4.782

[a]The units are such that the potential is in kcal/mol and distances in Å.

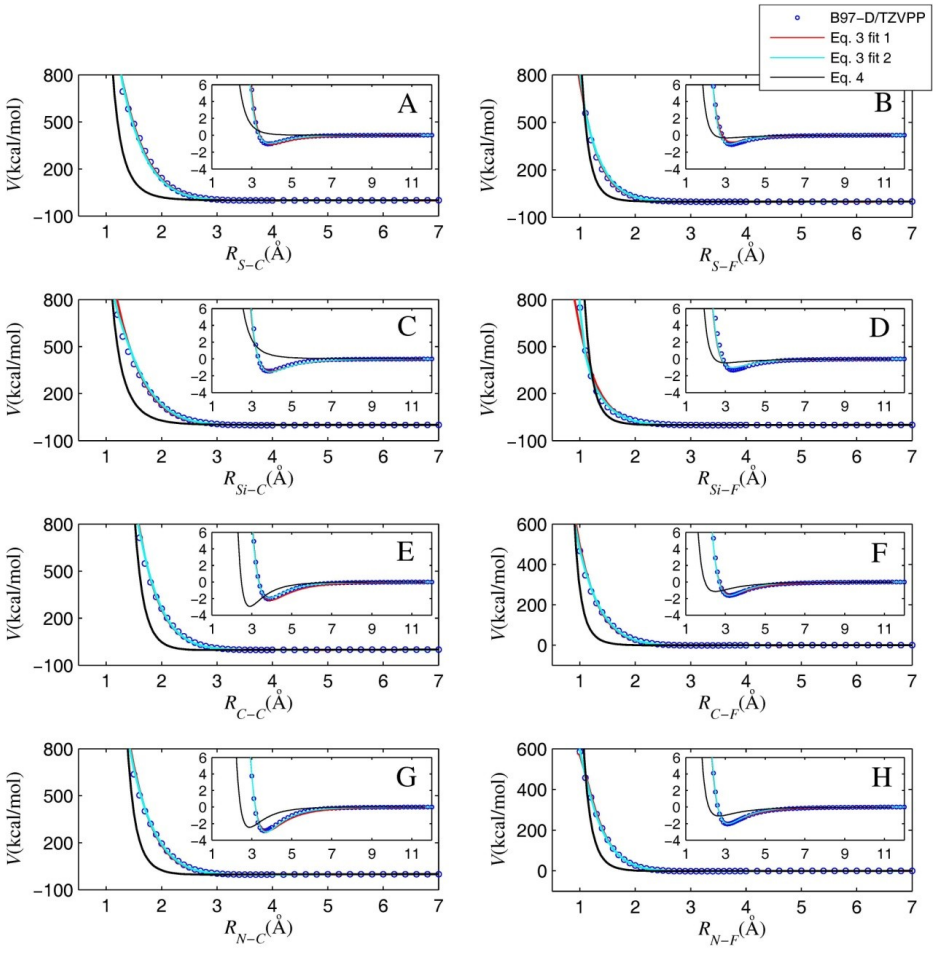

Figure 10.9: Intermolecular potential energy curves of $SiNCS^+/CF_4$ calculated at the B97-D/TZVPP level and fits to equations 10.3 and 10.4. See text.

Table 10.3. Parameters of equation 10.4 obtained for the $SiNCS^+/CF_4$ system.[a]

	A	*B*	*C*	*D*
Si-C	1082.545	8.000	-	-
Si-F	1547.894	8.000	-	-
N-C	5560.997	8.000	-800.000	5.000
N-F	1010.489	8.000	-	-
C-C	12764.578	8.000	-1143.714	5.000
C-F	245.054	8.000	-	-
S-C	1470.957	8.000	-	-
S-F	1062.301	8.000	-	-

[a]The units are such that the potential is in kcal/mol and distances in Å.

Table 10.4. Parameters of equation 10.4 obtained for the $SiNCS^+$/miniSAM system.[a]

	A	*B*	*C*	*D*	*E*	*F*
Si-C_3	18534.817	2.382	-564.543	4.537	-22.199	6.405
Si-C_2	64855.770	3.008	-223.620	4.486	-437.059	5.522
Si-F_3	23491.237	3.496	-126.166	4.800	-448.122	6.137
Si-F_2	23913.193	3.488	-89.798	4.581	-0.205	6.888
N-C_3	27551.371	3.687	-65.528	4.567	-956.760	5.760
N-C_2	31397.593	3.982	-313.098	4.935	-1038.343	6.187
N-F_3	35624.283	3.672	-150.146	4.953	-293.498	6.225
N-F_2	68943.696	4.558	-93.177	4.999	-229.920	6.328
C-C_3	18372.699	3.152	-37.022	4.751	-554.617	5.635
C-C_2	22315.273	3.481	-8.033	4.090	-381.924	5.992
C-F_3	5311.952	2.710	-7.966	4.574	-0.819	5.955
C-F_2	30400.976	3.348	-0.884	4.928	-600.325	5.829
S-C_3	34713.238	3.849	-125.240	4.518	-580.811	5.893
S-C_2	66403.057	4.485	-609.191	4.974	-1709.718	6.957
S-F_3	22734.176	3.083	-78.161	4.767	-238.581	5.252
S-F_2	73637.242	4.036	-2.673	4.848	-472.422	6.108

[a]The units are such that the potential is in kcal/mol and distances in Å. Subscripts 2 and 3 refer to perfluoromethylene and perfluoromethyl atoms, respectively.

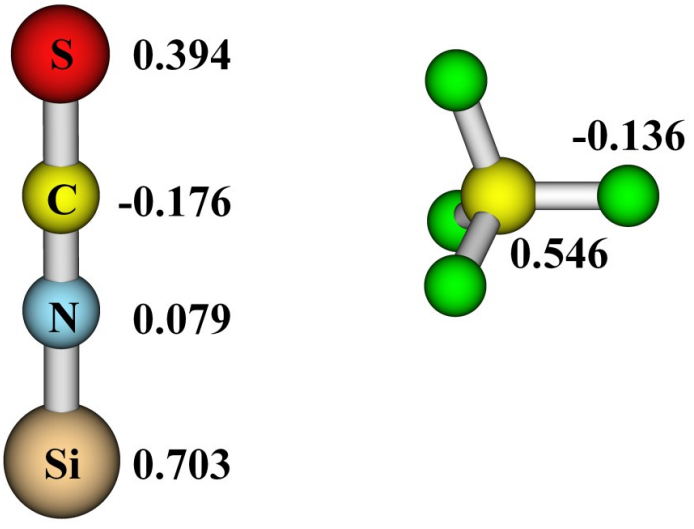

Figure 10.10: Partial atomic charges (in a.u.) calculated at the B97-D/TZVPP level and using the Merz-Singh-Kolman scheme.

For the $(CH_3)_2SiNCS^+/CF_4$ system, the fit of the B97-D data to equation 10.3 is shown graphically in Figure 10.6 and the parameters are listed in Table 10.5. As can be seen, for all the orientations described in Figure 10.2, the analytical potential gives IPECs (red lines) in good agreement with the

B97-D curves (open circles). The largest average error of the fit is 14.3%, and corresponds to the energy range 10-100 kcal/mol. Using the parameters of Table 10.5, we calculated IPECs for $(CH_3)_2SiNCS^+$ interacting with the miniSAM for all the orientations of Figure 10.4, and we compared them, in Figure 10.8, with the IPECs determined at the B97-D level of theory. We also performed a fit of the B97-D curves of the $(CH_3)_2SiNCS^+$/miniSAM system to equation 10.3 (orientation H was not used in the fitting), which led to the black lines in Figure 10.8 and the parameters reported in Table 10.6. From the comparison, it is clear that the analytical potential derived from the $(CH_3)_2SiNCS^+/CF_4$ fit is in rather good agreement with that obtained from the $(CH_3)_2SiNCS^+$/miniSAM fit, and both potentials reproduce the B97-D IPECs of the $(CH_3)_2SiNCS^+$/miniSAM system reasonably well. The largest differences between the well depths computed with equation 10.3 and the parameters of Table 10.5 and those calculated at the B97-D level are less than 2 kcal/mol, and correspond to orientations E, F, and G. These results, therefore, corroborate that CF_4 may be a valid model for developing intermolecular potentials for interactions of gases with F-SAM surfaces.

Table 10.5. Parameters of equation 10.3 derived for the $(CH_3)_2SiNCS^+/CF_4$ system.[a]

	A	*B*	*C*	*D*	*E*	*F*
Si-C	13513.187	2.462	-3.163	4.342	-6.819	5.210
Si-F	28382.750	3.868	-45.367	3.938	-	-
N-C	162748.891	4.302	-169.184	4.801	-2022.234	5.407
N-F	35890.509	3.603	-39.288	4.936	-302.611	5.452
C-C	4331.934	2.279	-1.030	4.847	-1699.847	6.721
C-F	6942.115	2.924	-	-	-	-
S-C	7848.930	2.419	-64.457	4.837	-99.473	5.209
S-F	31990.682	3.427	-106.739	4.487	-70.368	5.002
C(Me)-C	29243.460	3.024	-1.766	3.980	-1475.676	5.856
C(Me)-F	35473.244	3.631	-42.585	4.763	-269.543	5.293
H-C	2338.852	2.891	-	-	-	-
H-F	5405.861	4.137	-	-	-	-

[a]The units are such that the potential is in kcal/mol and distances in Å.

Table 10.6. Parameters of equation 10.3 derived for the $(CH_3)_2SiNCS^+$/miniSAM system.[a]

	A	*B*	*C*	*D*	*E*	*F*
Si-C_3	17465.327	2.427	-108.231	4.686	-571.057	6.558
Si-C_2	2299.708	4.010	-117.265	4.875	-58.430	6.478
Si-F_3	32868.276	3.352	-169.112	4.614	-822.938	6.010
Si-F_2	25024.365	2.237	-4.114	4.811	-1549.042	6.793
N-C_3	27551.371	3.687	-65.528	4.567	-956.760	5.760
N-C_2	31397.593	3.982	-313.098	4.935	-1038.343	6.187
N-F_3	35624.283	3.672	-150.146	4.953	-293.498	6.225
N-F_2	68943.696	4.558	-93.177	4.999	-229.920	6.328
C-C_3	18372.699	3.152	-37.022	4.751	-554.617	5.635
C-C_2	22315.273	3.481	-8.033	4.090	-381.924	5.992
C-F_3	5311.952	2.710	-7.966	4.574	-0.819	5.955
C-F_2	30400.976	3.348	-0.884	4.928	-600.325	5.829
S-C_3	75661.708	4.015	-18.972	4.046	-446.308	5.855
S-C_2	39070.416	4.814	-172.163	4.860	-1143.539	6.634
S-F_3	33856.220	3.213	-16.978	4.748	-932.123	6.175
S-F_2	59061.975	3.906	-5.893	4.305	-368.737	6.128
C(Me)-C_3	18481.512	4.717	-79.827	4.548	-1688.458	6.224
C(Me)-C_2	75083.448	4.801	-148.959	4.987	-1021.178	5.948
C(Me)-F_3	35578.422	3.288	-20.297	4.997	-1679.091	6.451
C(Me)-F_2	48902.266	3.872	-0.801	4.070	-1681.831	6.564
H-C_3	2836.462	2.446	-7.255	4.874	-1022.163	6.637
H-C_2	16995.767	4.913	-32.338	4.483	-329.418	5.948
H-F_3	9090.716	4.573	-0.195	3.582	-5.986	5.404
H-F_2	3415.155	2.972	-6.437	4.300	-7.623	5.199

[a]The units are such that the potential is in kcal/mol and distances in Å. Subscripts 2 and 3 refer to perfluoromethylene and perfluoromethyl atoms, respectively.

4. CONCLUSIONS

Molecular structure calculations were performed to compute intermolecular potential energy curves for interaction of $SiNCS^+$ and $(CH_3)_2SiNCS^+$ ions with CF_4 and with nine chains of perfluorobutane, which constitute a reliable model of an F-SAM surface for parameterizing intermolecular potentials. For the $SiNCS^+/CF_4$ system, the B97-D/TZVPP level of theory gives IPECs in reasonable agreement with fp-CCSD(T)/CBS calculations, which validates the use of the DFT-D method for the purposes of the present investigation.

The comparison between the B97-D IPECs calculated for the $SiNCS^+$/miniSAM system and those computed for $(CH_3)_2SiNCS^+$/miniSAM

shows, as expected, that inclusion of the methyl groups results, on average, in a slightly more attractive interaction in the well region. However, because the differences in the interaction strengths are rather small, there may be other factors that account for the contrasting behavior of these two ions for soft-landing onto F-SAM surfaces. For example, (i) entrapment of $(CH_3)_2SiNCS^+$ ions due to the methyl groups, as suggested by Cooks and co-workers;[1,5] (ii) additional degrees of freedom for $(CH_3)_2SiNCS^+$ (in particular the two rotors) may result in it receiving more internal energy and thus decreasing the amount in the projectile's translation as it scatters off the surface, which will increase the soft-landing efficiency; (iii) a much higher probability of ion neutralization for $SiNCS^+$, provided the ions can easily penetrate into the monolayer and approach the gold surface. All these possible factors will be investigated in future work.

Intermolecular pairwise potentials were parameterized by fits to the B97-D IPECs. The present study shows that, for the whole range of energies investigated, the B97-D IPECs calculated for interactions of silyl ions with CF_4 and the miniSAM cannot be accurately fitted to a combination of a Lennard-Jones type of potential and an electrostatic term for point charges. The analytical potentials given by equation 10.3 and the parameters obtained from the fits performed on the $SiNCS^+/CF_4$ and $(CH_3)_2SiNCS^+/CF_4$ systems can reproduce the B97-D IPECs calculated for the interaction of the silyl ions with the miniSAM. This supports the use of CF_4 as a simple, yet valid model of F-SAM for developing intermolecular potentials for interactions of gases with F-SAM surfaces. The intermolecular potentials derived here will be used, in future work, for exploring the dynamics of collisions and soft-landing of these silyl ions with a self-assembled monolayer surface of perfluorinated alkanethiols. Finally, we emphasize that, due to the complexity of this kind of systems, the use of fitting tools based on genetic algorithms are extremely valuable to obtain a good set of potential parameters.

REFERENCES

(1) Miller, S. A.; Luo, H.; Pachuta, S. J.; Cooks, R. G. *Science* **1997**, *275*, 1447-1450.

(2) Laskin, J.; Wang, P.; Hadjar, O. *Physical Chemistry Chemical Physics* **2008**, *10*, 1079-1090.

(3) Gologan, B.; Green, J. R.; Alvarez, J.; Laskin, J.; Graham Cooks, R. *Physical Chemistry Chemical Physics* **2005**, *7*, 1490-1500.

(4) Gologan, B.; Wiseman, J. M.; Cooks, R. G. *In: Laskin J, Lifshitz C (ed) Ion soft landing: instrumentation, phenomena, and applications*; John Wiley & Sons., Inc.: Hoboken, New Jersey, 2006.

(5) Luo, H.; Miller, S. A.; Cooks, R. G.; Pachuta, S. J. *International Journal of Mass Spectrometry and Ion Processes* **1998**, *174*, 193-217.

(6) Shen, J.; Yim, Y. H.; Feng, B.; Grill, V.; Evans, C.; Cooks, R. G. *International Journal of Mass Spectrometry* **1999**, *182-183*, 423-435.

(7) Wijesundara, M. B. J.; Hanley, L.; Ni, B.; Sinnott, S. B. *Proceedings of the National Academy of Sciences of the United States of America* **2000**, *97*, 23-27.

(8) Wijesundara, M. B. J.; Fuoco, E.; Hanley, L. *Langmuir* **2001**, *17*, 5721-5726.

(9) Volny, M.; Sengupta, A.; Wilson, C. B.; Swanson, B. D.; Davis, E. J.; Turecek, F. *Analytical Chemistry* **2007**, *79*, 4543-4551.

(10) Rauschenbach, S.; Vogelgesang, R.; Malinowski, N.; Gerlach, J. r. W.; Benyoucef, M.; Costantini, G.; Deng, Z.; Thontasen, N.; Kern, K. *ACS Nano* **2009**, *3*, 2901-2910.

(11) Nie, Z.; Li, G.; Goodwin, M. P.; Gao, L.; Cyriac, J.; Cooks, R. G. *Journal of the American Society for Mass Spectrometry* **2009**, *20*, 949-956.

(12) Miller, S. A.; Luo, H.; Jiang, X.; Rohrs, H. W.; Cooks, R. G. *International Journal of Mass Spectrometry and Ion Processes* **1997**, *160*, 83-105.

(13) Kaiser, B.; Bernhardt, T. M.; Stegemann, B.; Opitz, J.; Rademann, K. *Physical Review Letters* **1999**, *83*, 2918.

(14) Yamaguchi, W.; Yoshimura, K.; Tai, Y.; Maruyama, Y.; Igarashi, K.; Tanemura, S.; Murakami, J. *Chemical Physics Letters* **1999**, *311*, 341-345.

(15) Messerli, S.; Schintke, S.; Morgenstern, K.; Sanchez, A.; Heiz, U.; Schneider, W.-D. *Surface Science* **2000**, *465*, 331-338.

(16) Mitsui, M.; Nagaoka, S.; Matsumoto, T.; Nakajima, A. *The Journal of Physical Chemistry B* **2006**, *110*, 2968-2971.

(17) Claeyssens, F.; Pratontep, S.; Xirouchaki, C.; Palmer, R. E. *Nanotechnology* **2006**, *17*, 805.

(18) Nanita, S. C.; Takats, Z.; Cooks, R. G.; Myung, S.; Clemmer, D. E. *Journal of the American Society for Mass Spectrometry* **2004**, *15*, 1360-1365.

(19) Nagaoka, S.; Ikemoto, K.; Matsumoto, T.; Mitsui, M.; Nakajima, A. *The Journal of Physical Chemistry C* **2008**, *112*, 6891-6899.

(20) Nagaoka, S.; Ikemoto, K.; Matsumoto, T.; Mitsui, M.; Nakajima, A. *The Journal of Physical Chemistry C* **2008**, *112*, 15824-15831.

(21) Matsumoto, T.; Nagaoka, S.; Ikemoto, K.; Mitsui, M.; Ara, M.; Tada, H.; Nakajima, A. *Eur. Phys. J. D* **2009**, *52*, 99-102.

(22) Laskin, J.; Wang, P.; Hadjar, O. *The Journal of Physical Chemistry C* **2010**, *114*, 5305-5311.

(23) Johnson, G. E.; Lysonski, M.; Laskin, J. *Analytical Chemistry* **2010**, *82*, 5718-5727.

(24) Ikemoto, K.; Nagaoka, S.; Matsumoto, T.; Mitsui, M.; Nakajima, A. *The Journal of Physical Chemistry C* **2009**, *113*, 4476-4482.

(25) Gologan, B.; Takáts, Z.; Alvarez, J.; Wiseman, J. M.; Talaty, N.; Ouyang, Z.; Cooks, R. G. *Journal of the American Society for Mass Spectrometry* **2004**, *15*, 1874-1884.

(26) Alvarez, J.; Cooks, R. G.; Barlow, S. E.; Gaspar, D. J.; Futrell, J. H.; Laskin, J. *Analytical Chemistry* **2005**, *77*, 3452.

(27) Alvarez, J.; Futrell, J. H.; Laskin, J. *J. Phys. Chem. A* **2006**, *110*, 1678.

(28) Volny, M.; Elam, W. T.; Ratner, B. D.; Turecek, F. *Analytical Chemistry* **2005**, *77*, 4846-4853.

(29) Wang, P.; Laskin, J. *Angewandte Chemie International Edition* **2008**, *47*, 6678-6680.

(30) Hadjar, O.; Wang, P.; Futrell, J. H.; Laskin, J. *Journal of the American Society for Mass Spectrometry* **2009**, *20*, 901-906.

(31) Ouyang, Z.; Takats, Z.; Blake, T. A.; Gologan, B.; Guymon, A. J.; Wiseman, J. M.; Oliver, J. C.; Davisson, V. J.; Cooks, R. G. *Science* **2003**, *301*, 1351-1354.

(32) Volny, M.; Elam, W. T.; Branca, A.; Ratner, B. D.; Turecek, F. *Analytical Chemistry* **2005**, *77*, 4890-4896.

(33) Feng, B.; Wunschel, D. S.; Masselon, C. D.; Pasa-Tolic, L.; Smith, R. D. *Journal of the American Chemical Society* **1999**, *121*, 8961-8962.

(34) Siuzdak, G.; Bothner, B.; Yeager, M.; Brugidou, C.; Fauquet, C. M.; Hoey, K.; Change, C.-M. *Chemistry & Biology* **1996**, *3*, 45.

(35) Fenselau, C.; Demirev, P. A. *Mass Spectrometry Reviews* **2001**, *20*, 157-171.

(36) Love, J. C.; Estroff, L. A.; Kriebel, J. K.; Nuzzo, R. G.; Whitesides, G. M. *Chemical Reviews* **2005**, *105*, 1103.

(37) Alexander, W. A.; Day, B. S.; Moore, H. J.; Lee, T. R.; Morris, J. R.; Troya, D. *Journal of Chemical Physics* **2008**, *128*, 014713.

(38) Troya, D.; Schatz, G. C. *J. Chem. Phys.* **2004**, *120*, 7696.

(39) Yan, T.; Hase, W. L. *Phys. Chem. Chem. Phys* **2000**, *2*, 901.

(40) Yan, T.; Hase, W. L.; Barker, J. R. *Chem. Phys. Lett.* **2000**, *329*, 84.

(41) Yan, T.; Hase, W. L. *J. Phys. Chem. B* **2002**, *106*, 8029.

(42) Yan, T.; Isa, N.; Gibson, K. D.; Sibener, S. J.; Hase, W. L. *J. Phys. Chem. A* **2003**, *107*, 10600.

(43) Yan, T.; Hase, W. L. *J. Phys. Chem. A* **2001**, *105*, 2617.

(44) Day, B. S.; Morris, J. R.; Troya, D. *J. Chem. Phys.* **2005**, *122*, 214712.

(45) Day, B. S.; Morris, J. R.; Alexander, W. A.; Troya, D. *J. Phys. Chem. A* **2006**, *110*, 1319.

(46) Li, G.; Bosio, S. B. M.; Hase, W. L. *J. Mol. Struc.* **2000**, *556*, 43.

(47) Tasic, U. S.; Yan, T.; Hase, W. L. *J. Phys. Chem. B* **2006**, *110*, 11863.

(48) Martínez-Núñez, E.; Rahaman, A.; Hase, W. L. *J. Phys. Chem. C* **2007**, *111*, 354.

(49) Meroueh, O.; Hase, W. L. *Phys. Chem. Chem. Phys* **2001**, *3*, 2306.

(50) Vázquez, S. A.; Morris, J. R.; Rahaman, A.; Mazyar, O. A.; Vayner, G.; Addepalli, S. V.; Hase, W. L.; Martínez-Núñez, E. *J. Phys. Chem. A* **2007**, *111*, 12785.

(51) Tasic, U.; Troya, D. *Physical Chemistry Chemical Physics* **2008**, *10*, 5776-5786.

(52) Alexander, W. A.; Morris, J. R.; Troya, D. *Journal of Physical Chemistry A* **2009**, *113*, 4155-4167.

(53) Alexander, W. A.; Morris, J. R.; Troya, D. *Journal of Chemical Physics* **2009**, *130*, 084702.

(54) Layfield, J. P.; Troya, D. *Journal of Chemical Physics* **2010**, *132*, 134307.

(55) Meroueh, O.; Hase, W. L. *J. Am. Chem. Soc.* **2002**, *124*, 1524.

(56) Yang, L.; Mazyar, O. A.; Lourderaj, U.; Wang, J.; Rodgers, M. T.; Martínez-Núñez, E.; Addepalli, S. V.; Hase, W. L. *J. Phys. Chem. C* **2008**, *112*, 9377-9386.

(57) Barnes, G. L.; Hase, W. L. *Journal of the American Chemical Society* **2009**, *131*, 17185-17193.

(58) Bosio, S. B. M.; Hase, W. L. *J. Chem. Phys.* **1997**, *107*, 9677.

(59) Nogueira, J. J.; Vázquez, S. A.; Mazyar, O. A.; Hase, W. L.; Perkins Jr., B. G.; Nesbitt, D. J.; Martínez-Núñez, E. *J. Phys. Chem. A* **2009**, *113*, 3850-3865.

(60) Nogueira, J. J.; Vazquez, S. A.; Lourderaj, U.; Hase, W. L.; Martinez-Nunez, E. *The Journal of Physical Chemistry C* **2010**, *114*, 18455-18464.

(61) Buckingham, R. A. *Proceedings of the Royal Society of London A: Mathematical and Physical Sciences* **1938**, *168*, 264-283.

(62) Jones, J. E. *Proceedings of the Royal Society of London A: Mathematical and Physical Sciences* **1924**, *106*, 463-477.

(63) Kaplan, I. G. *Intermolecular Interactions: Physical Picture, Computational Methods and Model Potentials*; JohnWiley&Sons, Ltd.: Chichester, 2006.

(64) Vayner, G.; Alexeev, Y.; Wang, J.; Windus, T. L.; Hase, W. L. *The Journal of Physical Chemistry A* **2005**, *110*, 3174-3178.

(65) Wang, J.; Hase, W. L. *The Journal of Physical Chemistry B* **2005**, *109*, 8320-8324.

(66) Alexander, W. A.; Troya, D. *The Journal of Physical Chemistry A* **2006**, *110*, 10834-10843.

(67) Deb, B.; Hu, W.; Song, K.; Hase, W. L. *Physical Chemistry Chemical Physics* **2008**, *10*, 4565-4572.

(68) Tasic, U.; Hein, P.; Troya, D. *The Journal of Physical Chemistry A* **2007**, *111*, 3618-3632.

(69) Bader, R. F. W. *Atoms in Molecules: A Quantum Theory*; Oxford University Press: Oxford, UK, 1990.

(70) Bader, R. F. W. *Chemical Reviews* **1991**, *91*, 893.

(71) Quiñónez, P. B.; Vila, A.; Graña, A. M.; Mosquera, R. A. *Chemical Physics* **2003**, *287*, 227-236.

(72) Vila, A.; Mosquera, R. A. *The Journal of Physical Chemistry A* **2006**, *110*, 11752-11759.

(73) Wiberg, K. B.; Bader, R. F. W.; Lau, C. D. H. *Journal of the American Chemical Society* **1987**, *109*, 985-1001.

(74) Bader, R. F. W.; Carroll, M. T.; Cheeseman, J. R.; Chang, C. *Journal of the American Chemical Society* **1987**, *109*, 7968-7979.

(75) Lorenzo, L.; Mosquera, R. A. *Chemical Physics Letters* **2002**, *356*, 305-312.

(76) Boys, S. F.; Bernardi, F. *Molecular Physics* **1970**, *19*, 553 - 566.

(77) Simon, S.; Duran, M.; Dannenberg, J. J. *The Journal of Chemical Physics* **1996**, *105*, 11024-11031.

(78) Pople, J. A.; Head-Gordon, M.; Raghavachari, K. *The Journal of Chemical Physics* **1987**, *87*, 5968-5975.

(79) Martin, J. M. L. *Chemical Physics Letters* **1996**, *259*, 669-678.

(80) Halkier, A.; Helgaker, T.; Jørgensen, P.; Klopper, W.; Koch, H.; Olsen, J.; Wilson, A. K. *Chemical Physics Letters* **1998**, *286*, 243-252.

(81) Kirk, A. P.; David, E. W.; Thom H. Dunning, Jr. *The Journal of Chemical Physics* **1994**, *100*, 7410-7415.

(82) Truhlar, D. G. *Chemical Physics Letters* **1998**, *294*, 45-48.

(83) Schwenke, D. W. *The Journal of Chemical Physics* **2005**, *122*, 014107.

(84) Varandas, A. J. C. *The Journal of Chemical Physics* **2007**, *126*, 244105-15.

(85) Bakowies, D. *The Journal of Chemical Physics* **2007**, *127*, 164109-12.

(86) Hill, J. G.; Peterson, K. A.; Knizia, G.; Werner, H.-J. *The Journal of Chemical Physics* **2009**, *131*, 194105-13.

(87) Helgaker, T.; Klopper, W.; Tew, D. P. *Molecular Physics* **2008**, *106*, 2107 - 2143.

(88) Peterson, K. A.; Woon, D. E.; DunningT.H, Jr. *J. Chem. Phys.* **1994**, *100*, 7410.

(89) East, A. L. L.; Allen, W. D. *The Journal of Chemical Physics* **1993**, *99*, 4638-4650.

(90) Wladkowski, B. D.; Allen, W. D.; Brauman, J. I. *The Journal of Physical Chemistry* **1994**, *98*, 13532-13540.

(91) Csaszar, A. G.; Allen, W. D.; Schaefer III, H. F. *The Journal of Chemical Physics* **1998**, *108*, 9751-9764.

(92) Bartlett, R. J.; Silver, D. M. *Physical Review A* **1974**, *10*, 1927.

(93) Binkley, J. S.; Pople, J. A. *International Journal of Quantum Chemistry* **1975**, *9*, 229-236.

(94) Parr, R. G.; Yang, W. *Density-Functional Theory of Atoms and Molecules, International Series of Monographs on Chemistry Vol. 16*; Oxford University Press: New York, 1989.

(95) Sherrill, C. D. *The Journal of Chemical Physics* **2010**, *132*, 110902-7.

(96) Ahlrichs, R.; Bär, M.; Häser, M.; Horn, H.; Kölmel, C. *Chemical Physics Letters* **1989**, *162*, 165-169.

(97) Vahtras, O.; Almlöf, J.; Feyereisen, M. W. *Chemical Physics Letters* **1993**, *213*, 514-518.

(98) Feyereisen, M.; Fitzgerald, G.; Komornicki, A. *Chemical Physics Letters* **1993**, *208*, 359-363.

(99) Kendall, R. A.; Dunning, J. T. H.; Harrison, R. J. *The Journal of Chemical Physics* **1992**, *96*, 6796-6806.

(100) Weigend, F.; Häser, M.; Patzelt, H.; Ahlrichs, R. *Chemical Physics Letters* **1998**, *294*, 143-152.

(101) Grimme, S. *Journal of Computational Chemistry* **2004**, *25*, 1463-1473.

(102) Grimme, S. *Journal of Computational Chemistry* **2006**, *27*, 1787-1799.

(103) Eichkorn, K.; Treutler, O.; Ohm, H.; Haser, M.; Ahlrichs, R. *Chemical Physics Letters* **1995**, *240*, 283-289.

(104) Vázquez-Mayagoitia, A.; Sherrill, C. D.; Aprà, E.; Sumpter, B. G. *Journal of Chemical Theory and Computation* **2010**, *6*, 727-734.

(105) Borodin, O.; Smith, G. D.; Bedrov, D. *J. Phys. Chem. B* **2002**, *106*, 9912.

(106) Hase, W. L.; Venus 2005 ed.; Texas Tech University: 2005.

(107) Hu, X.; Hase, W. L.; Pirraglia, T. *Journal of Computational Chemistry* **1991**, *12*, 1014-1024.

(108) Marques, J. M. C.; Prudente, F. V.; Pereira, F. B.; Almeida, M. M.; Maniero, A. M.; Fellows, C. E. *Journal of Physics B: Atomic, Molecular and Optical Physics* **2008**, *41*, 085103.

(109) Besler, B. H.; Merz, K. M.; Kollman, P. A. *Journal of Computational Chemistry* **1990**, *11*, 431-439.

(110) Singh, U. C.; Kollman, P. A. *Journal of Computational Chemistry* **1984**, *5*, 129-145.

(111) Frisch, M. J. T., G. W.; Schlegel, H. B.; Scuseria, G. E.; Robb, M. A.; Cheeseman, J. R.; Montgomery, J. A., Jr.; Kudin, K. N.; Burant, J. C.; Millam, J. M.; Iyengar, S. S.; Tomasi, J.; Barone, V.; Mennucci, B.; Cossi, M.; Scalmani, G.; Rega, N.; Petersson, G. A.; Nakatsuji, H.; Hada, M.; Ehara, M.; Toyota, K.; Fukuda, R.; Hasegawa, J.; Ishida, M.; Nakajima, T.; Honda, Y.; Kitao, O.; Nakai, H.; Klene, M.; Li, X.; Knox, J. E.; Hratchian, H. P.; Cross, J. B.; Adamo, C.; Jaramillo, J.; Gomperts, R.; Stratmann, R. E.; Yazyev, O.; Austin, A. J.; Cammi, R.; Pomelli, C.; Ochterski, J. W.; Ayala, P. Y.; Morokuma, K.; Voth, G. A.; Salvador, P.; Dannenberg, J. J.; Zakrzewski, G.; Dapprich, S.; Daniels, A. D.; Strain, M. C.; Farkas, O.; Malick, D. K.; Rabuck, A. D.; Raghavachari, K.; Foresman, J. B.; Ortiz, J. V.; Cui, Q.; Baboul, A. G.;

Clifford, S.; Cioslowski, J.; Stefanov, B. B.; Liu, G.; Liashenko, A.; Piskorz, P.; Komaromi, I.; Martin, R. L.; Fox, D. J.; Keith, T.; Al-Laham, M. A.; Peng, C. Y.; Nanayakkara, A.; Challacombe, M.; Gill, P. M. W.; Johnson, B.; Chen, W.; Wong, M. W.; Gonzalez, C.; Pople, J. A.; Gaussian, Inc.: Wallingford CT: 2004.

(112) Cisneros, G. A.; Tholander, S. N. I.; Parisel, O.; Darden, T. A.; Elking, D.; Perera, L.; Piquemal, J. P. *International Journal of Quantum Chemistry* **2008**, *108*, 1905-1912.

Chapter 11

Dynamics of Silyl Ions/F-SAM: Analysis of Soft-landing Processes

1. INTRODUCTION

Collisions between ions and surfaces is a powerful technique for modifying the chemical and physical properties of surfaces.[1,2] During the collision, different process may take place depending on the energy of the projectile. Within the hyperthermal regime (1-100 eV), a great variety of interesting processes occur due to the energy transferred from the ion translation to the internal degrees of freedom, of both the surface and the ion. Among the most common processes (reactive and unreactive) we can find soft-landing, surface-induced dissociation (SID), chemical sputtering, ion/surface reactions and charge transfer.[3-6] As seen in Chapter 2, soft-landing consists in the intact deposition of an ion into the surface without chemical reaction. This process was first reported by Cooks and co-workers who detected intact bulky ions inside an F-SAM surface by means of mass spectrometry measurements.[7] As mentioned in Chapter 10, after the pioneering work of Cooks, a wide variety of projectile ions were utilized in soft-landing experiments.

The $SiNCS^+$ and $(CH_3)_2SiNCS^+$ (silyl) ions are among the projectiles that Cooks and co-workers have used in their experiments.[7-9] They carried out two types of experiments. Firstly, they studied the SID and ion/surface reactions[9] by colliding pseudohalogen-containing ions [$(CH_3)_2SiNCS^+$ among those] against an F-SAM surface. Immediately after the collision, the scattering mass spectra were examined to investigate the possible reactive processes that took place. In the second type of experiments,[7,8] they collided several polyatomic ions [$SiNCS^+$ and $(CH_3)_2SiNCS^+$ among those] with the surface and after 1 hour, the sputtering spectra were obtained by 60 eV Xe^+ bombardment over the modified surface. The analysis of these spectra allows to check if the ions, fragments of the ions or new species formed from ion/surface reactions were trapped into the surface, giving rise to soft-landing, dissociative soft-landing and reactive soft-landing, respectively.

In the first type of experiments they observed several SID processes, ion/surface reactions and sputtering mechanisms for the $(CH_3)_2SiNCS^+$ ion. In particular, the double methyl dissociation due to the Si-C bond cleavages was the major fragmentation process for this ion, giving rise to $SiNCS^+$ fragments.

In the second experiments, they found soft-landing for $(CH_3)_2SiNCS^+$, but not for the lighter ion $SiNCS^+$. The relative abundance of trapped $(CH_3)_2SiNCS^+$ ions was about 3% with respect to the most abundant peak CF_3. Quite surprisingly, in one experiment, they could observe that the $(CH_3)_2SiNCS^+$ ions remain trapped inside the surface for 14 days after the collision.

From their set of experiments, Cooks and co-workers concluded that soft-landing of bulky polyatomic ions may be explained by two facts: (i) intact ions are trapped in potential wells due to the interaction of the ion with its image charge on the metal, and (ii) the ions are trapped inside the surface due to steric interactions. Moreover, the steric bulk of the projectile ion helps to screen the reactive charged site from attack, and therefore, the trapped ions retain their charge intact.

In spite of the brilliant works of Cooks and co-workers, the reasons of why soft-landing takes place for bulky ions does not seem to be totally clear. Firstly, there exists an interaction potential between the ions and their image charge on the metal surface, but this potential is present not only for the bulky ions, but it exists for all ions, and probably this interaction will be stronger for the smallest ones because, they can penetrate deeper into the surface than the big ones, and their charges are not screened by bulky groups. Secondly, the ions may be sterically trapped which may help to prevent thermal desorption, but the bulky groups also interact repulsively with the fluorocarbon chains.

In this work we carry out classical trajectory simulations of collisions between the $SiNCS^+$ and $(CH_3)_2SiNCS^+$ ions and an F-SAM surface formed by $CH_3(CH_2)_7S$ radicals adsorbed on an Au{111} surface. The classical trajectory approach has been successfully used in the past for simulating energy transfer processes in gas/surface collisions.[10-22] Therefore, this method may be a powerful tool for trying to shed light on the soft-landing mechanism. These simulations are conducted using an analytic potential energy function; the intermolecular ion/F-SAM part was developed in a previous work using the CF_4 molecule as a model for the F-SAM surface.[23] In that work, we demonstrated that manybody effects are negligible for these systems, so that the C and F atoms of CF_4 are good models for those present in the fluorocarbon chains of the monolayer.

The goal of this work is to try to explain the different behaviour found in the experiments for $SiNCS^+$ and $(CH_3)_2SiNCS^+$. In addition, we try to simulate the SID processes which occur for the biggest ion causing the fragmentation of two methyl groups. This work is still in progress, and the results showed here are preliminary, therefore definitive conclusions will not be drawn here. Further calculations and analyses are needed to explain in detail the experiments.

2. COMPUTATIONAL DETAILS

2.1 Potential energy surfaces

The potential energy function of the system consists of the silyl ion intramolecular potential V_{silyl}, the F-SAM intramolecular potential V_{surf}, and the interaction between the silyl ion and the surface $V_{silyl-surf}$:

$$V = V_{silyl} + V_{surf} + V_{silyl-surf} \tag{11.1}$$

The intramolecular potential term for the F-SAM was explained in detail elsewhere[24,25] and in previous Chapters. The F-SAM surface consists of 48 chains of $CF_3(CF_2)_7S$ adsorbed on an Au{111} surface formed by 225 atoms, which are kept fixed during the simulations. The monolayer forms a hexagonal close-packed structure with the nearest-neighbor direction rotated 30º with respect to the Au{111} lattice and the backbone of the $CF_3(CF_2)_7S$ moiety has a tilt angle with respect to the surface normal of ~ 12º. This surface resembles that used by Cooks in his experiments formed by chains of $CF_3(CF_2)_7(CH_2)_2S$ adsorbed on gold, therefore our results can be compared to those obtained experimentally. The two additional methylene groups of the monolayer employed by Cooks in their experiments are not expected to play an important role in the dynamics as shown in previous work.[26]

We have two different intramolecular potentials for the two silyl ions $SiNCS^+$ and $(CH_3)_2SiNCS^+$ employed in the dynamics simulations. The intramolecular potential for the smallest ion is given by the sum of harmonic stretches and bends:

$$V_{ion} = \sum_i \frac{1}{2} k_s (r - r_0)^2 + \sum_i \frac{1}{2} k_\theta (\theta - \theta_0)^2 \tag{11.2}$$

where the force constants k_s and k_θ were obtained by fitting the vibrational frequencies calculated at the B97-D/TZVPP level of theory. The B97-D/TZVPP equilibrium distances r_0 and angles θ_0 were employed. All these potential parameters are listed in Table 11.1, and the comparison between the B97-D/TZVPP frequencies and those calculated analytically employing the potential parameters is showed in Table 11.2.

Table 11.1: Parameters of the intramolecular potential for $SiNCS^+$ ion.

Harmonic stretching parameters		
Bond	k_s [a]	r_0 [b]
Si-N	6.750	1.64748
N-C	9.650	1.23909
C-S	7.350	1.53573
Harmonic bending parameters		
Angle	k_θ [c]	θ_0 [d]
Si-N-C	0.230	180.000
N-C-S	0.465	180.000

[a]mdyn/Å; [b]Å; [c]mdynÅ/rad^2; [d]degrees.

Table 11.2: Frequencies for $SiNCS^+$ ion.

B97-D frequencies (cm^{-1})	Analytical frequencies (cm^{-1})
148.1 (2)[a]	147.9 (2)
498.0 (2)	497.0 (2)
541.6	531.4
1145.8	1145.6
1895.7	1895.2

[a]In parenthesis the number of degenerate vibrational normal modes.

The intramolecular potential function for the $(CH_3)_2SiNCS^+$ ion requires torsional and wag terms besides stretching and bending interactions. In addition, the Si-C stretching interactions were modeled using Morse functions for allowing the dissociation of these bonds during the collision with the surface. The methyl dissociation giving rise to the $SiNCS^+$ fragment is the main fragmentation process observed by Cooks and co-workers in their experiments.[9] Harmonic stretching functions were employed for the other bonds. Therefore the intramolecular potential for the $(CH_3)_2SiNCS^+$ is given by:

$$V_{ion} = \sum_{i\neq Si-C} \frac{1}{2}k_s(r-r_0)^2 + \sum_{i=Si-C} D_e\left(1-e^{-\beta(r-r_0)}\right)^2 + \sum_i \frac{1}{2}k_\theta(\theta-\theta_0)^2 + \sum_i \frac{1}{2}k_\alpha(\alpha-\pi)^2 + \sum_i \frac{1}{2}k_t(1+\cos(n\varphi-\gamma)) \quad (11.3)$$

where bending, wag and torsion force constants related to the Si-C bonds include a switching function that switches off these potential terms when a Si-C bond breaks.

$$k_\theta = k_\theta^0 s_{AB} s_{BC} \tag{11.4}$$

$$k_\alpha = k_\alpha^0 s_{AB} s_{AC} s_{AD} \tag{11.5}$$

$$k_t = k_t^0 s_{AB} s_{BC} s_{CD} \tag{11.6}$$

where the superscript 0 denotes the conventional force constants and the switching function between two atoms i and j, s_{ij}, has the form

$$s_{ij} = e^{-c_{ij}(r_{ij}-r_0)^2} \tag{11.7}$$

where c_{ij} was fixed to 0.1 for all cases. Figure 11.1a displays different interactions that include this switching function.

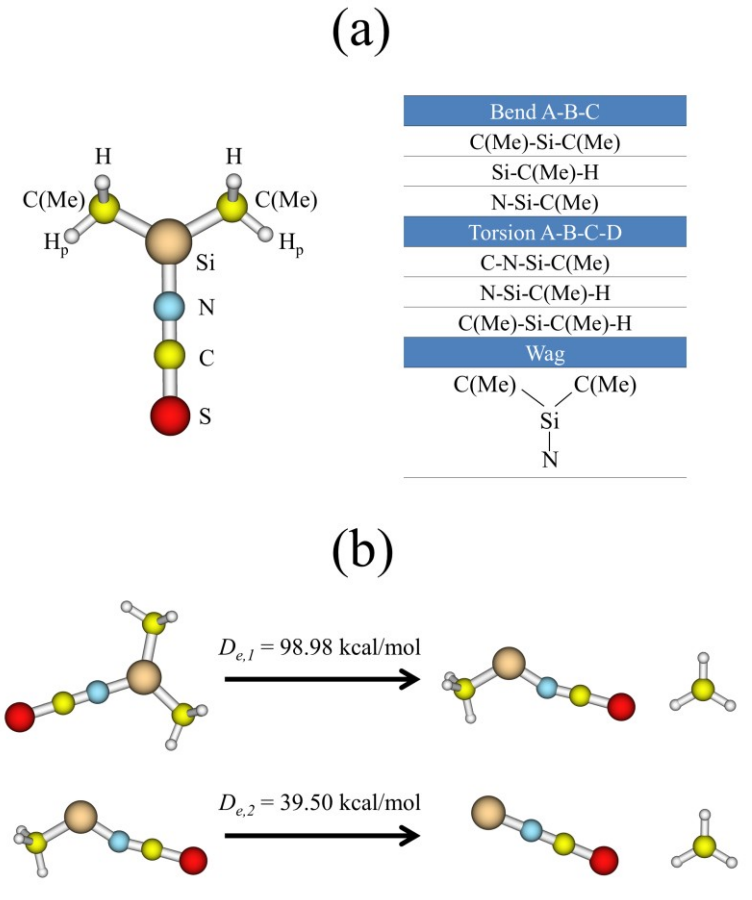

Figure 11.1: (a) Intramolecular interactions which need switching functions.
(b) Dissociation of methyl groups.

The second term in equation 11.3 represents the Morse potential for the Si-C(Me) bonds. D_e is the equilibrium dissociation energy, but since we have two Si-C(Me) bonds, when the first Si-C(Me) dissociates, the dissociation energy of the second one changes. Therefore it is necessary to include another function to smoothly switch from $D_{e,1}$ to $D_{e,2}$, that is, from the dissociation energy of the first Si-C(Me) bond to that of the second one:

$$D_e = D_{e,1} + \left(D_{e,2} - D_{e,1}\right)\frac{1}{2}(1 + \tanh(\bar{R}_{Si-C} - C)) \qquad (11.9)$$

The constant C was set to 5 to achieve good energy conservation during the fragmentation dynamics, and $\bar{R}_{Si-C}$ is the average Si-C bond length. The dissociation energies $D_{e,1}$ and $D_{e,2}$ were calculated using Gaussian-4 (G4) theory[27] and the values obtained were 98.98 kcal/mol and 39.50 kcal/mol, respectively.

The force constants of equation 11.3 were obtained by fitting the B97-D/TZVPP frequencies. The parameters and the comparison between the DFT and fitted frequencies are listed in Tables 11.3 and 11.4, respectively.

Table 11.3: Parameters of the intramolecular potential for $(CH_3)_2SiNCS^+$ ion.

Harmonic stretching parameters					
Bond	k_s [a]	r_{eq} [b]	Bond	k_s	r_{eq}
Si-N	8.400	1.65173	C(Me)-H	4.95	1.10025
N-C	9.300	1.22333	C(Me)-H_p [c]	4.95	1.09445
C-S	7.900	1.54574			
Morse parameters					
Bond	β [a]		r_{eq}		
Si-C(Me)	2.30		1.84575		
Harmonic bending parameters					
Angle	k_θ [d]	θ_{eq} [e]	Angle	k_θ	θ_{eq}
Si-N-C	0.052	180.000	H-C(Me)-Si	1.050	109.483
N-C-S	0.525	180.000	H_p-C(Me)-Si	1.150	111.687
N-Si-C(Me)	0.650	118.470	H-C(Me)-H	0.220	106.887
C(Me)-Si-C(Me)	0.250	123.061	H-C(Me)-H_p	0.170	109.588
Torsional parameters					
Torsion	Nº of terms		k_t [f]	γ [e]	
N-Si-C(Me)-H	2		2.200	180.000	
			1.000	180.000	
Wag parameters					
Angle			k_α [c]		
Si-N-C(Me)-C(Me)			0.218		

[a]mdyn/Å; [b]Å; [c]see Figure 11.1a for definition of the hydrogens; [d]mdynÅ/rad^2; [e]degrees; [f]kcal/mol.

The intermolecular potentials between the silyl ions and the F-SAM were developed in a previous work[23] and are described in Chapter 10. The CF_4 molecule was selected as a model for the fluorocarbon chains of the surface as in previous works.[28-30] As seen in Chapter 10, many-body effects are negligible for these systems and CF_4 represents faithfully the F-SAM surface for parameterization purposes. Briefly, several single point interaction energies were computed at the B97-D/TZVPP level of theory for different orientations between the silyl ions and the CF_4. Then, the analytical function employed to fit to the B97-D interaction energies was taken as a sum of two-body Buckingham potentials:

$$V_{silyl-surf} = \sum_{ij} A_{ij}\, exp\left(-B_{ij} R_{ij}\right) - \frac{C_{ij}}{R_{ij}^{D_{ij}}} - \frac{E_{ij}}{R_{ij}^{F_{ij}}} \qquad (11.10)$$

where i and j represent each of the atoms of the silyl ions and CF_4 molecules, respectively, R_{ij} is the $i-j$ interatomic distance and A_{ij}, B_{ij}, C_{ij}, D_{ij}, E_{ij} and F_{ij} are the parameters which were optimized with the help of a genetic algorithm.[31]

Table 11.4: Frequencies for $(CH_3)_2SiNCS^+$ ion.

B97-D frequencies (cm^{-1})	Analytical frequencies (cm^{-1})	B97-D frequencies (cm^{-1})	Analytical frequencies (cm^{-1})
19.8	25.0	855.2	835.8
30.7	29.0	1161.4	1226.4
49.9	45.8	1258.7	1337.7
94.4	61.3	1262.7	1500.4
192.7	199.3	1382.1	1307.0
217.7	238.3	1383.1	1285.4
262.3	290.3	1389.5	1362.8
459.6	494.7	1395.1	1498.1
479.3	458.5	1999.9	1915.7
492.7	479.5	2935.9	2934.7
662.5	632.4	2938.9	2934.7
680.7	781.2	3015.6	3043.2
712.2	696.9	3021.1	3043.6
787.3	774.5	3064.7	3051.4
824.5	835.4	3068.4	3052.8

In some simulations, an additional interaction term was added between the ion and the Au{111} surface to describe the image potential interaction. For describing this interaction, the classical point charge/metal surface expression was employed, and it reads[32]:

$$V_{image} = -\frac{83.02}{Z} \tag{11.11}$$

where Z is the perpendicular distance between the silicon atom and the Au{111} surface and the energy is expressed in kcal/mol. This means that if the ion is 10 Å above the metal surface, the ion/metal interaction energy is 8.3 kcal/mol, which means that it is not negligible. The influence of adding the image potential interaction will be discussed below.

The silicon atom was selected as the interaction site for the ion because it carries most of the positive charge of the molecule as seen in Figure 11.2. The charges of the figure were evaluated at the B97-D/TZVPP level of theory using the Merz-Singh-Kolman scheme[33,34]; in this method the charges are computed by a fit to the electrostatic potential.

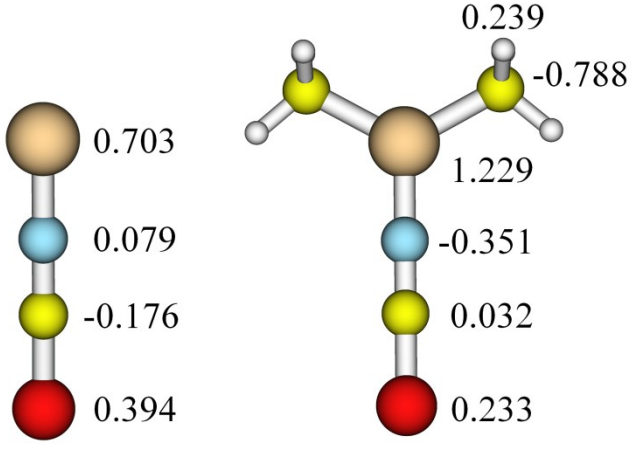

Figure 11.2: Partial atomic charges (in a.u.) calculated at the B97-D/TZVPP level and using the Merz-Singh-Kolman scheme.

2.2 Trajectory simulations

Three different initial conditions for $SiNCS^+$ and $(CH_3)_2SiNCS^+$ ions were considered. The difference among them is the incident collision energy E_i and the incident angle θ_i formed between the incident velocity and the surface normal. For E_i = 10 eV, the incident angle θ_i was fixed to 0º and 55º, and for E_i = 30 eV the angle was 0º. In addition, for the initial condition E_i = 10 eV and θ_i = 0º the simulations were carried out with and without the image potential between the ions and the gold surface to analyze the influence of this interaction on the dynamics. For all simulations the ZPE energy was added to the normal modes of both ions with their total rotational angular momentum set

to zero. These initial conditions were selected to mimic the experimental conditions employed by Cooks and co-workers in their experiments.[7-9]

All simulations of the present study have been carried out using the VENUS05[35] computer program. Ensembles of 2000 trajectories for each initial condition were integrated with a fixed step size of 0.3 fs using the Adams-Moulton algorithm in VENUS05 for a total integration time of 60 ps. The initial separation between the projectile and the surface aiming point was 40 Å (52Å above the gold atoms) and the trajectories were stopped when the distance between the ion and the surface was 45 Å or when 60 ps elapsed. Before the beginning of each trajectory simulation, the surface was relaxed to a thermodynamic equilibrium structure by a 2 ps molecular dynamics simulation[36] in which the atomic velocities are scaled to obtain a surface temperature of 300 K. This structure was then used as the initial structure of a 100 fs equilibration run at the beginning of each trajectory. Periodic boundary conditions were also utilized to simulate a larger surface.[36]

3. RESULTS

3.1 Collision types

Four collision types were found in the simulations. As in previous studies of this thesis, the different trajectories were classified according to both the minimum height of the projectile center-of-mass above the Au{111} surface $h_{\text{silyl},min}$, and to the number of inner turning points nITPs in the direction perpendicular to the surface that the projectile experiences during the collision with the surface. Thus, trajectories which drop below the intermediate height of 11.6 Å (see previous chapters) are identified as *penetrating*. There are two types of penetrating trajectories: those that penetrate directly the surface (*direct-penetration*) and those that penetrate the surface after the molecule has performed several ITPs on the surface (*physisorption-penetration*). When the projectile does not penetrate the surface, the collisions are classified as *direct* (nITPs = 1) or *physisorption* (nITPs > 1). Figure 11.3 shows the percentage of the different collision types for the three initial conditions investigated in this work.

As seen in the plots, collisions that penetrate directly the surface are the most abundant events for both molecules when θ_i = 0º. Another clear feature of the figure is that the vast majority of the trajectories do not leave the surface within the simulation time of 60 ps (those are called *incomplete* trajectories). The dynamics behaviour of the trapped trajectories inside the F-SAM surface will be examined below. The number of *direct*, *physisorbing* and

physisorption-penetrating collisions decreases and the number of *direct-penetrating* collisions increases with the incident energy for both ions. One can think of two different origins for the two types of penetrating trajectories. *Direct-penetration* is favored at high collision energies because the projectile has more energy to overcome the "penetrating barrier". On the other side, collisions at low energies tend to have longer residence times of the projectile, enhancing physisorption. Figure 11.3 shows that *direct-penetrating* collisions dominates clearly over the rest of events (for θ_i = 0º) while for CO_2/F-SAM[30] simulations the *physisorption-penetrating* collisions were more abundant. The main reason for this different trend is the collision energy range. For CO_2/F-SAM collisions, the gas was directed to the surface at 1-20 kcal/mol, while the ions of the present work were collided at 230.6 kcal/mol and 691.8 kcal/mol.

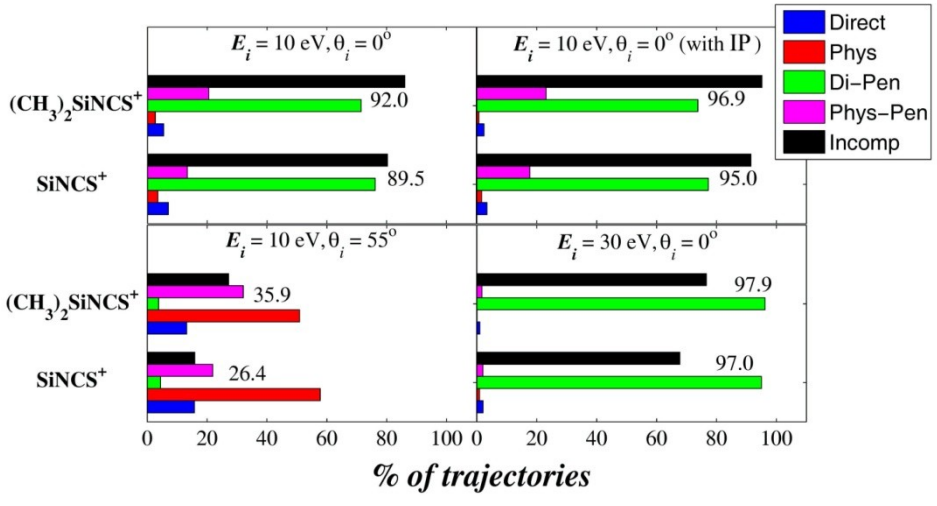

Figure 11.3: Percentage of trajectory types. The two numbers on each plot indicate the percentage of total penetration for both ions.

Physisorbing and *physisorption-penetrating* processes become important as the incident angle increases, as expected; the same behaviour was found for NO/F-SAM in a previous work[28] (Chapter 9).

As mentioned above, for the initial condition E_i = 10 eV and θ_i = 0º, the simulations were performed with and without the image potential (denoted as IP in Figure 11.3). This potential is caused by the interaction of an ion with its image charge generated on a metal surface. At relatively long distances the interaction between an ion and a surface is attractive; only at very small distance repulsion turns on. Thus, the potential used for the simulations has only an attractive term as seen in equation 11.11. This attractive term makes

that the penetrating and incomplete events increase at the expense of physisorption and direct processes, as Figure 11.3 shows.

Comparing the above results for $SiNCS^+$ and $(CH_3)_2SiNCS^+$ ions, only slight differences are found. In general, the same trends are observed for both ions, with a slight preference for *penetrating* events for the biggest ion. As seen above, Cooks found in his experiments[7,8] soft-landing for $(CH_3)_2SiNCS^+$ but not for $SiNCS^+$. This fact is not reflected in the above analysis of our simulations because the time scale employed in our study is far too short compared with the experimental one. The mass spectra of the trapped species in the experiments are plotted one hour (or more) after the collision with the surface, that is, molecules have plenty of time for desorption before being detected. This aspect will be discussed later on in this Chapter.

3.2 Behaviour of the projectile inside the bulk of the monolayer

A large percentage of trajectories are *incomplete*, that is, the ions remain into the F-SAM surface for all the simulation time. It is of interest to analyze the dynamics behaviour of the trapped ions in the bulk of the fluorocarbon matrix in order to find differences between both ions. Figures 11.5 and 11.6 show probability density plots as a function of the height of the center of mass of the projectile above the gold surface (h_{sylil}), the angle formed between the Si−S axis and the perpendicular to the surface (β), and the angle formed between the projection of the Si−S axis onto the gold surface and the X axis (angle χ); the chains of the monolayer are tilted in the $+X$ direction. Figure 11.4 displays the definition of h_{sylil}, β and χ.

Figures 11.5 and 11.6 indicate that both ions do not penetrate much into the surface for the lowest collision energy of 10 eV [panels (a), (c), (e) and (g)], showing a maximum around 10 Å above the gold surface. For the highest collision energy of 30 eV the projectiles penetrate slightly deeper [panels (d) and (h)] with maxima around 9 Å. Moreover, the probability distributions become broader with increasing the collision energy because projectiles have more energy to move throughout the monolayer. The incident angle does not affect significantly the distributions. No clear differences are found between $SiNCS^+$ and $(CH_3)_2SiNCS^+$ except for panels (b) and (f) where the image potential was introduced. This attractive potential helps the projectiles to penetrate deeper into the surface, especially for the smallest one. Maximum heights above the gold surface appear at 6 Å and 8 Å for $SiNCS^+$ and $(CH_3)_2SiNCS^+$ respectively. The distance between the ions and the gold surface may be short enough for neutralization of the cation (due to electron transfer from the gold surface) to take place. This possibility will be explored below.

As mentioned in the NO/F-SAM[28] study (Chapter 9), if the projectiles were aligned with the monolayer chains, the values of β would be 12º or 168º. Likewise, if the projectiles accommodated in the grooves of the monolayer (see Chapter 9), the peaks of the χ distributions should appear at around 0º, 180º, 60º and 120º because of the hexagonal package of the chains (see Figure 11.4b). The distributions deviate from these values due to the strong interactions between the projectiles and the chains of the monolayer. For instance, the distributions show a stable region at β angles close to 180º for both ions, that is, with the Si atoms pointing downwards. Similar values for these angles were observed for NO/F-SAM.

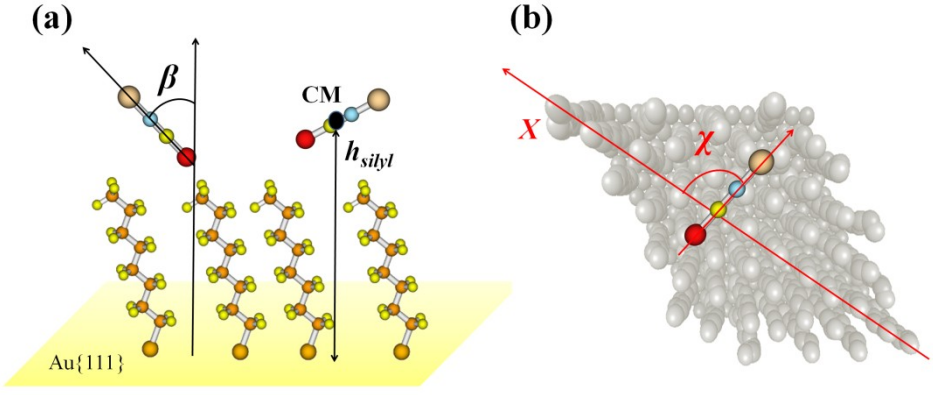

Figure 11.4: Definition of angles β and χ and height h_{sylil}.

Quite surprisingly the ions tend to penetrate into the surface with the Si atom pointing downwards (even in the absence of the image potential). In order to corroborate the result and discard the possibility of an artifact in the interaction potential, a geometry optimization at the B97-D/TZVPP level of theory for the ion inside a model for the F-SAM[23] (see Chapter 10) was carried out. This model is formed by nine chains of perfluorobutane $CF_3(CF_2)CF_3$, and will be referred to as miniSAM. Two different optimizations were performed. In the first one, the $SiNCS^+$ ion was introduced into the miniSAM with the Si atom pointing downwards (Figure 11.7a), and in the second optimization the Si atom points upwards (Figure 11.7b). When both structures are optimized, for the Si-upwards configuration the ion is ejected from the miniSAM adopting a parallel configuration on the F-SAM surface, whereas for the Si-downwards configuration there is a stable configuration similar to the initial one as Figure 11.7 shows.

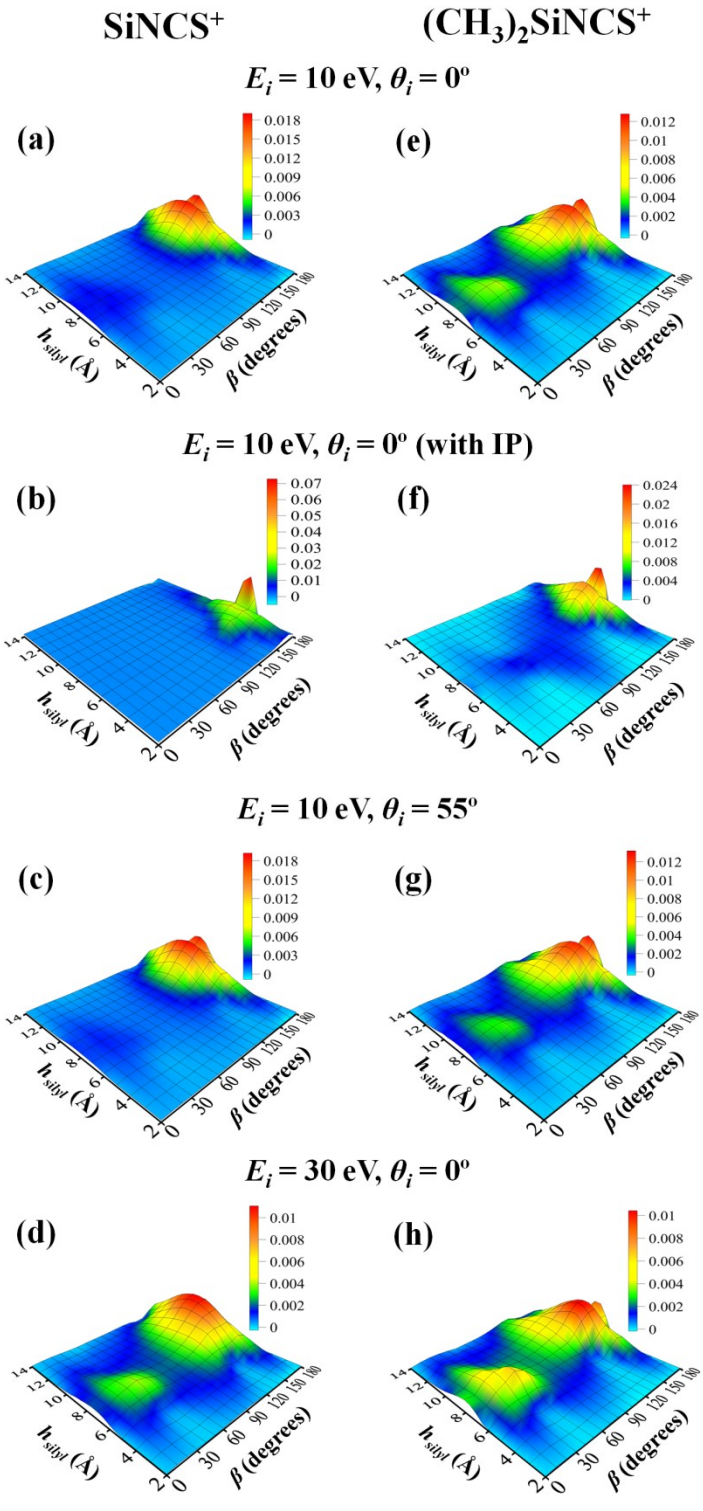

Figure 11.5: Probability density plots of the angle β for $SiNCS^+$ [panels (a)-(d)] and $(CH_3)_2SiNCS^+$ [panels (e)-(h)] inside the F-SAM surface.

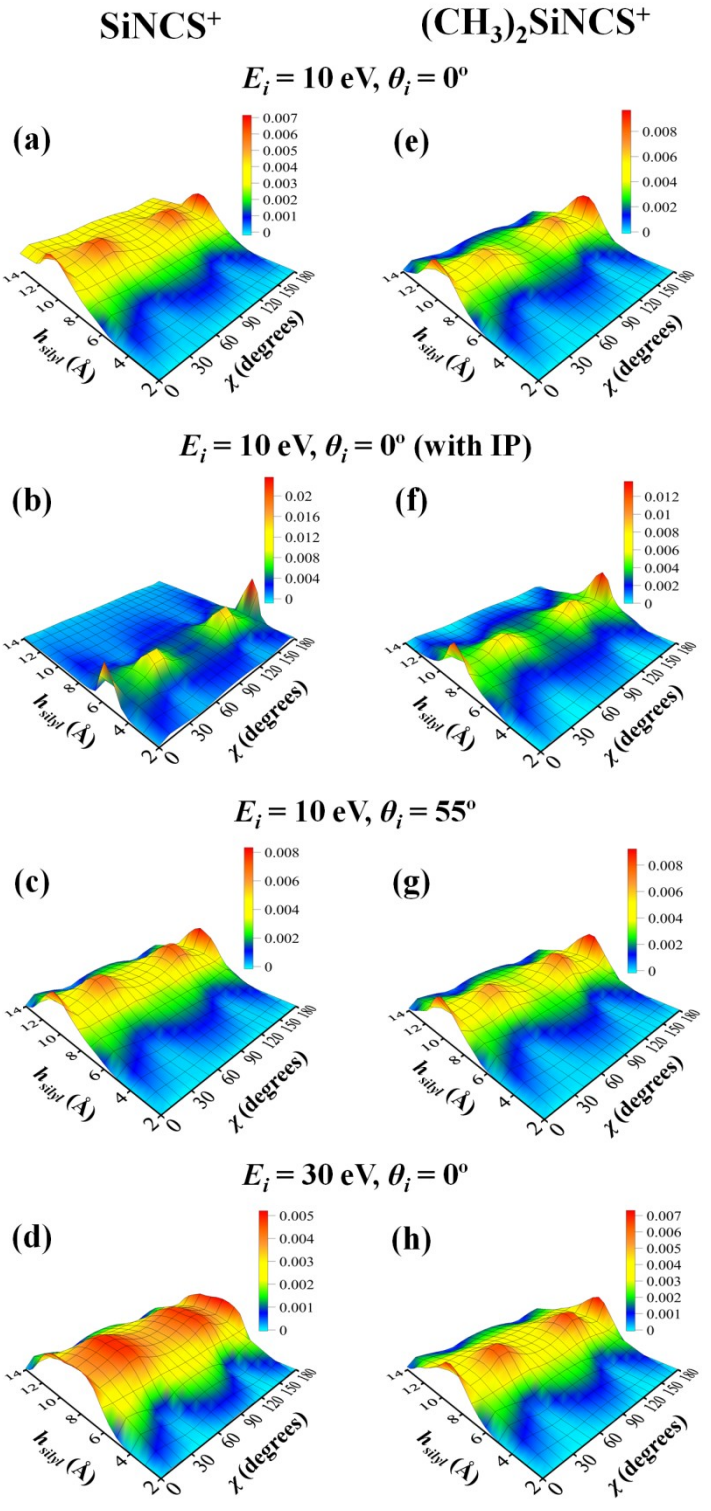

Figure 11.6: Probability density plots of the angle χ for $SiNCS^+$ [panels (a)-(d)] and $(CH_3)_2SiNCS^+$ [panels (e)-(h)] inside the F-SAM surface.

The structure optimizations (Figure 11.7) agree with the behaviour found in the simulations for trajectories trapped into the surface (Figure 11.5). In addition, when one analyzes the distributions as a function of β for trajectories which penetrate into the monolayer but desorb before the simulation time elapses (Figure 11.8), one finds a maximum corresponding to a configuration with Si atom pointing upwards. This means that trajectories which interact with the F-SAM in this Si-upwards configuration do not remain trapped into the monolayer for a long time.

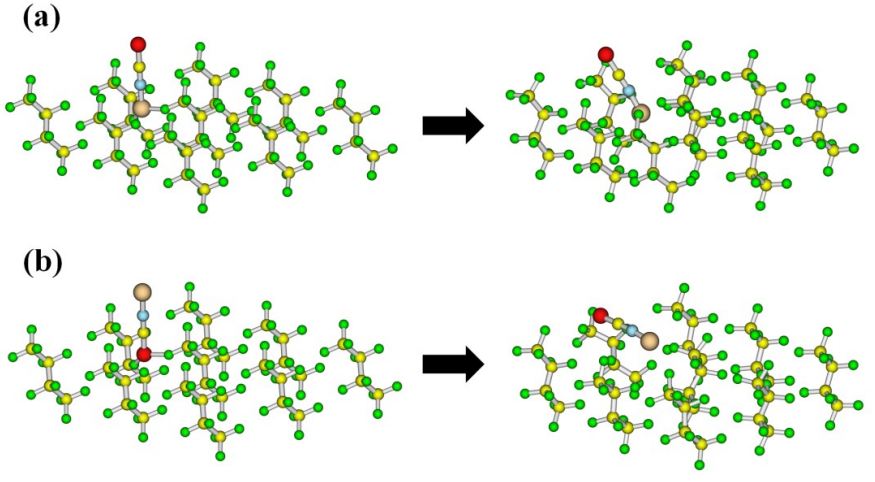

Figure 11.7: Optimization of SiNCS+/miniSAM structure with (a) Si-downwards and (b) Si-upwards.

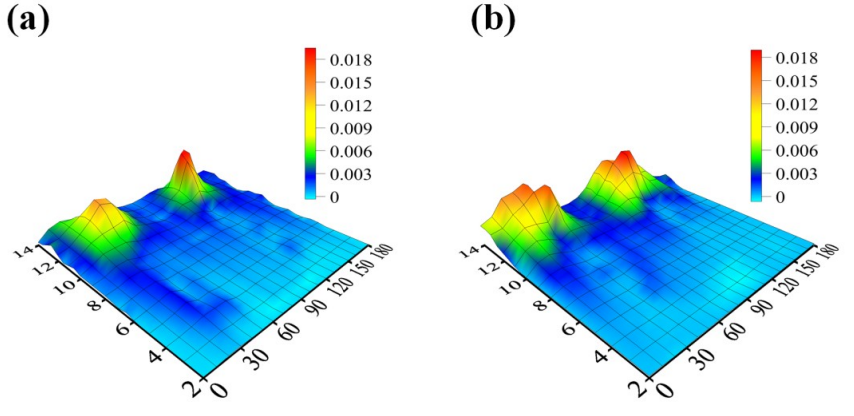

Figure 11.8: Probability density plots of the angle β of (a) $SiNCS^+$ and (b) $(CH_3)_2SiNCS^+$ for penetrating trajectories which desorb from the F-SAM during the simulation for the initial condition E_i = 10 eV and θ_i = 0° without image potential.

3.3 Energy transfer

Collisions of the silyl ions with the F-SAM surface result in variations in the ion translational energy from E_i to a final value E_f, as well as in changes in the internal energy of the ion, ΔE_{int}, and the surface energy, ΔE_{surf}; i.e.

$$E_i = E_f + \Delta E_{int} + \Delta E_{surf} \tag{11.12}$$

Assuming rotation and vibration are uncoupled, ΔE_{int} can be written as:

$$\Delta E_{int} = \Delta E_{rot} + \Delta E_{vib} \tag{11.13}$$

where ΔE_{vib} and ΔE_{rot} are the changes in vibrational and rotational energies of the silyl ions, respectively. The average percentage of E_i that goes to E_f, ΔE_{rot}, ΔE_{vib} and ΔE_{surf}, for trajectories that desorb from the surface during the simulation time of this study, is shown in Figure 11.9.

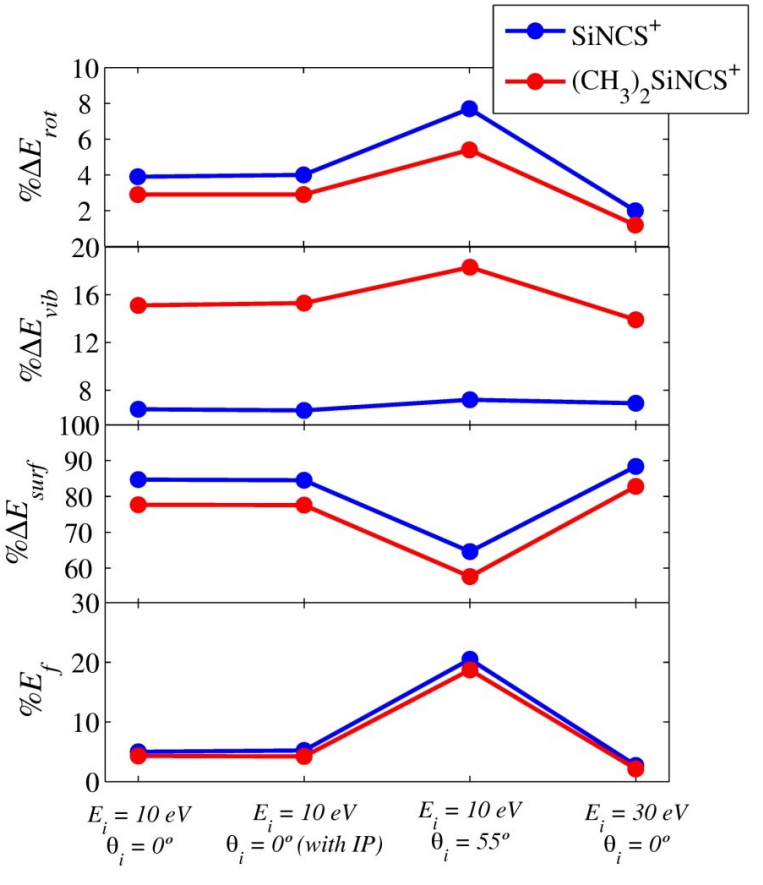

Figure 11.9: Average percentages of different energies ΔE_{rot}, ΔE_{vib}, ΔE_{surf} and E_f for $SiNCS^+$ and $(CH_3)_2SiNCS^+$ for the different initial conditions.

As seen in the plots, the variations for both ions follow the same pattern. The vibrational energy transfer ΔE_{vib} does not depend strongly on the initial conditions and it is higher for the $(CH_3)_2SiNCS^+$ ion because it has more vibrational normal modes than $SiNCS^+$. The energy transferred to the ion's rotational degrees of freedom is slightly larger for the smallest ion and it is more important for the incident angle of 55º as expected. ΔE_{surf} is lower for $(CH_3)_2SiNCS^+$ than for $SiNCS^+$ ion because the biggest ion retains more energy in its vibrational degrees of freedom. The final translational energy E_f is almost the same for both ions for all the initial conditions. Another feature showed in Figure 11.9 is that the image potential does not affect the energy transfer efficiencies. Energy transfer including the *incomplete* trajectories was also analyzed assuming that the projectiles trapped inside the surface will reach thermal equilibrium with the surface. The results including *incomplete* trajectories reveal, once again, no differences between both ions; these results are not shown for simplicity.

3.4 Neutralization of the projectile

Figure 11.5 shows that β presents a maximum close to 180º, i.e., the ions penetrate into the F-SAM surface preferably with the Si atom pointing to the gold surface. Moreover, panels (b) and (f) of Figure 11.5 show that the effect of the image potential is to bring the ion (particularly the smallest one) closer to the gold surface. A molecular orbital computation at the HF/6-31G(d,p) level of theory shows that the LUMO has a big contribution of the Si atom as shown in Figure 11.10. These results suggest that there is a possibility for the ion to get neutralized by resonant electron transfer from the gold surface. As seen in Chapter 2, this type of neutralization may occur if a projectile electronic state lies below the Fermi level E_F of the metal.[37]

The experimental value of the work function of gold modified by self-assembled monolayer of 1H,1H,2H,2H-perfluorodecanethiol (PFDT) is about 5.4-5.9 eV.[38,39] The structure of the PFDT surface (chains of $CF_3(CF_2)_7(CH_2)_2S$) is similar to that of our F-SAM surface (chains of $CF_3(CF_2)_7S$), therefore, we use the value of this work function in our study. We calculated the three lowest electronic states for the neutral species and the electronic ground states of the cations at the SAC-CI/aug-cc-pVTZ level of theory[40-42] with the general-R approach, implemented in Gaussian 09 package,[43] which includes up to 6th order excitations. The energy of these electronic states in gas phase and the work function of gold from the literature are shown schematically in Figure 11.11. The results suggest that electron transfer from the gold surface to the projectile may take place for the smallest ion since the energy of the $1^2\Pi$ electronic ground state is about 1 eV lower than that of the

gold Fermi level (E_F). The neutralization of $(CH_3)_2SiNCS^+$ will hardly occur because the only electronic state available for charge transfer has almost the same energy as the gold Fermi level and, as is well known, the energy of a cation state increases in the presence of a metal.[32] Therefore, a more realistic calculation of the 1^2B_1 level of $(CH_3)_2SiNCS^+$ ion in presence of Au would provide an energy higher than E_F, precluding the possibility of charge transfer to this molecule. Of course, the energy of the $1^2\Pi$ state of $SiNCS^+$ will also increase in presence of the metal, but this level is 1 eV lower than E_F, therefore it could be available for charge transfer.

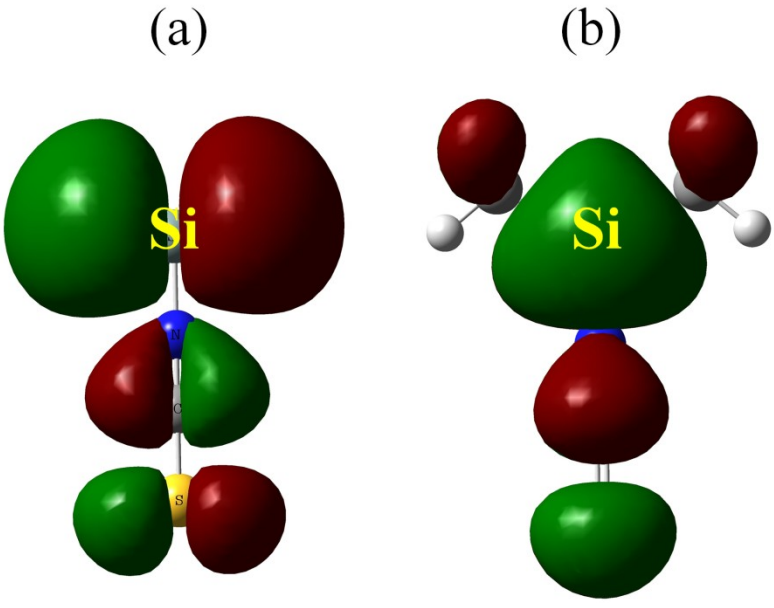

Figure 11.10: LUMO orbital for (a) $SiNCS^+$ (Π symmetry) and (b) $(CH_3)_2SiNCS^+$ (B_1 symmetry) at the HF/6-31G/(d,p) level.

This analysis of the electronic states in conjunction with the probability distributions as a function of β and h_{silyl} make $SiNCS^+$ neutralization a probable process, whereas neutralization is less likely for the big cation. Therefore, if $SiNCS^+$ gets neutralized in the collision process, it will not be detected in the experiments of Cooks and co-workers since the sputtering spectra only exhibit charged species. This fact could explain the experimental results of Cooks and co-workers[7,8] where only $(CH_3)_2SiNCS^+$ was observed in the spectra recorded after the collision. Of course, this result should be considered with caution. A more realistic image potential in the simulations and a more realistic calculation of the electronic states are needed to draw a definite conclusion.

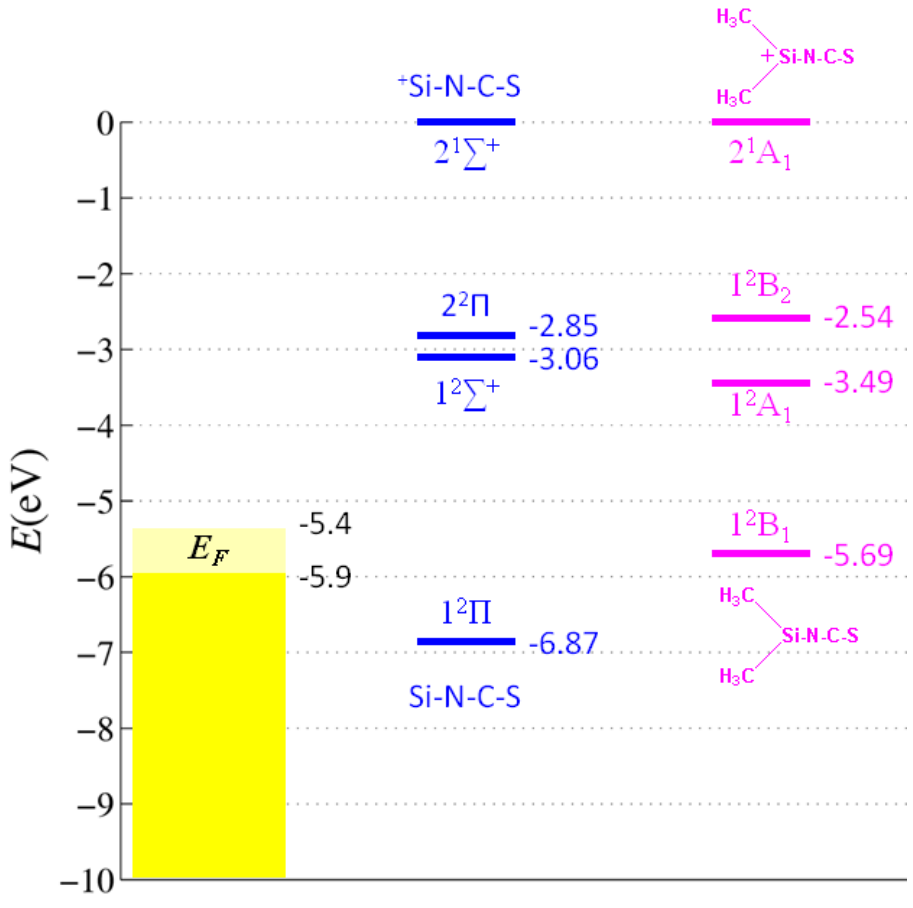

Figure 11.11: Electronic states for $SiNCS^+$ and $(CH_3)_2SiNCS^+$ ions computed at the SAC-CI/aug-cc-pVTZ level.

Other factors besides charge transfer may explain the experimental result. Thermal desorption of the small cation is expected to be faster than the corresponding process for the big cation, since the interaction energies with the monolayer are stronger for $(CH_3)_2SiNCS^+$ than for $SiNCS^+$. Also, we can not exclude the possibility of ion/surface reactions, such as F or CF_3 abstraction, which produce neutral species. This will be examined in future work.

3.5 Surface Induced Dissociation (SID)

As mentioned above, Cooks and co-workers found in their experiments that SID processes are abundant when $(CH_3)_2SiNCS^+$ is collided against the F-SAM surface.[9] In particular, for the collision energy of 30 eV, they observed that around of 85% of the scattered ions suffer SID. The scattering mass spectrum showed that most of these SID processes correspond to single and, above all, double methyl dissociations. A direct comparison

between experiments and simulations cannot be performed because we know only the dynamics of the system during 60 ps, and we cannot predict what happens for longer times. But an analysis of the scattered ions may provide a qualitative description of the importance of the SID processes.

For the initial condition of E_i = 30 eV and θ_i = 0º, we found that 11.1% of scattered projectiles dissociate by a shattering mechanism, while this percentage increases to 53.7% if the RRKM mechanism for dissociation is included, i.e., counting also those trajectories with final internal energies higher than the methyl dissociation energy. In these percentages both, single and double methyl dissociations are included. The values obtained from the simulations point in the same direction as the experimental results, indicating that methyl fragmentation is an abundant process in the collision of $(CH_3)_2SiNCS^+$/F-SAM.

4. CONCLUSIONS AND FUTURE WORK

Classical trajectory simulation of $SiNCS^+$ and $(CH_3)_2SiNCS^+$ colliding with an F-SAM surface were carried out in this work. Initial conditions were selected to mimic the experimental conditions of Cooks and co-workers. The aim of this work, still in progress, is to explain why the big ion is retained into the surface for a long time whereas the small ion is not detected in the sputtering spectrum.

A preliminary analysis of the simulations does not clearly explain the different behavior of both ions, but some indications were obtained. The analysis of the collision types and the energy transfer are very similar for both projectiles. The behavior of both ions inside the monolayer is essentially the same, except when the image potential is included. In this case the $SiNCS^+$ ion penetrates deeper into the surface than the big one does. The probability distributions as a function of the β angle show that the ions prefer to get trapped into the surface with the Si atom pointing to the gold surface. Since the LUMO is largely composed by Si orbitals and the ion approaches the gold surface with Si downwards configuration, electron transfer from the gold to the projectiles may take place. Ion neutralization by a resonance mechanism seems to be possible only for the smallest ion taking into account the relative energies of the projectile's electronic states with respect to the gold Fermi level. Charge transfer could be the reason why $SiNCS^+$ is not detected in the sputtering spectrum. But using a more accurate image potential and a more reliable calculation of the electronic states for the projectiles is required to tackle this issue in more detail. A general analysis of the dynamics results indicates that

the methyl fragmentation of $(CH_3)_2SiNCS^+$ takes place quite often. Similar results were found in the experiments.

The study of the thermal desorption rate constants of both ions may clarify the problem. These rate constants can be computed by the boxed molecular dynamics approach (BXD).[44] This technique accelerates the simulations by slicing the reaction coordinate (the height above the gold surface in our case) into several boxes. Then, running trajectories and locking them within each box allow one to calculate rate constants for exchange between neighboring boxes, and consequently a total rate constant for the whole process.

Finally, ion/surface reactions whose products are neutral species, which are not detected by mass spectrometry, could be another reason for the differences found between the ions. For instance, Somogyi et al.[45] found that CH_3^+ may be neutralized by hydrogen, fluorine and methyl anion addition when it is collided against F-SAM or H-SAM surfaces. Static quantum mechanical calculations of the stationary species involved in the reactive processes, or direct dynamics simulations, are two possible ways for studying this topic.

All these possibilities will be analyzed in the future to clarify all the features of soft-landing processes. Additional experiments could also elucidate the details of this type of events. For instance, the use of monolayers formed by different chains which interact in a different way with the projectiles, or the use of other metals with different work functions as support for the monolayer could be useful in this direction.

REFERENCES

(1) Hanley, L.; Sinnott, S. B. *Surf. Sci.* **2002**, *500*, 500-522.
(2) Bittner, A. M. *Surf. Sci. Rep.* **2006**, *61*, 383-428.
(3) Cooks, R. G.; Ast, T.; Pradeep, T.; Wysocki, V. *Acc. Chem. Res.* **1994**, *27*, 316-23.
(4) Cooks, R. G.; Jo, S.-C.; Green, J. *Appl. Surf. Sci.* **2004**, *231-232*, 13-21.
(5) Gologan, B.; Takats, Z.; Alvarez, J.; Wiseman, J. M.; Talaty, N.; Ouyang, Z.; Cooks, R. G. *J Am Soc Mass Spectrom* **2004**, *15*, 1874-84.
(6) Jacobs, D. C. *Annu. Rev. Phys. Chem.* **2002**, *53*, 379-407.
(7) Miller, S. A.; Luo, H.; Pachuta, S. J.; Cooks, R. G. *Science (Washington, D. C.)* **1997**, *275*, 1447-1450.
(8) Luo, H.; Miller, S. A.; Cooks, R. G.; Pachuta, S. J. *Int. J. Mass Spectrom. Ion Processes* **1998**, *174*, 193-217.
(9) Miller, S. A.; Luo, H.; Jiang, X.; Rohrs, H. W.; Cooks, R. G. *Int. J. Mass Spectrom. Ion Processes* **1997**, *160*, 83-105.
(10) Alexander, W. A.; Morris, J. R.; Troya, D. *J. Phys. Chem. A* **2009**, *113*, 4155-4167.
(11) Alexander, W. A.; Troya, D. *J. Phys. Chem. C* **2011**, *115*, 2273-2283.
(12) Bosio, S. B. M.; Hase, W. L. *J. Chem. Phys.* **1997**, *107*, 9677-9686.
(13) Day, B. S.; Morris, J. R.; Troya, D. *J. Chem. Phys.* **2005**, *122*, 214712/1-214712/12.
(14) Gibson, K. D.; Isa, N.; Sibener, S. J. *J. Chem. Phys.* **2003**, *119*, 13083-13095.
(15) Isa, N.; Gibson, K. D.; Yan, T.; Hase, W.; Sibener, S. J. *J. Chem. Phys.* **2004**, *120*, 2417-2433.
(16) Martinez-Nunez, E.; Rahaman, A.; Hase, W. L. *J. Phys. Chem. C* **2007**, *111*, 354-364.
(17) Tasic, U.; Troya, D. *Phys. Chem. Chem. Phys.* **2008**, *10*, 5776-5786.
(18) Yan, T.; Hase, W. L. *Phys. Chem. Chem. Phys.* **2000**, *2*, 901-910.
(19) Yan, T.; Hase, W. L. *J. Phys. Chem. A* **2001**, *105*, 2617-2625.
(20) Yan, T.; Hase, W. L. *J. Phys. Chem. B* **2002**, *106*, 8029-8037.
(21) Yan, T.; Hase, W. L.; Barker, J. R. *Chem. Phys. Lett.* **2000**, *329*, 84-91.
(22) Yan, T.; Isa, N.; Gibson, K. D.; Sibener, S. J.; Hase, W. L. *J. Phys. Chem. A* **2003**, *107*, 10600-10607.
(23) Nogueira, J. J.; Sánchez-Coronilla, A.; Marques, J. M. C.; Hase, W. L.; Martinez-Nunez, E.; Vazquez, S. A. *Chem. Phys.* **2011**, *doi: 10.1016/j.chemphys.2011.02.014*.
(24) Vazquez, S. A.; Morris, J. R.; Rahaman, A.; Mazyar, O. A.; Vayner, G.; Addepalli, S. V.; Hase, W. L.; Martinez-Nunez, E. *J. Phys. Chem. A* **2007**, *111*, 12785-12794.

(25) Martinez-Nunez, E.; Rahaman, A.; Hase, W. L. *Journal of Physical Chemistry C* **2007**, *111*, 354-364.

(26) Pradeep, T.; Miller, S. A.; Cooks, R. G. *J. Am. Soc. Mass. Spectrom.* **1993**, *4*, 769.

(27) Curtiss, L. A.; Redfern, P. C.; Raghavachari, K. *J Chem Phys* **2007**, *126*, 084108.

(28) Nogueira, J. J.; Homayoon, Z.; Vazquez, S. A.; Martinez-Nunez, E. *J. Phys. Chem. C* **2011**, *(submitted)*.

(29) Nogueira, J. J.; Vazquez, S. A.; Lourderaj, U.; Hase, W. L.; Martinez-Nunez, E. *J. Phys. Chem. C* **2010**, *114*, 18455-18464.

(30) Nogueira, J. J.; Vazquez, S. A.; Mazyar, O. A.; Hase, W. L.; Perkins, B. G.; Nesbitt, D. J.; Martinez-Nunez, E. *J. Phys. Chem. A* **2009**, *113*, 3850-3865.

(31) Marques, J. M. C.; Prudente, F. V.; Pereira, F. B.; Almeida, M. M.; Maniero, A. M.; Fellows, C. E. *J. Phys. B: At., Mol. Opt. Phys.* **2008**, *41*, 085103/1-085103/15.

(32) Los, J.; Geerlings, J. J. C. *Phys. Rep.* **1990**, *190*, 133-90.

(33) Besler, B. H.; Merz, K. M.; Kollman, P. A. *Journal of Computational Chemistry* **1990**, *11*, 431-439.

(34) Singh, U. C.; Kollman, P. A. *Journal of Computational Chemistry* **1984**, *5*, 129-145.

(35) VENUS05 is a modified version of VENUS96. (a) Hase, W. L.; Duchovic, R. J.; Hu, X.; Komornicki, A.; Lim, K. F.; Lu, D.-h.; Peslherbe, G. H.; Swamy, K. N.; Vande Linde, S. R.; Varandas, A.; Wang, H.; Wolf, R. J. QCPE 1996, 16, 671. (b) Hu, X.; Hase, W. L.; Pirraglia, T. J. Comput. Chem. 1991, 12, 1014 ed.

(36) Allen, M. P.; Tildesley, D. J. *Computer Simulation of Liquids*; Oxford University Press: New York, 1987.

(37) Cortenraad, R.; Denier, v. d. G. A. W.; Brongersma, H. H.; Ermolov, S. N.; Glebovsky, V. G. *Phys. Rev. B: Condens. Matter Mater. Phys.* **2002**, *65*, 195414/1-195414/10.

(38) Ge, Y.; Whitten, J. E. *J. Phys. Chem. C* **2008**, *112*, 1174-1182.

(39) De, B. B.; Hadipour, A.; Mandoc, M. M.; Van, W. T.; Blom, P. W. M. *Adv. Mater. (Weinheim, Ger.)* **2005**, *17*, 621-625.

(40) Nakatsuji, H. *Chem. Phys. Lett.* **1978**, *59*, 362-4.

(41) Nakatsuji, H. *Chem. Phys. Lett.* **1979**, *67*, 329-33.

(42) Nakatsuji, H. *Chem. Phys. Lett.* **1979**, *67*, 334-42.

(43) Gaussian 09, M. J. F., G. W. Trucks, H. B. Schlegel, G. E. Scuseria, M. A. Robb, J. R. Cheeseman, G. Scalmani, V. Barone, B. Mennucci, G. A. Petersson, H. Nakatsuji, M. Caricato, X. Li, H. P. Hratchian, A. F. Izmaylov, J. Bloino, G. Zheng, J. L. Sonnenberg, M. Hada, M. Ehara, K. Toyota, R. Fukuda, J. Hasegawa, M. Ishida, T. Nakajima, Y. Honda, O. Kitao, H. Nakai, T. Vreven, J. A. Montgomery, Jr., J. E. Peralta, F. Ogliaro, M. Bearpark, J. J. Heyd, E. Brothers, K. N. Kudin, V. N. Staroverov, R. Kobayashi, J. Normand, K. Raghavachari, A. Rendell, J. C. Burant, S. S. Iyengar, J. Tomasi, M. Cossi, N. Rega, J. M. Millam, M. Klene, J. E. Knox, J. B. Cross, V. Bakken, C. Adamo, J. Jaramillo, R. Gomperts, R. E. Stratmann, O. Yazyev, A. J. Austin, R. Cammi, C. Pomelli, J. W. Ochterski, R. L. Martin, K.

Morokuma, V. G. Zakrzewski, G. A. Voth, P. Salvador, J. J. Dannenberg, S. Dapprich, A. D. Daniels, Ö. Farkas, J. B. Foresman, J. V. Ortiz, J. Cioslowski, and D. J. Fox; Revision A02 ed.; Gaussian, Inc: Wallingford CT, 2009.

(44) Glowacki, D. R.; Paci, E.; Shalashilin, D. V. *J. Phys. Chem. B* **2009**, *113*, 16603-16611.

(45) Somogyi, A.; Smith, D. L.; Wysocki, V. H.; Colorado, R.; Lee, T. R. *J. Am. Soc. Mass Spectrom.* **2002**, *13*, 1151-1161.

Chapter 12

Conclusions

Collisions of polyatomic molecules with a perfluorinated self-assembled monolayer surface were simulated by the classical trajectory method using the VENUS05 computer program developed by Hase and co-workers. The most important conclusions of this thesis are mentioned below.

Dynamics results of CO_2/F-SAM for several collision energies and employing different models for the F-SAM potential were presented in Chapters 6, 7 and 8. First, the trajectories were carried out with an all atom (AA) and a united atom (UA) model for the surface potential. The former takes into account all the atoms of the monolayer explicitly, while the latter treats the CF_3 and CF_2 units as single pseudoatoms. The results indicate that the UA model overestimates the efficiency of energy transfer to the surface because the UA F-SAM surface is softer than the AA one. The simulations also show that the mass of the surface atoms plays an important role in the dynamics. The amount of energy transferred to the monolayer increases when the mass is reduced because of the rise in chain flexibility. Analysis of rotational quantum number distributions and Doppler profiles shows that the results obtained with the AA model are in good agreement with experiments.

Several UA models for the F-SAM were developed in order to improve the results obtained by the old one. The only method which gets it was that whose parameters were obtained by random full rotation of CF_3 and CF_2 groups. This new UA model was demonstrated to be very useful because it is 3 times faster than the AA model but without affecting significantly the accuracy of the results with respect to the AA model.

The coupling between the two degenerate bends of the CO_2 molecule generates a vibrational angular momentum. Thus, excitations of these degenerate bends provide a good opportunity to investigate vibrational energy transfer between carbon dioxide and the surface. Before the collision with the monolayer, we observed unphysical bend energy leakage from the CO_2. After a detailed analysis of this issue, we found that trajectories that conserved their bend energies fulfill a particular relationship between the phases of the stretching and bending normal modes. We could not explain clearly this curious behaviour. An analysis of the vibrational temperatures provides again a reasonably good agreement with the experiments, and shows that the time scale needed to achieve bend energy accommodation is at least 50 ps.

A detailed analysis of energy transfer and stereodynamics for NO/F-SAM collisions was performed in Chapter 9. There, we found that thermal accommodation of the rotational degrees of freedom in NO is explained in terms of a minimum number of moderate variations in the direction of the rotational angular momentum. In addition, a new model that describes correctly the energy transfer was presented. This model predicts 100% efficiency of

energy transfer to the surface in the high collision energy limit. The stereodynamics analysis shows that the two preferred rotational motions of the scattered molecules are corkscrew and cartwheel. The available experimental data were compared with the simulations and we found again a good agreement.

Intermolecular potential energy surfaces for $SiNCS^+$/F-SAM and $(CH_3)_2SiNCS^+$/F-SAM were constructed with the help of a genetic algorithm, as described in Chapter 10. A DFT functional which accounts for dispersion forces was validated by comparing with fp-CCSD(T)/CBS calculations. In this work, we found that the equation formed by a Lennard-Jones potential with an electrostatic term, employed in most of the universal force fields, is not flexible enough for adjusting simultaneously the short and the long range of energies. The validity of using the CF_4 molecule as a model for the F-SAM surface during the parameterization was demonstrated.

Finally, results of $SiNCS^+$/F-SAM and $(CH_3)_2SiNCS^+$/F-SAM simulations to try to explain soft-landing experiments were discussed in Chapter 11. In this unfinished work, electron transfer from the gold surface to the projectiles seems to be a reasonable reason to explain the fact that the biggest ion, but not the smallest one, undergoes soft-landing. But, additional analysis and calculations are necessary to corroborate that and other possible reasons.

In general, under the above remarks, we can conclude that the classical trajectory approach is a reliable and useful technique for modelling gas/surface inelastic collisions. The knowledge of the behaviour of the system at each time allows us to make not only the computation of some properties from final conditions, but interesting analysis of time-dependent features.

The choice of initial conditions is a relevant issue and it must be done carefully because it influences strongly the dynamics of the system. When one tries to reproduce an experiment, the initial conditions must be selected accordingly to mimic the conditions of that experiment.

The development of an analytical potential energy surface for this type of systems is not trivial. In spite of the use of a simple model for representing the surface, the number of degrees of freedom is large, and therefore, the parameterization is a tedious task. Moreover, the parameters must be fitted according to the sort of interaction that they are representing. This topic is of special importance when a small model is employed to represent a bigger system, as in our case. A bad election of the parameters on the model may give rise to unrealistic interactions on the big system.